

VERSLAGEN EN VERHANDELINGEN

REPORTS AND TRANSACTIONS

**NATIONAAL LUCHT- EN RUIMTEVAART-
LABORATORIUM**

NATIONAL AEROSPACE LABORATORY NLR

THE NETHERLANDS

*

XXXVI - 1970

PREFACE

This Volume of Reports and Transactions of the National Aerospace Laboratory NLR contains a selection of reports completed in recent years.

In reports G 49 and G 50 the results of studies performed for the Netherlands Ministry of Defence are presented. Report TR 68069 U relates to research work promoted by the Netherlands Aircraft Development Board and Report TR 69007 U covers investigations for the European Office of Aerospace Research of the U.S. Airforce. The sponsors' permission for publication is herewith acknowledged. In addition to the selected reports issued at more or less regular intervals in the series Reports and Transactions, numerous others are published on work carried out by NLR. A list of publications to date is available upon request.

Amsterdam, February 1971

A. J. Marx

(General Director)

CONTENTS

NLR-TR F.261

R. J. Zwaan

On a kernel-function method for the calculation of the pressure distribution on a two-dimensional wing with harmonically oscillating control surface in subsonic flow.

NLR-TR G.49

P. J. Zandbergen, Th. E. Labrujere and J. G. Wouters

A new approach to the numerical solution of the equation of subsonic lifting surface theory.

NLR-TR G.50

Th. E. Labrujere

Computer application of a linearised supersonic lifting surface theory on a certain class of wings.

NLR-TR 68069U

H. Bergh and H. Tijdeman

Binary flutter calculations with theoretical and empirical aerodynamic derivatives for a wing-control surface system in two-dimensional incompressible flow.

NLR-TR 68117U

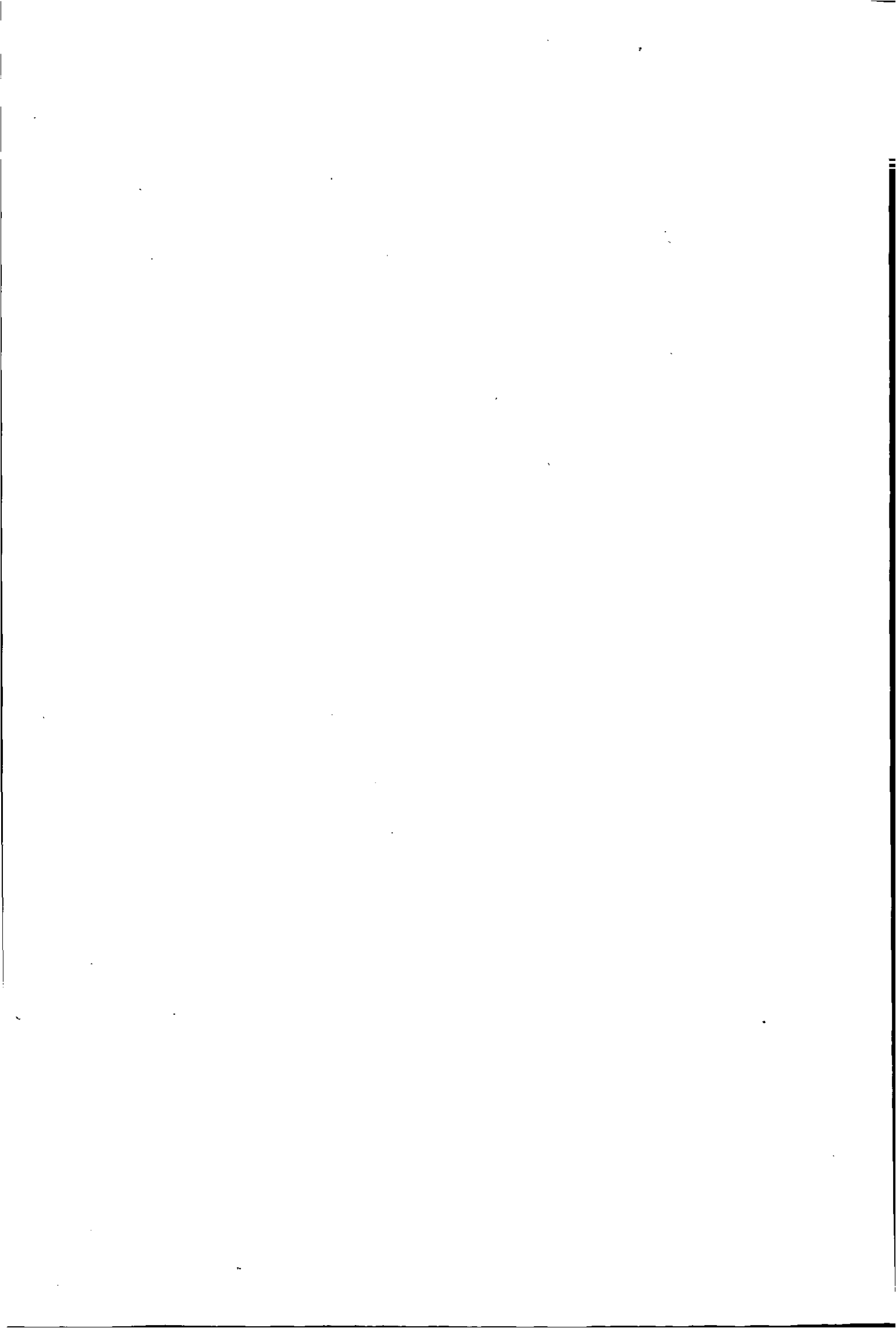
J. Schijve, F. A. Jacobs and P. J. Tromp

Crack propagation in aluminium alloy sheet materials under flight simulation loading.

NLR-TR 69007U

H. I. Baurdoux and J. W. Boerstael

Symmetrical transonic potential flows around quasi-elliptical aerofoil sections.



REPORT NLR-TR F.261

On a kernel-function method for the calculation of the pressure distribution on a two-dimensional wing with harmonically oscillating control surface in subsonic flow

by

R. J. Zwaan

Summary

The method presented contains the numerical solution of the Possio integral equation: the pressure distribution is approximated by a series of loading functions of which the coefficients are solved by collocation. Three terms in the series are singular; their type and strength are derived by a consideration of the local flow near the hinge axis. A convergence test on calculated results shows that two of them are important. A comparison with experimental results is given. This method may be extended very well to a wing of finite span.

Contents

	Page		
List of symbols	1	a_r	coefficients of regular terms in pressure series, (3.17)
1 Introduction	2		
2 Formulation of the problem	3	C_p	pressure coefficient, (2.8)
3 Pressure distribution in outer region	4	ΔC_p	pressure jump coefficient, (3.6)
4 Pressure distribution in inner region	5	$[D]$	matrix of aerodynamic influence coefficients, (6.11)
5 Matching procedure	6		
6 Determination of the matched pressure distribution	7	f_{ir}	(6.8) and (6.9)
6.1 Discussion of integral equation	7	g_{ij}	(6.8) and (6.9)
6.2 Collocation procedure	9	h	vibration mode, (2.2)
6.3 Calculation of pressure distribution and aerodynamic coefficients	9	h_r	pressure loading functions, (3.13)
7 Applications	9	k	reduced frequency, $=\omega l/U_\infty$
7.1 Comparison with results for incompressible flow	9	k_c	wing lift coefficient, (6.13)
7.2 Convergence test and comparison with results for compressible flow	10	K	kernel function, (6.3)
7.3 Comparison with experimental results for compressible flow	10	K_{s_1}, K_{s_2}, K_n	parts of kernel function, (6.5) to (6.7)
8 Concluding remarks	11	l	half wing chord length
9 Acknowledgement	11	L_0, L_1, L_2	logarithmic pressure loading functions, (3.15) to (3.17)
10 References	11	m_c	wing moment coefficient, (6.14)
Appendix A	12	M_∞	Mach number
Appendix B	13	n_c	hinge moment coefficient, (6.15)
Appendix C	14	p	static pressure
1 table		q	stagnation pressure
6 figures		R	number of h_r -functions in pressure series
		t	time
		U	velocity in x-direction
		x, z	cartesian co-ordinates
		α	normal wash, (6.2)
		α_m	modified normal wash, (6.4)
		β_∞	$=\sqrt{1-M_\infty^2}$
		γ	specific heat ratio
		δ	control surface deflection, (2.1)
		ε	stretching parameter, (4.1)
		θ	angular co-ordinate, (3.14)

List of Symbols

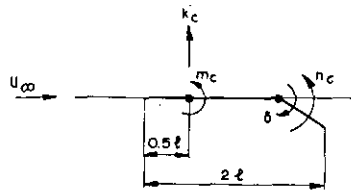
a	speed of sound, (2.5)
$a_{c_0}, a_{c_1}, a_{c_2}$	coefficients of logarithmic terms in pressure series, (3.17)

λ	coefficient in inner or outer expansion, (3.1) or (4.3)	c	relates to: hinge axis location
τ	ratio between control surface chord and wing chord	i	inner region
φ, ϕ	velocity potentials	o	outer region
ψ	acceleration potential, (3.7)		
ω	radial frequency		

Subscripts

∞ relates to: free stream

Positive directions:



1 Introduction

Two occasions have led to the work reported here:

- theoretical unsteady pressure distributions were needed to compare with distributions measured on a two-dimensional wing with a harmonically oscillating control surface in subsonic flow;
- recently the need was felt of possessing a computer programme for the calculation of pressure distributions on wings of finite span provided with oscillating control surfaces. In an introductory study some new ideas had to be checked for the limit case of a two-dimensional wing.

These occasions effected the development of a computer programme to calculate pressure distributions on a two-dimensional wing with an oscillating aerodynamically unbalanced control surface (surface rotating about its leading edge).

Already years ago Timman and van de Vooren formulated an analytical method for such configurations, proceeding directly from the linearised differential equation for the acceleration potential (ref. 1). In this work the singular behaviour of the boundary conditions at the hinge axis was taken into account. Accurate numerical results for the aerodynamic wing and control surface coefficients were obtained (ref. 2), which are used for comparison in the present report. However, the expressions for the pressure distribution were rather complicated and unattractive for programming, as – even more heavily weighing disadvantage – this method basically did not contain the possibility to be extended to wings of finite span.

Methods for subsonic flow that have shown a large flexibility in the application to numerous types of wing planform, are the kernel-function methods, based on the solution of the linearised integral equation relating the given normal wash at the wing and the unknown pressure distribution. For a two-dimensional wing this equation degenerates to the well-known Possio integral equation (see expressions (6.1) to (6.3) in this report):

$$\alpha(x) = \frac{1}{4\pi} \int_{-1}^1 \Delta C_p(x') K(x, x'; k, M_\infty) dx'$$

If a control surface is present a singularity occurs in the normal wash $\alpha(x)$ and, through that, also in the pressure distribution $\Delta C_p(x)$.

Two such methods have been developed in the past dealing with oscillating control surfaces. Essence of the first one, devised by Dietze (ref. 3), was to start from the solution for zero Mach number, given by Küssner and Schwarz (ref. 4) and to apply an iterative procedure to the integral equation. Numerical results have been given in ref. 5. In the second method, devised by Schade (ref. 6), the pressure distribution and kernel-function were expanded in Legendre polynomials through which, making use of their orthogonality properties, the integral equation was transformed to a matrix equation for the unknown coefficients in the expansion of $\Delta C_p(x)$. One difference between both methods should be noted: in the first one the convergence of the solution for the pressure distribution is rather poor, especially in the neighbourhood of the hinge axis, as has been pointed out already by Karp and Weil (ref. 7). The convergence in the second method has been improved by including a singular term in the expansion of $\Delta C_p(x)$. Schade demonstrated by a limit process that the singularity should be logarithmic and calculated the strength of it. No numerical results were given by him. Although extension to wings of finite span is possible, both methods have been superseded by the use of modern computers.

Recently the correctness of Schade's logarithmic term has been confirmed by Landahl (ref. 8). He considered the local flow near the hinge axis by stretching the geometrical co-ordinates in the differential equation for the pressure potential.

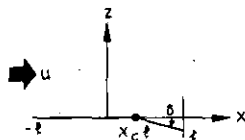
At the NLR experience has been gained with the application of a kernel-function method to wings without control surface (ref. 9). In this method the pressure distribution is approximated by a series of prescribed functions. The coefficients in this series are determined by collocation, i.e. by requiring that in a number of points on the wing

the calculated normal wash should be equal to the wash derived from the vibration mode. Because of this experience extensions are being investigated in order to deal also with control surfaces. A combination of this method together with Landahl's technique seems to yield an attractive way.

In the present report the two-dimensional wing is considered as a first step. The method discussed extends refs. 6 and 8 in that it regards two more logarithmic terms in the series for the pressure distribution. Results are compared with values taken from refs. 2 and 4. A convergence test is made for a combination of high Mach number and reduced frequency. Finally, comparisons are made with experimental values obtained by Tijdeman and Bergh (ref. 10).

2 Formulation of the problem

An infinitely thin aerofoil of length $2l$ is considered, immersed in an ideal fluid that is moving with an uniform subsonic velocity U_∞ far upstream in the direction of the positive x -axis. The aerofoil consists of a stationary front part and a control surface with hinge at $x = x_c l$, oscillating harmonically with amplitude δ and radial frequency ω . In the mean position the aerofoil has zero incidence.



In the following considerations only dimensionless quantities will be used: lengths divided by l , velocities by U_∞ and time by l/U_∞ . The aerofoil motion is defined by

$$z\langle x \rangle = -\delta h\langle x \rangle e^{ikt}, \quad (2.1)$$

where

$$h\langle x \rangle = (x - x_c) u\langle x - x_c \rangle. \quad (2.2)$$

$u\langle x \rangle$ represents the unit-step function and k the reduced frequency $\omega l/U_\infty$. Premise in the following considerations is that δ be a small quantity,

$$\delta \ll 1. \quad (2.3)$$

Assuming an isentropic non-viscous flow, it is allowed to introduce a velocity potential $\phi\langle x, z, t \rangle$. From the continuity equation, Bernoulli equation and equation of state a non-linear second order partial differential equation can be derived that should be satisfied by ϕ (see ref. 11):

$$(a^2 - U^2)\phi_{xx} + (a^2 - \phi_z^2)\phi_{zz} - 2U\phi_z\phi_{xz} - \phi_{tt} - 2(U\phi_{xt} + \phi_z\phi_{zt}) = 0, \quad (2.4)$$

where a denotes the local speed of sound given by

$$a^2 = M_\infty^{-2} - \frac{\gamma-1}{2} (2\phi_x + \phi_x^2 + \phi_z^2 + 2\phi_t) \quad (2.5)$$

and where U denotes the local velocity in x -direction

$$U = 1 + \phi_x. \quad (2.6)$$

The boundary conditions at the aerofoil are dictated by the requirement that the flow be tangential to the surface:

$$\phi_z = -\delta(Uh_x + ikh)e^{ikt} = -\delta[Uu\langle x - x_c \rangle + ik(x - x_c)u\langle x - x_c \rangle]e^{ikt} \text{ on } z = -\delta h e^{ikt}. \quad (2.7)$$

Additional boundary conditions require that the flow should be undisturbed at infinity and that the pressure should be continuous at the trailing edge. The pressure coefficient depends on the velocity potential as follows:

$$C_p = \frac{p - p_\infty}{q_\infty} = \frac{2}{\gamma M_\infty^2} \{ [1 - (\gamma - 1)M_\infty^2 (\phi_t + \phi_x + \frac{1}{2}\phi_x^2 + \frac{1}{2}\phi_z^2)]^{\gamma-1} - 1 \}. \quad (2.8)$$

It is immediately seen from (2.7) that a singularity occurs in the boundary condition at $x = x_c$. One may expect that this gives rise to a singularity in the pressure distribution at the aerofoil as well. The problem that will be studied in the following chapters is how to obtain a solution for the pressure distribution along the aerofoil to first order in δ in which the influence of the discontinuity at $x = x_c$ has been fully taken into account. In order to investigate this singular behaviour the flow in the vicinity of the hinge line will be subjected to a detailed study.

The pressure distribution found in this region – designated as “inner region” – will be matched afterwards with the distribution in the “outer region” that extends from leading to trailing edge, but excludes the small inner region at $x = x_c$.

3 Pressure distribution in outer region

First a straight forward solution for ϕ in the outer region is sought without bothering about the singularity in the boundary conditions at $x = x_c$. For ϕ the following asymptotic expansion, the “outer expansion”, is substituted

$$\phi_0 \langle x, z, t \rangle = \sum_n \lambda_0^{(n)} \langle \delta \rangle \varphi_0^{(n)} \langle x, z, t \rangle, \quad (3.1)$$

where the coefficients $\lambda_0^{(n)}$, representing the orders of the corresponding solutions $\varphi_0^{(n)}$, depend on the parameter δ . By doing this in boundary condition (2.7), δ will appear explicitly as well as implicitly in the derivatives of ϕ . To remove this inconvenience primarily Taylor expansions for ϕ are used to express the boundary condition in terms valid for $z=0$ (it is assumed that ϕ is analytic in z). Thus, the boundary condition becomes

$$\phi_z \langle x, 0, t \rangle + \delta h \phi_{zz} \langle x, 0, t \rangle + \dots = -\delta [(1 + \phi_x \langle x, 0, t \rangle + \delta h \phi_{xz} \langle x, 0, t \rangle + \dots) h_x e^{ikt} + ikh e^{ikt}] \quad \text{on } z=0 \quad (3.2)$$

After substitution of ϕ_0 in cond. (2.7) terms of equal order are compared. Then it appears that a proper choice for the coefficients $\lambda_0^{(n)}$ is

$$\lambda_0^{(n)} = \delta^n. \quad (3.3)$$

The solutions $\varphi_0^{(n)}$ can be found from a series of linear differential equations with linear boundary conditions. To first order, $\lambda_0^{(1)} = \delta$, they read (after dividing by the time-dependent factor e^{ikt}):

$$\begin{aligned} (1 - M_\infty^2) \varphi_{0_{xx}}^{(1)} + \varphi_{0_{zz}}^{(1)} - 2ik M_\infty^2 \varphi_{0_x}^{(1)} + k^2 M_\infty^2 \varphi_0^{(1)} &= 0 \\ \varphi_{0_z}^{(1)} &= -(h_x + ikh) \text{ at } z = 0. \end{aligned} \quad (3.4)$$

Higher order solutions will not be considered here. To first order the pressure coefficient becomes

$$C_{p_0}^{(1)} = -2(\varphi_{0_x}^{(1)} + ik\varphi_0^{(1)}). \quad (3.5)$$

Due to the antisymmetry of $\varphi_0^{(1)}$ with respect to z , the pressure jump across the aerofoil is

$$\Delta C_{p_0}^{(1)} = C_{p_0}^{(1)} \langle x, -0 \rangle - C_{p_0}^{(1)} \langle x, +0 \rangle = 4(\varphi_{0_x}^{(1)} + ik\varphi_0^{(1)}). \quad (3.6)$$

The solution of (3.4) together with the additional boundary conditions mentioned in sect. 2, has been subject of most studies referred to in sect. 1. It proved advantageous to introduce the acceleration potential defined by

$$\psi_0^{(1)} = \varphi_{0_x}^{(1)} + ik\varphi_0^{(1)}. \quad (3.7)$$

$\psi_0^{(1)}$ also satisfies eq. (3.4) and simplifies the boundary condition on the x -axis to

$$\psi_0^{(1)} = 0 \text{ for } x < -1 \text{ and } x \geq 1. \quad (3.8)$$

Moreover, the pressure jump is simply obtained by

$$\Delta C_{p_0}^{(1)} = 4\psi_0^{(1)}. \quad (3.9)$$

A solution for $\psi_0^{(1)}$ is conveniently found after transforming the differential equation and boundary conditions into an integral equation. This equation, derived at first by Possio (see ref. 12), relates the unknown $\Delta C_{p_0}^{(1)}$ and the given normal wash $\varphi_{0_z}^{(1)}$ at the aerofoil. The integral equation may be solved by approximating the pressure distribution by the series expression

$$\Delta C_{p_0}^{(1)} = \sum_{r=0}^R a_r h_r \langle x \rangle \quad (3.10)$$

in which each function $h_r \langle x \rangle$ should exhibit a singularity for $x \rightarrow -1$ of the type

$$\lim_{\varepsilon \rightarrow 0} \varepsilon^{-\frac{1}{2}} \quad (3.11)$$

and $h_r \langle x \rangle$ should become zero for $x \rightarrow 1$ like

$$\lim_{\varepsilon \rightarrow 0} \varepsilon^{\frac{1}{2}} \quad (3.12)$$

This behaviour can be revealed in an analogous way as is discussed here for the region near the hinge axis, by studying the local flow at leading and trailing edge (see ref. 8). Such a study is not pursued here and the behaviour of $h_r \langle x \rangle$ at leading and trailing edge is put to be given by (3.11) and (3.12). Functions that meet these requirements are

$$h_r \langle x \rangle = \frac{2}{\pi} \frac{\cos r\theta + \cos(r+1)\theta}{\sin \theta}, \quad r=0, 1, \dots, R \quad (3.13)$$

where θ is an angular co-ordinate, given by

$$\cos \theta = -x. \quad (3.14)$$

The first three functions are shown in fig. 1. After substitution of (3.10) in the integral equation the unknown coefficients $a_r^{(1)}$ may be solved by some collocation procedure. Details about the integral equation and the collocation procedure are not given here with reference to sect. 6.

It is important to realise that all functions $h_r \langle x \rangle$ are continuous at $x = x_c$, so that they are potentially unfit for approximating the singular behaviour of the pressure distribution with a finite (and preferably small) number R . However, to the series (3.10) other functions may be added that are singular themselves or in its derivatives at $x = x_c$, but otherwise do not violate the behaviour as expressed by (3.11) and (3.12). This means that the singularity at the leading edge may not be stronger than $\varepsilon^{-\frac{1}{2}}$ as $\varepsilon \rightarrow 0$ and the exponent of ε at the trailing edge may not be less than $\frac{1}{2}$. Such functions are:

$$L_0 = \frac{2}{\pi} \ln \left| \frac{1 - \cos(\theta + \theta_c)}{1 - \cos(\theta - \theta_c)} \right|, \quad (3.15)$$

$$L_1 = (x - x_c) L_0, \quad (3.16)$$

$$L_2 = (x - x_c)^2 L_0. \quad (3.17)$$

These functions have been drawn in fig. 2 for $\tau = 0.25$. They have been taken from the analytic solution of $\psi_0^{(1)}$ for $M_\infty = 0$, which has been derived by Küssner and Schwarz (ref. 4). Of course also other functions with singularities at $x = x_c$ and satisfying the above requirements may be added.

Allowing for the singular terms, the pressure distribution can be written as

$$\Delta C_{p_0}^{(1)} = \sum_{r=0}^R a_r h_r \langle x \rangle + a_{c_0} L_0 \langle x, x_c \rangle + a_{c_1} L_1 \langle x, x_c \rangle + a_{c_2} L_2 \langle x, x_c \rangle + \dots \quad (3.18)$$

The coefficients a_{c_0} , a_{c_1} and a_{c_2} are unknown as yet, but should be determined after matching $\Delta C_{p_0}^{(1)}$ with the pressure distribution in the inner region.

4 Pressure distribution in inner region

In order to study the local flow in the vicinity of the hinge line at $x = x_c$, the x - and z -co-ordinate are stretched using a stretching parameter ε :

$$x_i = \frac{x - x_c}{\varepsilon}, \quad z_i = \frac{z}{\varepsilon}. \quad (4.1)$$

This proceeding pushes away the influence of leading and trailing edge on the local flow at the hinge line. To obtain a well-posed inner problem the velocity potential should be transformed simultaneously

$$\phi_i = \frac{\phi}{\varepsilon}. \quad (4.2)$$

Like for the outer region an "inner expansion" is introduced for ϕ_i :

$$\phi_i \langle x, z, t \rangle = \sum_n \lambda_i^{(n)} \langle \delta, \varepsilon \rangle \varphi_i^{(n)} \langle x, z, t \rangle \quad (4.3)$$

and substituted in eq. (2.4) and cond. (3.2) (also in this case the boundary condition for $x > x_c$ or $x_i > 0$ may be expressed in terms valid for $z_i = 0$ as the control surface deflection δ has not been changed under the stretching of x and z). Examination of the boundary condition reveals that a proper choice for the coefficients is

$$\lambda_i^{(1)} = \delta, \lambda_i^{(2)} = \delta\varepsilon, \lambda_i^{(3)} = \delta\varepsilon^2, \lambda_i^{(4)} = \delta^2, \text{ etc.} \quad (4.4)$$

To first order in δ the following series of linear differential equations with corresponding boundary conditions are found:

$$\left. \begin{aligned} &\text{order } \lambda_i^{(1)}: \\ &(1 - M_\infty^2) \varphi_{i_{x_i z_i}}^{(1)} + \varphi_{i_{z_i z_i}}^{(1)} = 0, \\ &\varphi_{i_{z_i}}^{(1)} = -u \langle x_i \rangle \quad \text{at } z_i = 0; \end{aligned} \right\} \quad (4.5)$$

$$\left. \begin{aligned} &\text{order } \lambda_i^{(2)}: \\ &(1 - M_\infty^2) \varphi_{i_{x_i x_i}}^{(2)} + \varphi_{i_{z_i z_i}}^{(2)} = 2ik M_\infty^2 \varphi_{i_{x_i}}^{(1)}, \\ &\varphi_{i_{z_i}}^{(2)} = -ik x_i u \langle x_i \rangle \quad \text{at } z_i = 0; \end{aligned} \right\} \quad (4.6)$$

$$\left. \begin{aligned} &\text{order } \lambda_i^{(3)}: \\ &(1 - M_\infty^2) \varphi_{i_{x_i x_i}}^{(3)} + \varphi_{i_{z_i z_i}}^{(3)} = 2ik M_\infty^2 \varphi_{i_{x_i}}^{(2)} - k^2 M_\infty^2 \varphi_{i_{x_i}}^{(1)}, \\ &\varphi_{i_{z_i}}^{(3)} = 0 \quad \text{at } z_i = 0. \end{aligned} \right\} \quad (4.7)$$

The additional boundary conditions mentioned in sect. 2 are not relevant here, as they belong completely to the outer region.

The pressure coefficient, expressed in inner variables, becomes to first order

$$\left. \begin{aligned} C_{p_i}^{(1)} &= C_{p_i}^{(10)} + \varepsilon C_{p_i}^{(11)} + \varepsilon^2 C_{p_i}^{(12)}, \\ \text{where: } C_{p_i}^{(10)} &= -2\varphi_{i_{x_i}}^{(1)}, \\ C_{p_i}^{(11)} &= -2(\varphi_{i_{x_i}}^{(2)} + ik \varphi_{i_{x_i}}^{(1)}), \\ C_{p_i}^{(12)} &= -2(\varphi_{i_{x_i}}^{(3)} + ik \varphi_{i_{x_i}}^{(2)}). \end{aligned} \right\} \quad (4.8)$$

The pressure jump across the aerofoil is defined analogous to (3.6):

$$\Delta C_{p_i}^{(1)} = C_{p_i}^{(1)} \langle x_i, -0 \rangle - C_{p_i}^{(1)} \langle x_i, +0 \rangle = -2C_{p_i}^{(1)} \langle x_i, +0 \rangle. \quad (4.9)$$

The solutions of (4.5) to (4.7) are not given here, but reference is made to appendix A for details. When these solutions are substituted in (4.9) the pressure distribution appears to be

$$\left. \begin{aligned} \Delta C_{p_i}^{(1)} &= \Delta C_{p_i}^{(10)} + \varepsilon \Delta C_{p_i}^{(11)} + \varepsilon^2 \Delta C_{p_i}^{(12)} + P^{(1)} \\ \text{where: } \Delta C_{p_i}^{(10)} &= -\frac{4}{\pi \beta_\infty} \ln |x_i| \\ \Delta C_{p_i}^{(11)} &= -\frac{4ik}{\pi \beta_\infty} \frac{2 - M_\infty^2}{\beta_\infty^2} x_i \ln |x_i| \\ \Delta C_{p_i}^{(12)} &= \frac{k^2}{\pi \beta_\infty} \frac{2 + 7M_\infty^2 - 6M_\infty^4}{\beta_\infty^4} x_i^2 \ln |x_i| \end{aligned} \right\} \quad (4.10)$$

with $\beta_\infty = \sqrt{1 - M_\infty^2}$. $P^{(1)}$ represents a set of regular eigensolutions of all kinds of order; besides 1, ε and ε^2 also $\ln \varepsilon$, $\varepsilon \ln \varepsilon$, etc. may occur. Some of these eigensolutions may be determined after matching with the pressure distribution in the outer region.

5 Matching procedure

The outer expansion (3.17) shall be matched with the inner expansion (4.10) according to the limit matching principle, stating:

the outer limit of the inner expansion = the inner limit of the outer expansion.

(for a discussion of this principle, see ref. 13).

The inner limit of the outer expansion as $x \rightarrow x_\infty$ is:

$$\begin{aligned} \Delta C_{p0}^{(1)} \sim & -\frac{4}{\pi} a_{c0} \ln |x-x_c| - \frac{4}{\pi} a_{c1} (x-x_c) \ln |x-x_c| - \\ & - \frac{4}{\pi} a_{c2} (x-x_c)^2 \ln |x-x_c| + \text{regular terms in } x. \end{aligned} \quad (5.1)$$

The outer limit of the inner expansion as $|x_i| \rightarrow \infty$, is:

$$\begin{aligned} \Delta C_{p1}^{(1)} \sim & -\frac{4}{\pi\beta_\infty} \ln |x_i| - \varepsilon \frac{4ik}{\pi\beta_\infty} \frac{2-M_\infty^2}{\beta_\infty^2} x_i \ln |x_i| + \varepsilon^2 \frac{k^2}{\pi\beta_\infty} \frac{2+7M_\infty^2-6M_\infty^4}{\beta_\infty^4} x_i^2 \ln |x_i| + \text{regular terms in } x_i \\ \sim & -\frac{4}{\pi\beta_\infty} \ln |x-x_c| - \frac{4ik}{\pi\beta_\infty} \frac{2-M_\infty^2}{\beta_\infty^2} (x-x_c) \ln |x-x_c| + \frac{k^2}{\pi\beta_\infty} \frac{2+7M_\infty^2-6M_\infty^4}{\beta_\infty^4} (x-x_c)^2 \ln |x-x_c| + \\ & + \text{regular terms in } x. \end{aligned} \quad (5.2)$$

Comparison of (5.1) and (5.2) reveals that

$$a_{c0} = \frac{1}{\beta_\infty}, \quad (5.3)$$

$$a_{c1} = ik \frac{2-M_\infty^2}{\beta_\infty^3}, \quad (5.4)$$

$$a_{c2} = -k^2 \frac{2+7M_\infty^2-6M_\infty^4}{4\beta_\infty^5}. \quad (5.5)$$

The above matching principle has only applied to the terms that are singular or have singular derivatives as $x \rightarrow x_c$. When this principle is also applied to terms that are regular in x as $x \rightarrow x_c$, some unknown eigensolutions in the inner region (see (4.10)) may be determined. Because they play no role furthermore, they will not be investigated.

Thus, the final result of the matching procedure is that the pressure distribution along the aerofoil can be represented to order δ by the series

$$\Delta C_p = \delta \Delta C_p^{(1)} = \delta \left[\sum_{r=0}^R a_r h_r + \frac{1}{\beta_\infty} L_0 + ik \frac{2-M_\infty^2}{\beta_\infty^3} L_1 - k^2 \frac{2+7M_\infty^2-6M_\infty^4}{4\beta_\infty^5} L_2 \right] \quad (5.6)$$

in which full allowance has been made for the profile discontinuity at the hinge axis.

6 Determination of the matched pressure distribution

6.1 Discussion of integral equation

The Possio integral equation, already mentioned in sect. 3, reads

$$\alpha \langle x \rangle = \frac{1}{4\pi} \oint_{-1}^1 \Delta C_p \langle x' \rangle K \langle x, x'; k, M_\infty \rangle dx' \quad (6.1)$$

where the normal wash α is given by

$$\alpha \langle x \rangle = -\delta \left(\frac{\partial h}{\partial x} + ikh \right) = -\delta (u \langle x-x_c \rangle + ik(x-x_c)u \langle x-x_c \rangle), \quad (6.2)$$

and the kernel-function K is given by

$$\begin{aligned} K \langle x, x'; k, M_\infty \rangle = & \frac{\pi k e^{-ik(x-x')}}{4\beta_\infty} \left\{ e^{i(k(x-x')/\beta_\infty^2)} \left[i \frac{M_\infty(x-x')}{|x-x'|} H_1^{(2)} \left\langle \frac{M_\infty k |x-x'|}{\beta_\infty^2} \right\rangle - H_0^{(2)} \left\langle \frac{M_\infty k |x-x'|}{\beta_\infty^2} \right\rangle \right] \right. \\ & \left. + 2 \frac{i\beta_\infty}{\pi} \ln \left\langle \frac{1+\beta_\infty}{M_\infty} \right\rangle + i\beta_\infty^2 \int_0^{k(x-x')/\beta_\infty^2} e^{iu} H_0^{(2)} \langle M_\infty |u| \rangle du \right\}. \end{aligned} \quad (6.3)$$

This equation has been derived in ref. 12. The unknown pressure distribution ΔC_p is approximated by the series expression (5.6).

Thus, the solution of the pressure distribution involves the determination of the coefficients a_r . Rearranging terms, eq. (6.1) can be written as (per unit δ)

$$\begin{aligned}
\alpha_m \langle x \rangle &= \alpha \langle x \rangle - \frac{1}{4\pi\beta_\infty} \oint_{-1}^1 L_0 \langle x' \rangle K \langle x, x'; k, M_\infty \rangle dx' - ik \frac{2-M_\infty^2}{4\pi\beta_\infty^3} \oint_{-1}^1 L_1 \langle x' \rangle K \langle x, x'; k, M_\infty \rangle dx' + \\
&+ k^2 \frac{2+7M_\infty^2-6M_\infty^4}{16\pi\beta_\infty^5} \oint_{-1}^1 L_2 \langle x' \rangle K \langle x, x'; k, M_\infty \rangle dx' = \\
&= \frac{1}{4\pi} \sum_{r=0}^R a_r \oint_{-1}^1 h_r \langle x' \rangle K \langle x, x'; k, M_\infty \rangle dx'. \tag{6.4}
\end{aligned}$$

The left hand side of this equation, $\alpha_m \langle x \rangle$, represents a modified normal wash that is smoothly distributed from leading to trailing edge. In this way the difficulties have been removed in approximating the pressure distribution by functions h_r , that were due to the discontinuous distribution of the normal wash $\alpha \langle x \rangle$.

The kernel-function is singular for $x' \rightarrow x$. In the integration procedure it is convenient to separate the singular parts, being

$$K_{s_1} = -\frac{\beta_\infty}{2(x-x')}, \tag{6.5}$$

$$K_{s_2} = i \frac{k}{2\beta_\infty} \ln |x-x'|. \tag{6.6}$$

The remaining regular part is

$$K_n = K - K_{s_1} - K_{s_2}. \tag{6.7}$$

In a condense notation eq. (6.4) can be written as

$$\begin{aligned}
\alpha \langle x \rangle &- \frac{1}{4\pi} a_{c_0} (g_{01} + g_{11} + g_{21}) - \frac{1}{4\pi} a_{c_1} (g_{02} + g_{12} + g_{22}) + \\
&- \frac{1}{4\pi} a_{c_2} (g_{03} + g_{13} + g_{23}) = \frac{1}{4\pi} \sum_{r=0}^R a_r (f_{0r} + f_{1r} + f_{2r}) \tag{6.8}
\end{aligned}$$

where:

$$g_{01} = \oint_{-1}^1 L_0 \langle x' \rangle K_{s_1} \langle x, x'; k, M_\infty \rangle dx'$$

$$g_{11} = \int_{-1}^1 L_0 \langle x' \rangle K_{s_2} \langle x, x'; k, M_\infty \rangle dx'$$

$$g_{21} = \int_{-1}^1 L_0 \langle x' \rangle K_n \langle x, x'; k, M_\infty \rangle dx'$$

$$g_{02} = \oint_{-1}^1 L_1 \langle x' \rangle K_{s_1} \langle x, x'; k, M_\infty \rangle dx'$$

$$g_{12} = \int_{-1}^1 L_1 \langle x' \rangle K_{s_2} \langle x, x'; k, M_\infty \rangle dx'$$

$$g_{22} = \int_{-1}^1 L_1 \langle x' \rangle K_n \langle x, x'; k, M_\infty \rangle dx'$$

$$g_{03} = \oint_{-1}^1 L_2 \langle x' \rangle K_{s_1} \langle x, x'; k, M_\infty \rangle dx'$$

$$g_{13} = \int_{-1}^1 L_2 \langle x' \rangle K_{s_2} \langle x, x'; k, M_\infty \rangle dx'$$

$$g_{23} = \int_{-1}^1 L_2 \langle x' \rangle K_n \langle x, x'; k, M_\infty \rangle dx'$$

$$f_{0r} = \oint_{-1}^1 h_r \langle x' \rangle K_{s_1} \langle x, x'; k, M_\infty \rangle dx'$$

$$f_{1r} = \int_{-1}^1 h_r \langle x' \rangle K_{s_2} \langle x, x'; k, M_\infty \rangle dx'$$

$$f_{2r} = \int_{-1}^1 h_r \langle x' \rangle K_n \langle x, x'; k, M_\infty \rangle dx'. \tag{6.9}$$

The functions g_{21} , g_{22} , g_{23} and f_{2r} are calculated numerically using a trapezoidal rule; the inner integral in K_n is calculated analytically after approximating the Hankel function by a polynomial. The remaining functions in (6.9) can be calculated analytically; results are given in appendix B.

6.2 Collocation procedure

The unknown coefficients a_r in eq. (6.8) are determined by a collocation procedure: in $R+1$ points $x=x_p$ on the aerofoil, of which the location is given by

$$x_p = -\cos \frac{2\pi(p+1)}{2R+3}, \quad p=0, 1, \dots, R, \quad (6.10)$$

the modified normal wash is calculated (right hand side of (6.8)) and put equal to the prescribed wash (left hand side of (6.8)). In this way a set of $R+1$ linear algebraic equations for a_r is formed which can be represented in matrix notation:

$$\{4\pi\alpha_m\} = [D]\{a_r\}. \quad (6.11)$$

Then, the coefficients a_r are easily solved:

$$\{a_r\} = [D]^{-1}\{4\pi\alpha_m\}. \quad (6.12)$$

A useful alternative to improve the accuracy of the a_r 's is the application of a least squares method (refs. 14 and 15) or a variational method (refs. 16 and 17). The latter can be reduced to a collocation method as described above with an optimum location of the collocation points as given by (6.10).

6.3 Calculation of pressure distributions and aerodynamic coefficients

Once the coefficients a_r are known, the pressure distribution is readily calculated from (5.6).

Other aerodynamic quantities of interest are the wing lift and moment coefficient and the hinge moment coefficient. They will be defined here according to the notation introduced by Küssner:

$$k_c = \frac{1}{2\pi} \int_{-1}^1 \Delta C_p^{(1)} dx, \quad (6.13)$$

$$m_c = \frac{1}{2\pi} \int_{-1}^1 \Delta C_p^{(1)}(x+0.25) dx, \quad (\text{about } \frac{1}{4}\text{-chord point}) \quad (6.14)$$

$$n_c = \frac{1}{2\pi} \int_{x_c}^1 \Delta C_p^{(1)}(x-x_c) dx. \quad (6.15)$$

All three coefficients can be expressed in analytical forms, see appendix C.

7 Applications

7.1 Comparison with results for incompressible flow

In ref. 4 Küssner and Schwarz have given an analytical solution of the first order problem in case of incompressible flow. Their results for the pressure distribution should be exactly the same as the results obtained with the present method for $R=2$. In the following table the coefficients a_r in the pressure series as well as the wing and control surface coefficients have been compared for $\tau=0.25$ and $k=1$.

M=0 k=1	Küssner/Schwarz		Present method	
a_0	+0.55291	+1.79722i	+0.55286	+1.79720i
a_1	+0.17122	-2.09435i	+0.17115	-2.09431i
a_2	-0.26180	0	-0.26170	0
k_c	+0.65841	+0.29642i	+0.65839	+0.29640i
m_c	+0.37763	+0.33333i	+0.37764	+0.33332i
n_c	+0.02631	+0.04155i	+0.02631	+0.04155i

The values obtained with the present method did not change after increasing the accuracy of the integrations in (6.9).

The agreement of the above values is satisfactory.

7.2 Convergence test and comparison with results for compressible flow

To get an idea of the effectiveness of the logarithmic terms in the pressure series a convergence test has been made on the wing and control surface coefficients for $\tau=0.3$, $M_\infty=0.8$ and $k=0.9$. The procedure is that the logarithmic terms have been added successively to the pressure series, as in each stage the value of R has been increased from 2 to 14 by steps of 2. The results should be compared with "exact" values, i.e. values corresponding to such large R that an increase of it has no influence on the coefficients any more. In the test this value of R has not been pursued in order to avoid a lengthy computational labour, but the "exact" coefficients have been estimated by taking the mean values for $R=10, 12$ and 14 with all logarithmic terms included in the pressure series. The convergence test is presented in table 1. The accuracy of the coefficients is indicated by asterisks: one asterisk marks that the signed values and also those for higher R are accurate within 1% of the modulus of the "exact" values, two asterisks mark an accuracy of 1%/ ∞ .

Although the procedure in this test may be somewhat rough, nevertheless two facts can be observed:

- a satisfactory convergence is only obtained by including the first two logarithmic terms in the pressure series;
- the influence of the third logarithmic term on the convergence may be neglected.

To illustrate the effectiveness of the logarithmic terms the original normal wash as well as the wash modified by successively adding the terms to the pressure series, have been depicted in fig. 3. They show that the discontinuity in the slope of $\text{Im} \langle \alpha_m \rangle$ has been completely removed after adding the term $a_{c1} L_1$.

Another illustration of the influence of the logarithmic terms is given in fig. 4 by the pressure distributions for $R=8$. The mutual differences between the distributions 1, 2 and (3,4) are not negligible as those between 3 and 4 are too small to be drawn in the figure.

In the following table the "exact" values are compared with coefficients given in ref. 2:

$M=0.8$ $k=0.9$	Timman/van de Vooren		Present method	
k_c	0.48031	-0.08675i	0.47953	-0.08752i
m_c	0.65482	-0.06814i	0.65478	-0.06776i
n_c	0.09313	0.07388i	0.09319	0.07379i

The agreement is satisfactory.

7.3 Comparison with experimental results for compressible flow.

In ref. 10 Tijdeman and Bergh have given measured pressure distributions and aerodynamic coefficients for a wing-control surface system in subsonic flow. Control surface chord was 25% and wing thickness 6%. The experimental results cover a large number of Mach numbers and reduced frequencies.

In fig. 5 the measured coefficients have been compared with those calculated with the present method for a radial frequency $\omega=150$ cps. A striking feature is that the qualitative agreement - even to high Mach numbers - appears to be rather good: both experimental and theoretical k_c - and m_c -values show a rapid decrease, the theoretical one lagging about 0.05 in Mach number. The decreases in the imaginary parts of n_c coincide, however.

An analysis of this feature may be given after considering the corresponding pressure distributions in fig. 6. The greater part of this figure has been taken from ref. 10. When the free stream Mach number exceeds the critical Mach number $M_\infty=0.85$, a supersonic region appears at about 40% of the wing chord. As easily can be observed from the distributions of local Mach numbers, the average M_L -values relating to the flow patterns which are still subsonic or to those which contain only small supersonic regions, are higher than the corresponding values of M_∞ . Considering $M_\infty=0.8, 0.825, 0.85$ and 0.875 , an estimate of this difference yields about 0.05 in Mach number. This means that it should be fair to compare the measured distribution for $M_\infty=0.8$ with the calculated one for $M_\infty=0.85$, and so on. Indeed, on this basis the agreement is qualitatively good.

An analogous difference in Mach number does not appear in the n_c -distribution, because the average M_L -values over the control surface are nearly equal to the corresponding M_∞ -values.

8 Concluding remarks

1. The results of the convergence test indicate clearly that the presence of the logarithmic loading functions L_0 and L_1 in the approximating pressure series is necessary to assure a satisfactory convergence rate of the pressure distribution as the number of "regular" loading functions is increased. In the example given, i.e. for $\tau = 0.3$, $M_\infty = 0.8$ and $k = 0.9$, already four regular loading functions provide for an accuracy of 1% and ten functions for an accuracy of $1^{\circ}/\infty$. For a combination of both low M_∞ - and k -values a smaller number of loading functions may be needed. The influence of L_2 on the convergence rate is small.

It is expected that analogous results are found when the present method is extended to a wing of finite span. Of course then, additional loading functions should be included in the pressure series to treat the discontinuities in the boundary conditions at the control surface side edges.

2. Calculated and experimental results show a good qualitative agreement up to the lower transonic Mach numbers where a small supersonic region is present. The influence of the mean flow field on the unsteady pressure distribution at the higher Mach numbers, explained in ref. 10, is not considered in the present method, but can be roughly taken into account by introducing an average Mach number for which the calculations are to be performed. The theory should be improved if also characteristics of the mean flow field could be considered, e.g. in a way as has been pointed out in ref. 18.

9 Acknowledgement

The author is indebted to Mr. W. Kuipers who started the preparation of the computer programme and to Mr. A. L. Bleekrode who completed it.

10 References

- ¹ Timman, R. and van de Vooren, A. I., Theory of the oscillating wing with aerodynamically balanced control surface in a two-dimensional, subsonic, compressible flow. NLL Report F. 54, (1949).
- ² Timman, R. and van de Vooren, A. I., Tables of aerodynamic coefficients for an oscillating wing-flap system in a subsonic compressible flow. NLL TR F. 151, (1954).
- ³ Dietze, F., Die Luftkräfte des harmonisch schwingenden Flügels in kompressiblen Medium bei Unterschallgeschwindigkeit. Teil I. Deutsche Luftfahrtforschung, Forschungsbericht Nr. 1733, (1943).
- ⁴ Küssner, H. G. and Schwarz, L., Der schwingende Flügel mit aerodynamisch ausgeglichenem Ruder. Luftfahrt-Forschung 17, Lfg. 11/12, (1940).
- ⁵ Turner, M. J. and Rabinowitz, S., Aerodynamic coefficients for an oscillating airfoil with hinged flap, with tables for a Mach number of 0.7. NACA TN 2213, (1950).
- ⁶ Schade, T., Numerische Lösung der Possioschen Integralgleichung der schwingenden Tragfläche in ebener Unterschallströmung. Teil II. AVA Bericht B 44/J/43, (1944). English translation in ARC Techn. Rep. 9506, (1946).
- ⁷ Karp, S. N. and Weil, H., The oscillating airfoil in compressible flow. Part II. Air Material Command, U.S. Air Force, Techn. Rep. No. F-TR-1195-ND, (1948).
- ⁸ Landahl, M. T., Pressure-loading functions for oscillating wings with control surfaces. AIAA Journal, 6, No. 2, (1968).
- ⁹ Zwaan, R. J., Some comparative calculations with the lifting surface theory of Laschka for circular and elliptic wings in subsonic flow. NLR TN F. 241, (1964).
- ¹⁰ Tijdeman, H. and Bergh, H., Analysis of pressure distributions measured on a wing with oscillating control surface in two-dimensional high subsonic and transonic flow. NLR TR F. 253, (1967).
- ¹¹ Ashley, H. and Landahl, M. T., Aerodynamics of wings and bodies. Addison-Wesley Publishing Company, Inc., (1965).
- ¹² Bisplinghoff, R. L., Ashley, H. and Halfman, R. L., Aeroelasticity. Addison-Wesley Publishing Company, Inc., (1955).
- ¹³ Van Dyke, M., Perturbation methods in fluid mechanics. Academic Press, (1964).
- ¹⁴ Rodden, W. P. and Revell, J. D., The status of unsteady aerodynamic influence coefficients. IAS Preprint FF-33, (1962).
- ¹⁵ Fromme, J. A., Least-squares approach to unsteady kernel-function aerodynamics. AIAA Journal 2, No. 7, (1964).
- ¹⁶ Stark, V. J. E., On the approximation of the normal velocity on oscillating wings. AIAA Journal 4, No. 12, (1966).
- ¹⁷ Davies, D. E., An application of Flax's variational principle to lifting surface theory. RAE TR 67103, (1967).
- ¹⁸ Zwaan, R. J., On the use of asymptotic expansions in two-dimensional unsteady transonic flow. NLR TN F. 263, (1967).

APPENDIX A

Determination of the inner solution

The determination of the inner solution involves the solution of a series of linear boundary value problems of which the first three have been given in (4.5) to (4.7). As the boundary conditions are elementary the method of conformal transformations may be used to obtain the desired solutions.

First the x_i -co-ordinate is transformed like

$$\bar{x}_i = \frac{x_i}{\beta_\infty} \quad (\text{A.1})$$

which makes the differential equations of the Laplace type. Then, problems (4.5) to (4.7) become

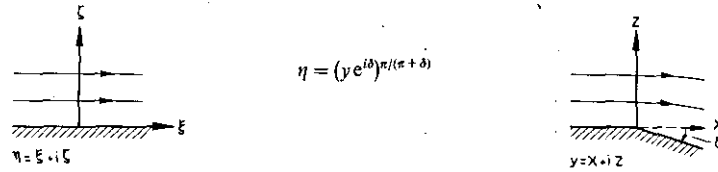
$$\left. \begin{aligned} \varphi_{i_{\bar{x}_i}}^{(1)} + \varphi_{i_{z_i}}^{(1)} &= 0, \\ \varphi_{i_{\bar{x}_i}}^{(1)} &= -u \langle \bar{x}_i \rangle \quad \text{at } z_i = 0; \end{aligned} \right\} \quad (\text{A.2})$$

$$\left. \begin{aligned} \varphi_{i_{\bar{x}_i}}^{(2)} + \varphi_{i_{z_i}}^{(2)} &= 2ik \frac{M_\infty^2}{\beta_\infty} \varphi_{i_{\bar{x}_i}}^{(1)}, \\ \varphi_{i_{z_i}}^{(2)} &= -ik\beta_\infty \bar{x}_i u \langle \bar{x}_i \rangle \quad \text{at } z_i = 0; \end{aligned} \right\} \quad (\text{A.3})$$

$$\left. \begin{aligned} \varphi_{i_{\bar{x}_i}}^{(3)} + \varphi_{i_{z_i}}^{(3)} &= 2ik \frac{M_\infty^2}{\beta_\infty} \varphi_{i_{\bar{x}_i}}^{(2)} - k^2 M_\infty^2 \varphi_{i_{\bar{x}_i}}^{(1)}, \\ \varphi_{i_{z_i}}^{(3)} &= 0 \quad \text{at } z_i = 0. \end{aligned} \right\} \quad (\text{A.4})$$

1 Solution of $\varphi_i^{(1)}$

A conformal transformation is applied to a uniform parallel flow as indicated in the following figure.



Thus, the complex velocity potential $\Phi_i^{(1)}$ becomes

$$\Phi_i^{(1)} = \eta = (y e^{i\delta})^{\pi/(\pi+\delta)}. \quad (\text{A.5})$$

After expanding (A.5) asymptotically to δ , the following expression for the velocity potential $\varphi_i^{(1)}$ is found:

$$\varphi_i^{(1)} = -\frac{\delta}{\pi} \left[\frac{1}{2} \bar{x}_i \ln(\bar{x}_i^2 + z_i^2) + \left(\pi - \text{arctg} \frac{z_i}{\bar{x}_i} \right) z_i \right] + O\langle \delta^2 \rangle. \quad (\text{A.6})$$

2 Solution of $\varphi_i^{(2)}$

A particular solution making eq. (A.3) homogeneous and satisfying the zero boundary condition at $z_i=0$ is

$$\varphi_{i_p}^{(2)} = -\frac{ik M_\infty^2 \delta}{4\pi\beta_\infty} (\bar{x}_i^2 + z_i^2) \ln(\bar{x}_i^2 + z_i^2). \quad (\text{A.7})$$

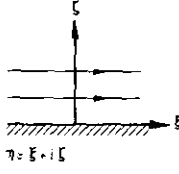
The boundary value problem for the remaining part of $\varphi_i^{(2)}$,

$$\varphi_{i_p}^{(21)} = \varphi_i^{(2)} - \varphi_{i_p}^{(2)}, \quad (\text{A.8})$$

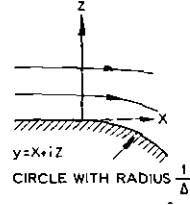
becomes:

$$\left. \begin{aligned} \varphi_{i_{\bar{x}_i}}^{(21)} + \varphi_{i_{z_i}}^{(21)} &= 0 \\ \varphi_{i_{z_i}}^{(21)} &= -ik\beta_\infty \delta \bar{x}_i u \langle \bar{x}_i \rangle \quad \text{at } z_i = 0. \end{aligned} \right\} \quad (\text{A.9})$$

Its solution may be found using the conformal transformation



$$\eta = (ye^{\pm i\delta y})^{n/(\pi + \frac{1}{2}\delta y)}$$



yielding, after expanding terms asymptotically to Δ and putting Δ equal to $i\delta k\beta$

$$\varphi_i^{(21)} = i \frac{\delta k \beta_\infty}{\pi} \left[\frac{1}{4}(z_i^2 - \bar{x}_i^2) \ln(\bar{x}_i^2 + z_i^2) + \left(\arctg \frac{z_i}{\bar{x}_i} - \pi \right) \bar{x}_i z_i \right] + O\langle \delta^2 \rangle. \quad (\text{A.10})$$

Addition of $\varphi_i^{(21)}$ and $\varphi_p^{(2)}$ results in

$$\varphi_i^{(2)} = -i \frac{k\delta}{4\pi\beta_\infty} \left[\bar{x}_i^2 + (2M_\infty^2 - 1)z_i^2 \ln(\bar{x}_i^2 + z_i^2) - 4\beta_\infty^2 \left(\arctg \frac{z_i}{\bar{x}_i} - \pi \right) \bar{x}_i z_i \right] + O\langle \delta^2 \rangle. \quad (\text{A.11})$$

3 Solution of $\varphi_i^{(3)}$

The only solution is a particular solution making eq. (A.4) homogeneous and satisfying the zero boundary condition at $z_i=0$:

$$\varphi_{ip}^{(3)} = \varphi_i^{(3)} = \frac{k^2 M_\infty^2 \delta}{\pi \beta_\infty^2} \left[\left(\frac{3 - 2M_\infty^2}{8} \bar{x}_i^2 + \frac{-3 + 4M_\infty^2}{8} z_i^2 \right) \bar{x}_i \ln(\bar{x}_i^2 + z_i^2) - \frac{3}{2} \beta_\infty^2 \bar{x}_i^2 z_i \arctg \frac{z_i}{\bar{x}_i} - \frac{1}{4} \bar{x}_i z_i^2 + \frac{\pi}{2} \beta_\infty^2 z_i^3 \right] \quad (\text{A.12})$$

APPENDIX B

Analytic expressions for some integrals in (6.9)

$$g_{01} = \delta \beta_\infty Q$$

$$g_{11} = -4i \frac{k}{\beta_\infty} [(1 + 2 \ln 2) \sin \theta_c + 2(\cos \theta_c - \cos \theta) Q]$$

$$g_{02} = 2\beta_\infty [\sin \theta_c - 2(\cos \theta - \cos \theta_c) Q]$$

$$g_{12} = 2i \frac{k}{\beta_\infty} [\sin \theta_c \cos \theta - (\frac{3}{4} + \ln 2) \sin \theta_c \cos \theta_c - (\cos \theta_c - \cos \theta)^2 Q]$$

$$g_{03} = \frac{1}{2} \beta_\infty [\sin \theta_c (3 \cos \theta_c - 2 \cos \theta) + 4(\cos \theta_c - \cos \theta)^2 Q]$$

$$g_{13} = i \frac{k}{2\beta_\infty} \left[-\frac{1}{18}(1 + 6 \ln 2) \sin 3\theta_c - \frac{1}{2}(1 + 2 \ln 2) \sin \theta_c - \frac{1}{2} \sin \theta_c \cos 2\theta + \frac{3}{2} \sin 2\theta_c \cos \theta - \frac{1}{2} \sin 2\theta_c \cos \theta_c - \frac{4}{3} (\cos \theta_c - \cos \theta)^3 Q \right]$$

where

$$Q = \begin{cases} \frac{1}{2}(\pi - \theta_c), & \theta < \theta_c \\ -\frac{1}{2}\theta_c, & \theta > \theta_c \end{cases}$$

$$f_{0r} = -2\beta_\infty \frac{\sin r\theta + \sin(r+1)\theta}{\sin \theta}$$

$$f_{1r} = \begin{cases} -2i \frac{k}{\beta_\infty} \left[\frac{\cos r\theta}{r} + \frac{\cos(r+1)\theta}{r+1} \right] & r > 0 \\ -2i \frac{k}{\beta_\infty} [2 \ln 2 + \cos \theta], & r = 0 \end{cases}$$

APPENDIX C

Analytic expressions for wing lift and moment coefficient and hinge moment coefficient

$$k_c = \frac{1}{\pi} [a_0 + 2a_{c_0} \sin \theta_c + a_{c_1} \sin \theta_c \cos \theta_c + \frac{1}{3}a_{c_2} \sin \theta_c (1 + 2 \cos^2 \theta_c)]$$

$$m_c = \frac{2}{\pi} \left\{ -\frac{1}{4}\pi k_c + \frac{1}{4}(a_0 - a_1) + \frac{1}{2}a_{c_0} \sin \theta_c (2 - \cos \theta_c) - \frac{1}{6}a_{c_1} \sin \theta_c (\cos^2 \theta_c - 3 \cos \theta_c - 1) + \right. \\ \left. + \frac{1}{2}a_{c_2} \sin \theta_c \left[\left(\frac{1}{3} + \frac{5}{12} \cos \theta_c \right) \right] [(1 + 2 \cos^2 \theta_c) - \cos^3 \theta_c] \right\}$$

$$n_c = \frac{2}{\pi} \left\{ -\pi x_c r_c + \frac{1}{4} \left[1 - \frac{1}{\pi} (\theta_c - \sin \theta_c \cos \theta_c) \right] a_0 - \frac{1}{4} \left[1 - \frac{1}{\pi} (\theta_R - \sin \theta_R \cos \theta_R - \frac{4}{3} \sin^3 \theta_R) \right] a_1 + \right. \\ \left. + \frac{1}{4\pi} \sum_{r=2}^R a_r \left[\frac{\sin(r+2)\theta_c}{r+2} - \frac{\sin(r+1)\theta_c}{r+1} - \frac{\sin r\theta_c}{r} + \frac{\sin(r-1)\theta_c}{r-1} \right] + \right. \\ \left. + \frac{1}{2}a_{c_0} \left[\left(1 - \frac{\theta_c}{\pi} \right) \sin \theta_c (2 - \cos \theta_c) + \frac{1}{\pi} \sin^2 \theta_c \right] - \frac{1}{6}a_{c_1} \left[\left(1 - \frac{\theta_c}{\pi} \right) \sin \theta_c (\cos^2 \theta_c - 3 \cos \theta_c - 1) - \frac{3}{\pi} \sin^2 \theta_c \right] + \right. \\ \left. + a_{c_2} \left[\frac{1}{2} \left(1 - \frac{\theta_c}{\pi} \right) \sin \theta_c \left[\left(\frac{1}{3} + \frac{5}{12} \cos \theta_c \right) (1 + 2 \cos^2 \theta_c) - \cos^3 \theta_c \right] + \right. \right. \\ \left. \left. + \frac{1}{2\pi} (\sin^2 \theta_c \cos \theta_c + \frac{1}{3} \sin^2 \theta_c - \frac{1}{12} \sin^2 \theta_c \cos^2 \theta_c) \right] \right\}$$

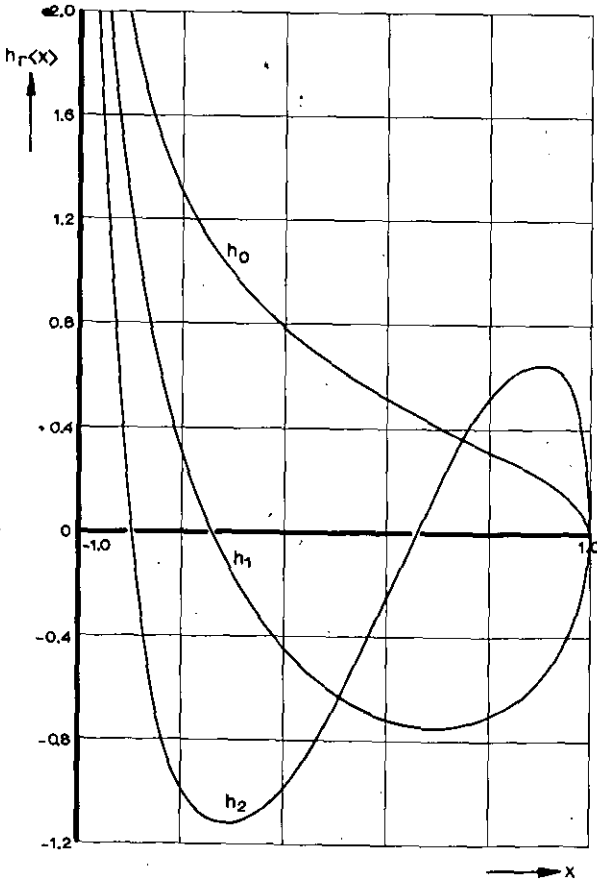
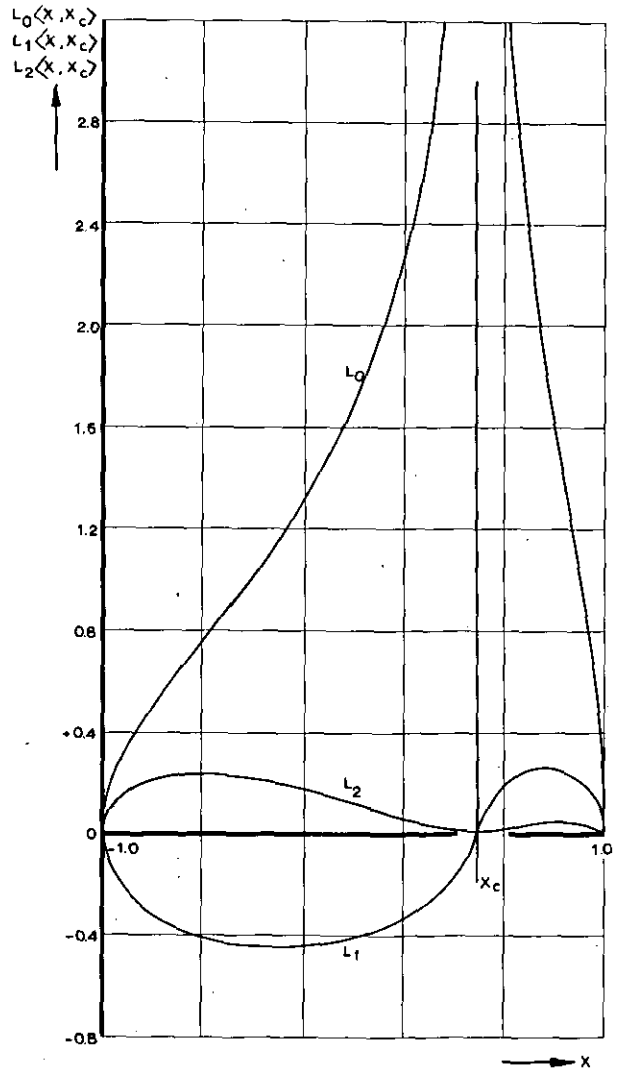
where:

$$r_c = \frac{1}{\pi} \left\{ \left[1 - \frac{1}{\pi} (\theta_c + \sin \theta_c) \right] a_0 - \frac{1}{\pi} \sum_{r=1}^R a_r \left[\frac{\sin r\theta_c}{r} + \frac{\sin(r+1)\theta_c}{r+1} \right] + \right. \\ \left. + 2a_{c_0} \left(1 - \frac{\theta_c}{\pi} \right) \sin \theta_c + a_{c_1} \left[\left(1 - \frac{\theta_c}{\pi} \right) \sin \theta_c \cos \theta_c + \frac{1}{\pi} \sin^2 \theta_c \right] + \right. \\ \left. + a_{c_2} \left[\frac{1}{3} \left(1 - \frac{\theta_c}{\pi} \right) \sin \theta_c (1 + 2 \cos^2 \theta_c) + \frac{1}{\pi} \sin^2 \theta_c \cos \theta_c \right] \right\}$$

TABLE 1: Convergence test on wing and control surface coefficients for $\tau=0.3$, $M_\infty=0.8$, $k=0.9$.

R	$a_{c_0}, a_{c_1}, a_{c_2}=0$		$a_{c_0} \neq 0; a_{c_1}, a_{c_2}=0$		$a_{c_0}, a_{c_1} \neq 0; a_{c_2}=0$		$a_{c_0}, a_{c_1}, a_{c_2} \neq 0$		
	Re	Im	Re	Im	Re	Im	Re	Im	
k_c	2	0.32592	-0.12223	0.46913	-0.20817	0.44840	-0.11586	0.39679	-0.15663
	4	0.46250	-0.08047	0.48461	-0.07700	0.47507	-0.08604*	0.47929	-0.08913*
	6	0.51526	-0.10330	0.48151	-0.08281	0.48088	-0.08830	0.47938	-0.08715**
	8	0.54602	-0.12061	0.47430	-0.09814	0.47999	-0.08761**	0.47953	-0.08753*)
	10	0.45324	-0.07594	0.47942	-0.08733*	0.47928	-0.08720	0.47989	-0.08752
	12	0.48015	-0.08754	0.48040	-0.08514	0.47959	-0.08758	0.47964	-0.08756
	14	0.50129	-0.09770	0.47929	-0.08750**	0.47975	-0.08761	0.47949	-0.08748
m_c	2	0.61872	-0.13671	0.78763	-0.05082	0.66651	-0.07957	0.76725	-0.14594
	4	0.64831	-0.08349	0.65399	-0.04739	0.65369	-0.07282*	0.65819	-0.06513*
	6	0.70070	-0.05571	0.64955	-0.06381	0.65688	-0.06774	0.65355	-0.06772
	8	0.73359	-0.03819	0.65830	-0.08171	0.65491	-0.06725	0.65471	-0.06806***)
	10	0.62265	-0.07868	0.65517	-0.06706	0.65414	-0.06783**	0.65500	-0.06760
	12	0.65634	-0.06895	0.65346	-0.06488*	0.65479	-0.06798	0.65476	-0.06783
	14	0.68166	-0.05975	0.65406	-0.06812	0.65495	-0.06776	0.65459	-0.06786
n_c	2	0.12179	0.01880	0.09960	0.04934	0.10181	0.04617	0.08134	0.07139
	4	0.09837	0.06974	0.09050	0.06631	0.09408	0.07267*	0.09263	0.07152
	6	0.08591	0.08094	0.09357	0.07359	0.09285	0.07421	0.09358	0.07380***)
	8	0.08251	0.08433	0.09525	0.07654	0.09340	0.07372	0.09315	0.07388***)
	10	0.10051	0.06915	0.09292	0.07303*	0.09336	0.07370**	0.09311	0.07379
	12	0.09258	0.07415	0.09280	0.07298	0.09320	0.07384	0.09323	0.07381
	14	0.08828	0.07749	0.09329	0.07386**	0.09318	0.07380	0.09324	0.07377

* accuracy: 1% ** accuracy: 1°/∞° *) One collocation point nearly coincides with $x_c=0.50$.

Fig. 1. Approximating functions $h_r(x)$.Fig. 2. Approximating functions L_0, L_1 and L_2 .

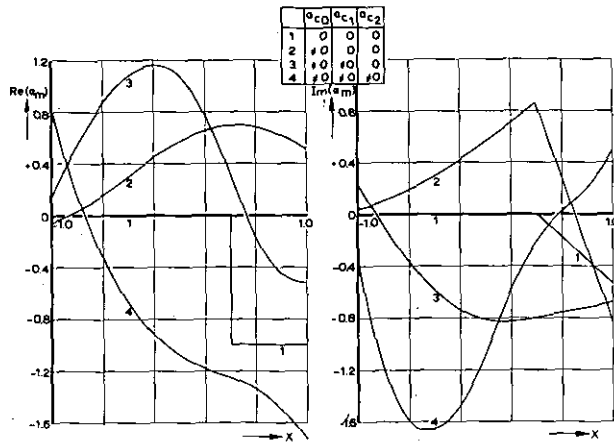


Fig. 3. Distribution of normal wash over wing chord in different approximations.

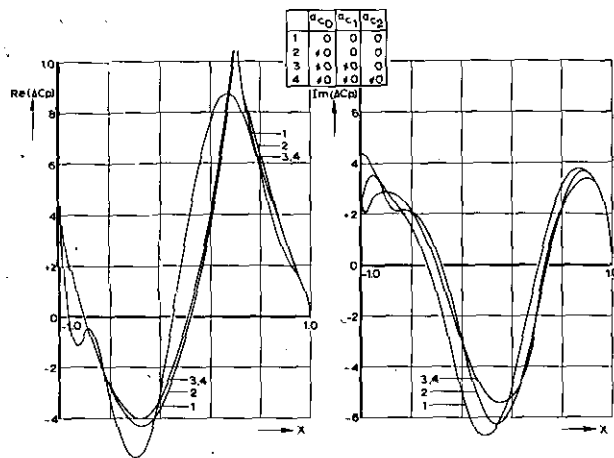


Fig. 4. Pressure distributions over wing chord in different approximations.

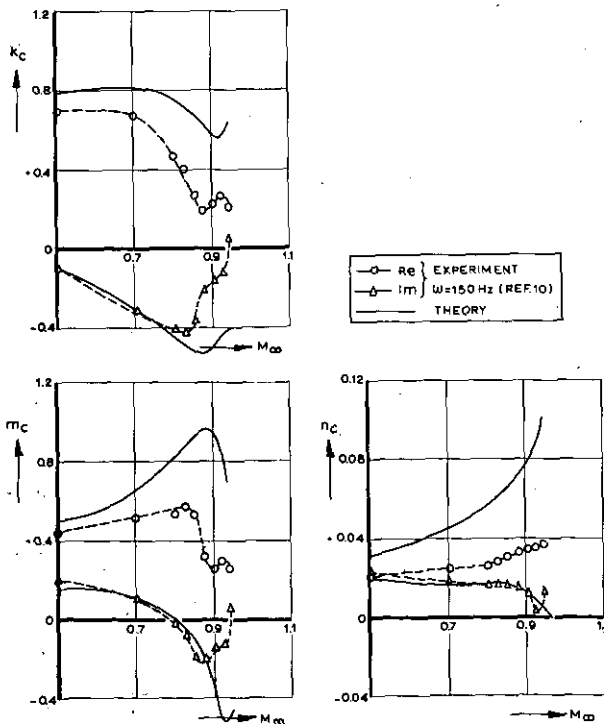


Fig. 5. Aerodynamic coefficients vs. Mach number.

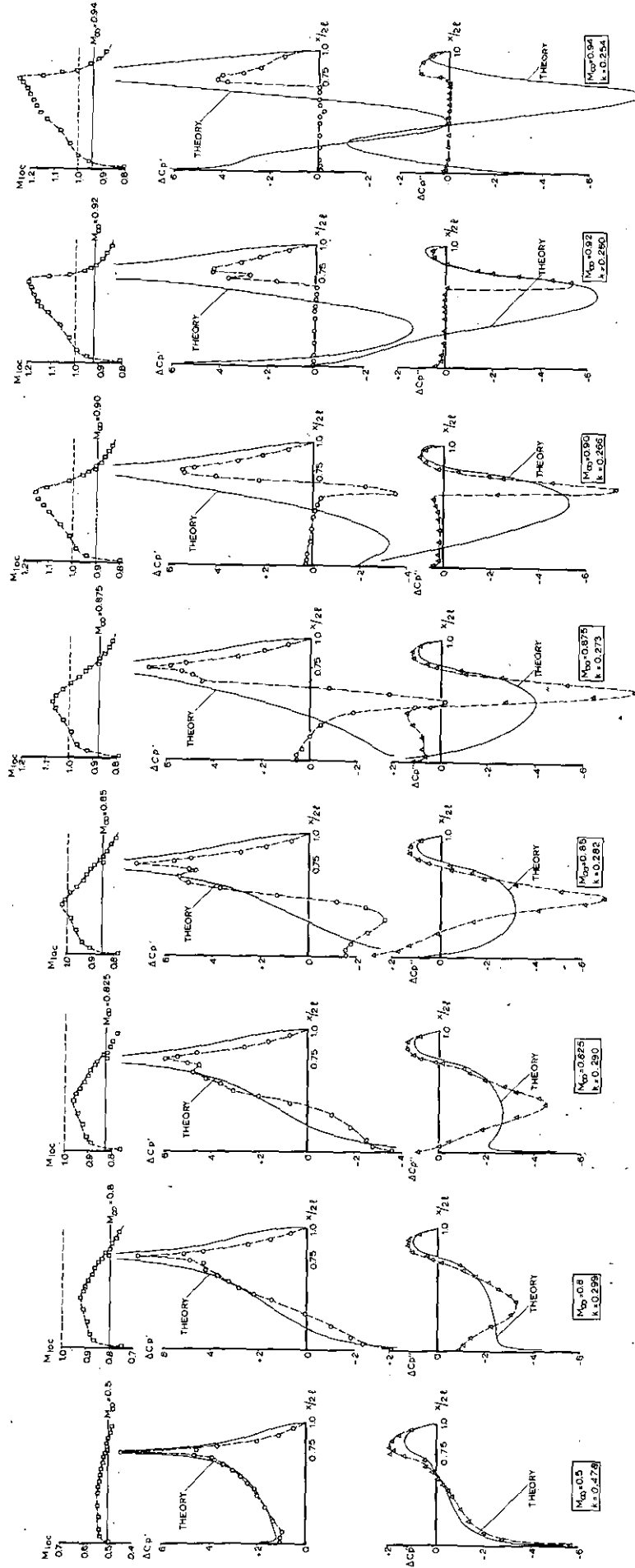
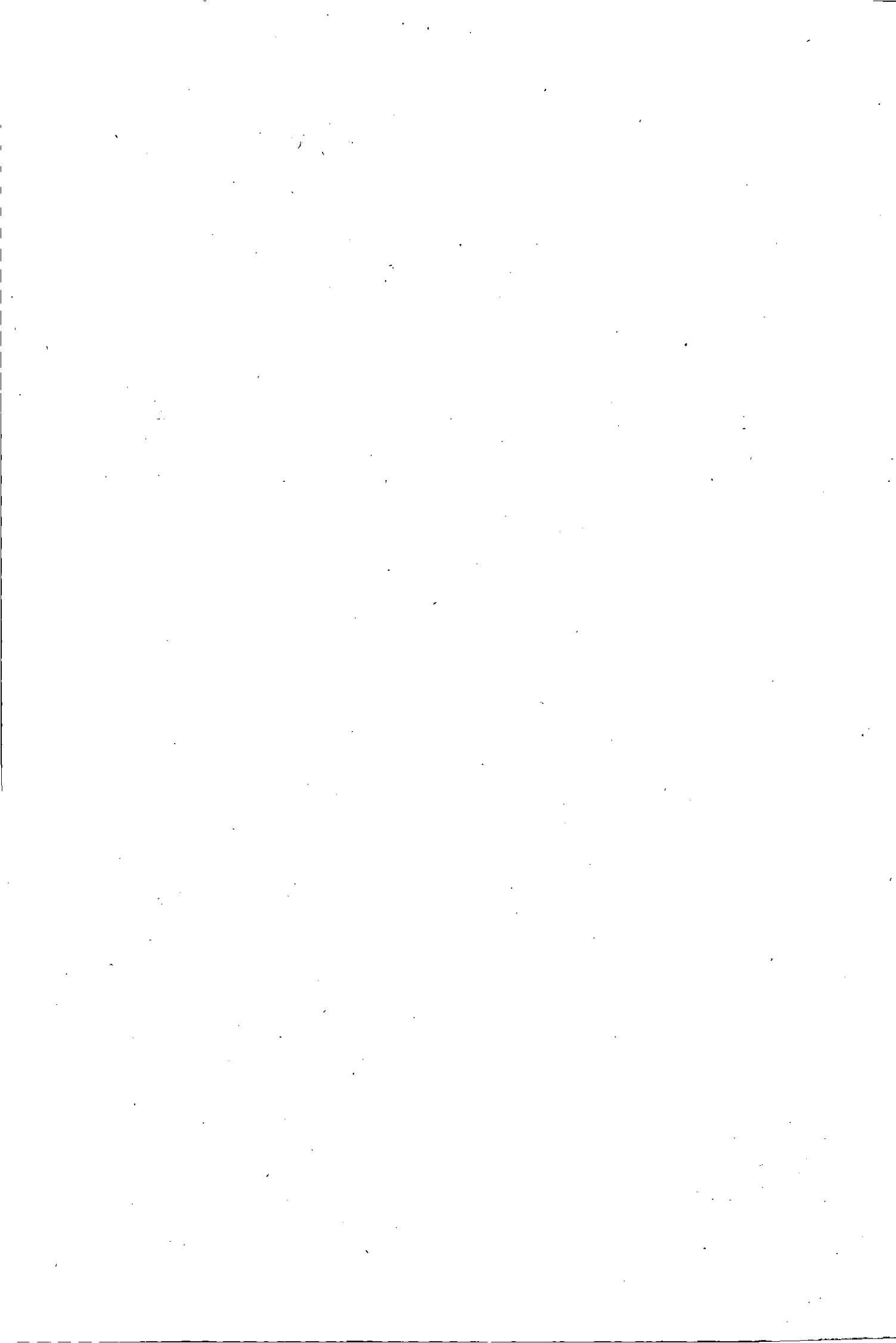


Fig. 6. Chordwise distributions of mean local Mach number and unsteady pressures.



A new approach to the numerical solution of the equation of subsonic lifting surface theory

by

P. J. Zandbergen*, Th. E. Labrujere and J. G. Wouters

Summary

The present report deals with the numerical treatment of the linearised lifting surface theory through a method which is based upon the representation of the pressure distribution on chordwise direction by a series of Chebyshev polynomials according to Laschka, and upon the determination of the spanwise integral involved by means of trigonometric polynomials such as also applied by Multhopp.

When calculations are performed using Multhopp's method the results show strong variations with increasing number of the spanwise stations and chordwise points, to which the boundary condition is applied. This makes it impossible to obtain a plausible solution. Hence a new method has been developed, where the representation of the pressure distribution in spanwise direction is separated from the representation of the regularised kernel function in spanwise direction. This makes it possible to obtain accurate integrals for a given distribution of pivotal points and leads to results which show a rapid decrease of variation as either the number of spanwise stations or the number of chordwise points or both are increased. This is demonstrated by including a number of results for some well-known wings.

As the method allows of the possibility to take arbitrary positions for the pivotal points, some computations have been performed for different distributions of spanwise stations. The results indicate that further investigations may be useful.

This investigation has been performed under contract for the Ministry of Defence of the Netherlands.

Contents

	Page
List of symbols	1
1 Introduction	2
2 An outline of the method	3
3 Numerical evaluation of the method	5
4 Discussion of some numerical results	6
4.1 An example of the improvement obtained in comparison with Multhopp's method	6
4.2 The convergence with respect to a , m and R	6
4.2.1 The circular wing at $M_\infty = 0$	7
4.2.2 The Warren 12 wing at $M_\infty = 0$	7
4.2.3 The Warren 12 wing at $M_\infty = 0.6$	7
4.2.4 The Multhopp wing at $M_\infty = 0$	8
4.3 Some results obtained with arbitrary distribution of pivotal points	8
5 Concluding remarks	9
6 References	9

Appendix B: The integration in chordwise direction (2 pages)
1 figure

List of symbols

a	factor, indicating the number of spanwise integration points
a_r	coefficients of the chordwise function h_r , varying in spanwise direction
b	factor, indicating the number of pivotal points
c_p	pressure coefficient
f	chordwise integrand (appendix B)
h_r	chordwise functions
l	length of local chord
m	integer indicating the number of spanwise functions
n	index indicating a station, used in the spanwise interpolation polynomial
p	index indicating the pivotal points in chordwise direction
r	index indicating one of the chordwise functions
s	semi-span of the wing
x_1, x_t	leading and trailing edges

Appendix A: A detailed derivation of the basic equations (5 pages)

A.1 The calculation of the quantities $\gamma_{n\lambda}$, ϵ_{vn} , ζ_{vn} and S_{vn}

A.2 The calculation of the quantities $\frac{\partial F}{\partial \eta'}(\theta' = \theta_v)$ and $H_r(\xi, \theta_v, \theta_v)$

* Professor of Mathematics, Twente Institute of Technology, consultant to the NLR.

x	} physical co-ordinates of wing	A	} coefficients defining rounding (fig. 3)
y		$B_{1,2}$	
z		F_r	spanwise function
α	local angle of attack	H_r	chordwise integral
β	compressibility factor	\bar{H}_r	regularized kernel function
β_1, β_2	quantities used in evaluating the chordwise integration	I_r	integral occurring in chordwise integration procedure
ξ	x co-ordinate non-dimensionalized by s	K	kernel function
η	y co-ordinate non-dimensionalized by s	$K_{1,2}$	measure for radius of curvature of wing edges
ψ	angular co-ordinate in chordwise direction	$H_{1,2}$	local slope of wing edges
ϕ	value of ψ in pivotal points	R	number of chordwise functions - 1
θ	angular co-ordinate in spanwise direction	T_r	Chebyshev polynomial of order r
ν	index of spanwise co-ordinate of pivotal points	X	} auxiliary wing co-ordinates
λ	index of integration points	Y	
γ	} influence functions	M_∞	Mach number of free stream
ε		A	number of integration points in spanwise direction
ζ			
S			

1 Introduction

One of the most important problems of aerodynamics is the calculation of the lift-distribution over a wing of arbitrary planform. It is therefore not surprising that famous names in aerodynamics are connected with the study of this problem.

One of the first solutions was given by Prandtl, when he developed his so-called "lifting line" theory. In this theory the lift on a wing is represented by a bound vortex, the strength of which is a function of the spanwise co-ordinate, followed by a trailing vortex sheet. The theory leads to a singular integral equation, which was solved by a collocation method.

Although a tremendous number of papers all based on this theory was produced, no real approach to a more satisfactory description of the pressure distribution over a wing was made, until "lifting surface" theory was used. The most successful method for the evaluation of this theory is due to Multhopp (ref. 1). In this method the pressure distribution over a wing is represented by means of trigonometric series; the chordwise distribution is based on a series, which had turned out to be suitable for two-dimensional thin wings with arbitrary camber, while the spanwise distribution is given by a sine series. The coefficients of these series are found by using a collocation technique, starting from the appropriate integral equation and applying the boundary condition at a number of pivotal points distributed over the wing in spanwise and chordwise direction. Originally it was thought sufficient to use two functions in the chordwise direction and up to 15 stations in spanwise direction. Although it is true that this may give a fair indication for wings with small sweep and camber, it was found later that there are examples of inaccurate results due to this limitation, especially for the center of pressure line. This has resulted in attempts to perform calculations with more than two functions in chordwise direction. One such an attempt is the subject of ref. 2, which presents a modification of Multhopp's method with a view to the application of digital computers. During recent years computations have been made, using this method, especially with the objective to obtain an insight into the requirements for an accurate solution.

These computations show that for a given number of spanwise stations and for different numbers of chordwise points there exist very strong variations in the results which do not decrease as the number of chordwise points is increased. Moreover the deviation between the different results becomes worse when increasing either aspect ratio or sweep of the wing.

Considering the method used in these computations, there are at least three reasons which may explain this phenomenon.

In the first place it had been observed that the spanwise integrand is not completely regular for all values of the spanwise co-ordinate. This must lead to serious difficulties in trying to represent this function by a polynomial.

The two other reasons are connected with the fact that occur in the Multhopp method. The spanwise integrand consisting of the product of the pressure series coefficient and the spanwise influence function is represented by a single trigonometric polynomial. After integration of this polynomial, it is not possible to judge from the results whether the representation of the pressure series coefficients or the accuracy of the integral gives rise to poor results. This makes it difficult to investigate the separate influence of each.

Since the need for more accurate methods for calculating wing characteristics is growing rapidly, it is quite obvious that the results, described above, have given rise to a search for more reliable methods for computing the lift distribution over a thin wing both in this country and abroad.

The first requirement that should be met is the achievement of an accurate integration. This can be accomplished by regularizing the spanwise integrand and by using an integration scheme that is independent of the number of pivotal points. Such a method would avoid the errors due to the singularity of the integrand mentioned above and would allow the separate study of the two effects of representation and integration. Now of course this can be done in a number of ways, each having its own pitfalls.

The method which will be described is the result of a development in which several schemes were tried and rejected, until at last one remained for which all major difficulties seemed to be resolved.

In essence the method is still closely connected with Multhopp's method because Multhopp's interpolation polynomials have been applied both for the representation of the pressure series coefficients in spanwise direction and as an aid for the determination of the spanwise integrals.

It differs from Multhopp's method with respect to the regularization of the spanwise integrand and with regard to the determination of the spanwise integrals, which has been made independent of the number of pivotal stations. Moreover a sufficient accuracy of the chordwise integrals is guaranteed.

Due to the time-consuming character of the computer operations required by these measures, special attention has been given to the optimization of the programme. A remarkable saving of computer time has been obtained by using rather simple methods.

In the meantime some of the essential features of the present method have been applied by van de Vooren to some problems connected with the calculation of T-tails (ref. 4).

The present report gives an outline of the method and discusses and analyses the specific characteristics of the results which can be obtained.

A detailed derivation of the necessary formulae has been given in appendix A, while in appendix B the features of the chordwise integration have been described. The computer programme, written in ALGOL, together with general purpose input and output programmes will be presented in a separate report.

2 An outline of the method

As usual in lifting surface theory, the wing is assumed to be thin and to deviate so slightly from the $z=0$ plane that the boundary conditions can be applied at points in the projection of the wing onto this plane (see fig. 1 for the definition of the co-ordinate system). From the linearized potential equation for compressible flow

$$\beta^2 \phi_{xx} + \phi_{yy} + \phi_{zz} = 0 \quad (2.1)$$

it can be derived (see ref. 4) that the following representation is valid for the local angle of incidence in terms of the pressure distribution Δc_p over the wing:

$$\alpha(x, y) = \frac{1}{8\pi} \int_{-s_x}^{+s} \int_{x_l(y')}^{x_t(y')} \Delta c_p(x', y') K(x, y; x', y') dx' dy' \quad (2.2)$$

in which s denotes the semi-span, $x_l(y')$ and $x_t(y')$ are the equations for respectively the leading edge and the trailing edge, and where K is given by

$$K(x, y; x', y') = \frac{-1}{(y-y')^2} \left[1 + \frac{x-x'}{\sqrt{(x-x')^2 + \beta^2(y-y')^2}} \right] \quad (2.3)$$

Since the problem to be solved is the determination of the unknown Δc_p for given values of α , eq. (2.3) is a highly singular integral equation*. By making a number of appropriate assumptions, the solution of this integral equation can be reduced to the solution of a system of linear equations.

As is common in lifting surface theory, it is assumed that Δc_p can be represented by the following formula

$$\Delta c_p(\xi', \eta') = \frac{4s}{l(\eta')} \sum_{r=0}^R a_r(\eta') h_r(X') \quad (2.4)$$

* To give a sense to this equation, some kind of regularizing process has to be applied, e.g.,

$$\int_a^b \frac{f(y')}{(y-y')^2} dy' = \lim_{\epsilon \rightarrow 0} \left\{ \int_a^{\eta-\epsilon} \frac{f(y')}{(y-y')^2} dy' + \int_{\eta+\epsilon}^b \frac{f(y')}{(y-y')^2} dy' - \frac{2f(\eta)}{\epsilon} \right\}$$

where instead of x and y the following dimensionless quantities are used

$$\xi = \frac{x}{s} \quad \eta = \frac{y}{s} \quad (2.5)$$

and

$$X' = \frac{s}{l(\eta')} \{ \xi' - \xi_1(\eta') \}. \quad (2.6)$$

The quantity $l(\eta')$ is the local chord.

According to Laschka (ref. 5) the functions h_r have been chosen as follows.

$$h_r(X') = \frac{1}{\pi} \frac{T_r(1-2X') + T_{r+1}(1-2X')}{\sqrt{X'(1-X')}} \quad (2.7)$$

where T_r is a Chebysev polynomial of order r .

By introducing the angular co-ordinate ψ defined by

$$X' = \frac{1 - \cos \psi}{2} \quad (2.8)$$

the functions h_r can be written as

$$h_r(\psi) = \frac{2}{\pi} \frac{\cos \frac{2r+1}{2} \psi}{\sin \frac{\psi}{2}} \quad (2.9)$$

By eqs (2.4), (2.5) and (2.6) the integral equation (2.2) can be written as follows.

$$\alpha(\xi, \eta) = -\frac{1}{2\pi} \sum_{r=0}^R \int_{-1}^{+1} \frac{a_r(\eta') H_r(\xi, \eta; \eta')}{(\eta - \eta')^2} d\eta' \quad (2.10)$$

where the bar through the integral sign denotes the principal value according to Mangler (see note and ref. 1) and where H_r is given by

$$H_r(\xi, \eta; \eta') = \int_0^1 h_r(X') \left[1 + \frac{X - X'}{\sqrt{(X - X')^2 + \frac{\beta^2 s^2}{l(\eta')^2} (\eta - \eta')^2}} \right] dX' \quad (2.11)$$

To allow for the fact that the integrand of eq. (2.10) contains a logarithmic singularity, this equation can be rewritten as (see appendix A)

$$\alpha(\xi, \eta) = -\frac{1}{2\pi} \sum_{r=0}^R \int_{-1}^{+1} \frac{a_r(\eta') F_r(\xi, \eta; \eta')}{(\eta - \eta')^2} d\eta' + \frac{1}{2\pi} \frac{\beta^2 s^2}{l(\eta)^2} \sum_{r=0}^R \frac{dh_r}{dX'} (\eta' = \eta) \int_{-1}^{+1} a_r(\eta') \ln |\eta - \eta'| d\eta' \quad (2.12)$$

where

$$F_r = H_r(\xi, \eta; \eta') + \frac{\beta^2 s^2}{l(\eta')^2} (\eta - \eta')^2 \ln |\eta - \eta'| \left\{ \frac{dh_r}{dX'} (\eta' = \eta) \right\}. \quad (2.13)$$

So far the analysis is identical to that of Multhopp, at least in principle; from here on however a different way will be followed, which, although being more tedious, is also more flexible.

First it is assumed that the functions $a_r(\eta')$ can be represented by a trigonometric interpolation formula

$$a_r(\eta') = \frac{1}{m+1} \sum_{n=1}^m a_r(\eta_n) \sum_{\mu=1}^m \sin \mu \theta' \sin \mu \theta_n \quad (2.14)$$

$$\text{where } \eta = -\cos \theta \text{ and } \theta_n = \frac{n\pi}{m+1}. \quad (2.15)$$

When this is inserted in equation (2.12) one obtains

$$\begin{aligned} \alpha(\xi, \eta) = & -\frac{1}{2\pi} \sum_{r=0}^R \frac{2}{m+1} \sum_{n=1}^m a_r(\eta_n) \sum_{\mu=1}^m \sin \mu \theta_n \int_0^\pi \frac{F_r(\xi, \eta; \theta') \sin \mu \theta' \sin \theta'}{(\cos \theta - \cos \theta')^2} d\theta' + \\ & + \frac{1}{2} \sum_{r=0}^R \frac{2}{m+1} \frac{\beta^2 s^2}{l(\eta)^2} \frac{dh_r}{dX'} (\theta' = \theta) \sum_{n=1}^m a_r(\eta_n) \sum_{\mu=1}^m \sin \mu \theta_n \int_0^\pi \ln |\cos \theta - \cos \theta'| \sin \mu \theta' \sin \theta' d\theta'. \end{aligned} \quad (2.16)$$

When considering this equation, it will be clear that, if in a number of N points on the wing the quantities $\alpha(\xi, \eta)$ are given, with $N \geq m(R+1)$, and provided the integrals can be determined, a system of linear equations for the unknowns $a_r(\eta_n)$ is the result. This system may be solved by using a least squares technique. In general the solution for given m and R will depend on the number N and the positions of the collocation points, while moreover the accuracy of the integrals will play an important role.

The attention will be focussed on the latter point first. Instead of the function F_r , a new function \bar{H}_r is constructed.

$$\bar{H}_r(\xi, \eta; \theta') = \frac{\left\{ F_r(\xi, \eta; \theta') - F_r(\xi, \eta; \theta) - (\cos \theta - \cos \theta') \frac{\partial F_r}{\partial \eta'}(\theta' = \theta) \sin \theta' \right\}}{(\cos \theta - \cos \theta')^2} \quad (2.17)$$

The introduction of this function is of essential importance because the determination of the spanwise integral by using interpolation polynomials can only be achieved with sufficient accuracy if the integrand is completely regular. The fact that Multhopp considered the function F_r instead of \bar{H}_r may be one of the reasons for the difficulties that arise when it is tried to get a plausible solution using his method. When the function \bar{H}_r itself is written as a sum of trigonometric terms, the resulting integrals can be determined, and provided the number of terms used to represent \bar{H}_r is sufficiently large a good result for the first integral in eq. (2.16) is obtained. In the present case the number chosen is $a(m+1) - 1$, a being an integer. Using eq. (2.16) together with eq. (2.17) and evaluating the integrals involved, the following algebraic relation is found (ξ and η are replaced now by ξ_p and η_v)

$$\alpha(\xi_p, \eta_v) = -\frac{1}{2} \sum_{r=0}^R \sum_{n=1}^m a_r(\eta_n) \left\{ \sum_{\lambda=1}^{a(m+1)-1} \frac{1}{a(m+1)} \bar{H}_r(\xi_p, \theta_v; \theta_\lambda) \gamma_{n\lambda} + F_r(\xi_p, \theta_v; \theta_v) \frac{\sin \theta_n}{\sin \theta_v} \varepsilon_{vn} + \frac{\partial F_r}{\partial \eta'}(\theta' = \theta_v) \zeta_{vn} - \frac{\beta^2 s^2}{l(\eta_v)^2} \frac{dh_r}{dX'}(\theta' = \theta_v) S_{vn} \right\} \quad (2.18)$$

The detailed derivation of the quantities occurring in this formula, is given in Appendix A. The meaning of the abbreviations γ , ε , ζ and S is summarized in table 1. Special care has to be taken in those cases where $\theta_\lambda = \theta_v$, since the calculation of the function \bar{H}_r is not trivial then (see also Appendix A).

By specifying the points (ξ_p, η_v) eq. (2.18) becomes a system of linear equations. In the present investigation the points ξ_p are chosen in the usual way, such that

$$X_p = \frac{1 - \cos \frac{2(p+1)\pi}{2R+3}}{2} \quad p = 0, 1, 2, \dots, R \quad (2.19)$$

while the stations η_v can be chosen arbitrarily. In the following section the numerical evaluation of eq. (2.18) will be discussed.

3 The numerical evaluation of the method

In order to obtain a solution of eq. (2.18) it is necessary to calculate the functions $\bar{H}_r(\xi_p, \theta_v; \theta_\lambda)$, $F_r(\xi_p, \theta; \theta_\lambda)$ and $\frac{\partial F_r}{\partial \eta'}(\xi_p, \theta_v; \theta_\lambda)$. As is evident from eq. (2.13) the real problem here is to investigate the function $H_r(\xi, \eta; \eta')$ given by eq. (2.11). If $\eta \neq \eta'$ the evaluation of the function H_r requires the calculation of the integral in eq. (2.11). Although in principle H_r can be expressed in terms of elliptical functions, this in itself does not provide a useful way for the evaluation, certainly not for the higher values of the index r . Therefore a numerical method was applied. To achieve a maximum of accuracy at a minimum of computer time it was decided to establish a separate procedure for the calculation of the function H_r . This procedure has been described in Appendix B. It assures an accuracy of 9 decimal places for the H_r with r ranging from 0 to 10. As will be clear from Appendix B, a separate analysis was needed of the behaviour of this function in the vicinity of $Y=0$. If $\eta = \eta'$ the evaluation of the function \bar{H}_r requires in essence the calculation of the second derivative of the function H_r . At the same time this involves the calculation of the quantities $F_r(\xi_p, \theta_v; \theta_v)$ and $\frac{\partial F_r}{\partial \eta'}(\xi_p, \theta_v; \theta_v)$. The above mentioned analysis, given in Appendix A, section A.2, provided analytical expressions which did not lead to numerical difficulties. The function $F_r(\xi_p, \theta_v; \theta_v)$ is given in principle by eq. A(13). Using the trigonometric representation of h_r it follows that

$$F_r(\xi_p, \theta_v; \theta_v) = \frac{1}{\pi} \left\{ \frac{1}{r} \sin r\phi + \frac{1}{r+1} \sin(r+1)\phi \right\} \quad (3.1)$$

The value of $\frac{\partial F_r}{\partial \eta'}(\xi_p, \theta_v; \theta_v)$ is given by eq. A(15), while the very complicated expression A(18) gives the value of $\bar{H}_r(\xi_p, \theta_v; \theta_v)$.

As will be evident from the analysis leading to eq. A(18), it is assumed that the second derivatives of the leading and trailing edges of the planform with respect to the spanwise co-ordinate exist. In other words it is assumed that the edge of the planform has a continuous radius of curvature. It should be stressed that it is not shown, and probably not even true, that the lifting surface problem of a wing with one or more kinks can be obtained as the limit of a sequence of solutions with continuous radius of curvature, which in one way or another gives an increasing degree of approximation to the kinked wing.

Another assumption which has been made implicitly is that for this class of wings a unique solution exists with a regular part which is continuous and continuously differentiable, and a singular part having a coefficient which is a continuous and continuously differentiable function of the spanwise co-ordinate. The series of functions used to represent the pressure coefficient lies dense in this class of continuous functions and will therefore converge to the function to be approximated for increasing values of m and R .

Since also the integration procedures used have either known accuracy or rely on a convergent process, it is allowed to consider the successive decreasing deviations of the numerical results as convergence to the solution of the problem.

In the following section the results for a number of cases are discussed, especially with regard to the speed of convergence i.e. the number of pivotal points necessary to obtain results of a given accuracy.

4 Discussion of some numerical results

In this section a survey will be given of the results obtained at the study of the following subjects:

1. The improvement achieved by the present method in comparison with Multhopp's method.
2. The convergence of the results with respect to the various parameters.
3. The influence of the way in which the pivotal points are distributed.

4.1 An example of the improvement obtained in comparison with Multhopp's method

As has been mentioned before serious difficulties will be encountered at the determination of a plausible solution if the method of ref. 2 is applied. These difficulties are due to the strong variation of the solution when the number of chordwise points is increased. An illustration of these difficulties is given on the basis of some results for a rectangular wing with $s=1$, $l(\eta) = \frac{1}{4}$ at $M_\infty=0$ and for $m=21$ and $R=1, 2, 3, 4$. The results are presented in table 12a. It is clear that the fluctuations are so strong that it is impossible to derive a plausible solution from these results.

When the method, presented in this report, is applied to this wing for the same values of m and R , without making use of the possibility to improve the spanwise integration accuracy, in other words taking $a=1$, the results show a very similar behaviour (see table 12b). When the integration accuracy is increased at the same values of m and R , a completely different behaviour of the solution is obtained, as appears from table 12c.

A good comparison of these results becomes possible when the deviations between the solutions for succeeding values of R are considered. From table 12d it appears that:

- the deviations between the results for different values of R obtained with the method of ref. 2, hardly decrease with regard to a_0 and fluctuate strongly with respect to a_1 .
- the deviations between the solutions obtained with the present method for $A=1$ are somewhat smaller, but when R is increased, they increase very rapidly with respect to a_0 and they are nearly constant with regard to a_1 .
- there are hardly any deviations between the solutions for $A=8$. When R is increased they decrease very rapidly.

From these observations it may be concluded, that the possibility to increase the spanwise integration accuracy independently of the number of pivotal spanwise stations, which is offered by the present method, can be a great advantage. Apparently the integration inaccuracy may offset the attainment of a plausible result. Also it may be stated that there possibly are cases where with the application of the present method a plausible solution may be obtained at a lower value of m than with the application of Multhopp's method. This should be the case when the number of spanwise stations to provide a sufficient accurate spanwise interpolation polynomial is less than the number of stations to provide a sufficient accurate spanwise integration.

In order to obtain a better insight into the merits of the method presented, it is necessary to investigate the variation of the solution not only with respect to R but also with regard to m and with the elimination of the effect of the integration inaccuracy.

4.2 The convergence with respect to a , m and R

The essential and new feature of the method is that in principle, for a given representation of the lift distribution

by means of a number of $(R+1)$ chordwise terms and m spanwise terms (see eqs. (2.4) and (2.14)) and for given positions and given number of pivotal points, a solution can be obtained with an accuracy which can be checked.*

Therefore it is possible to investigate the convergence of the solution with respect to m and R , maintaining for each set of m and R a constant accuracy of the integrations.

In the cases to be studied here, the distribution of the pivotal points along the span has been chosen in the usual way, that is

$$\theta_v = \frac{v\pi}{b(m+1)} \quad (4.1)$$

Moreover b has been taken equal to 1, i.e. the number of equations is equal to the number of pivotal points.

For illustrative reasons the chosen examples belong to those which have been studied extensively throughout the years. They comprise

- The circular wing at $M_\infty = 0$
- The Warren 12 wing at $M_\infty = 0$
- The Warren 12 wing at $M_\infty = 0.6$
- The Multhopp wing at $M_\infty = 0$

where M_∞ indicates the free stream Mach number.

Both the Warren 12 and the Multhopp wing are swept wings with a kink at the centre. The geometry of these wings has been given in figs. 2a and 2b. Since, as has been said, this method is not appropriate for such planforms, a rounding of these kinks, so that the radius of curvature remains continuous, is necessary. In fig. 3 a general scheme has been given for defining such a rounding. As is evident, the amount of rounding is dependent on the arbitrary co-ordinates η_1 and η_2 . This makes it possible to investigate the influence of the rounding on the solution; for the time being a constant rounding has been applied. In the following sections the four cases will be discussed one at a time by considering the variation of the quantities a_r . The first two of these quantities (a_0 and a_1) are directly related to the local lift and the local centre of pressure.

4.2.1 The circular wing at $M_\infty = 0$

For a number of cases with different m and R , the coefficients a_r have been calculated. First we will consider the convergence of these coefficients with respect to the number of spanwise integration points for given m and R . Typical examples have been given in tables 2a and 2b. As can be seen, the convergence in the two cases is evident and at $a=6$ the results may be considered to be correct in 4 to 5 decimal places. In table 3a the convergence of a_0 and a_1 with respect to R is shown for fixed numbers m and a . As can be expected, the convergence of a_1 is somewhat slower than that of a_0 , but still remarkable. In table 3b the convergence with respect to m is shown for fixed number R and constant integration accuracy.

It is concluded from these results, that a plausible solution of the circular wing problem, which is accurate in 3 to 4 decimal places can be obtained with $m=7$, $R=3$ and $a=6$.

4.2.2 The Warren 12 wing at $M_\infty = 0$

Since the Warren 12 wing has a kink at the centre in both the leading and the trailing edges (see fig. 2a), at these places a rounding has been applied according to fig. 3. In the present case the co-ordinates η_1 and η_2 have been chosen as follows $\eta_1 = -\eta_2 = 0.195090$.

This rounding has been maintained throughout the calculations to be discussed here.

In tables 4a and 4b typical examples have been presented to show the convergence of a_r with respect to the number of spanwise integration points for fixed m and R .

In table 5a the convergence with respect to R is shown, while in table 5b the convergence with respect to m has been given. In all these cases the convergence is evident, although that with respect to m (table 5b) clearly shows, that in this case far more spanwise terms are required than for the circular wing.

In fig. 4a and 4b the convergence with respect to a of the pressure difference Δc_p (eq. (2.4)) along two spanwise stations has been presented. From these figures it will be quite clear how fast the convergence really is obtained.

4.2.3 The Warren 12 wing at $M_\infty = 0.6$

Since the present method allows the free-stream Mach number to be changed, the same set of cases has been computed for the free-stream Mach number $M_\infty = 0.6$ as for the Mach number $M_\infty = 0$. From these results something

* This accuracy is dependent on the integer a which is a measure of the number of integration points (see eq. (2.18)).

can be learned about the influence of the free-stream Mach number (i.e. the effective aspect ratio) on the rate of convergence. As is evident when studying the tables 6a-b and 7a-b, the convergence is analogous to that for the case $M_\infty = 0$.

4.2.4 The Multhopp wing at $M_\infty = 0$.

The wing studied by Multhopp as a test-case for his method (ref. 1) has ever since remained a test-case for new developments in lifting surface theory. This is the reason why it was felt that it could not be left out here as an example.

The kink, which is again present, has been rounded according to fig. 3 with $\eta_1 = -\eta_2 = 0.195090$.

In table 8a the convergence with respect to the number of integration points has been studied for $m = 15$ and $R = 1$. As can be seen, even at $a = 6$ convergence is not achieved. Therefore in table 8b the same convergence has been studied for $m = 31$ and $R = 3$ at higher values of a . It is clear that in this case sufficient accuracy has been reached at $a = 8$.

From table 9a it can be concluded that convergence with respect to the number of chordwise points is reached at $R = 4$. Convergence with regard to m is not convincing from the results presented in table 9b.

In figs. 5a and 5b the convergence of Δc_p with respect to a is shown for two spanwise stations. The convergence is again remarkable.

The results presented so far, clearly show that with the method presented here the convergence of the results can be judged. This is true not only as far as the lift is concerned, but also for the higher moments. This leads to the fact that the chordwise loading also can be calculated with a high degree of accuracy. This is especially important as far as the determination of the local centre of pressure line is concerned.

4.3 Some results obtained with arbitrary distribution of pivotal points

As has been explained in the introduction, the method presented here allows an arbitrary choice of the spanwise points. This can be of advantage in those cases where strong gradients are expected in the solution. It is then possible to choose a greater density of the pivotal points in the region where the gradients should occur, thereby giving this region more "weight" than the rest. It may be hoped then that a better solution will be obtained.

In the Multhopp distribution of spanwise stations weighting occurs at the tip region. It is, however, totally absent at the centre section. This is not at all serious for straight wings, but certainly it is for swept wings. For the latter class of wings the freedom of choice offered by the present method should be beneficial. One of the great problems, of course, is to take optimal advantage of this possibility. That this is not a trivial question will appear when discussing the results of some of the trials made with arbitrary positions of the spanwise stations for the Warren 12 wing at $M_\infty = 0$. In table 10a the results are given for various values of a for a distribution of pivotal stations differing from Multhopp's distribution halfway between the tip and the centre only in having one point less in the tip region and one point more in the centre region.

In table 10b the results for another distribution are given. In this case the density of pivotal stations in the tip region is the same as in the Multhopp distribution, but the centre region has one point more and the region in between one point less.

Table 10c again shows the results that occur if the tip region has very few spanwise stations.

These three results, which are also presented in fig. 6a and 6b, together with the solution belonging to Multhopp's distribution of pivotal points, make it quite clear that the solution of the lifting surface problem is rather sensitive to the position of the pivotal stations.

However, it may be assumed that this effect becomes less important as the number of the points in any distribution is increased and that finally the solutions obtained will be the same.

Furthermore fig. 6 suggests that the basic distribution should not deviate too much from Multhopp's distribution. This is confirmed by the results shown in table 11a and in figs. 7a and 7b. In these the solution for Multhopp's distribution of pivotal points ($m = 17$) is compared with those for three other cases given in table 11b. The latter distributions are in fact those of tables 10, with one point added in each case. It is seen that the agreement of the results is much better indeed, except for case 4. Although it looks much more sensible than in table 10c, it still deviates quite severely from the other solutions.

On the basis of the results presented here it remains an open question whether the freedom of choice of the pivotal points will be useful in trying to obtain plausible solutions for the centre of a swept wing. This should be the subject of a special investigation. It seems plausible from the results obtained so far that in order to obtain better results for the centre, one should choose a distribution with some more density in the vicinity of the centre.

There is one other possibility which so far has not been tested. Since the number and the place of the pivotal stations can be prescribed independently of the number of functions representing the pressure difference across

the wing, it is possible to obtain more equations than unknowns. This system can then be solved by applying a least squares approximation. In this way it is also possible to give more weight to the centre region than to the rest of the wing. It seems worthwhile to investigate this point also.

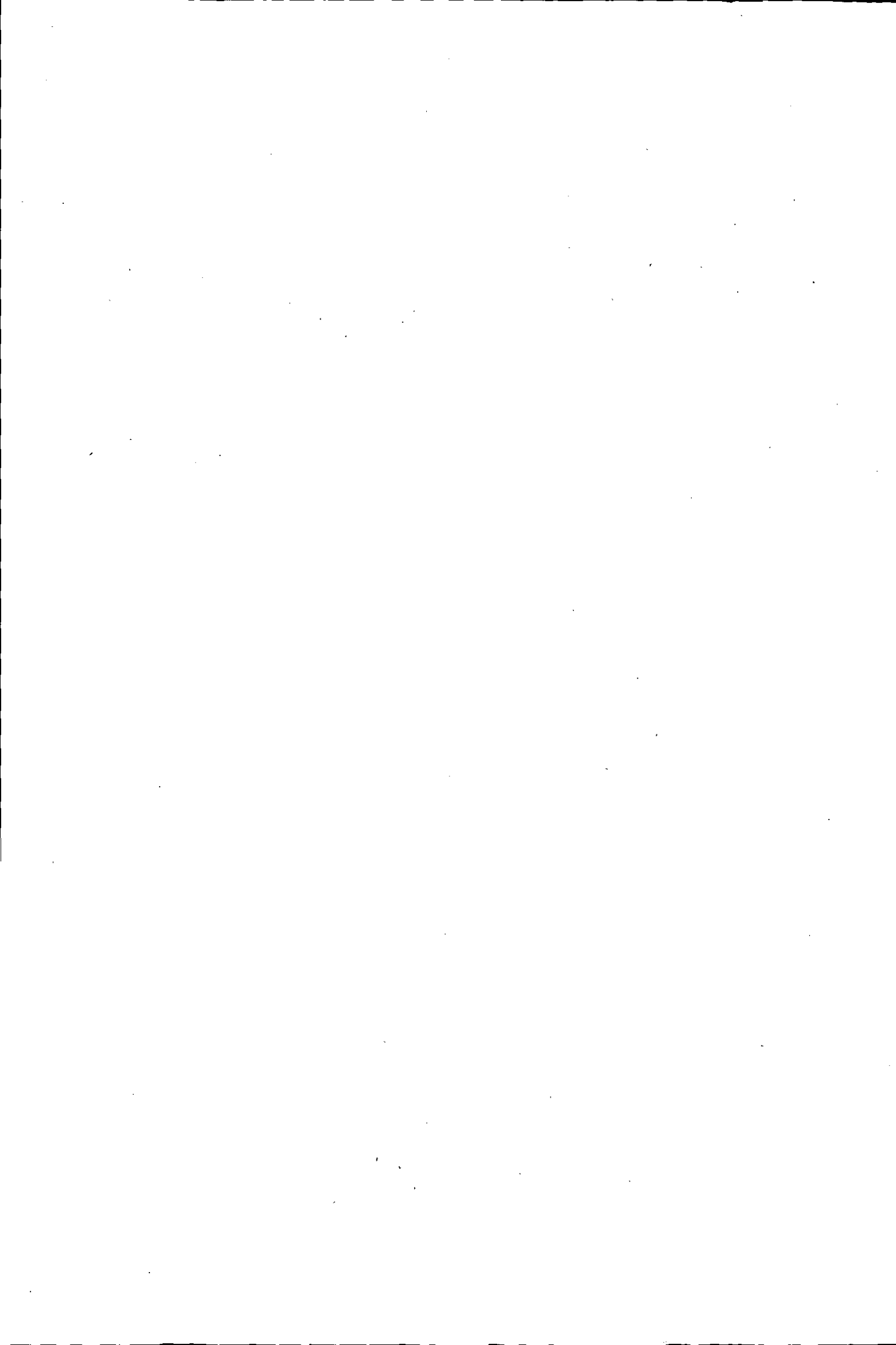
5 Concluding remarks

In this report a new method has been outlined, by which it is possible to obtain accurate numerical results for the pressure difference across a lifting surface. The theory has been formulated such that exact results are possible for wings with a continuous radius of curvature along the leading and trailing edges of the planform. The pressure difference across the wing is given as a series of chordwise terms with coefficients which are functions dependent on the spanwise co-ordinate. These functions themselves are also represented as a series of terms. The convergence of the results for an increasing number of chordwise and spanwise terms can be judged, and this is confirmed by the numerical results presented, which are based on Multhopp's distribution of pivotal points. It should be emphasized that one of the great advantages of the method seems to be the accurate determination of the local centre of pressure line.

Since the method permits of the arbitrary choice of pivotal stations, their distribution has been varied. It is shown that one has to be rather careful in selecting the positions. It seems that further investigations are required to decide whether or not this freedom of choice may be used to reduce the number of pivotal points at which plausible solutions are obtained for swept wings.

6 References

- ¹ Multhopp, H., Methods for calculating the lift distribution of wings. (Subsonic lifting-surface theory) A.R.C.R. + M 2884.
- ² Van Spiegel, E. and Wouters, J. G., Modification of Multhopp's lifting-surface theory with a view to automatic computation. NLR Report TN-W.2. 1962.
- ³ Garner, H. C., Accuracy of downwash evaluation by Multhopp's lifting-surface theory. A.R.C.R. + M. 3431.
- ⁴ Van de Vooren, A. I., Some additions to lifting-surface theory. Mathematisch Instituut, Universiteit Groningen. Report TW-35, 1966.
- ⁵ Laschka, B., Zur Theorie der harmonischen schwingenden tragenden Fläche bei Unterschallanströmung. Zeitschr.f. Flugw., July 1966.



APPENDIX A

A detailed derivation of the basic equations

A.1 The calculation of the quantities $\gamma_{n\lambda}$, ϵ_{vn} , ζ_{vn} and S_{vn}

In this appendix a detailed derivation will be given of eq. (2.18), starting from eq. (2.16). First the latter equation will be written down again for reference

$$\alpha(\xi, \eta) = -\frac{1}{2\pi} \sum_{r=0}^R \frac{2}{m+1} \sum_{n=1}^m a_r(\eta_n) \sum_{\mu=1}^m \sin \mu \theta_n \int_0^\pi \frac{F_r(\xi, \eta; \theta^1) \sin \mu \theta^1 \sin \theta^1}{(\cos \theta - \cos \theta^1)^2} d\theta^1 +$$

$$+ \frac{1}{2\pi} \sum_{r=0}^R \frac{2}{m+1} \frac{\beta^2 s^2}{l(\eta)^2} \frac{dh_r}{dX^1} (\theta^1 = \theta) \sum_{n=1}^m a_r(\eta_n) \sum_{\mu=1}^m \sin \mu \theta_n \int_0^\pi \ln(\cos \theta - \cos \theta^1) \sin \mu \theta^1 \sin \theta^1 d\theta^1. \quad A(1)$$

The singularity occurring in the first integral demands a special treatment. To reduce the integration to a formal procedure, the following function is constructed

$$\bar{F}_r(\xi, \theta; \theta^1) = F_r(\xi, \theta; \theta^1) - F_r(\xi, \theta; \theta) - (\cos \theta - \cos \theta^1) \frac{dF_r}{d\eta^1} (\theta^1 = \theta). \quad A(2)$$

As will be clear the function $\bar{F}_r(\xi, \theta; \theta^1)$ is of order $(\cos \theta - \cos \theta^1)^2$ near the point $\theta^1 = \theta$. This then leads to the introduction of a new function \bar{H}_r , which is completely regular for all values of θ^1 .

$$\bar{H}_r(\xi, \theta; \theta^1) = \frac{\bar{F}_r(\xi, \theta; \theta^1) \sin \theta^1}{(\cos \theta - \cos \theta^1)^2}. \quad A(3)$$

To avoid a numerical integration in spanwise direction, the function \bar{H}_r has been represented by a sum of sine terms

$$\bar{H}_r(\xi, \theta; \theta^1) = \frac{2}{\Lambda+1} \sum_{\lambda=1}^{\Lambda} \bar{H}_r(\xi, \theta; \theta_\lambda) \sum_{\omega=1}^{\Lambda} \sin \omega \theta^1 \sin \omega \theta_\lambda \quad A(4)$$

$$\text{where } \theta = \frac{\lambda\pi}{\lambda+1}$$

In the case considered here Λ will be taken equal to $a(m+1)-1$, where a is an integer. By taking a large enough, a sufficiently accurate representation of \bar{H}_r can be obtained.

Inserting the equations A(2), A(3) and A(4) into eq. A(1) one obtains, when performing the summation over ω in eq. A(4)

$$\alpha(\xi, \eta) = -\frac{1}{2\pi} \sum_{r=0}^R \frac{2}{m+1} \sum_{n=1}^m a_r(\eta_n) \sum_{\mu=1}^m \sin \mu \theta_n \sum_{\lambda=1}^{\Lambda} \frac{1}{\lambda+1} \bar{H}_r(\xi, \theta; \theta_\lambda) (-)^{\lambda} \sin \theta_\lambda \int_0^\pi \frac{\sin(\Lambda+1)\theta^1 \sin \mu \theta^1}{\cos \theta_\lambda - \cos \theta^1} d\theta^1 +$$

$$-\frac{1}{2\pi} \sum_{r=0}^R \frac{2}{m+1} \sum_{n=1}^m a_r(\eta_n) F_r(\xi, \theta; \theta) \sum_{\mu=1}^m \sin \mu \theta_n \int_0^\pi \frac{\sin \theta^1 \sin \mu \theta^1}{(\cos \theta - \cos \theta^1)^2} d\theta^1 +$$

$$-\frac{1}{2\pi} \sum_{r=0}^R \frac{2}{m+1} \sum_{n=1}^m a_r(\eta_n) \frac{dF_r}{d\eta^1} (\theta^1 = \theta) \sum_{\mu=1}^m \sin \mu \theta_n \frac{\sin \theta^1 \sin \mu \theta^1}{(\cos \theta - \cos \theta^1)} d\theta^1 +$$

$$+ \frac{1}{2\pi} \sum_{r=0}^R \frac{2}{m+1} \frac{\beta^2 s^2}{l(\eta)^2} \frac{dh_r}{dX^1} (\theta^1 = \theta) \sum_{n=1}^m a_r(\eta_n) \sum_{\mu=1}^m \sin \mu \theta_n \int_0^\pi \ln|\cos \theta - \cos \theta^1| \sin \mu \theta^1 \sin \theta^1 d\theta^1. \quad A(5)$$

The problem has now been reduced to the determination of the integrals in eq. A(5). The following abbreviations will be used where θ has been replaced by θ_v

$$\gamma_{n\lambda} = \frac{2(-)^{\lambda} \sin \theta_\lambda}{\pi(m+1)} \sum_{\mu=1}^m \sin \mu \theta_n \int_0^\pi \frac{\sin(\Lambda+1)\theta^1 \sin \mu \theta^1}{\cos \theta_\lambda - \cos \theta^1} d\theta^1 \quad A(6a)$$

$$\epsilon_{vn} = \frac{2 \sin \theta_v}{\pi(m+1)(\sin \theta_n)} \sum_{\mu=1}^m \sin \mu \theta_n \int_0^\pi \frac{\sin \theta^1 \sin \mu \theta^1}{(\cos \theta_v - \cos \theta^1)^2} d\theta^1 \quad A(6b)$$

$$\zeta_{vn} = \frac{2}{\pi(m+1)} \sum_{\mu=1}^m \sin \mu \theta_n \int_0^\pi \frac{\sin \theta^1 \sin \mu \theta^1}{\cos \theta_v - \cos \theta^1} d\theta^1 \quad A(6c)$$

$$S_{vn} = \frac{2}{\pi(m+1)} \sum_{\mu=1}^m \sin \mu \theta_n \int_0^\pi \ln|\cos \theta_v - \cos \theta^1| \sin \mu \theta^1 \sin \theta^1 d\theta^1 \quad A(6d)$$

These functions will subsequently be evaluated.

The integral in eq. A(6)a becomes

$$\begin{aligned} \int_0^\pi \frac{\sin(\lambda+1)\theta^1 \sin \mu\theta^1}{\cos \theta_\lambda - \cos \theta^1} d\theta^1 &= \frac{1}{2} \int_0^\pi \frac{\cos(\lambda+1-\mu)\theta^1 - \cos(\lambda+1+\mu)\theta^1}{\cos \theta_\lambda - \cos \theta^1} d\theta^1 \\ &= -\frac{1}{2}\pi \frac{\sin(\lambda+1-\mu)\theta_\lambda - \sin(\lambda+1+\mu)\theta_\lambda}{\sin \theta_\lambda} \\ &= \pi \frac{\cos(\lambda+1)\theta_\lambda \sin \theta_\lambda}{\sin \theta_\lambda} = \pi(-)^{\lambda} \frac{\sin \mu\theta_\lambda}{\sin \theta_\lambda}. \end{aligned}$$

This leads to

$$\gamma_{n\lambda} = \frac{2}{m+1} \sum_{\mu=1}^m \sin \mu\theta_n \sin \mu\theta_\lambda,$$

and after summation to

$$\gamma_{n\lambda} = \frac{1}{m+1} \begin{cases} \sin \frac{\lambda\pi}{a} \sin \theta_n \\ (-)^n \frac{\sin \frac{\lambda\pi}{a} \sin \theta_n}{\cos \theta_n - \cos \theta_\lambda}, & \text{if } \theta_n \neq \theta_\lambda \\ m+1 & \text{if } \theta_n = \theta_\lambda \end{cases} \quad \text{A(7)}$$

For the integral in eq. A(6)b, it follows immediately, by partial integration, that

$$\int_0^\pi \frac{\sin \mu\theta^1 \sin \theta^1}{(\cos \theta_v - \cos \theta^1)^2} d\theta^1 = -\mu\pi \frac{\sin \mu\theta_v}{\sin \theta_v}.$$

It should be observed that this formal procedure is in accordance with the definition of the principal value. Hence it is found

$$\varepsilon_{vn} = -\frac{2}{(m+1)\sin \theta_n} \sum_{\mu=1}^m \mu \sin \mu\theta_v \sin \mu\theta_n.$$

Since

$$\sum_{\mu=1}^m \mu \sin \mu\theta_v \sin \mu\theta_n = -\frac{d}{d\theta} \sum_{\mu=1}^m \cos \mu\theta_v \sin \mu\theta_n,$$

it is found after some manipulation that

$$\varepsilon_{vn} = +\frac{1}{m+1} \frac{d}{d\theta_v} \left\{ \frac{1 - (-)^n \cos(m+1)\theta_v}{\cos \theta_v - \cos \theta_n} \right\}, \text{ and hence}$$

$$\varepsilon_{vn} = \frac{(-1)^n \sin(m+1)\theta_v}{\cos \theta_v - \cos \theta_n} + \frac{1}{m+1} \frac{1 - (-)^n \cos(m+1)\theta_v}{(\cos \theta_v - \cos \theta_n)^2} \sin \theta_v, \quad \theta_v \neq \theta_n. \quad \text{A(8)a}$$

$$\varepsilon_{vn} = -\frac{1}{2} \frac{m+1}{\sin \theta_n}, \quad \theta_v = \theta_n. \quad \text{A(8)b}$$

To calculate the function ζ_{vn} , the following integral has to be considered.

$$\int_0^\pi \frac{\sin \mu\theta^1 \sin \theta^1}{\cos \theta_v - \cos \theta^1} d\theta^1 = \pi \cos \mu\theta_v.$$

Inserting this result into the expression for ζ_{vn} , gives

$$\zeta_{vn} = \frac{2}{m+1} \sum_{\mu=1}^m \sin \mu\theta_n \cos \mu\theta_v,$$

and by the procedure used for ε_{vn} , it is immediately clear that

$$\zeta_{vn} = \frac{\sin \theta_n}{m+1} \frac{1 - (-)^n \cos(m+1)\theta_v}{\cos \theta_v - \cos \theta_n}, \quad \theta_v \neq \theta_n \quad \text{A(9)a}$$

$$\zeta_{vn} = 0, \quad \theta_v = \theta_n. \quad \text{A(9)b}$$

The last quantity that has to be considered is S_{vn} . First it is remarked that for $\mu > 1$ the following relation is valid

$$\int_0^\pi \sin \mu\theta^1 \sin \theta^1 \ln |\cos \theta_v - \cos \theta^1| d\theta^1 = -\frac{\pi}{\mu^2 - 1} (\mu \sin \mu\theta_v \sin \theta_v + \cos \mu\theta_v \cos \theta_v)$$

This follows by applying partial integration and some of the previous results. The integral for $\mu=1$ proves to be

$$\int_0^\pi \sin^2 \theta^1 \ln |\cos \theta_v - \cos \theta^1| d\theta^1 = -\frac{\pi}{2} \ln 2 + \frac{\pi}{4} \cos 2\theta_v.$$

Hence the total result is

$$S_{vm} = \frac{2}{m+1} \left[\left(-\frac{1}{2} \ln 2 + \frac{1}{4} \cos 2\theta_v\right) \sin \theta_n - \sum_2^m \frac{(\mu \sin \mu\theta_v \sin \theta_v + \cos \mu\theta_v \cos \theta_v) \sin \mu\theta_n}{\mu^2 - 1} \right] \quad \text{A(10)}$$

In table 1 the expressions for the quantities $\gamma_{n\lambda}$, ε_{vm} , ζ_{vm} and S_{vm} have been summarized.

A.2 The calculation of the quantities $\frac{\partial F_r}{\partial \eta^1}(\theta^1 = \theta_v)$ and $\bar{H}_r(\xi, \theta_v; \theta_v)$

In order to calculate the quantities $\frac{\partial F_r}{\partial \eta}(\theta^1 = \theta_v)$ and $\bar{H}_r(\xi, \theta_v; \theta_v)$ it is necessary to consider the expression for $H_r(\xi, \eta; \eta^1)$

$$H_r(\xi, \eta; \eta^1) = \int_0^1 h_r(x^1) \left[1 + \frac{x-x^1}{\sqrt{(x-x^1)^2 + \beta^2 y^2}} \right] dx^1. \quad \text{A(11)}$$

The quantities x and y are defined as follows

$$x = \frac{s}{l(\eta^1)} \{\xi - \xi_1(\eta^1)\} \quad \text{and} \quad y = \frac{s}{l(\eta^1)} (\eta - \eta^1)$$

The value of x for $\eta = \eta^1$ will be denoted by x_0 so that

$$x_0 = \frac{s}{l(\eta)} \{\xi - \xi_1(\eta)\}.$$

This shows that x is dependent on η^1 and hence on y . Therefore the following series expansion is valid.

$$x = x_0 + (\eta^1 - \eta) \frac{dx_0}{d\eta} + \frac{1}{2} (\eta^1 - \eta)^2 \frac{d^2 x_0}{d\eta^2} + \dots \quad \text{A(12)}$$

where $\frac{dx_0}{d\eta}$ is equal to $\frac{dx}{d\eta^1}$ for $\eta^1 = \eta$ and $\frac{d^2 x_0}{d\eta^2}$ is defined correspondingly. Since the point of interest is the behaviour of H_r at $\theta^1 = \theta_v$, the investigation can be restricted to small values of y .

First it is remarked that

$$H_r(\xi, \eta; \eta) = 2 \int_0^{x_0} h_r(x^1) dx^1. \quad \text{A(13)}$$

The first derivative of H_r with respect to η^1 can be written as

$$\begin{aligned} \frac{dH_r}{d\eta^1} = & -\frac{dx}{d\eta^1} \int_0^1 h_r(x^1) \frac{d}{dx^1} \left\{ \frac{x-x^1}{\sqrt{(x-x^1)^2 + \beta^2 y^2}} \right\} dx^1 + \\ & -\beta^2 y \frac{dy}{d\eta^1} \int_0^1 h_r(x^1) \frac{d}{dx^1} \left\{ \frac{1}{\sqrt{(x-x^1)^2 + \beta^2 y^2}} \right\} dx^1. \end{aligned}$$

By using the expansion $h_r(x^1) = h_r(x_0) + (x^1 - x_0) \frac{dh_r}{dx^1}(x_0) + \dots$ and performing some partial integrations it is found that

$$\begin{aligned} \frac{dH_r}{d\eta^1} = & \frac{dx}{d\eta^1} \left\{ \frac{x}{\sqrt{x^2 + \beta^2 y^2}} + \frac{1-x}{\sqrt{(1-x)^2 + \beta^2 y^2}} \right\} \left[h_r(x_0) + (x-x_0) \frac{dh_r}{dx^1} \right] + O(y^2) + \\ & + \beta^2 y \frac{dy}{d\eta^1} \int_0^1 \frac{dh_r}{dx^1} \left\{ \frac{1}{\sqrt{(x-x^1)^2 + \beta^2 y^2}} - \frac{1}{\sqrt{x^2 + \beta^2 y^2}} \right\} dx^1. \end{aligned} \quad \text{A(14)}$$

It can be observed that the integrand occurring in this expression is integrable for $x^1=0$, but that difficulties can arise when $x^1 \rightarrow x_0$ and $y \rightarrow 0$. Using again the series expression for $h_r(x^1)$, it is found immediately that

$$\frac{dH_r}{d\eta^1} = \frac{dx}{d\eta^1} \left\{ \frac{x}{\sqrt{x^2 + \beta^2 y^2}} + \frac{1-x}{\sqrt{(1-x)^2 + \beta^2 y^2}} \right\} \left[h_r(x_0) + (x-x_0) \frac{dh_r}{dx^1}(x_0) + \right. \\ \left. + O(y^2) - \frac{dh_r}{dx^1}(x_0) \cdot \beta^2 y \frac{dy}{d\eta^1} \ln(\beta^2 y^2) + O(y) \right].$$

From this it follows at once that

$$\frac{dH_r}{d\eta^1} (\eta^1 = \eta) = \frac{dF_r}{d\eta^1} (\theta^1 = \theta_v) = 2h_r(x_0) \frac{dx_0}{d\eta} \quad \text{A(15)}$$

In order to obtain the function $\bar{H}_r(\xi, \theta_v; \theta_v)$ it is necessary to consider the expression for $\frac{d^2 H_r}{d\eta^{1^2}}$. From eq. A(14) it is clear that the following expression is valid.

$$\frac{d^2 H_r}{d\eta^{1^2}} = \frac{d^2 x}{d\eta^{1^2}} \left\{ \frac{x}{\sqrt{x^2 + \beta^2 y^2}} + \frac{1-x}{\sqrt{(1-x)^2 + \beta^2 y^2}} \right\} h_r(x_0) + \left(\frac{dx}{d\eta^1} \right)^2 \left\{ \frac{x}{\sqrt{x^2 + \beta^2 y^2}} + \frac{1-x}{\sqrt{(1-x)^2 + \beta^2 y^2}} \right\} \frac{dh_r}{dx^1}(x_0) + \\ + O(y) + \beta^2 \left(\frac{dy}{d\eta^1} \right)^2 \int_0^1 \frac{dh_r}{dx^1} \left\{ \frac{1}{\sqrt{(x-x^1)^2 + \beta^2 y^2}} - \frac{1}{\sqrt{x^2 + \beta^2 y^2}} \right\} dx^1 + \\ + \beta^2 y^2 \frac{dy}{d\eta^1} \int_0^1 \frac{dh_r}{dx^1} \left\{ -\frac{dx}{d\eta^1} \frac{d}{dx^1} \left[\frac{1}{\sqrt{(x-x^1)^2 + \beta^2 y^2}} \right] + \frac{1}{y} \frac{dy}{d\eta^1} \frac{d}{dx^1} \left[\frac{x-x^1}{\sqrt{(x-x^1)^2 + \beta^2 y^2}} \right] \right\} dx^1 \quad \text{A(16)}$$

This can be written as follows by using some of the results obtained when deriving the expressions for $\frac{dH_r}{d\eta^1}$

$$\frac{d^2 H_r}{d\eta^{1^2}} = \left\{ \frac{d^2 x_0}{d\eta^{1^2}} h_r(x_0) + \left(\frac{dx_0}{d\eta^1} \right)^2 \frac{dh_r}{dx^1}(x_0) - \beta^2 \left(\frac{dy}{d\eta^1} \right)^2 \frac{dh_r}{dx^1}(x_0) \right\} \left[\frac{x}{\sqrt{x^2 + \beta^2 y^2}} + \frac{1-x}{\sqrt{(1-x)^2 + \beta^2 y^2}} \right] + \\ + \beta^2 \left(\frac{dy}{d\eta^1} \right)^2 \int_0^1 \frac{dh_r}{dx^1} \left\{ \frac{1}{\sqrt{(x-x^1)^2 + \beta^2 y^2}} - \frac{1}{\sqrt{x^2 + \beta^2 y^2}} \right\} dx^1 + O(y).$$

The real problem now is to evaluate the integral occurring in this expression, and the objective is a formula which can easily be calculated numerically.

The integral is written as follows

$$\int_0^1 \frac{dh_r}{dx^1} \left\{ \frac{1}{\sqrt{(x-x^1)^2 + \beta^2 y^2}} - \frac{1}{\sqrt{x^2 + \beta^2 y^2}} \right\} dx^1 = \\ \frac{1}{\sqrt{x^2 + \beta^2 y^2}} \int_0^x \frac{dh_r}{dx^1} \frac{x^1}{\sqrt{(x-x^1)^2 + \beta^2 y^2}} \frac{2x-x^1}{\sqrt{(x-x^1)^2 + \beta^2 y^2} + \sqrt{x^2 + \beta^2 y^2}} dx^1 + \\ + \int_x^1 \frac{dh_r}{dx^1} \frac{dx}{\sqrt{(x-x^1)^2 + \beta^2 y^2}} + \frac{1}{\sqrt{x^2 + \beta^2 y^2}} h_r(x)$$

The next step is to add expressions which are identically equal to zero, but which serve two purposes; first to control expressions in which the limits $x \rightarrow x_0$ and $y \rightarrow 0$ may be applied, and second to obtain expressions which can be calculated analytically. Hence the above expression is rewritten as

$$\frac{1}{\sqrt{x^2 + \beta^2 y^2}} \left\{ \int_0^x \frac{dh_r}{dx^1} \frac{x^1}{\sqrt{(x-x^1)^2 + \beta^2 y^2}} \frac{(2x-x^1) dx^1}{\sqrt{(x-x^1)^2 + \beta^2 y^2} + \sqrt{x^2 + \beta^2 y^2}} - \int_x^1 \frac{dh_r}{dx^1} \frac{x^1 dx^1}{\sqrt{(x-x^1)^2 + \beta^2 y^2}} \right\} + \\ + \frac{2}{\sqrt{x^2 + \beta^2 y^2}} \int_x^1 \left\{ x^1 \frac{dh_r}{dx^1} - \sqrt{x^2 + \beta^2 y^2} \frac{dh_r}{dx^1}(x_0) \sqrt{\frac{x(1-x)}{x^1(1-x^1)}} \right\} \frac{dx^1}{\sqrt{(x-x^1)^2 + \beta^2 y^2}} \\ + 2 \frac{dh_r}{dx^1}(x_0) \int_x^1 \left\{ \sqrt{\frac{x(1-x)}{x^1(1-x^1)}} - 1 \right\} \frac{dx^1}{\sqrt{(x-x^1)^2 + \beta^2 y^2}} + \\ + 2 \frac{dh_r}{dx_0} \int_x^1 \frac{dx^1}{\sqrt{(x-x^1)^2 + \beta^2 y^2}} + \frac{1}{\sqrt{x^2 + \beta^2 y^2}} \int_x^1 \frac{dh_r}{dx^1} \frac{\sqrt{x^2 + \beta^2 y^2 - x^1}}{\sqrt{(x-x^1)^2 + \beta^2 y^2}} dx^1 + \frac{1}{\sqrt{x^2 + \beta^2 y^2}} h_r(x).$$

This expression can be simplified considerably by observing that almost all integrands remain bounded for $x \rightarrow x_0$ and $y \rightarrow 0$. The result is

$$\begin{aligned} \frac{1}{x_0} \int_0^1 \frac{dh_r}{dx^1} \frac{x^1}{x_0 - x^1} dx^1 + \frac{2}{x_0} \int_{x_0}^1 \left\{ x^1 \frac{dh_r}{dx^1} - x_0 \frac{dh_r}{dx^1}(x_0) \sqrt{\frac{x_0(1-x_0)}{x^1(1-x^1)}} \right\} \frac{dx^1}{x^1 - x_0} + \\ + 2 \frac{dh_r}{dx^1}(x_0) \int_{x_0}^1 \left\{ \sqrt{\frac{x_0(1-x_0)}{x^1(1-x^1)}} - 1 \right\} \frac{dx^1}{x^1 - x_0} + 2 \frac{dh_r}{dx_0} \ln \frac{2(1-x_0)}{\beta y} + \frac{2}{x_0} h_r(x_0). \quad A(16) \end{aligned}$$

The integrals occurring in eq. A(16) can now easily be expressed by using the trigonometric representation of eqs. (2.8) and (2.9). It follows that

$$\int_0^1 \frac{dh_r}{dx^1} \frac{x^1}{x_0 - x^1} dx^1 = -\frac{2}{\sin \psi_0} \left[(r+1) \sin r\psi_0 - r \sin(r+1)\psi_0 \right]$$

while

$$\int_{x_0}^1 \left\{ x^1 \frac{dh_r}{dx^1} - x_0 \frac{dh_r}{dx^1}(x_0) \sqrt{\frac{x_0(1-x_0)}{x^1(1-x^1)}} \right\} \frac{dx^1}{x^1 - x_0} = \frac{2}{\pi} [(r+1)I_r - rI_{r+1}]$$

where

$$I_r = \int_{\psi_0}^{\pi} \frac{\cos r\psi_0 - \cos r\psi}{\cos \psi_0 - \cos \psi} d\psi. \quad A(17)$$

The calculation of this integral can be performed by using the recursive relation

$$I_r - 2 \cos \psi_0 I_{r-1} + I_{r-2} = -\frac{2}{r-1} \sin(r-1)\psi_0$$

with the accessory relations $I_0 = 0$ and $I_1 = \pi - \psi_0$.

Finally the last integral occurring in eqn. A(16) proves to be

$$\int_{x_0}^1 \left\{ \sqrt{\frac{x_0(1-x_0)}{x^1(1-x^1)}} - 1 \right\} \frac{dx^1}{x^1 - x_0} = \ln 4x_0.$$

Combining the results we at last obtain

$$\begin{aligned} \frac{d^2 H_r}{d\eta^{12}} = 2 \left\{ \frac{d^2 x_0}{d\eta^2} h_r(x_0) + \left[\frac{dx_0}{d\eta} \right]^2 \frac{dh_r}{dx^1}(x_0) - \beta^2 \left[\frac{dy}{d\eta} \right]^2 \frac{dh_r}{dx^1}(x_0) \right\} + 2\beta^2 \left[\frac{dy}{d\eta} \right]^2 \\ \cdot \left\{ -\frac{1}{x_0 \sin \psi_0} [(r+1) \sin r\psi_0 - r \sin(r+1)\psi_0] + \frac{2}{\pi x_0} [(r+1)I_r - rI_{r+1}] + \frac{dh_r}{dx^1}(x_0) \ln 8x_0(1-x_0) + \frac{1}{x_0} h_r(x_0) \right\} \\ - 2\beta^2 \left[\frac{dy}{d\eta} \right]^2 \frac{dh_r}{dx^1}(x_0) \ln \beta y + O(y). \end{aligned}$$

It follows from eq. (2.17) that

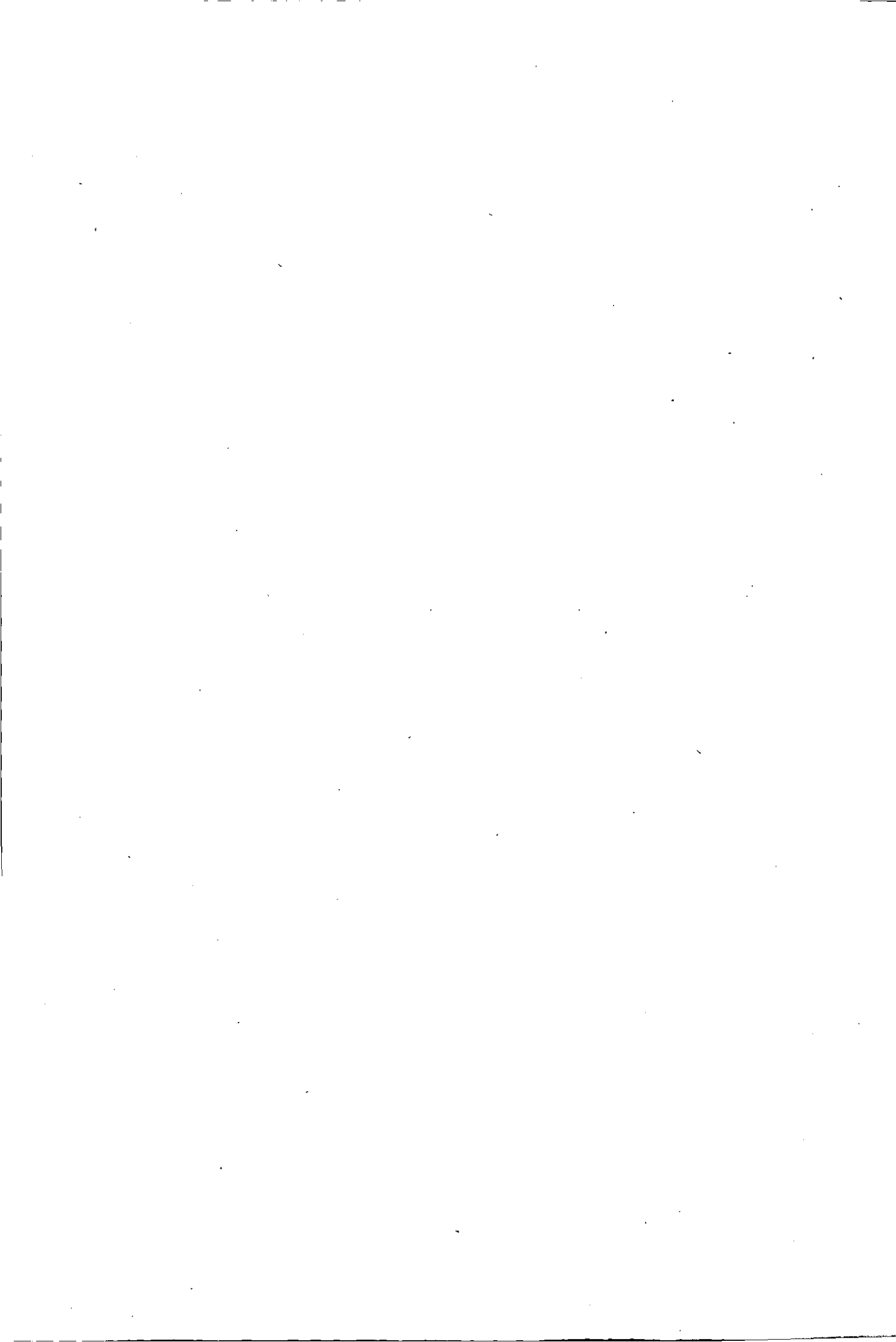
$$\bar{H}_r(\xi, \theta_v; \theta_v) = \frac{1}{2} \sin \theta_v \frac{\partial^2 F_r}{\partial \eta^2} (\theta^1 = \theta_v)$$

while further from eq. (2.13) it is evident that

$$\frac{d^2 F}{d\eta^{12}} = \frac{d^2 H_r}{d\eta^{12}} + \left\{ 2 \frac{\beta^2 s^2}{l(\eta)^2} \ln |\eta - \eta^1| + 3 \frac{\beta^2 s^2}{l(\eta)^2} \right\} \frac{dh_r}{dx^1}(x_0).$$

With the observation that $\left[\frac{dy}{d\eta} \right]^2 = \left\{ \frac{s}{l(\eta)} \right\}^2$, there is finally obtained

$$\begin{aligned} \bar{H}_r(\xi, \theta_v; \theta_v) = \left\{ \frac{d^2 x_0}{d\eta^2} h_r(\psi_0) + 2 \left[\frac{dx_0}{d\eta} \right]^2 \frac{dh_r}{d\psi}(\psi_0) \frac{1}{\sin \psi_0} \right\} \sin \theta_v + \sin \theta_v \frac{\beta^2 s^2}{l(\eta)^2} \\ \cdot \left\{ -\frac{1}{x_0 \sin \psi_0} [(r+1) \sin r\psi_0 - r \sin(r+1)\psi_0] + \frac{2}{\pi x_0} [(r+1)I_r - rI_{r+1}] + \frac{1}{x_0} h_r(x_0) \right. \\ \left. + \frac{dh_r}{d\psi}(\psi_0) \frac{1}{\sin \psi_0} + \frac{2}{\sin \psi_0} \frac{dh_r}{d\psi}(\psi_0) \ln \left[\frac{2l(\eta)}{\beta s} \sin^2 \psi_0 \right] \right\} \quad A(18) \end{aligned}$$



APPENDIX B

The integration in chordwise direction

In this appendix a detailed description will be given of the numerical procedure used in evaluating the function $H_r(\xi, \eta; \eta^1)$.

$$H_r(\xi, \eta; \eta^1) = \int_0^1 h_r(X^1) \frac{X - X^1}{\sqrt{(X - X^1)^2 + \beta^2 Y^2}} dX^1 \quad \text{B(1)}$$

In terms of the angular co-ordinate given by $X^1 = \frac{1 - \cos \psi}{2}$ the integral can be written as

$$H_r(\xi, \eta; \eta^1) = \frac{1}{2} \int_0^\pi [\cos r\psi + \cos(r+1)\psi] f(\psi) d\psi \quad \text{B(2)}$$

$$\text{where } f(\psi) = \frac{\beta_1 + \cos \psi}{\sqrt{(\beta_1 + \cos \psi)^2 + \beta_2^2}} \quad \text{B(3)}$$

while the quantities β_1 and β_2 are defined as follows

$$\beta_1 = 2X - 1 \quad \text{B(4)a}$$

$$\beta_2 = \beta Y \quad \text{B(4)b}$$

Since the integrand is periodic with period 2π and since the integral from 0 to π is equal to the integral from π to 2π the best fitting integration rule is the simple trapezoidal rule.

Thus

$$H_r(\xi, \eta; \eta^1) = \frac{1}{(L+1)} \left\{ f(\psi_0) + \sum_{j=1}^L [\cos r\psi_j + \cos(r+1)\psi_j] f(\psi_j) \right\} \quad \text{B(5)}$$

where $L+1$ is the number of integration points and $\psi_j = \frac{j\pi}{L+1}$. It is obvious that the quantity L will depend on the parameters β_1 and β_2 and it seems quite natural to rely on a test of accuracy in the programme for its determination. This, however, proves to be a very time-consuming procedure, especially when small values of β_2 are encountered, in which case the function $f(\psi)$ is almost discontinuous at $\psi = \arccos \beta_1$. Therefore another way was followed. It was decided to investigate the function H_r as a function of β_1 and β_2 and to establish regions in the $\beta_1 - \beta_2$ plane where a given number L would assure an integration accuracy up to 9 decimals for $r=0$ up to $r=10$. It appeared that in this way an accurate result could be obtained for almost the whole region of interest. Only for very small values of β_2 a different scheme had to be followed. These regions with the accessory number L are given in figure B.1. These procedures, though less elegant, provided a very fast programme.

As is indicated in the figure, the region where the above mentioned integration rule does not apply is $|\beta_2| \leq 0,02$ and $|\beta_1| < 1$. In this region a new parameter is introduced by defining $\beta_1 = -\cos \phi$. Hence

$$f(\psi) = \frac{\cos \psi - \cos \phi}{\sqrt{(\cos \psi - \cos \phi)^2 + \beta_2^2}} \quad \text{B(6)}$$

As can be seen, the following relations are valid

$$\lim_{\substack{\beta_2 \rightarrow 0 \\ \psi \rightarrow \phi^+}} f(\psi) = -1 \quad \text{B(7)a}$$

and

$$\lim_{\substack{\beta_2 \rightarrow 0 \\ \psi \rightarrow \phi^-}} f(\psi) = +1 \quad \text{B(7)b}$$

The integral can then be written as

$$H_r = \frac{1}{\pi} \left[\int_0^P (\cos r\psi + \cos(r+1)\psi) [f(\psi) - 1] d\psi + \int_P^\phi (\cos r\psi + \cos(r+1)\psi) [f(\psi) - 1] d\psi \right. \\ \left. + \int_\phi^Q (\cos r\psi + \cos(r+1)\psi) [f(\psi) + 1] d\psi + \int_\phi^\pi (\cos r\psi + \cos(r+1)\psi) [f(\psi) + 1] d\psi + g_r(\phi) \right] \quad \text{B(8)}$$

where
$$g_0(\phi) = \left\{ \phi + \sin \phi - \frac{\pi}{2} \right\} \frac{2}{\pi} \quad g_r(\phi) = \left\{ \frac{1}{r} \sin r\phi + \frac{1}{r+1} \sin(r+1)\phi \right\} \frac{2}{\pi}$$

The quantities P and Q are defined as follows.

$$P = \arccos(\cos \phi + 10\beta_2) \quad \text{B(9)a}$$

$$Q = \arccos(\cos \phi - 10\beta_2) \quad \text{B(9)b}$$

Taking this into account the integrals from 0 to P and from Q to π are easily computable without loss of accuracy. The attention can now be focussed on the remaining integrals. We consider the second integral

$$\int_P^\phi (\cos r\psi + \cos(r+1)\psi) [f(\psi) - 1] d\psi = 2 \int_P^\phi \cos \frac{1}{2}(2r+1)\psi \cos \frac{1}{2}\psi [f(\psi) - 1] d\psi.$$

Now the main part of this integral will be subtracted in such a way that it can be integrated analytically while the remaining part again can be computed numerically in an accurate way. We therefore write

$$2 \int_P^\phi \cos \frac{1}{2}(2r+1)\psi \cos \frac{1}{2}\psi [f(\psi) - 1] d\psi = 2 \int_P^\phi \frac{\cos \frac{1}{2}(2r+1)\psi \cos \frac{1}{2}\psi \sin \phi - \cos \frac{1}{2}(2r+1)\phi \cos \frac{1}{2}\phi \sin \psi}{\sin \phi} [f(\psi) - 1] d\psi + 2 \frac{\cos \frac{1}{2}(2r+1)\phi \cos \frac{1}{2}\phi}{\sin \phi} \int_P^\phi [f(\psi) - 1] \sin \psi d\psi.$$

The second integration can be performed analytically and gives

$$\frac{2}{\sin \frac{1}{2}\phi} \int_P^\phi \cos \frac{1}{2}\psi [\cos \frac{1}{2}(2r+1)\psi \sin \frac{1}{2}\phi - \cos \frac{1}{2}(2r+1)\phi \sin \frac{1}{2}\psi] [f(\psi) - 1] d\psi + \frac{\cos \frac{1}{2}(2r+1)\phi}{\sin \frac{1}{2}\phi} [-|\beta_2| + |\beta_2| \sqrt{101 - 10\beta_2}]. \quad \text{B(10)}$$

This may be written as

$$\frac{2}{\sin \frac{1}{2}\phi} \int_{P-\phi}^0 \cos \frac{1}{2}(\xi + \phi) \{ \sin \frac{1}{2}r\xi \cos \frac{1}{2}(r+1)(\xi + 2\phi) - \sin \frac{1}{2}(r+1)\xi \cos \frac{1}{2}r(\xi + 2\phi) \} [f(\xi + \phi) - 1] d\xi + \frac{\cos \frac{1}{2}(2r+1)\phi}{\sin \frac{1}{2}\phi} [-|\beta_2| + |\beta_2| \sqrt{101 - 10\beta_2}].$$

In the same way it is found that

$$\int_\phi^Q \{ \cos r\psi + \cos(r+1)\psi \} [f(\psi) + 1] d\psi = \frac{2}{\sin \frac{1}{2}\phi} \int_0^{Q-\phi} \cos \frac{1}{2}(\xi + \phi) \{ \sin \frac{1}{2}r\xi \cos \frac{1}{2}(r+1)(\xi + 2\phi) - \sin \frac{1}{2}(r+1)\xi \cos \frac{1}{2}r(\xi + 2\phi) \} [f(\xi + \phi) + 1] d\xi + \frac{\cos \frac{1}{2}(2r+1)\phi}{\sin \frac{1}{2}\phi} [|\beta_2| - |\beta_2| \sqrt{101 + 10\beta_2}]. \quad \text{B(11)}$$

By combining the various terms it is found at last that

$$H_r = \frac{1}{\pi} \left[\int_0^P \{ \cos r\psi + \cos(r+1)\psi \} [f(\psi) - 1] d\psi + \int_\phi^\pi \{ \cos r\psi + \cos(r+1)\psi \} [f(\psi) + 1] d\psi \right] + g_r(\phi) + \frac{2}{\pi \sin \frac{1}{2}\phi} \left[\int_{P-\phi}^0 \cos \frac{1}{2}(\xi + \phi) \{ \sin \frac{1}{2}r\xi \cos \frac{1}{2}(r+1)(\xi + 2\phi) - \sin \frac{1}{2}(r+1)\xi \cos \frac{1}{2}r(\xi + 2\phi) \} [f(\xi + \phi) - 1] d\xi + \int_0^{Q-\phi} \cos \frac{1}{2}(\xi + \phi) \{ \sin \frac{1}{2}r\xi \cos \frac{1}{2}(r+1)(\xi + 2\phi) - \sin \frac{1}{2}(r+1)\xi \cos \frac{1}{2}r(\xi + 2\phi) \} [f(\xi + \phi) + 1] d\xi \right]$$

This formula offers no serious difficulties in numerical computation and gives good results as long as

$$|\cos \phi \pm 10|\beta_2|| \leq 1$$

or

$$|-\beta_1 \pm 10|\beta_2|| \leq 1$$

This restriction amounts to $|\beta_1| \leq 1 - 10|\beta_2|$. Therefore the procedure is successful in the shaded part of fig. B.1.

TABLE 1
The various influence functions in spanwise direction.

$\gamma_{n\lambda}$	$\frac{(-1)^n \sin \frac{\lambda\pi}{a} \sin \theta_n}{m+1 \cos \theta_n - \cos \theta_\lambda}$	$\theta_n \neq \theta_\lambda$
	1	$\theta_n = \theta_\lambda$
ϵ_{vn}	$\frac{(-1)^n \sin(m+1)\theta_v}{\cos \theta_v - \cos \theta_n} + \frac{1}{m+1} \frac{1 - (-1)^n \cos(m+1)\theta_v}{(\cos \theta_v - \cos \theta_n)^2} \sin \theta_v$	$\theta_v \neq \theta_n$
	$-\frac{1}{2} \frac{m+1}{\sin \theta_n}$	$\theta_v = \theta_n$
ζ_{vn}	$\frac{\sin \theta_n}{m+1} \frac{1 - (-1)^n \cos(m+1)\theta_v}{\cos \theta_v - \cos \theta_n}$	$\theta_v \neq \theta_n$
	0	$\theta_v = \theta_n$
S_{vn}	$\frac{2}{m+1} \left[\left(-\frac{1}{2} \ln 2 + \frac{1}{4} \cos 2\theta \right) \sin \theta_n - \sum_{\mu=2}^m \frac{(\mu \sin \mu\theta_v \sin \theta_v + \cos \mu\theta_v \cos \theta_v) \sin \mu\theta_n}{\mu^2 - 1} \right]$	

TABLE 2A
Wing: circle; Machnumber - 0
Convergence of the quantities a_r with respect to a (corresponding to number of spanwise integration points)
 $m=5 \quad R=2$

coeff.	η	a	1	2	3	4	6	8
a_0		0.866025	0.438516	0.439264	0.439101	0.439138	0.439071	0.439046
		0.5	0.776970	0.777409	0.777249	0.777294	0.777256	0.777245
		0.	0.903304	0.903592	0.903452	0.903503	0.903481	0.903475
a_1		0.866025	0.130948	0.128578	0.122295	0.123775	0.123618	0.123687
		0.5	0.177755	0.175390	0.173908	0.174195	0.174165	0.174182
		0.	0.188145	0.187484	0.187048	0.187106	0.187098	0.187103
a_2		0.866025	0.017825	0.019095	0.011190	0.013121	0.012710	0.012707
		0.5	0.009661	0.008996	0.007991	0.008212	0.008146	0.008140
		0.	0.003711	0.004762	0.005024	0.005024	0.005042	0.005045

TABLE 2B
Wing: circle; Machnumber - 0
Convergence of the quantities a_r with respect to a (corresponding to number of spanwise integration points)
 $m=11 \quad R=3$

coeff.	η	a	4	6	8	10	coeff.	η	a	4	6	8	10
a_0		0.96593	0.22081	0.22077	0.22070	0.22067	a_2		0.96593	0.00555	0.01013	0.00864	0.00895
		0.86603	0.43741	0.43735	0.43731	0.43730			0.86603	0.01079	0.01089	0.01075	0.01077
		0.70711	0.62840	0.62838	0.62835	0.62835			0.70711	0.00942	0.00923	0.00925	0.00924
		0.5	0.77686	0.77685	0.77683	0.77683			0.5	0.00695	0.00692	0.00692	0.00692
		0.25882	0.87086	0.87087	0.87085	0.87085			0.25882	0.00512	0.00509	0.00510	0.00510
	0.	0.90302	0.90303	0.90301	0.90301		0.	0.00443	0.00443	0.00444	0.00444		
a_1		0.96593	0.07859	0.08186	0.08109	0.08139	a_3		0.96593	-0.01664	-0.01260	-0.01370	-0.01336
		0.86603	0.12727	0.12816	0.12798	0.12806			0.86603	-0.01743	-0.01759	-0.01756	-0.01758
		0.70711	0.15648	0.15669	0.15666	0.15668			0.70711	-0.01469	-0.01504	-0.01495	-0.01498
		0.5	0.17454	0.17467	0.17465	0.17466			0.5	-0.01117	-0.01125	-0.01123	-0.01124
		0.25882	0.18446	0.18452	0.18452	0.18452			0.25882	-0.00841	-0.00847	-0.00845	-0.00846
	0.	0.18765	0.18771	0.18770	0.18771		0.	-0.00745	-0.00746	-0.00746	-0.00746		

TABLE 3A

Wing: circle; Machnumber - 0
 Convergence of a_0 and a_1 with respect to R ($R+1$ =number of chordwise collocation points) at a selected accuracy of the spanwise integration
 $m=5$

coeff.	R			
	η	1	2	3
a_0	0.866025	0.438174	0.439046	0.438876
	0.5	0.776237	0.777245	0.777248
	0.	0.902756	0.903475	0.903488
a_1	0.866025	0.136106	0.123687	0.125616
	0.5	0.184655	0.174182	0.174529
	0.	0.195090	0.187103	0.187240

TABLE 3B

Wing: circle; Machnumber - 0
 Convergence of the quantities a_i with respect to m (number of spanwise collocation points) at a selected accuracy of the spanwise integration
 $R=3$

coeff.	m					coeff.	m				
	η	5	7	9	11		η	5	7	9	11
a_0	0.8660	0.4389			0.4373	a_2	0.8660	0.0107			0.0108
	0.7071		0.6285		0.6284		0.7071		0.0092		0.0092
	0.5	0.7772			0.7768		0.5	0.0069			0.0069
	0.	0.9035	0.9031	0.9031	0.9030		0.	0.0044	0.0044	0.0044	0.0044
a_1	0.8660	0.1256			0.1281	a_3	0.8660	-0.0143			-0.0176
	0.7071		0.1567		0.1567		0.7071		-0.0015		-0.0149
	0.5	0.1745			0.1747		0.5	-0.0111			-0.0112
	0.	0.1872	0.1877	0.1876	0.1877		0.	-0.0074	-0.0074	-0.0075	-0.0075

TABLE 4A

Wing: Warren 12; Machnumber - 0.
 Convergence of the quantities a_i with respect to a (number of spanwise integration points)
 $m=15$ $R=1$

coeff.	a					
	η	1	2	3	4	6
a_0	0.980785	0.138462	0.138383	0.138369	0.138366	0.138365
	0.923880	0.268391	0.268206	0.268176	0.268169	0.268167
	0.831470	0.377686	0.377365	0.377307	0.377294	0.377289
	0.707107	0.461157	0.460756	0.460680	0.460663	0.460656
	0.555570	0.523118	0.522600	0.522509	0.522489	0.522481
	0.382683	0.565057	0.564505	0.564416	0.564397	0.564389
	0.195090	0.585560	0.585017	0.584929	0.584911	0.584902
	0.	0.584859	0.584745	0.584740	0.584745	0.584751
a_1	0.980785	0.077877	0.077831	0.077832	0.077833	0.077833
	0.923880	0.097727	0.097410	0.097401	0.097398	0.097397
	0.831470	0.066016	0.064695	0.064660	0.064652	0.064647
	0.707107	0.029628	0.027177	0.027113	0.027099	0.027090
	0.555570	0.000155	-0.002702	-0.002770	-0.002783	-0.002792
	0.382683	-0.032498	-0.034638	-0.034733	-0.034756	-0.034772
	0.195090	-0.098055	-0.099471	-0.09961	-0.099649	-0.099679
	0.	-0.185548	-0.183778	-0.183491	-0.183388	-0.183313

TABLE 4B
Wing: Warren 12; Machnumber - 0
Convergence of the quantities a_i with respect to a (number of spanwise integration points)
 $m = 31$ $R = 3$

coeff.	a				coeff.	a			
	η	2	4	8		η	2	4	8
a_0	0.980785	0.139480	0.139478	0.139476	a_2	0.980785	0.050628	0.050623	0.050622
	0.923880	0.268329	0.268324	0.268319		0.923880	0.019119	0.019066	0.019055
	0.831470	0.376985	0.376979	0.376971		0.831470	-0.011617	-0.011612	-0.011634
	0.707107	0.461019	0.461014	0.461002		0.707107	-0.012474	-0.012476	-0.012511
	0.555570	0.522742	0.522738	0.522725		0.555570	-0.008999	-0.008973	-0.009013
	0.382683	0.564570	0.564566	0.564553		0.382683	-0.010205	-0.010152	-0.010187
	0.195090	0.584875	0.584875	0.584864		0.195090	-0.016755	-0.016788	-0.016818
	0.	0.586769	0.586813	0.586809		0.	-0.014644	-0.014558	-0.014541
a_1	0.980785	0.085443	0.085445	0.085444	a_3	0.980785	+0.024060	+0.024060	+0.024059
	0.923880	0.101676	0.101662	0.101657		0.923880	-0.006795	-0.006821	-0.006828
	0.831470	0.066549	0.066556	0.066546		0.831470	-0.006551	-0.006528	-0.006540
	0.707107	0.026665	0.026674	0.026661		0.707107	-0.000190	-0.000183	-0.000197
	0.555570	-0.002435	-0.002411	-0.002424		0.555570	+0.000717	+0.000748	+0.000737
	0.382683	-0.034222	-0.034166	-0.034176		0.382683	+0.000949	+0.001004	+0.000996
	0.195090	-0.100440	-0.100459	-0.100478		0.195090	+0.000357	+0.000354	+0.000347
	0.	-0.190276	-0.190275	-0.190262		0.	-0.007622	-0.007662	-0.007655

TABLE 5A

Wing: Warren 12; Machnumber - 0
Convergence of a_0 and a_1 with respect to R ($R+1$ = number of chordwise collocation points) at a selected accuracy of the spanwise integration
 $m = 15$

coeff.	R				coeff.	R			
	η	1	3	4		η	1	3	4
a_0	0.98079	0.13837	0.13952	0.13954	a_1	0.98079	0.07783	0.08562	0.08579
	0.92388	0.26817	0.26829	0.26827		0.92388	0.09740	0.10207	0.10244
	0.83147	0.37729	0.37706	0.37711		0.83147	0.06465	0.06611	0.06603
	0.70711	0.46066	0.46096	0.46097		0.70711	0.02709	0.02720	0.02732
	0.55557	0.52248	0.52285	0.52290		0.55557	-0.00279	-0.00308	-0.00314
	0.38268	0.56439	0.56452	0.56454		0.38268	-0.03477	-0.03305	-0.03297
	0.19509	0.58490	0.58512	0.58515		0.19509	-0.09968	-0.10040	-0.10040
	0.	0.58475	0.58652	0.58659		0.	-0.18331	-0.19306	-0.19325

TABLE 5B

Wing: Warren 12; Machnumber - 0
Convergence of the quantities a_i with respect to m (number of spanwise collocation points) at a selected accuracy of the spanwise integration
 $R = 3$

coeff.	m				coeff.	m			
	η	15	23	31		η	15	23	31
a_0	0.98079	0.13952		0.13948	a_2	0.98079	0.050948		0.050622
	0.92388	0.26829	0.26826	0.26832		0.92388	0.019612	0.019085	0.019055
	0.83147	0.37706		0.37697		0.83147	-0.012441		-0.011634
	0.70711	0.46096	0.46085	0.46100		0.70711	-0.011574	-0.012490	-0.012511
	0.55557	0.52285		0.52273		0.55557	-0.010028		-0.009013
	0.38268	0.56452	0.56427	0.56455		0.38268	-0.008848	-0.010248	-0.010187
	0.19509	0.58512		0.58486		0.19509	-0.018354		-0.016818
	0.	0.58652	0.58624	0.58681		0.	-0.012932	-0.014033	-0.014541
a_1	0.98079	0.08562		0.08544	a_3	0.98079	0.024432		0.024059
	0.92388	0.10207	0.10162	0.10166		0.92388	-0.006976	-0.006779	-0.006828
	0.83147	0.06611		0.06655		0.83147	-0.006477		-0.006540
	0.70711	0.02720	0.02668	0.02666		0.70711	-0.000175	-0.000233	-0.000197
	0.55557	-0.00308		-0.00242		0.55557	+0.000684		+0.000737
	0.38268	-0.03305	-0.03449	-0.03418		0.38268	+0.001198	+0.001124	+0.000996
	0.19509	-0.10040		-0.10048		0.19509	+0.000116		+0.000347
	0.	-0.19306	-0.19173	-0.19026		0.	-0.007603	-0.007376	-0.007655

TABLE 6A
Wing: Warren 12; Machnumber - 0.6
Convergence of the quantities a_i with respect to a .
 $m=15$ $R=1$

coeff.			1	4	6	8
	η	a				
a_0		0.980785	0.146866	0.146803	0.146802	0.146801
		0.923880	0.286347	0.286192	0.286190	0.286189
		0.831470	0.405808	0.405492	0.405488	0.405487
		0.707107	0.497080	0.496691	0.496685	0.496684
		0.555570	0.563152	0.562690	0.562683	0.562681
		0.382683	0.606349	0.605903	0.605895	0.605893
		0.195090	0.626288	0.625888	0.625879	0.625877
		0.	0.623969	0.624194	0.624200	0.624203
a_1		0.980785	0.089657	0.089666	0.089666	0.089666
		0.923880	0.117391	0.117303	0.117302	0.117301
		0.831470	0.080932	0.080595	0.080590	0.080589
		0.707107	0.032353	0.031699	0.031690	0.031689
		0.55557	-0.009379	-0.009885	-0.009892	-0.009894
		0.382683	-0.054843	-0.054590	-0.054604	-0.054609
		0.195090	-0.137523	-0.137139	-0.137167	-0.137177
		0.	-0.238777	-0.235630	-0.235540	-0.235509

TABLE 6B
Wing: Warren 12; Machnumber - 0.6
Convergence of the quantities a_i with respect to a .
 $m=31$ $R=3$

coeff.					coeff.					
	η	a	2	4		8	η	a	2	4
a_0		0.980785	0.148202	0.148196	0.148195		0.980785	0.061018	0.061012	0.061011
		0.923880	0.286406	0.286395	0.286390		0.923880	0.025789	0.025716	0.025708
		0.831470	0.404826	0.404807	0.404802		0.831470	-0.018478	-0.018394	-0.018411
		0.707107	0.497137	0.497108	0.497100		0.707107	-0.021574	-0.021277	-0.021301
		0.555570	0.563231	0.563202	0.563192		0.555570	-0.015548	-0.015277	-0.015305
		0.382683	0.606315	0.606291	0.606281		0.382683	-0.016056	-0.015993	-0.016021
		0.195090	0.626280	0.626267	0.626259		0.195090	-0.020276	-0.020488	-0.020513
		0.	0.627485	0.627521	0.627518		0.	-0.009792	-0.009844	-0.009830
a_1		0.980785	0.098699	0.098702	0.098701		0.980785	0.029813	0.029806	0.029805
		0.923880	0.123376	0.123363	0.123359		0.923880	-0.009500	-0.009541	-0.009547
		0.831470	0.084705	0.084785	0.084777		0.831470	-0.010669	-0.010547	-0.010557
		0.707107	0.031928	0.032220	0.032212		0.707107	0.000359	0.000609	0.000601
		0.555570	-0.009585	-0.009204	-0.009210		0.555570	0.001878	0.002110	0.002103
		0.382683	-0.054116	-0.053827	-0.053834		0.382683	0.002218	0.002328	0.002322
		0.195090	-0.139378	-0.139335	-0.139353		0.195090	0.001811	0.001778	0.001773
		0.	-0.246157	-0.246109	-0.246087		0.	-0.009134	-0.009117	-0.009103

TABLE 7A
Wing: Warren 12; Machnumber - 0.6
Convergence of a_0 and a_1 with respect to R at a selected accuracy of the spanwise integration
 $m=15$

coeff.						
	η	R	1	2	3	4
a_0		0.980785	0.146801	0.148499	0.148253	0.148270
		0.923880	0.286189	0.286971	0.286341	0.286320
		0.831470	0.405487	0.404948	0.404948	0.405018
		0.707107	0.496684	0.497003	0.497040	0.497055
		0.555570	0.562681	0.563234	0.563353	0.563443
		0.382683	0.605893	0.606187	0.606231	0.606363
		0.195090	0.625877	0.626471	0.626570	0.626643
		0.	0.624203	0.626678	0.627207	0.627390

(continued on next page)

TABLE 7A (continued)

coeff.	η	R	1	2	3	4
a_1		0.980785	0.089666	0.094643	0.098948	0.099439
		0.923880	0.117301	0.124385	0.123811	0.124532
		0.831470	0.080589	0.083881	0.084204	0.084035
		0.707107	0.031689	0.032743	0.032898	0.033138
		0.555570	-0.009894	-0.009832	-0.010030	-0.010136
		0.382683	-0.054609	-0.052424	-0.052438	-0.052294
		0.195090	-0.137177	-0.139349	-0.139377	-0.139476
		0.	-0.235509	-0.247673	-0.249368	-0.249799

TABLE 7B

Wing: Warren 12; Machnumber -0.6

Convergence of the quantities a_n with respect to m (number of spanwise collocation points) at a selected accuracy of the spanwise integration
 $R=3$ $a=8$

coeff.	η	m	15	23	31	coeff.	η	m	15	23	31
a_0		0.980785	0.148253		0.148195		0.980785		0.061675		0.061011
		0.923880	0.286341	0.286322	0.286390		0.923880		0.026013	0.025753	0.025708
		0.831470	0.404919		0.404802		0.831470		-0.019158		-0.018411
		0.707107	0.497040	0.496920	0.497100		0.707107		-0.020310	-0.021288	-0.021301
		0.555570	0.563353		0.563192		0.555570		-0.016375		-0.015305
		0.382683	0.606231	0.605958	0.606281		0.382683		-0.014582	-0.016100	-0.016021
		0.195090	0.626570		0.626259		0.195090		-0.022309		-0.020513
		0.	0.627207	0.626877	0.627518		0.		-0.007677	-0.009107	-0.009830
a_1		0.980785	0.098948		0.098701		0.980785		0.030306		0.029805
		0.923880	0.123811	0.123309	0.123359		0.923880		-0.009873	-0.009491	-0.009547
		0.831470	0.084204		0.084777		0.831470		-0.010343		-0.010557
		0.707107	0.032898	0.032223	0.032212		0.707107		0.000521	0.000553	0.000601
		0.555570	-0.010030		-0.009210		0.555570		0.002139		0.002103
		0.382683	-0.052438	-0.054258	-0.053834		0.382683		0.002438	0.002485	0.002322
		0.195090	-0.139377		-0.139353		0.195090		0.001668		0.001773
		0.	-0.249368	-0.247890	-0.246087		0.		-0.009317	-0.008779	-0.009103

TABLE 8A

Wing: Multhopp; Machnumber -0
Convergence of the quantities a_n with respect to a
 $m=15$ $R=1$

coeff.	η	a	1	2	3	4	6
a_0		0.980785	0.123783	0.123799	0.123810	0.123812	0.123814
		0.923880	0.237135	0.237167	0.237185	0.237188	0.237193
		0.831470	0.328093	0.328124	0.328142	0.328143	0.328149
		0.707107	0.393449	0.393593	0.393639	0.393642	0.393652
		0.555570	0.440277	0.440424	0.440505	0.440516	0.440533
		0.382683	0.470153	0.470515	0.470665	0.470702	0.470738
		0.195090	0.481011	0.481797	0.482078	0.482168	0.482242
		0.	0.468048	0.470315	0.470945	0.471157	0.471310
a_1		0.980785	0.063295	0.063349	0.063368	0.063372	0.063376
		0.923880	0.076618	0.076459	0.076480	0.076485	0.076488
		0.831470	0.050332	0.048946	0.048944	0.048948	0.048949
		0.707107	0.025522	0.022727	0.022671	0.022666	0.022663
		0.555570	0.007741	0.003681	0.003617	0.003615	0.003617
		0.382683	-0.007540	-0.011387	-0.011428	-0.011420	-0.011411
		0.195090	-0.055216	-0.057101	-0.056773	-0.056632	-0.056527
		0.	-0.168714	-0.163311	-0.162117	-0.161657	-0.161313

TABLE 8B
Wing: Multhopp; Machnumber - 0
Convergence of the quantities a_r with respect to a
 $m=31$ $R=3$

coeff.	η	a	6	8	10
a_0	0.980785		0.124860	0.124860	0.124860
	0.923880		0.237803	0.237802	0.237801
	0.831470		0.328771	0.328768	0.328768
	0.707107		0.395133	0.395130	0.395129
	0.555570		0.442237	0.442233	0.442233
	0.382683		0.473361	0.473358	0.473357
	0.195090		0.486069	0.486068	0.486068
	0.		0.480531	0.480537	0.480539
a_1	0.980785		0.069646	0.069646	0.069646
	0.923880		0.079967	0.079966	0.079966
	0.831470		0.050292	0.050291	0.050290
	0.707107		0.021827	0.021826	0.021825
	0.555570		0.004513	0.004512	0.004511
	0.382683		-0.011638	-0.011639	-0.011640
	0.195090		-0.049158	-0.049154	-0.049152
	0.		-0.156372	-0.156348	-0.156335
a_2	0.980785		0.039303	0.039303	0.039302
	0.923880		0.015004	0.015002	0.015002
	0.831470		-0.005227	-0.005232	-0.005234
	0.707107		-0.005299	-0.005308	-0.005311
	0.555570		-0.003227	-0.003239	-0.003243
	0.382683		-0.003574	-0.003586	-0.003590
	0.195090		-0.008804	-0.008813	-0.008815
	0.		-0.017566	-0.017557	-0.017553
a_3	0.980785		0.018399	0.018399	0.018399
	0.923880		-0.003211	-0.003212	-0.003213
	0.831470		-0.003358	-0.003360	-0.003361
	0.707107		-0.000343	-0.000346	-0.000347
	0.555570		0.000122	0.000119	0.000118
	0.382683		0.000307	0.000305	0.000304
	0.195090		0.001143	0.001142	0.001142
	0.		-0.011437	-0.011433	-0.011431

TABLE 9A
(continued)

coeff.	η	R	1	2	3	4
a_1	0.980785		0.063377	0.067042	0.069387	0.069495
	0.923880		0.076489	0.080550	0.080405	0.080577
	0.831470		0.048950	0.049304	0.049377	0.049340
	0.707107		0.022662	0.022626	0.022649	0.022740
	0.555570		0.003617	0.002950	0.002930	0.002946
	0.382683		-0.011408	-0.010109	-0.010097	-0.010012
	0.195090		-0.056490	-0.056251	-0.056156	-0.056139
	0.		-0.161189	-0.170862	-0.171789	-0.171816

TABLE 9B
Wing: Multhopp; Machnumber - 0
Convergence of the quantities a_r with respect to m at a selected accuracy of the spanwise integrations
 $R=3$

coeff.	η	m	15	23	31
a_0	0.980785		0.124669		0.124859
	0.923880		0.237242	0.237783	0.237801
	0.831470		0.328140		0.328768
	0.707107		0.393921	0.394992	0.395129
	0.555570		0.440841		0.442233
	0.382683		0.470925	0.473186	0.473357
	0.195090		0.482437		0.486068
	0.		0.473113	0.479581	0.480539
a_1	0.980785		0.069387		0.069646
	0.923880		0.080404	0.079806	0.079966
	0.831470		0.049373		0.050290
	0.707107		0.022639	0.021985	0.021825
	0.555570		0.002918		0.004511
	0.382683		-0.010108	-0.012360	-0.011640
	0.195090		-0.056145		-0.049152
	0.		-0.171745	-0.160089	-0.156335
a_2	0.980785		0.038951		0.039302
	0.923880		0.015941	0.014730	0.015002
	0.831470		-0.006559		-0.005234
	0.707107		-0.003926	-0.004999	-0.005311
	0.555570		-0.005155		-0.003243
	0.382683		-0.001339	-0.004467	-0.003590
	0.195090		-0.013092		-0.008815
	0.		-0.008405	-0.016135	-0.017553
a_3	0.980785		0.018615		0.018399
	0.923880		-0.003265	-0.003222	-0.003213
	0.831470		-0.003352		-0.003361
	0.707107		-0.000319	-0.000288	-0.000347
	0.555570		-0.000018		0.000118
	0.382683		0.000638	0.000044	0.000304
	0.195090		0.000572		0.001142
	0.		-0.009122	-0.011198	-0.011431

TABLE 9A
Wing: Multhopp; Machnumber - 0.0
Convergence of a_0 and a_1 with respect to R at a selected accuracy of the spanwise integration
 $m=15$ $a=8$

coeff.	η	R	1	2	3	4
a_0	0.980785		0.123816	0.124812	0.124670	0.124681
	0.923880		0.237196	0.237094	0.237243	0.237227
	0.831470		0.328153	0.328138	0.328144	0.328155
	0.707107		0.393657	0.393883	0.393925	0.393908
	0.555570		0.440542	0.440802	0.440844	0.440839
	0.382683		0.470753	0.470900	0.470925	0.470907
	0.195090		0.482270	0.482390	0.482429	0.482422
	0.		0.471364	0.472893	0.473085	0.473094

(continued)

TABLE 10A

Wing: Warren 12; Machnumber - 0

The calculated quantities a_i corresponding to the indicated distribution of pivotal points with $R=3$

$\eta_v = 0; 0.14; 0.28; 0.42; 0.56; 0.70; 0.84; 0.98.$

coeff. η \ a	2	4	6	8
0.980785	0.086539	0.084322	0.085608	0.085209
0.923880	0.113566	0.109576	0.113764	0.112357
0.831470	0.290223	0.282916	0.281717	0.282841
0.707107	0.431075	0.422188	0.420811	0.421772
0.555570	0.507037	0.501783	0.501037	0.501573
0.382683	0.555283	0.552054	0.551521	0.551813
0.195090	0.577776	0.575538	0.575111	0.575341
0.	0.579888	0.578162	0.577931	0.578120
0.980785	-0.007309	-0.039439	-0.048253	-0.043019
0.923880	-0.026031	-0.220318	-0.262538	-0.238093
0.831470	0.173258	0.123081	0.116323	0.119662
0.707107	0.067208	0.075048	0.076792	0.075844
0.555570	0.019402	0.016698	0.017255	0.016616
0.382683	-0.028755	-0.027055	-0.025567	-0.026122
0.195090	-0.098296	-0.095609	-0.094171	-0.094588
0.	-0.187770	-0.184849	-0.183937	-0.184262
0.980785	0.119859	0.071265	0.067979	0.070394
0.923880	0.663476	0.444302	0.435112	0.441189
0.831470	0.030688	0.065350	0.071503	0.067619
0.707107	-0.054988	-0.035825	-0.033880	-0.034619
0.555570	-0.002657	-0.012212	-0.012291	-0.012463
0.382683	-0.012979	-0.012690	-0.012186	-0.012291
0.195090	-0.022523	-0.020940	-0.020921	-0.020837
0.	-0.017125	-0.015871	-0.016007	-0.015918
0.980785	0.071437	0.041586	0.038191	0.040144
0.923880	-0.040583	-0.079713	-0.097797	-0.089503
0.831470	-0.090929	-0.047675	-0.043842	-0.046395
0.707107	0.004820	-0.005074	-0.005734	-0.005013
0.555570	0.006454	0.001291	0.001273	0.000954
0.382683	0.000075	0.000421	0.000999	0.001011
0.195090	-0.001777	-0.000386	0.000235	0.000076
0.	-0.006935	-0.007001	-0.006940	-0.007025

TABLE 10B

Wing: Warren 12; Machnumber - 0

The calculated quantities a_i corresponding to the indicated distribution of pivotal points with $R=3$

$\eta_v = 0.0; 0.07; 0.17; 0.39; 0.61; 0.83; 0.93; 0.98.$

coeff. η \ a	2	4	6	8
0.980785	0.130925	0.132117	0.132272	0.132287
0.923880	0.248250	0.249982	0.250201	0.250323
0.831470	0.324508	0.332491	0.333583	0.333382
0.707107	0.338555	0.356970	0.359669	0.359149
0.555570	0.484269	0.483301	0.483130	0.484228
0.382683	0.547365	0.550145	0.550359	0.550650
0.195090	0.569586	0.571600	0.571830	0.571954
0.	0.574081	0.575432	0.575602	0.575722
0.980785	0.084201	0.083481	0.083656	0.083357
0.923880	0.120701	0.118333	0.118464	0.117615
0.831470	-0.019835	-0.022800	-0.022718	-0.020904
0.707107	-0.288949	-0.261132	-0.262718	-0.252367
0.555570	0.137573	0.141573	0.141452	0.137651
0.382683	0.008611	-0.002589	-0.003134	-0.004416
0.195090	-0.103455	-0.103846	-0.103884	-0.104015
0.	-0.182052	-0.182260	-0.182256	-0.182525
0.980785	0.035030	0.034855	0.035084	0.035193
0.923880	0.012494	0.000844	0.000157	0.000024
0.831470	-0.047657	-0.037570	-0.036631	-0.035673
0.707107	0.112154	0.188665	0.190808	0.190915
0.555570	0.036909	0.000808	-0.000821	-0.003354
0.382683	-0.038938	-0.045932	-0.045618	-0.045245
0.195090	-0.023449	-0.017597	-0.017333	-0.017147
0.	-0.014786	-0.013500	-0.013400	-0.013357
0.970785	0.021952	0.024998	0.025280	0.025263
0.923880	-0.002153	-0.004253	-0.003900	-0.004453
0.831470	-0.001524	0.007355	0.007698	0.008256
0.707107	-0.020674	-0.040024	-0.045593	-0.042230
0.555570	0.005759	0.001595	0.003385	0.000679
0.382683	-0.009043	-0.005899	-0.005756	-0.005214
0.195090	0.003062	0.003940	0.003756	0.003498
0.	-0.004211	-0.005022	-0.005052	-0.005252

TABLE 10C

Wing: Warren 12; Machnumber - 0

The calculated quantities a_i corresponding to the indicated distribution of pivotal points with $R=3$

$\eta_v = 0; 0.076; 0.17; 0.30; 0.45; 0.62; 0.79; 0.96.$

coeff. η \ a	2	4	6	8
0.980785	0.599408	0.698325	0.679017	0.676590
0.923880	-1.179589	-1.221134	-1.179459	-1.182906
0.831470	-1.374013	-1.326563	-1.303413	-1.305802
0.707107	-0.533708	-0.365390	-0.364885	-0.367610
0.555570	-0.017553	0.096466	0.098392	0.096104
0.382683	0.266528	0.322793	0.323527	0.322299
0.195090	0.376935	0.414240	0.414927	0.414124
0.	0.404267	0.437349	0.437988	0.437300
0.980785	6.637549	4.077165	4.180148	4.245443
0.923880	-9.667894	-7.096393	-7.194322	-7.229340
0.831470	-4.646490	-2.762343	-2.829259	-2.864295
0.707107	1.430219	1.255849	1.254755	1.255551
0.555570	0.423418	0.323673	0.325619	0.325639
0.382683	0.239740	0.185119	0.184624	0.185972
0.195090	0.079067	0.045557	0.045016	0.045538
0.	-0.006378	-0.039397	-0.039868	-0.039240

(continued on next page)

TABLE 10C
(continued)

coeff. η	coeff. η									
	a	2	4	6	8	a	2	4	6	8
0.980785	3.95389	-5.240939	-5.199113	-5.083174	0.980785	-0.999392	-0.000131	0.103270	0.085771	0.367834
0.923880	-1.065143	2.338632	2.311049	2.165738	0.923880	0.008026	0.526162	0.408788	0.302440	0.285883
0.831470	2.548267	3.210462	3.201494	3.145434	0.831470	0.734947	-0.044099	0.008455	0.030240	-0.285883
0.707107	0.887807	0.175017	0.184538	0.207803	0.707107	-0.178785	-0.311073	-0.295269	-0.059587	-0.059587
0.555570	-0.242805	-0.140089	-0.137651	-0.139809	0.555570	-0.145260	-0.051595	-0.055879	-0.059587	0.012128
0.382683	-0.063651	-0.062272	-0.062272	-0.062272	0.382683	0.028499	0.011460	0.011524	0.012128	0.000906
0.195090	-0.059806	-0.051371	-0.051231	-0.051711	0.195090	-0.001290	0.001070	0.001104	0.000906	-0.002103
0	-0.063385	-0.054147	-0.053846	-0.054031	0	-0.001755	-0.002205	-0.002175	-0.002175	-0.002103

TABLE 11A
Wing: Warren 12; Mach number - 0
The solution for several different distributions of pivotal stations with $a=6$ and $R=3$

coeff. η	coeff. η				
	a	case 1	case 2	case 3	case 4
0.984808	0.124255	0.123640	0.119313	-0.117376	0.984808
0.939693	0.241175	0.244626	0.242108	-0.119946	0.939693
0.866025	0.343313	0.344634	0.336382	-0.194944	0.866025
0.766044	0.426650	0.430888	0.435883	0.147211	0.766044
0.642787	0.490799	0.492169	0.501681	0.378824	0.642787
0.500000	0.538816	0.539749	0.556640	0.463251	0.500000
0.342020	0.570757	0.571136	0.579631	0.523586	0.342020
0.173648	0.585502	0.585645	0.589538	0.548239	0.173648
0.0	0.586317	0.586519	0.589992	0.552863	0.0

TABLE 11B
The spanwise pivotal stations of the cases presented in table 11A.

case number	normal Muthopp distribution			
	1.	2.	3.	4.
	0.0, 0.14, 0.28, 0.42, 0.56, 0.70, 0.84, 0.92, 0.98	0.0, 0.07, 0.17, 0.39, 0.61, 0.70, 0.83, 0.93, 0.98	0.0, 0.076, 0.17, 0.30, 0.45, 0.62, 0.79, 0.96, 0.9856	0.0, 0.076, 0.17, 0.30, 0.45, 0.62, 0.79, 0.96, 0.9856

coeff. η	coeff. η			
	1	2	3	4
0.0000	0.3331	0.3236	0.3166	0.3125
0.1423	0.3318	0.3226	0.3156	0.3116
0.2817	0.3280	0.3193	0.3126	0.3087
0.4154	0.3209	0.3131	0.3069	0.3032
0.5406	0.3096	0.3030	0.2975	0.2941
0.6549	0.2926	0.2874	0.2827	0.2797
0.7557	0.2682	0.2644	0.2606	0.2581
0.8413	0.2343	0.2317	0.2289	0.2269
0.9096	0.1894	0.1878	0.1859	0.1845
0.9595	0.1336	0.1329	0.1317	0.1308
0.9898	0.0692	0.0690	0.0684	0.0680

coeff. η	coeff. η			
	1	2	3	4
0.0000	0.0089	0.0002	-0.0113	-0.0192
0.1423	0.0090	0.0007	-0.0108	-0.0186
0.2817	0.0095	0.0021	-0.0090	-0.0167
0.4154	0.0104	0.0045	-0.0059	-0.0135
0.5406	0.0118	0.0078	-0.0015	-0.0088
0.6549	0.0140	0.0122	0.0045	-0.0023
0.7557	0.0174	0.0176	0.0120	0.0062
0.8413	0.0219	0.0236	0.0204	0.0159
0.9096	0.0259	0.0284	0.0274	0.0245
0.9595	0.0255	0.0281	0.0283	0.0268
0.9898	0.0166	0.0183	0.0187	0.0181

coeff. η	coeff. η				
	a	case 1	case 2	case 3	case 4
0.984808	0.049501	0.060013	0.072082	0.004242	0.984808
0.939693	0.029362	0.016042	0.017003	0.365948	0.939693
0.866025	0.005437	0.002127	0.032766	0.981911	0.866025
0.766044	-0.014021	-0.028608	-0.031643	0.192325	0.766044
0.642788	-0.010097	-0.006660	-0.012735	-0.140362	0.642788
0.500000	-0.009216	-0.010800	-0.010800	-0.019554	0.500000
0.342020	-0.010739	-0.009697	-0.018718	-0.021078	0.342020
0.173648	-0.018923	-0.019422	-0.012041	-0.025022	0.173648
0.0	-0.013396	-0.013679	-0.008594	-0.022701	0.0

coeff. η	coeff. η				
	a	case 1	case 2	case 3	case 4
0.984808	0.25372	0.222190	0.017662	0.013450	0.984808
0.939693	-0.01257	0.002720	0.004917	-0.039842	0.939693
0.866025	-0.09453	-0.011853	-0.021755	-0.227001	0.866025
0.766044	-0.01974	+0.001037	+0.004289	-0.055384	0.766044
0.642788	+0.00542	+0.000308	-0.003267	-0.021359	0.642788
0.500000	+0.00809	+0.001179	+0.012319	-0.001155	0.500000
0.342020	+0.01152	+0.000694	-0.002404	0.0005965	0.342020
0.173648	-0.00709	-0.000905	+0.001915	-0.000809	0.173648
0.0	-0.07522	-0.007350	-0.006471	-0.006195	0.0

TABLE 12B

Results obtained with the present method for the rectangular wing with $s = 1$ $l(\eta) = \frac{1}{4}$ at $M_\infty = 0$ and for $m = 21$ $a = 1$, the variation with respect to R

η \ R	1	2	3	4	coeff.
.0000	.3298	.3303	.3334	.3393	
.1423	.3286	.3290	.3319	.3377	
.2817	.3247	.3249	.3276	.3329	
.4154	.3176	.3177	.3199	.3244	
.5406	.3064	.3063	.3080	.3117	
.6549	.2897	.2895	.2907	.2935	a_0
.7557	.2657	.2654	.2662	.2682	
.8413	.2324	.2321	.2325	.2339	
.9096	.1881	.1879	.1882	.1891	
.9595	.1328	.1329	.1330	.1335	
.9898	.0688	.0690	.0690	.0693	
.0000	.0009	-.0038	-.0058	-.0080	
.1423	.0012	-.0035	-.0055	-.0076	
.2817	.0019	-.0026	-.0046	-.0063	
.4154	.0033	-.0009	-.0029	-.0043	
.5406	.0055	.0018	-.0002	-.0013	
.6549	.0087	.0058	.0039	.0029	a_1
.7557	.0134	.0114	.0096	.0087	
.8413	.0193	.0183	.0168	.0159	
.9096	.0244	.0247	.0237	.0230	
.9595	.0246	.0258	.0257	.0253	
.9898	.0160	.0171	.0177	.0177	

TABLE 12C

Results obtained with the present method for the rectangular wing with $s = 1$ $l(\eta) = \frac{1}{4}$ at $M_\infty = 0$ and for $m = 21$ $a = 8$, the variation with respect to R

η \ R	1	2	3	4	coeff.
.0000	.3330	.3329	.3329	.3328	
.1423	.3317	.3316	.3316	.3315	
.2817	.3276	.3275	.3275	.3274	
.4154	.3202	.3201	.3201	.3200	
.5406	.3086	.3086	.3085	.3085	
.6549	.2915	.2915	.2914	.2914	a_0
.7557	.2670	.2670	.2670	.2670	
.8413	.2333	.2333	.2333	.2333	
.9096	.1887	.1888	.1888	.1887	
.9595	.1332	.1334	.1334	.1334	
.9898	.0690	.0692	.0692	.0692	
.0000	.0028	.0028	.0028	.0028	
.1423	.0030	.0030	.0030	.0030	
.2817	.0035	.0035	.0035	.0035	
.4154	.0046	.0046	.0046	.0046	
.5406	.0064	.0064	.0064	.0064	
.6549	.0093	.0093	.0093	.0093	a_1
.7557	.0137	.0137	.0137	.0137	
.8413	.0194	.0196	.0196	.0196	
.9096	.0244	.0252	.0252	.0252	
.9595	.0246	.0260	.0264	.0264	
.9898	.0160	.0172	.0179	.0180	

TABLE 12D

Comparison of the results presented in tables 12a, 12b, 12c; differences between the results obtained for succeeding values of R

Method of ref. 2					Present method					coeff.
					A=1		A=8			
η	Δ_1	Δ_2	Δ_3	Δ_4	Δ_2	Δ_3	Δ_1	Δ_2	Δ_3	
.0000	.0095	.0070	.0041	-.0005	-.0001	-.0059	.0001	.0000	.0001	a_0
.1423	.0092	.0070	.0040	-.0004	-.0029	-.0058	.0001	.0000	.0001	
.2817	.0087	.0067	.0039	-.0002	-.0027	-.0053	.0001	.0000	.0001	
.4154	.0078	.0062	.0037	-.0001	-.0022	-.0045	.0001	.0000	.0001	
.5406	.0066	.0055	.0034	.0001	-.0017	-.0037	.0000	.0001	.0000	
.6549	.0052	.0047	.0030	.0002	-.0012	-.0028	.0000	.0001	.0000	
.7557	.0038	.0038	.0025	.0003	-.0008	-.0020	.0000	.0000	.0000	
.8413	.0026	.0028	.0020	.0003	-.0004	-.0014	.0000	.0000	.0000	
.9096	.0016	.0019	.0014	.0002	-.0003	-.0009	-.0001	.0000	.0001	
.9595	.0007	.0012	.0009	-.0001	-.0001	-.0005	-.0002	.0000	.0000	
.9898	.0002	.0006	.0004	-.0002	.0000	-.0003	-.0002	.0000	.0000	
.0000	.0087	.0115	.0079	.0047	.0020	.0022	.0000	.0000	.0000	a_1
.1423	.0083	.0115	.0078	.0047	.0020	.0021	.0000	.0000	.0000	
.2817	.0074	.0111	.0077	.0045	.0020	.0017	.0000	.0000	.0000	
.4154	.0059	.0104	.0076	.0042	.0020	.0014	.0000	.0000	.0000	
.5406	.0040	.0093	.0073	.0037	.0020	.0011	.0000	.0000	.0000	
.6549	.0018	.0077	.0068	.0029	.0019	.0010	.0000	.0000	.0000	
.7557	-.0002	.0056	.0058	.0020	.0018	.0009	.0000	.0000	.0000	
.8413	-.0017	.0032	.0045	.0010	.0015	.0009	-.0002	.0000	.0000	
.9096	-.0025	.0010	.0029	-.0003	.0010	.0007	-.0008	.0000	.0000	
.9595	-.0026	-.0002	.0015	-.0012	.0001	.0004	-.0016	-.0004	.0000	
.9898	-.0017	-.0004	.0006	-.0011	-.0006	.0000	-.0012	-.0007	-.0001	

$\Delta_i = (\text{result})_{R=i} - (\text{result})_{R=i+1}$

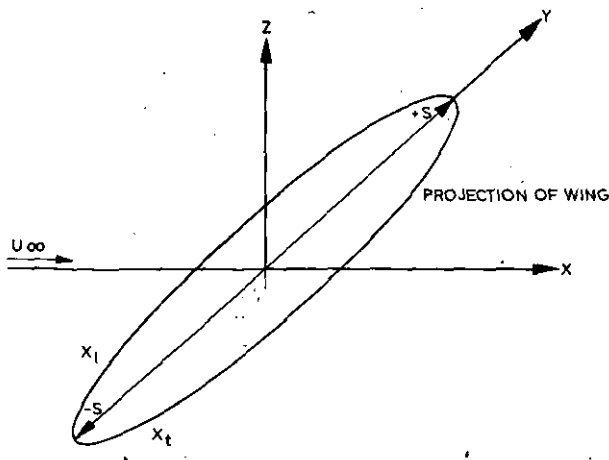
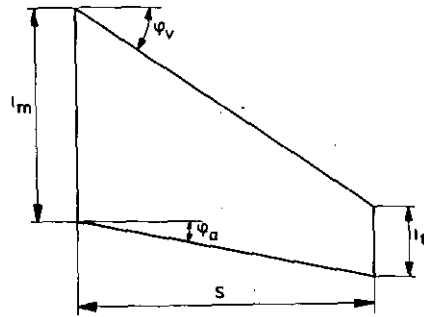


Fig. 1. Geometry of wing planform and co-ordinate system.



- (a) WARREN 12 WING
 $\phi_v = 53.5^\circ$
 $\phi_a = 32.9^\circ$
 $l_m = 1.0607s$
 $l_t = 0.35356s$
- (b) MULTHOPP WING
 $\phi_v = 45^\circ$
 $\phi_a = 26.89^\circ$
 $l_m = 7 \text{ ft}$
 $l_t = 3 \text{ ft}$

Fig. 2. Geometry of the Warren 12 and the Multhopp wing.

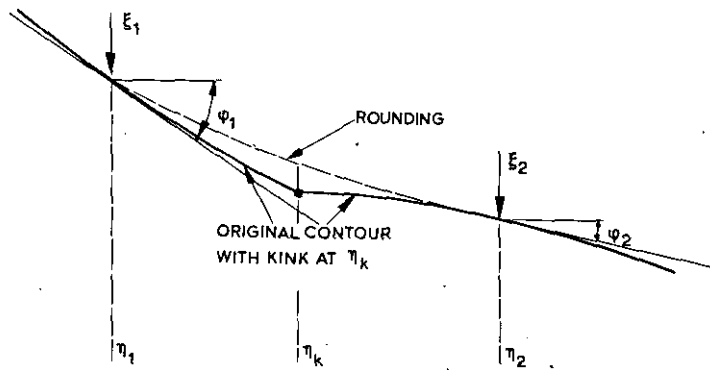


Fig. 3. The rounding at a kink in the wing planform. Given are:

$$\text{at } \eta_1: \xi_1, \text{tg } \phi_1, \left(\frac{d^2\xi}{dy^2}\right)_1$$

$$\text{at } \eta_2: \xi_2, \text{tg } \phi_2, \left(\frac{d^2\xi}{dy^2}\right)_2$$

$$\text{at } \eta_k: \text{continuity of } \xi, \frac{d\xi}{d\eta} \text{ and } \frac{d^2\xi}{d\eta^2}$$

$$\text{If } K_1 = (\eta_k - \eta_1)^2 \left(\frac{d^2\xi}{d\eta^2}\right)_1, \quad H_1 = (\eta_k - \eta_1) \text{tg } \phi_1, \quad K_2 = (\eta_k - \eta_2)^2 \left(\frac{d^2\xi}{d\eta^2}\right)_2, \quad H_2 = (\eta_k - \eta_2) \text{tg } \phi_2$$

there holds

$$\text{If } \eta \in [(\eta_1, \eta_k)]: \quad \xi = A \left(\frac{\eta - \eta_1}{\eta_k - \eta_1}\right)^4 + B_1 \left(\frac{\eta - \eta_1}{\eta_k - \eta_1}\right)^3 + \frac{1}{2} K_1 \left(\frac{\eta - \eta_1}{\eta_k - \eta_1}\right)^2 + H_1 \frac{\eta - \eta_1}{\eta_k - \eta_1} + \xi_1.$$

$$\text{If } \eta \in (\eta_k, \eta_2): \quad \xi = B_2 \left(\frac{\eta - \eta_2}{\eta_k - \eta_2}\right)^3 + \frac{1}{2} K_2 \left(\frac{\eta - \eta_2}{\eta_k - \eta_2}\right)^2 + H_2 \frac{\eta - \eta_2}{\eta_k - \eta_2} + \xi_2$$

where

$$A = \frac{\eta_2 - \eta_1}{\eta_k - \eta_2} \{3B_2 + K_2 + H_2\} - \frac{1}{2}(K_2 - K_1) - 2(H_2 - H_1) - 3(\xi_2 - \xi_1)$$

$$B_1 = B_2 - A + \frac{1}{2}(K_2 - K_1) + H_2 - H_1 + \xi_2 - \xi_1$$

$$B_2 = \frac{1}{6(2\eta_2 - \eta_k - \eta_1)} \left\{ 6(\eta_k - \eta_2)H_2 - (5\eta_2 - \eta_1 - 4\eta_k)K_2 - \frac{(\eta_k - \eta_2)^2}{\eta_2 - \eta_1} [(K_2 - K_1) + 6(H_2 - H_1) + 12(\xi_2 - \xi_1)] \right\}$$

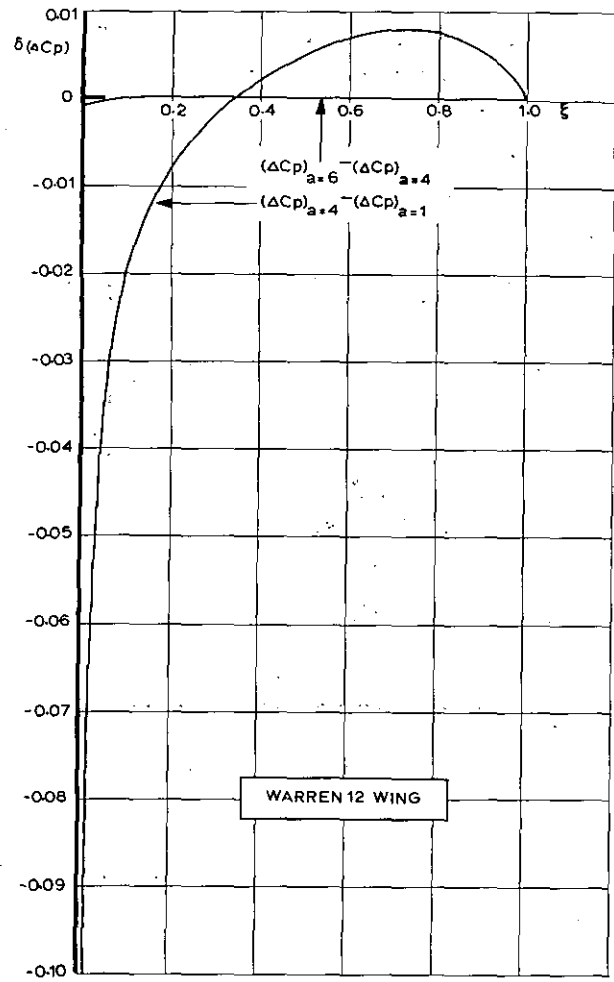


Fig. 4a. Convergence of ΔC_p as a function of the number of integration points $\eta=0.38268$ ($m=15$ $R=2$ $M_\infty=0$).

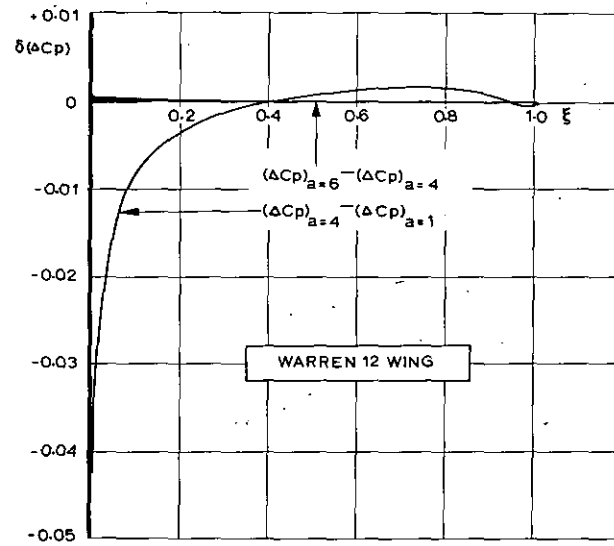


Fig. 4b. Convergence of ΔC_p as a function of the number of integration points. $\eta=0.92388$ ($m=15$ $R=2$ $M_\infty=0$).

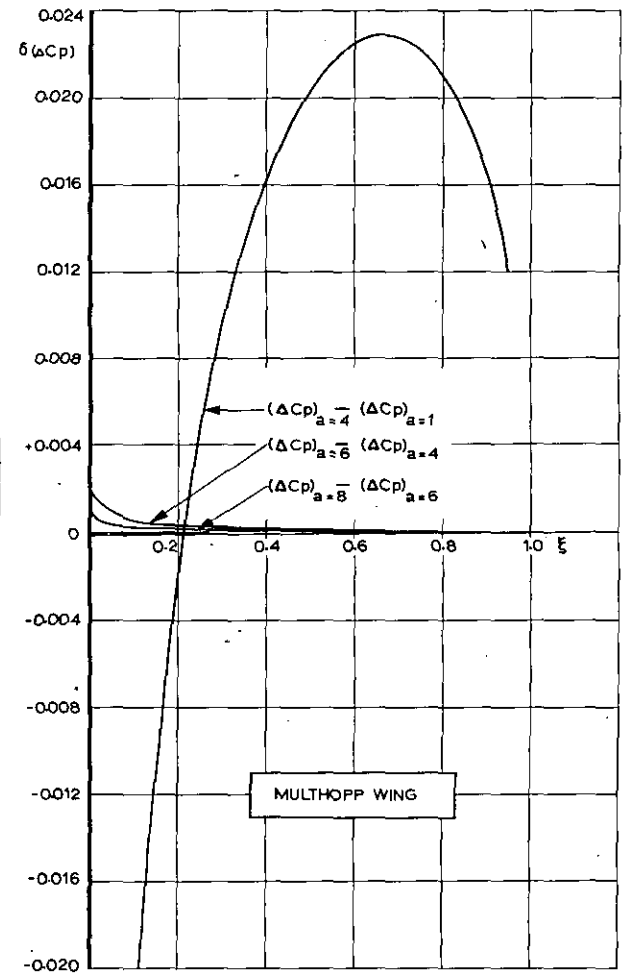


Fig. 5a. Convergence of ΔC_p with respect to the number of integration points for $\eta=0.38268$ ($m=15$ $R=2$ $M_\infty=0$).

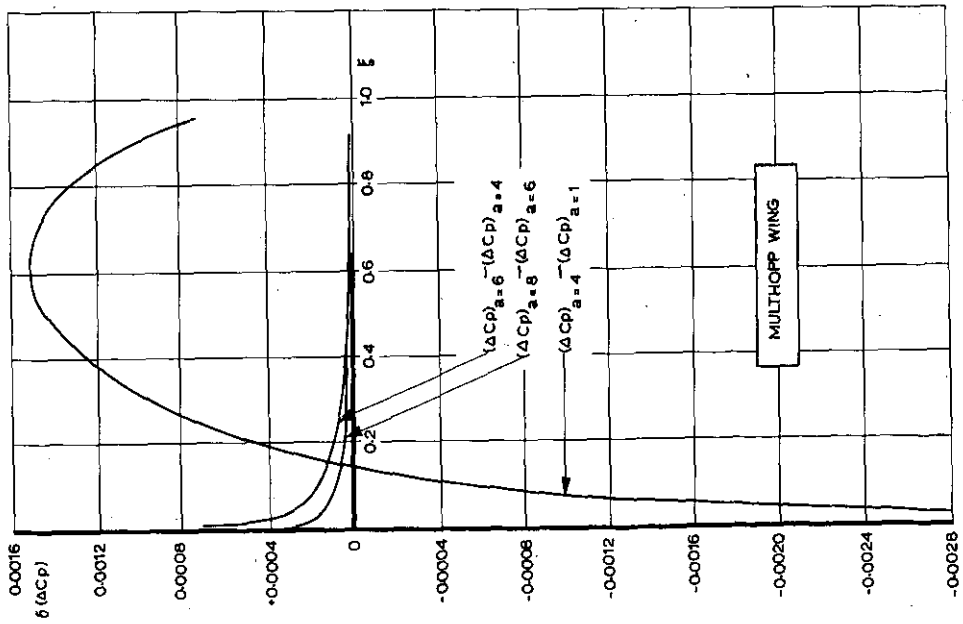


Fig. 5b. Convergence of ΔC_p with respect to the number of integration points for $\eta = 0.92388$ ($m = 15$ $R = 2$ $M_\infty = 0$).

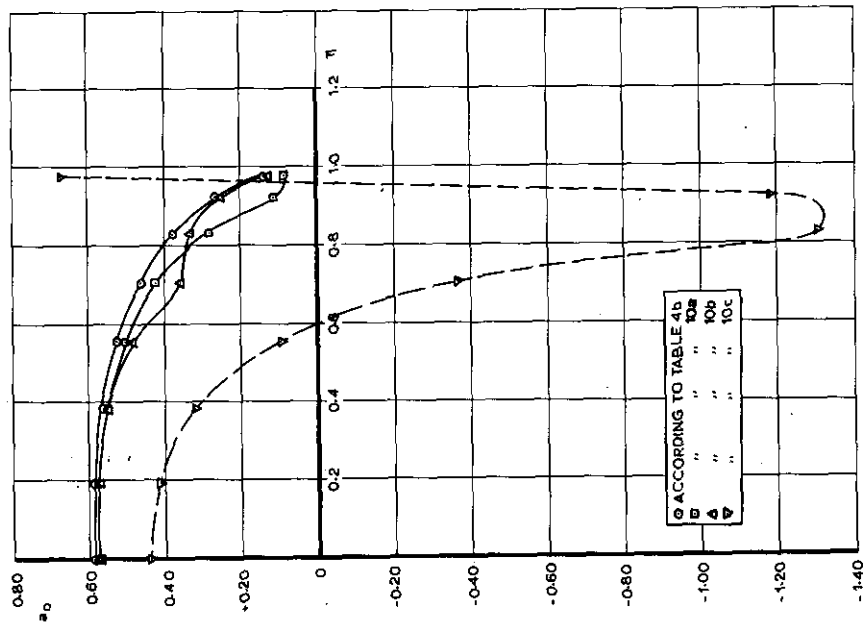


Fig. 6a. The quantity a_0 as a function of η for some different distributions of the spanwise stations.

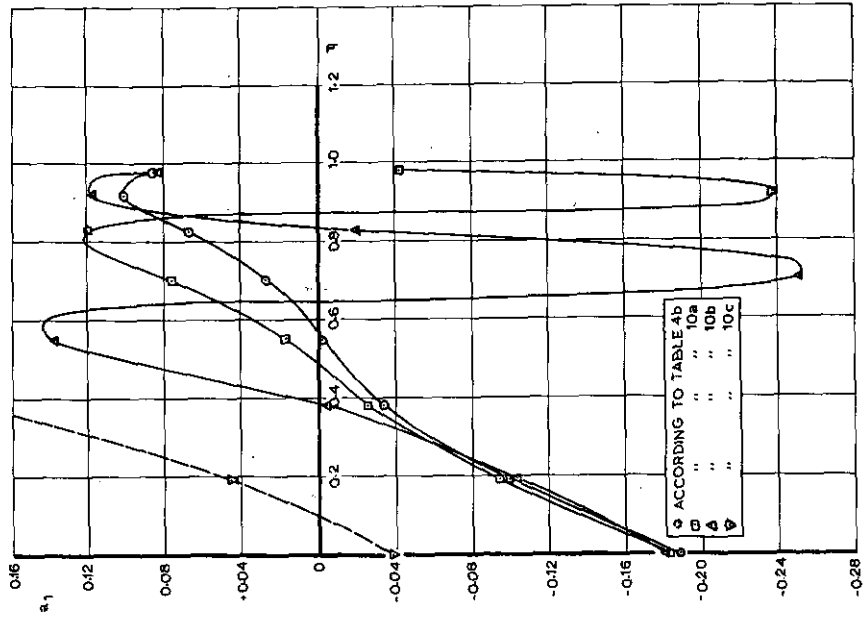


Fig. 6b. The quantity a_1 as a function of η for some different distributions of the spanwise stations.

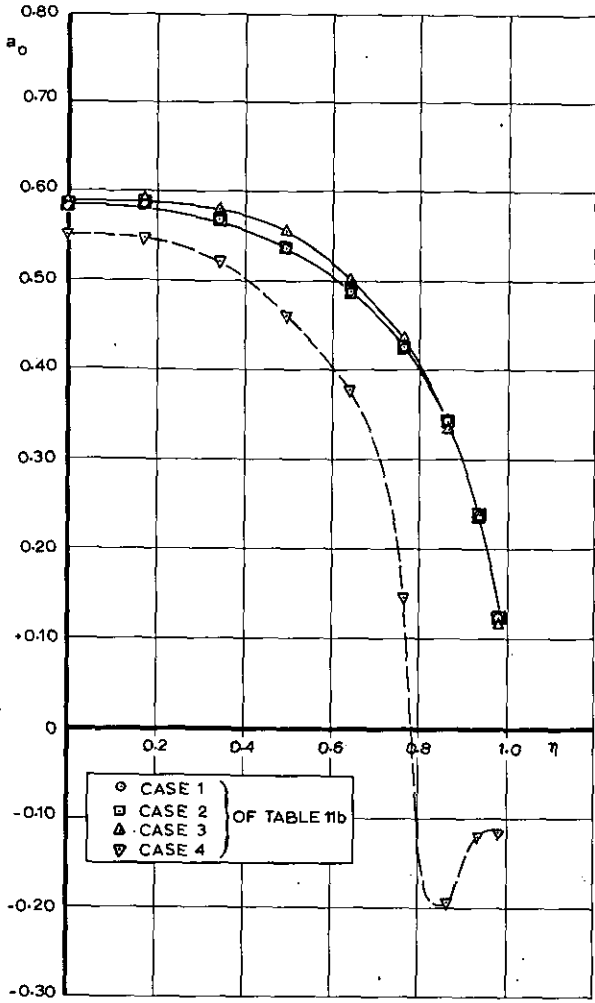


Fig. 7a. The quantity a_0 as a function of η for some different distributions of the spanwise stations.

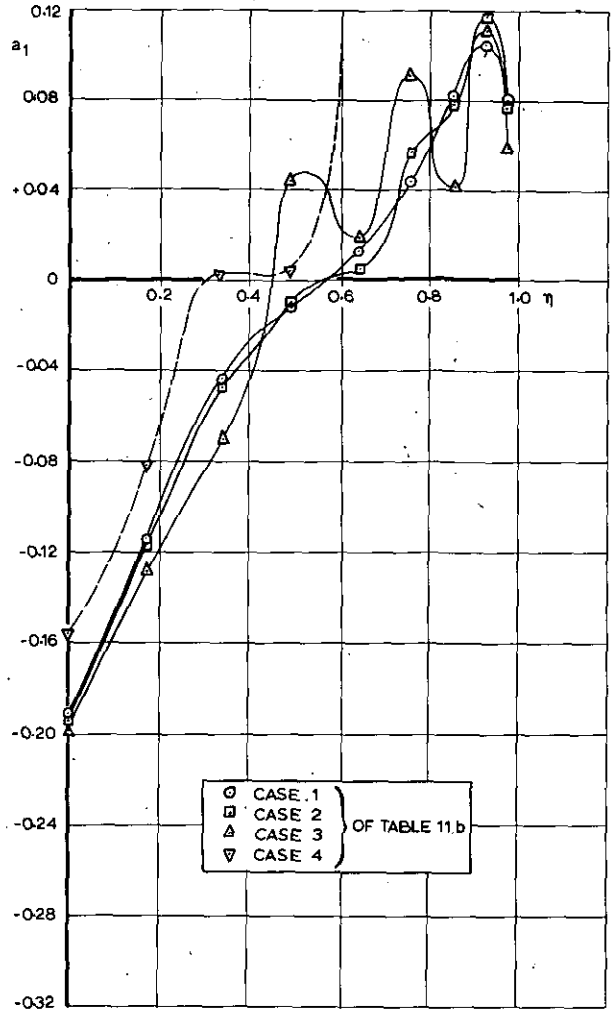
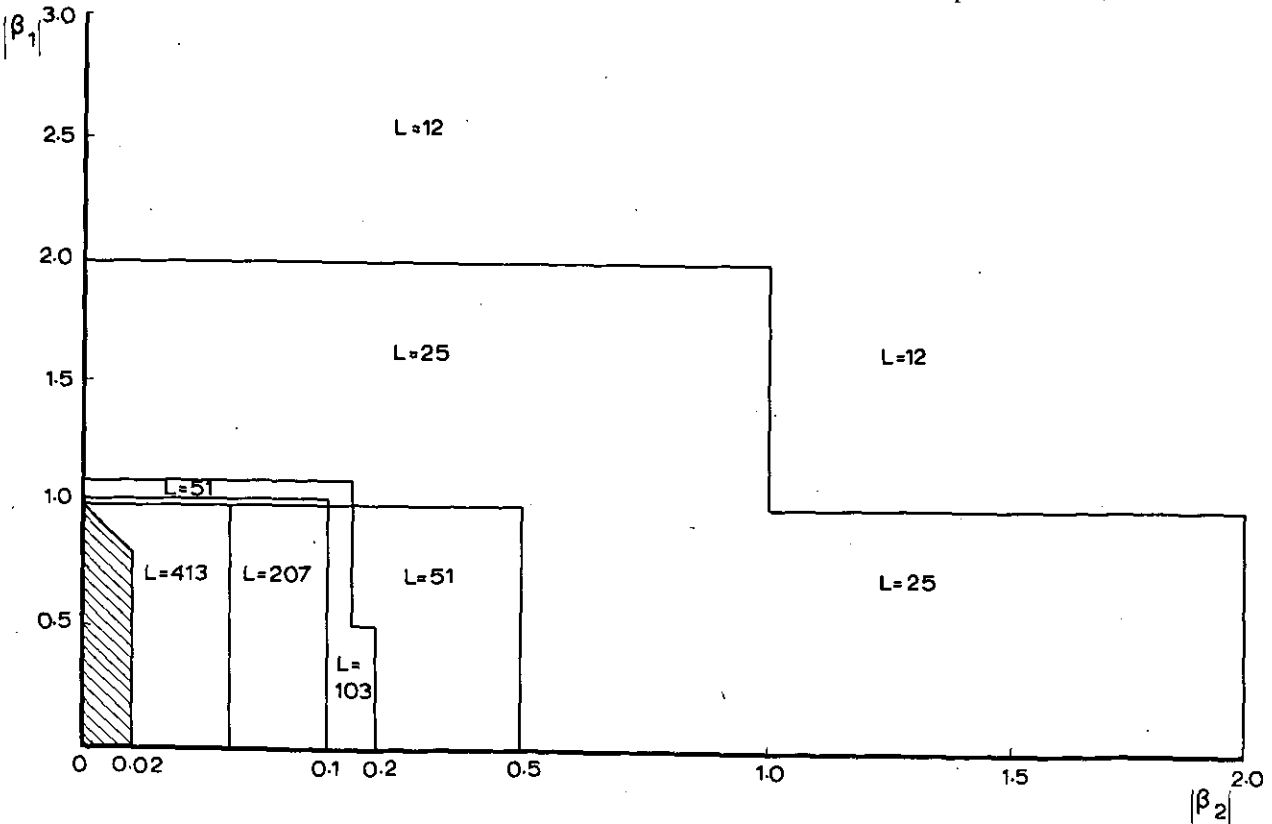
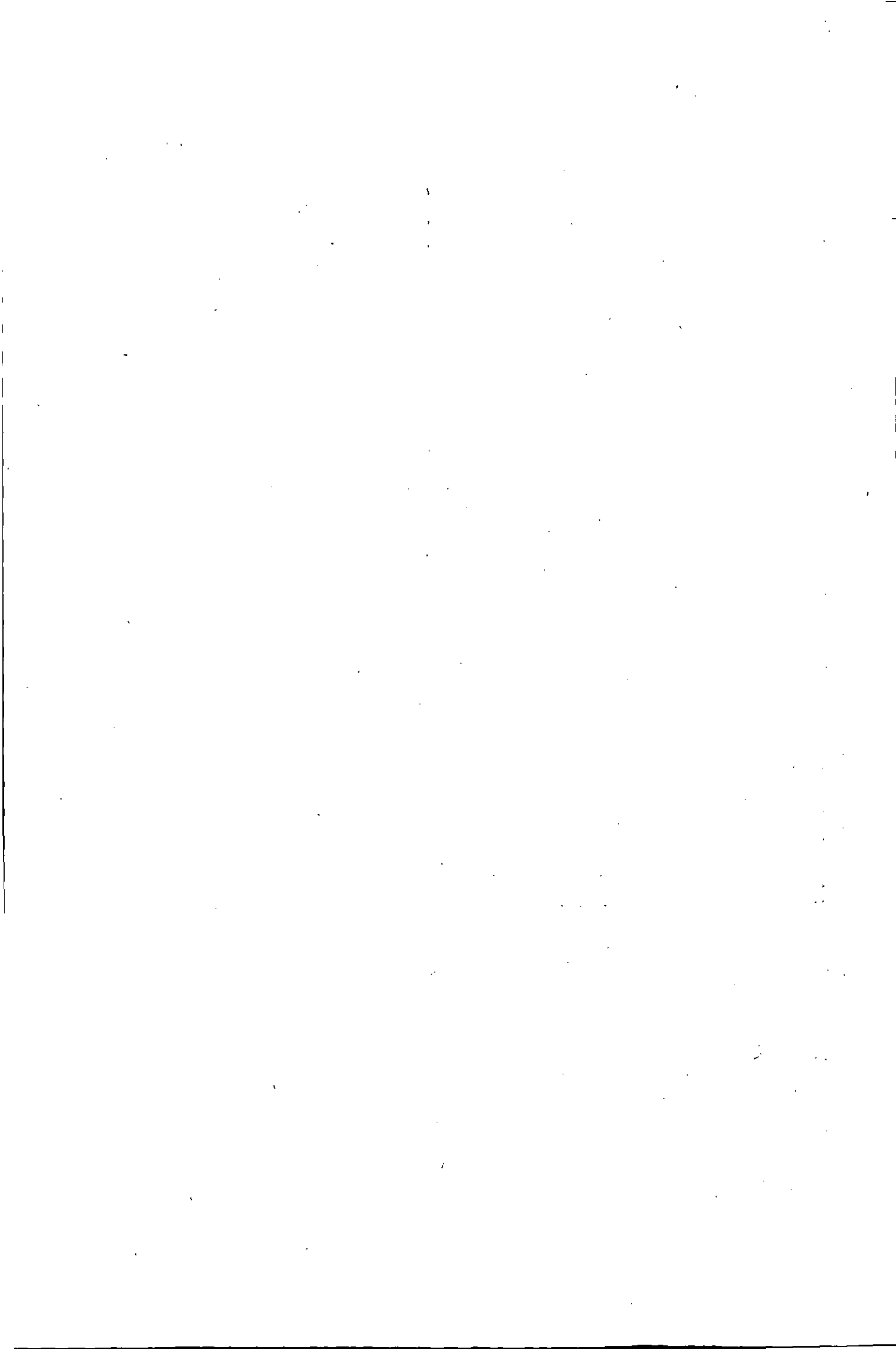


Fig. 7b. The quantity a_1 as a function of η for some different distributions of spanwise stations.



Appendix B, fig. 1: The regions in the $\beta_1 - \beta_2$ plane where an indicated number L is sufficient to obtain an accurate integration in chordwise direction.



Computer application of a linearised supersonic lifting surface theory on a certain class of wings

by

Th. E. Labrijere

Summary

A computer program has been prepared for the determination of the pressure distribution on a thin wing in supersonic flow. The applicability of the program is restricted to cases with completely supersonic trailing edges in the absence of interacting subsonic regions. The present report describes the theory, the numerical evaluation and the computer program and gives some numerical results. This investigation has been performed under contract for the Netherlands Ministry of Defence.

Contents		Page
List of symbols		1
1 Introduction		2
2 Description of the method		2
3 Numerical evaluation		6
3.1 Representation of the wing surface and the wing planform		6
3.2 The numerical integration		7
3.3 Description of the Algol program		9
4 Numerical results		11
5 Conclusions		12
6 References		12
Appendix A: Survey of the formulae used in the computer program		13
Appendix B: Flow diagram of the program		17
Appendix C: The Algol program		19
Appendix D: Survey of the formulae used to obtain analytical results		25
2 tables		
8 figures		
List of symbols		
a_i	coefficient in eq. (3.1.1).	
b_i	coefficient in eq. (3.2.5).	
$c(y)$	chord of wing profile at station y .	
n	highest degree of Chebyshev polynomials	
s	semi span	
U_0	velocity of the undisturbed flow	
M_0	Mach number of the undisturbed flow	
S	area enclosed by the forward Mach cone emanating from the point (x, y)	
$T_i(n)$	$\cos \{i \cos^{-1} u\}$ Chebyshev polynomial of the first kind of degree i and argument u	
l_p	$= \int_{u_0}^{u_1} \frac{u^p du}{\sqrt{(u_1 - u)^2 - B^2}}$ (eq. (3.2.8))	
$F(x, y, n)$	function defined by eq. (3.2.1)	
$F^x(x, y, n)$	function defined by eq. (3.2.3)	
$G(x, y)$	functions introduced in eq. (3.2.10)	
$H(x, y)$	functions introduced in eq. (3.2.10)	
B	$= \frac{2\beta}{c(n)}(v - n)$	
$z_s(x, y)$	representation of the leading edge of x and y	
$xl(y)$	representation of the leading edge of the wing	
x, y, z	coordinate system with x -axis along the root chord and y -axis normal to the plane of symmetry and through the most forward point of the wing	
$w(x, y)$	downwash at the point (x, y) , positive when pointing outwards from the wing surface.	
$n(x, y)$	$= 2 \frac{c(y)}{x - xl(y)} - 1$	

$V_i(u)$	$= \frac{\sin \{i \cos^{-1} u\}}{\sin \{\cos^{-1} u\}}$ Chebychew polynomial of the second kind of degree i and argument u	ξ	integration variable in chordwise direction
β	$= \sqrt{M_0^2 - 1}$	$\sigma(x, y)$	$= \frac{\partial z_s}{\partial x}(x, y)$ slope of the wing contour
η	integration variable in spanwise direction	σ_B	σ belonging to the bottom of the wing
$\lambda(x, y)$	slope of the streamline at the point (x, y) in a plane $y = \text{constant}$	σ_T	σ belonging to the top of the wing
		$\varphi(x, y, z)$	velocity potential

1 Introduction

In linearised theory the perturbation caused by a lifting surface can be resolved into two components, one due to the thickness and one due to the camber of that surface. The respective pressure distributions can be determined separately and by superposition the complete flowfield around the surface can be obtained.

The method and the computer program used to determine these fields strongly depend on the relation between the Mach number of the undisturbed flow and the planform of the surface.

The boundaries of a surface in a supersonic flowfield can be divided into subsonic and supersonic leading edges and trailing edges; by definition an edge is called subsonic when the component of the undisturbed velocity normal to this edge is subsonic and supersonic when this component is supersonic.

Though based on the same principles the methods for treating different combinations of subsonic and supersonic edges vary considerably in degree of complication.

The present report deals with one of the least complicated cases, i.e. the determination of the lift on a surface with a possible partly subsonic leading edge with a completely supersonic trailing edge subject to the condition that the subsonic regions do not interfere with each other.

For the determination of the pressure distribution due to thickness reference can be made to NLR report TN-G.48 "The calculation of the pressure distribution due to thickness for thin wings of arbitrary planform at supersonic speed" (ref. 3).

The applied method is based on the thin wing theory of Evvard (ref. 1). Special attention has been given to the numerical evaluation. By applying Chebychew polynomials to describe the camber distribution in chordwise direction, it was possible to perform the chordwise integration analytically thus coupling the accuracy of this integral directly to the accuracy of the camber representation. In order to perform the spanwise integration the integral has been regularised by subtracting the singularities. The actual integration is achieved by means of the 5-point Gauss formula.

A description and a complete print of the Algol program for the determination of the liftfield, written for the Electrologica XI computer, has been inserted.

2 Description of the method

From the linearised potential equation for supersonic flow

$$-\beta^2 \frac{\partial^2 \varphi}{\partial x^2} + \frac{\partial^2 \varphi}{\partial y^2} + \frac{\partial^2 \varphi}{\partial z^2} = 0 \quad (2.1)$$

with

$$\beta^2 = M_0^2 - 1$$

it has been demonstrated by Evvard (ref. 1) that the velocity potential at a point $(x, y, 0)$ can be determined by

$$\varphi(x, y, 0) = -\frac{1}{\pi} \iint_S \frac{w(\xi, \eta)}{\sqrt{(x-\xi)^2 - \beta^2(y-\eta)^2}} d\xi d\eta \quad (2.2)$$

in which S is the region in the plane $z=0$ enclosed by the forward Mach cone emanating from the point $(x, y, 0)$, the downwash w being related to the local slope of the streamline - measured in the plane $z=0$ along a line $\eta = \text{constant}$ - by

$$w(\xi, \eta) = \begin{cases} U_0 \sigma(\xi, \eta) & \text{in a point on the wing} \end{cases} \quad (2.3a)$$

$$\begin{cases} U_0 \lambda(\xi, \eta) & \text{in a point outside the wing} \end{cases} \quad (2.3b)$$

$z_s(\xi, \eta)$ representing the wing surface, σ given by:

$$\sigma(\xi, \eta) = \frac{\partial z_s(\xi, \eta)}{\partial \xi} \quad (2.4)$$

In order to determine the boundaries of S , the region within the forward Mach cone where the downwash w has values deviating from zero, must be considered. If the wing part lying within the Mach cone is bounded by supersonic edges the region S is limited by the Mach cone and the wing boundary (see fig. 1a). In that case the integral of eq. (2.2) can be evaluated immediately for then w is a known function of ξ and η by virtue of the relation expressed in eq. (2.3a) and thus

$$\varphi(x, y, 0) = -\frac{U_0}{\pi} \iint_S \frac{\sigma(\xi, \eta)}{\sqrt{(x-\xi)^2 - \beta^2(y-\eta)^2}} d\xi d\eta \quad (2.5)$$

If the forward Mach cone includes both supersonic and subsonic leading edges, the region S is limited by the Mach cone, the supersonic part of the wing boundary, and the Mach lines originating in the points of intersection of the supersonic and subsonic edges (see fig. 1b). In that case the determination of the integral of eq. (2.2) must be preceded by the evaluation of an integral over the region S_d between the subsonic edge and the foremost Mach line, as indicated in fig. 1b.

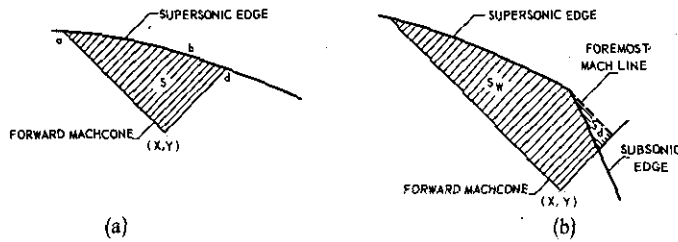


Fig. 1. Supersonic and subsonic edges included by the forward Mach cone.

In the region S_d , w is related to the local slopes of the streamlines, which are unknown (eq. (2.3b)). In ref. 1 it is shown, that in case of a subsonic leading edge the integral over S_d can be replaced by an integral over that part of the wing which generates this part of the downwash field. To understand this, one has to bear in mind that in a supersonic flow the velocity potential in a point of S_d may be independently determined with respect to either the top or the bottom of the wing surface. Thus considering a point (x_D, y_D) in the flowfield near the wing (see fig. 2) the integral relation:

$$-\frac{2}{\pi} U_0 \iint_{S_d} \frac{\lambda d\xi d\eta}{\sqrt{(x_D-\xi)^2 - \beta^2(y_D-\eta)^2}} = \frac{U_0}{\pi} \iint_{S_w} \frac{(\sigma_T - \sigma_B) d\xi d\eta}{\sqrt{(x_D-\xi)^2 - \beta^2(y_D-\eta)^2}} + H(y_D) \quad (2.6)$$

can be derived by applying eq. (2.2) to the top and bottom of the wing respectively and requiring the pressure to be continuous across the region S_d of the plane $z=0$. The function H , introduced here, represents the jump in the velocity potential across the plane $z=0$.

With regard to this function two different kinds of regions S_d can be distinguished (see fig. 3). In region S_{d1} ,

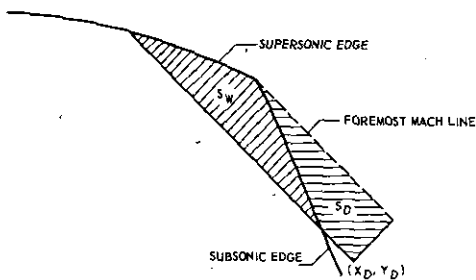


Fig. 2. Fields of integration for equation (2.6).

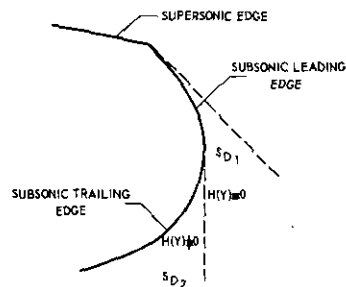


Fig. 3. Difference between subsonic leading and subsonic trailing edge.

$H(y_D) \equiv 0$ due to the fact that the foremost Mach line, originating on the leading edge, generally represents a line of infinitesimal disturbance, along which H may be set equal to zero. The function H remains zero along $y = \text{constant}$ lines for values of x not intercepted by the wing. In region S_{d2} , $H(y_D) \neq 0$, due to the perturbation caused by the wing. In the latter case, i.e. a subsonic trailing edge, eq. (2.6) can only be solved by making a further assumption for the flow in this region, e.g. by applying the Kutta condition. The present report, however, does not consider this case, so that only wings with completely supersonic trailing edges can be treated by the computer programme presented. In the former case, that of a subsonic leading edge, the integration over S_d can simply be replaced by an integral

over the region S_{w_2} , as indicated in fig. 4. Then the expression for the velocity potential, eq. (2.2) applied to the top of the wing, becomes:

$$\begin{aligned} \varphi(x, y, 0) &= -\frac{U_0}{\pi} \iint_{S_{w_1} + S_{w_2}} \frac{\sigma_T d\xi d\eta}{\sqrt{(x-\xi)^2 - \beta^2(y-\eta)^2}} - \frac{U_0}{\pi} \iint_{S_D} \frac{\lambda d\xi d\eta}{\sqrt{(x-\xi)^2 - \beta^2(y-\eta)^2}} \\ &= -\frac{U_0}{\pi} \iint_{S_{w_2}} \frac{\frac{\sigma_B + \sigma_T}{2} d\xi d\eta}{\sqrt{(x-\xi)^2 - \beta^2(y-\eta)^2}} - \frac{U_0}{\pi} \iint_{S_{w_1}} \frac{\sigma_T d\xi d\eta}{\sqrt{(x-\xi)^2 - \beta^2(y-\eta)^2}} \end{aligned} \quad (2.7a)$$

A complication occurs if the supersonic leading edge is connected to two subsonic leading edges, being located in the forward Mach cone emanating from the point (x, y) (see fig. 5). In the case that the subsonic regions do not

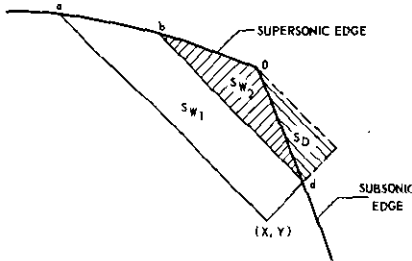


Fig. 4. Replacement of flow field region by wing region at the integration of eq. (2.7a).

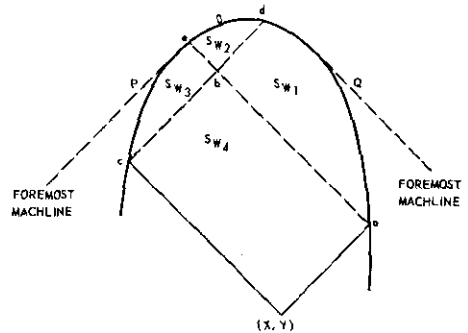


Fig. 5. Two subsonic leading edges included in the forward Mach cone, not interfering subsonic regions.

interfere, the velocity potential can be determined straightforwardly from the following expression, which has been derived in a way similar to that indicated above:

$$\varphi(x, y, 0) = -\frac{U_0}{\pi} \iint_{S_{w_1} + S_{w_3}} \frac{\frac{\sigma_B + \sigma_T}{2} d\xi d\eta}{\sqrt{(x-\xi)^2 - \beta^2(y-\eta)^2}} - \frac{U_0}{\pi} \iint_{S_{w_2}} \frac{\sigma_B d\xi d\eta}{\sqrt{(x-\xi)^2 - \beta^2(y-\eta)^2}} - \frac{U_0}{\pi} \iint_{S_{w_4}} \frac{\sigma_T d\xi d\eta}{\sqrt{(x-\xi)^2 - \beta^2(y-\eta)^2}} \quad (2.7b)$$

In the case that the subsonic regions interact, similar formulae can be derived. This leads to expressions which are getting more complicated as the interaction is more pronounced. If the interaction is continuous, as is the case for wings with completely subsonic leading edges, the solution of an integral equation for the streamline slopes in the subsonic regions concerned is required. These cases, however, will not be considered.

Thus three expressions have been obtained for the determination of the velocity potential in the plane $z=0$, namely, eq. (2.5) in the case of a supersonic edge and eqs. (2.7a) and (2.7b) in the cases that a supersonic edge is connected to one or two subsonic edges respectively. With the aid of these equations the velocity potential can be determined in any point of a wing in a supersonic flow under the conditions mentioned before, namely that the subsonic regions do not interact and that the trailing edge is completely supersonic.

By partial differentiation of the velocity potential the perturbation velocity components may be obtained. From the three equations mentioned above the following can be derived:

– in the case of a supersonic edge as indicated in fig. 1a:

$$\frac{d\varphi}{dx} = -\frac{U_0}{\pi} \iint_S \frac{\frac{d\sigma}{d\xi} d\xi d\eta}{\sqrt{(x-\xi)^2 - \beta^2(y-\eta)^2}} - \frac{U_0}{\pi} \int_{abd} \frac{\sigma d\eta}{\sqrt{(x-\xi)^2 - \beta^2(y-\eta)^2}} \quad (2.8a)$$

$$\frac{d\varphi}{dy} = -\frac{U_0}{\pi} \iint_S \frac{\frac{d\sigma}{d\eta} d\xi d\eta}{\sqrt{(x-\xi)^2 - \beta^2(y-\eta)^2}} + \frac{U_0}{\pi} \int_{abd} \frac{\sigma d\xi}{\sqrt{(x-\xi)^2 - \beta^2(y-\eta)^2}} \quad (2.8b)$$

– in the case of a supersonic edge connected with one subsonic edge as indicated in fig. 4:

$$\begin{aligned} \frac{d\varphi}{dx} = & -\frac{U_0}{\pi} \iint_{sw_1} \frac{\frac{d\sigma_T}{d\xi} d\xi d\eta}{\sqrt{(x-\xi)^2 - \beta^2(y-\eta)^2}} - \frac{U_0}{2\pi} \iint_{sw_2} \frac{\frac{d}{d\xi}(\sigma_B + \sigma_T) d\xi d\eta}{\sqrt{(x-\xi)^2 - \beta^2(y-\eta)^2}} - \frac{U_0}{\pi} \int_{ab} \frac{\sigma_T d\eta}{\sqrt{(x-\xi)^2 - \beta^2(y-\eta)^2}} \\ & - \frac{U_0}{2\pi} \int_{bOa} \frac{(\sigma_B + \sigma_T) d\eta}{\sqrt{(x-\xi)^2 - \beta^2(y-\eta)^2}} - \frac{U_0}{\pi} \left(\frac{\beta}{\frac{dx}{dy} + \beta} \right)_d \int_{bd} \frac{(\sigma_T - \sigma_B) d\eta}{\sqrt{(x-\xi)^2 - \beta^2(y-\eta)^2}} \end{aligned} \quad (2.9a)$$

$$\begin{aligned} \frac{d\varphi}{dy} = & -\frac{U_0}{\pi} \iint_{sw_1} \frac{\frac{d\sigma_T}{d\eta} d\xi d\eta}{\sqrt{(x-\xi)^2 - \beta^2(y-\eta)^2}} - \frac{U_0}{2\pi} \iint_{sw_2} \frac{\frac{d}{d\eta}(\sigma_B + \sigma_T) d\xi d\eta}{\sqrt{(x-\xi)^2 - \beta^2(y-\eta)^2}} + \frac{U_0}{\pi} \int_{ab} \frac{\sigma_T d\xi}{\sqrt{(x-\xi)^2 - \beta^2(y-\eta)^2}} \\ & + \frac{U_0}{2\pi} \int_{bOa} \frac{(\sigma_B + \sigma_T) d\xi}{\sqrt{(x-\xi)^2 - \beta^2(y-\eta)^2}} + \frac{U_0}{\pi} \left(\frac{\frac{dx}{dy}}{\beta + \frac{dx}{dy}} \right)_d \int_{bd} \frac{(\sigma_T - \sigma_B) d\xi}{\sqrt{(x-\xi)^2 - \beta^2(y-\eta)^2}} \end{aligned} \quad (2.9b)$$

in the case of a supersonic edge connected to two subsonic edges as indicated in fig. 5.

$$\begin{aligned} \frac{d\varphi}{dx} = & -\frac{U_0}{\pi} \iint_{sw_1} \frac{\frac{d\sigma_T}{d\xi} d\xi d\eta}{\sqrt{(x-\xi)^2 - \beta^2(y-\eta)^2}} - \frac{U_0}{\pi} \iint_{sw_2} \frac{\frac{d\sigma_B}{d\xi} d\xi d\eta}{\sqrt{(x-\xi)^2 - \beta^2(y-\eta)^2}} - \frac{U_0}{2\pi} \iint_{sw_3+sw_1} \frac{\frac{d}{d\xi}(\sigma_B + \sigma_T) d\xi d\eta}{\sqrt{(x-\xi)^2 - \beta^2(y-\eta)^2}} \\ & + \frac{U_0}{\pi} \left(\frac{\beta}{\beta + \frac{dx}{dy}} \right)_1 \int_{ac} \frac{(\sigma_B - \sigma_T) d\eta}{\sqrt{(x-\xi)^2 - \beta^2(y-\eta)^2}} + \frac{U_0}{\pi} \left(\frac{\beta}{\frac{dx}{dy} + \beta} \right)_c \int_{cd} \frac{(\sigma_B - \sigma_T) d\eta}{\sqrt{(x-\xi)^2 - \beta^2(y-\eta)^2}} \\ & - \frac{U_0}{2\pi} \int_{cOa} \frac{(\sigma_B + \sigma_T) d\eta}{\sqrt{(x-\xi)^2 - \beta^2(y-\eta)^2}} - \frac{U_0}{2\pi} \int_{eOd} \frac{(\sigma_B - \sigma_T) d\eta}{\sqrt{(x-\xi)^2 - \beta^2(y-\eta)^2}} \end{aligned} \quad (2.10a)$$

$$\begin{aligned} \frac{d\varphi}{dy} = & -\frac{U_0}{\pi} \iint_{sw_1} \frac{\frac{d\sigma_T}{d\eta} d\xi d\eta}{\sqrt{(x-\xi)^2 - \beta^2(y-\eta)^2}} - \frac{U_0}{\pi} \iint_{sw_2} \frac{\frac{d\sigma_B}{d\eta} d\xi d\eta}{\sqrt{(x-\xi)^2 - \beta^2(y-\eta)^2}} - \frac{U_0}{2\pi} \iint_{sw_1+sw_3} \frac{\frac{d}{d\eta}(\sigma_B + \sigma_T) d\xi d\eta}{\sqrt{(x-\xi)^2 - \beta^2(y-\eta)^2}} \\ & - \frac{U_0}{\pi} \left(\frac{\frac{dx}{dy}}{\beta + \frac{dx}{dy}} \right)_a \int_{abe} \frac{(\sigma_B - \sigma_T) d\xi}{\sqrt{(x-\xi)^2 - \beta^2(y-\eta)^2}} + \frac{U_0}{\pi} \left(\frac{\frac{dx}{dy}}{\beta + \frac{dx}{dy}} \right)_c \int_{cbd} \frac{(\sigma_B - \sigma_T) d\xi}{\sqrt{(x-\xi)^2 - \beta^2(y-\eta)^2}} \\ & - \frac{U_0}{2\pi} \int_{cPe} \frac{(\sigma_B + \sigma_T) d\xi}{\sqrt{(x-\xi)^2 - \beta^2(y-\eta)^2}} - \frac{U_0}{\pi} \int_{eOd} \frac{\sigma_B d\xi}{\sqrt{(x-\xi)^2 - \beta^2(y-\eta)^2}} + \frac{U_0}{2\pi} \int_{aOa} \frac{(\sigma_B + \sigma_T) d\xi}{\sqrt{(x-\xi)^2 - \beta^2(y-\eta)^2}} \end{aligned} \quad (2.10b)$$

Considering a liftfield the expressions (2.9) and (2.10) may be simplified by introducing $\sigma_B + \sigma_T \equiv 0$ and putting $\sigma = \sigma_T = -\sigma_B$, thus obtaining:

$$\frac{d\varphi}{dx} = -\frac{U_0}{\pi} \iint_{sw_1} \frac{\frac{d\sigma}{d\xi} d\xi d\eta}{\sqrt{(x-\xi)^2 - \beta^2(y-\eta)^2}} - \frac{U_0}{\pi} \int_{ab} \frac{\sigma d\eta}{\sqrt{(x-\xi)^2 - \beta^2(y-\eta)^2}} - \frac{U_0}{\pi} \left(\frac{2\beta}{\beta + \frac{dx}{dy}} \right)_d \int_{bd} \frac{\sigma d\eta}{\sqrt{(x-\xi)^2 - \beta^2(y-\eta)^2}} \quad (2.11a)$$

$$\frac{d\varphi}{dy} = -\frac{U_0}{\pi} \iint_{sw_1} \frac{\frac{d\sigma}{d\eta} d\xi d\eta}{\sqrt{(x-\xi)^2 - \beta^2(y-\eta)^2}} + \frac{U_0}{\pi} \int_{ab} \frac{\sigma d\xi}{\sqrt{(x-\xi)^2 - \beta^2(y-\eta)^2}} + \frac{U_0}{\pi} \left(\frac{2 \frac{dx}{dy}}{\beta + \frac{dx}{dy}} \right)_d \int_{bd} \frac{\sigma d\xi}{\sqrt{(x-\xi)^2 - \beta^2(y-\eta)^2}} \quad (2.11b)$$

$$\begin{aligned}
\frac{d\varphi}{dx} = & -\frac{U_0}{\pi} \iint_{S_{w_4}} \frac{\frac{d\sigma}{d\xi} d\xi d\eta}{\sqrt{(x-\xi)^2 - \beta^2(y-\eta)^2}} + \frac{U_0}{\pi} \iint_{S_{w_2}} \frac{\frac{d\sigma}{d\xi} d\xi d\eta}{\sqrt{(x-\xi)^2 - \beta^2(y-\eta)^2}} \\
& - \frac{U_0}{\pi} \left(\frac{2\beta}{\beta + \frac{dxl}{dy}} \right)_a \int_{ae} \frac{\sigma d\eta}{\sqrt{(x-\xi)^2 - \beta^2(y-\eta)^2}} - \frac{U_0}{\pi} \left(\frac{2\beta}{\beta + \frac{dxl}{dy}} \right)_c \int_{cd} \frac{\sigma d\eta}{\sqrt{(x-\xi)^2 - \beta^2(y-\eta)^2}} \\
& + \frac{U_0}{\pi} \int_{eOd} \frac{\sigma d\eta}{\sqrt{(x-\xi)^2 - \beta^2(y-\eta)^2}}
\end{aligned} \tag{2.12a}$$

$$\begin{aligned}
\frac{d\varphi}{dy} = & -\frac{U_0}{\pi} \iint_{S_{w_4}} \frac{\frac{d\sigma}{d\eta} d\xi d\eta}{\sqrt{(x-\xi)^2 - \beta^2(y-\eta)^2}} + \frac{U_0}{\pi} \iint_{S_{w_2}} \frac{\frac{d\sigma}{d\eta} d\xi d\eta}{\sqrt{(x-\xi)^2 - \beta^2(y-\eta)^2}} + \\
& + \frac{U_0}{\pi} \left(\frac{2 \frac{dxl}{dy}}{\beta + \frac{dxl}{dy}} \right)_a \int_{ae} \frac{\sigma d\xi}{\sqrt{(x-\xi)^2 - \beta^2(y-\eta)^2}} - \frac{U_0}{\pi} \left(\frac{2 \frac{dxl}{dy}}{\beta + \frac{dxl}{dy}} \right)_c \int_{cd} \frac{\sigma d\xi}{\sqrt{(x-\xi)^2 - \beta^2(y-\eta)^2}} \\
& + \frac{U_0}{\pi} \int_{eOd} \frac{\sigma d\xi}{\sqrt{(x-\xi)^2 - \beta^2(y-\eta)^2}}
\end{aligned} \tag{2.12b}$$

The linearized relation between the pressure coefficient c_p and the velocity reads:

$$c_p = -\frac{2}{U_0} \frac{d\varphi}{dx} \tag{2.13}$$

So the pressure distribution on a given wing at a given Mach number of the undisturbed stream can be determined with the aid of eqs (2.8a) (2.11a) and (2.12a). For this purpose an Algol programme has been written using numerical techniques, which are described in the following chapter.

3 Numerical evaluations

From eqs (2.4) through (2.13) it appears that the slopes of the profile camberlines and their first derivatives must be known. Generally, the camber distribution is not given analytically, but only in a number of discrete points. This number may be insufficient to perform an accurate numerical determination of the integrals appearing in the equations mentioned above. Hence it may be necessary to increase this number by interpolation. In order to make the interpolation as simple as possible the wing will be represented analytically.

3.1 Representation of the wing surface and the wing planform

The analytical representation of the camber distribution may be performed in several ways. For two reasons a series of Chebyshev polynomials has been applied in the present method. The first reason is that for a fairly smooth camber distribution the coefficients of this series can very easily be obtained by taking advantage of the orthogonality of the polynomials. The second is that the chordwise integration can be performed analytically when Chebyshev polynomials are used.

Thus the camber distribution in chordwise direction is represented by:

$$\sigma(x, y) = \sum_{i=0}^n a_i(y) T_i \left\{ 2 \frac{x - xl(y)}{c(y)} - 1 \right\} \tag{3.1.1}$$

where T_i is a Chebyshev polynomial of the first kind, defined by:

$$T_i(u) = \cos(i \cos^{-1} u) \tag{3.1.2}$$

and where $xl(y)$ is the x -co-ordinate of the leading edge and $c(y)$ is the local chord of the wing profile.

The coefficients a_i can be determined by integration from:

$$a_i(y) = \varepsilon \int_{xl(y)}^{xl(y)+c(y)} \frac{\sigma(x, y) T_i \left\{ 2 \frac{x - xl(y)}{c(y)} - 1 \right\}}{\sqrt{\{x - xl(y)\} \{xl(y) + c(y) - x\}}} dx \quad \varepsilon = \begin{cases} \frac{1}{\pi} & \text{when } i = 0 \\ \frac{2}{\pi} & \text{when } i \geq 1 \end{cases} \quad (3.1.3)$$

The determination of the coefficients a_i is not performed by the computer program presented in this report. The coefficients a_i are assumed to be known in a number of spanwise stations and thus form part of the input of the program.

When the camber distribution is given analytically in some way, the determination of a_i may be achieved by formal integration.

In the case that the camber is given in a number of discrete points, the integration can be performed by connecting the given points linearly and integrating analytically over the segments thus obtained. The number of points given and the number of terms in the polynomial series both influence of course the accuracy of the approximation of the contour.

Further the assumption has been made that the number of spanwise stations with given camber distribution will be large enough to make a quadratic interpolation of the coefficients $a_i(y)$ in spanwise direction possible. Thus, during the actual computations, the camber in each desired point on the wing, is calculated by means of a series of Chebyshev polynomials the coefficients of which are determined by quadratic interpolation.

Concerning the planform it has been assumed that the leading edge may be represented by means of two polynomials, each valid over a certain part of the span, and that the trailing edge is a straight line.

3.2 The numerical integration

The integrals appearing in eqs (2.8a) (2.11a) and (2.12a) must be calculated numerically and so it is necessary that the integrands have a sufficiently smooth behaviour.

Considering, however, an integrand of the type

$$\frac{\frac{d\sigma}{d\xi}}{\sqrt{(x-\xi)^2 - \beta^2(y-\eta)^2}}$$

it can be seen that this integrand contains a singularity at the point $\xi = x, \eta = y$.

Accordingly the function:

$$F(x, y, \eta) = \int_{\xi_0}^{\xi_b} \frac{\frac{d\sigma}{d\xi}}{\sqrt{(x-\xi)^2 - \beta^2(y-\eta)^2}} d\xi \quad (3.2.1)$$

is singular for $\eta = y, \xi_b = x$.

However, this singularity being logarithmic the integration in spanwise direction is possible. Hence the numerical integration can be performed once $F(x, y, \eta)$ has been regularized by subtraction of this singularity.

Putting:

$$F(x, y, \eta) = F'(x, y, \eta) - \left(\frac{d\sigma}{d\xi} \right)_{x,y} \ln|\beta(y-\eta)| \quad (3.2.2)$$

a function F' is obtained which is regular over the whole integration range, but which has one disadvantage namely

an infinite derivative $\frac{dF'}{d\eta}$ at the point (x, y) .

So putting:

$$F(x, y, \eta) = F^*(x, y, \eta) - \left\{ \left(\frac{d\sigma}{d\xi} \right)_{x,y} + \frac{d}{d\eta} \left(\frac{d\sigma}{d\xi} \right)_{x,y} (|\eta - y|) \right\} \ln|\beta(y-\eta)| \quad (3.2.3)$$

a function F^* is obtained which behaves in such a way that the numerical integration can be performed without any difficulty.

The reason for putting $|\eta|$ as a factor of $\frac{d}{d\eta} \left(\frac{d\sigma}{d\xi} \right)_{x,y}$ becomes clear when considering the fact that the plane $\eta = 0$ is a plane of symmetry for the wing.

The chordwise integration can be performed, taking advantage of the approximation of the profile-slopes by Chebyshev polynomials.

From eq. (3.1.1) it follows that

$$F(x, y, \eta) = \int_{\xi_0}^{\xi_b} \frac{2}{c(\eta)} \sum_{i=1}^n ia_i V_i \left\{ \frac{2(\xi - xl(\eta))}{c(\eta)} \right\} \frac{d\xi}{\sqrt{(x-\xi)^2 - \beta^2(y-\eta)^2}} \quad (3.2.4)$$

where

$$V_i = \frac{\sin i\psi}{\sin \psi} \quad \psi = \cos^{-1} \left\{ \frac{2(\xi - xl(\eta))}{c(\eta)} - 1 \right\}$$

V_i can be written as follows:

$$V_i = \sum_{j=1}^N b_{ij} u^{i+1-2j} \quad u = \frac{2(\xi - xl(\eta))}{c(\eta)} - 1 \quad N = \text{entier} \left(\frac{i+1}{2} \right) \quad (3.2.5)$$

where b_{ij} can be determined from the recurrence relation:

$$V_i = 2uV_{i-1} - V_{i-2} \quad V_0 = 0 \quad V_1 = 1 \quad (3.2.6)$$

Thus can be obtained:

$$F(x, y, \eta) = \frac{2}{c(\eta)} \sum_{i=1}^n ia_i(\eta) \sum_{j=1}^N b_{ij} \int_{u_0}^{u_b} \frac{u^{i+1-2j} du}{\sqrt{(u-u_1)^2 - B^2}} \quad (3.2.7)$$

with $u_1 = \frac{2(x - xl(\eta))}{c(\eta)} - 1$ $u_0 = \frac{2(\xi_0 - xl(\eta))}{c(\eta)}$ $u_b = \frac{2(\xi_b - xl(\eta))}{c(\eta)} - 1$ $B = \beta(y - \eta) \cdot \frac{2}{c(\eta)}$

From the integrals $I_p = \int_{u_0}^{u_b} \frac{u^p du}{\sqrt{(u-u_1)^2 - B^2}}$ another recurrence relation can be derived; viz.:

$$(p+1)I_{p+1} - (2p+1)u_1 I_p + (u_1^2 - B^2) p I_{p-1} = (u_b)^p \sqrt{(u_b - u_1)^2 - B^2} - (u_0)^p \sqrt{(u_0 - u_1)^2 - B^2} \quad (3.2.8)$$

by means of which it is possible to determine the integrals I_p consecutively from:

$$I_0 = \ln \left| \frac{u_b - u_1 + \sqrt{-B^2 + (u_b - u_1)^2}}{-u_0 + u_1 - \sqrt{(-u_0 + u_1)^2 - B^2}} \right| \quad \text{and} \quad I_1 = u_1 I_0 = \sqrt{(-u_0 + u_1)^2 - B^2} + \sqrt{(u_b - u_1)^2 - B^2} \quad (3.2.9)$$

In this way I_p can be determined with a slight decrease in accuracy for increasing values of p . The growth of the error has been investigated by introducing a small perturbation of I_0 and comparing the results for I_p determined from disturbed and undisturbed values of I_0 . The conclusion may be drawn that for values of p up to 15 the accuracy of I_p is sufficient. Because of the fact that the expression $\sum_{i=1}^N b_{ij} I_{i+1-2j}$ appearing in eq. (3.2.7) contains the coefficients b_{ij} which increase rapidly as the value of i increases, a small deviation in I_{i+1-2j} may cause a much larger deviation in the value of this sum. On the other hand it may be assumed that for increasing i the values of a_i will decrease and also that the number of terms in the series representing the camber distribution will in general be limited.

So it seems reasonable to assume that the chordwise integration may be performed by means of the eqs (3.2.7) through (3.2.9) when i does not exceed the value 20.

The spanwise integration must be carried out with the aid of some integration rule.

Assuming that the coefficients $a_i(\eta)$ can be determined in any spanwise station a 5-point Gauss formula can be used, which has the advantage of giving a high accuracy using relatively few integration points. Of course, the application of this formula is only advantageous if the accuracy thus obtained is known to be sufficient. The computer program presents the possibility to subdivide the integration domain into a number of intervals to each of which the integration formula is applied. Thus the integration accuracy can be checked by increasing this number. It is assumed that it will not be necessary to vary the number of intervals during the actual calculations for each wing, but that for a given class of wings the number of intervals can be determined by means of a suitable test-case.

When the integration domain S_w contains the point (x, y) the integral in spanwise direction, which has the shape:

$$\int_{\eta_0}^{\eta_b} F(x, y, \eta) d\eta$$

must be treated according to eq. (3.2.3) as follows:

$$\int_{\eta_0}^{\eta_b} F(x, y, \eta) d\eta = \int_{\eta_0}^{\eta_b} F^*(x, y, \eta) d\eta - \left(\frac{d\sigma}{d\xi} \right)_{x,y} G(x, y) - H(x, y) \frac{d}{d\eta} \left(\frac{d\sigma}{d\xi} \right)_{x,y} \quad (3.2.10)$$

in which $F^*(x, y, \eta)$ is defined by eq. (3.2.3) and the functions G and H are obtained by formally integrating the singular part of this expression.

$$G(x, y) = (\eta_b - y) \ln |\beta(\eta_b - y)| - (\eta_0 - y) \ln |\beta(\eta_0 - y)| - (\eta_b - \eta_0)$$

$$H(x, y) = \begin{cases} \frac{(\eta_b - y)^2}{4} \{2 \ln |\beta(\eta_b - y)| - 1\} - \frac{(\eta_0 - y)^2}{4} \{2 \ln |\beta(\eta_0 - y)| - 1\} & \eta_0 \geq 0 \\ \frac{(\eta_b - y)^2}{4} \{2 \ln |\beta(\eta_b - y)| - 1\} + \frac{\eta_0 - y}{4} \{2(\eta_0 + 3y) \ln |\beta(\eta_0 - y)| - (\eta_0 + 7y)\} + \frac{y^2}{2} \{2 \ln (\beta y) - 3\} & \eta_0 \leq 0 \end{cases}$$

In the case that the integration domain S_w does not contain the point (x, y) the function $F(x, y, \eta)$ can be integrated directly.

The line integrals in spanwise direction which have one of the integration boundaries, or both, on a Mach line through (x, y) give another complication.

The integrand of the shape:

$$\frac{\sigma}{\sqrt{\{x - xl(\eta)\}^2 - \beta^2(y - \eta)^2}}$$

contains a singularity for $\{x - xl(\eta)\}^2 - \beta^2(y - \eta)^2 = 0$. This is the case whenever an integration boundary coincides with a Mach line through (x, y) . This difficulty is solved by transformation to another integration variable by means of

$$\eta = \frac{\eta_0 + \eta_b}{2} + \frac{\eta_b - \eta_0}{2} \cos \theta \quad (3.2.11)$$

Putting

$$\xi_b = x - \beta(y - \eta) \quad \xi_c = x + \beta(y - \eta) \quad (3.2.12)$$

gives:

$$\frac{\sigma}{\sqrt{\{x - xl(\eta)\}^2 - \beta^2(y - \eta)^2}} = \frac{\sigma}{\sqrt{\{\xi_b - xl(\eta)\} \{\xi_c - xl(\eta)\}}}$$

For $\eta \approx \eta_0$ there may be written

$$x(\eta) \approx xl(\eta_0) + \frac{dxl}{d\eta}(\eta - \eta_0) = \xi_b(\eta_0) + \frac{dxl}{d\eta}(\eta - \eta_0) \quad \text{and} \quad \xi_b(\eta) = \xi_b(\eta_0) + \beta(\eta - \eta_0)$$

So:

$$\xi_b(\eta) - xl(\eta) \approx \left(\beta - \frac{dxl}{d\eta} \right) (\eta - \eta_0)$$

From this it follows that:

$$\frac{d\eta}{\sqrt{(\xi_b - xl)(\xi_c - xl)}} \approx \frac{-\frac{\eta_b - \eta_0}{2} \sqrt{1 + \cos \theta} d\theta}{\sqrt{\left(\beta - \frac{dxl}{d\eta} \right) \left(\frac{\eta_0 - \eta_b}{2} \right) \sqrt{\xi_c - x}}} \quad \text{for } \eta \approx \eta_0$$

and the boundary singularity has vanished.

The same derivation holds for $\eta \approx \eta_b$.

So, using the appropriate integration variables, all spanwise integrations can be performed by means of the Gauss formula. All formulae concerning the determination of $\frac{d\varphi}{dx}$ in the three different cases as indicated in chapter 2 are presented in Appendix A in the form in which they appear in the Algol program. A flow diagram of the program is presented in appendix B and the program itself in appendix C.

3.3 Description of the Algol program

Though the flow-diagram of the program is sufficient to provide insight into its structure it would be convenient, however, to have more detailed information. Therefore a short outline of the various procedures will be given first.

The procedures xle , dxl , xte , dxt refer to the planform of the wing and do not need any further description.

The procedure $estac$ requires some explanation. Assuming the camber of the wing profiles to be given in a number of spanwise stations (ygs) in a form as indicated by eq. (3.1.1):

$$\sigma(x, ygs) = \sum_{i=1}^n acgs_i(ygs) T_i(u) \quad u = 2 \frac{x - xle(ygs)}{c(ygs)} - 1,$$

and also assuming that the number of the given stations is large enough to enable a quadratic interpolation in spanwise direction, the Chebychew coefficients for a certain value of η may be obtained from:

$$ac_i(\eta) = ap_{1,i}^{(k)} \{\eta - ygs(k)\}^2 + ap_{2,i}^{(k)} \{\eta - ygs(k)\} + acgs_i \{ygs(k)\}$$

The value of k is chosen in such a way that $ygs(k)$ refers to the given spanwise station nearest to η , this to get the best possible results within the limits of the quadratic interpolation. The formulae for $ap_{j,i}^{(k)}$ are given in appendix A.

In the case that the derivative of $\sigma \frac{d^2\sigma}{d\eta d\xi}$ must be determined, the derivatives of $ac_i(\eta) \frac{dac_i}{d\eta}$ are needed as well.

Therefore the procedure *estac* possesses a boolean parameter *derac*, which must be true if $\frac{dac_i}{d\eta}$ has to be calculated.

In that case the following formula is used:

$$\frac{dac_i}{d\eta} = 2ap_{1,i}^{(k)} \{\eta - ygs(k)\} + ap_{2,i}^{(k)}$$

The procedure *intersl* delivers the co-ordinates of the intersection point of some line $\xi = a + b\eta$ and the leading edge $\xi = xle(\eta)$. During this procedure the real procedure ZERO is used which delivers the root of the function $f(x) = 0$ by means of the Regula Falsi. $e[1]$ and $e[2]$ are array elements which determine the accuracy of the root.

The boolean variable B04 has been used in order to deal with the special case when the subsonic leading edge coincides with the line $\eta = \pm s$. In that case B04 = false and the intersection point of the line $\xi = a + b\eta$ and the subsonic leading edge is determined by $\eta = \pm s$ and $\xi = a \pm bs$.

The procedure *dercamber* delivers the values $d\sigma = \left(\frac{d\sigma}{d\xi}\right)_{x,y}$ and $d2\sigma = \frac{d}{d\eta} \left(\frac{d\sigma}{d\xi}\right)_{x,y}$ according to the formulae of eqs (A.24) to (A.26) and does not need any further explanation.

The procedure *chebint* delivers the integrals in

$$[in] = \int_{u_0}^{u_b} \frac{u^p du}{\sqrt{(u-u_1)^2 - B^2}}$$

according to eqs (A.19) through (A.20).

The procedure *surfint* delivers the surface integrals I_1 or I_2 of eqs (A.2) through (A.4), where the difference between the calculation of I_1 and I_2 is indicated by means of the boolean variable B03, which should be false when I_2 has to be calculated.

The procedure *lineint* delivers the line integrals I_3 to I_5 of eqs (A.2) through (A.5). It has a special feature that, in view of the kink which often appears at the centre section in the leading edge, the integration has been divided into two parts in case one of the integration boundaries has a negative value.

The possible appearance of a kink at another point of the leading edge has not been taken into account. In that case the integration accuracy may be checked by making use of the possibility, mentioned before, i.e. to increase the number of integration intervals.

The procedure XEEN is an internal machine-code procedure, which offers the possibility to influence the flow of the computation by means of the control desk of the computer.

Finally a survey of the *input data* will be given:

$n1$ = degree of the polynomial, describing the first part of the leading edge

$n2$ = degree of the polynomial, describing the second part of the leading edge

np = highest degree of the used Chebychew polynomials

ns = number of given spanwise stations counting from 0 (centre section) to ns (tip)

$al[1, i] i = 0 \rightarrow n1$ coefficients of polynomial of first part of leading edge

$al[2, i] i = 0 \rightarrow n2$ coefficients of polynomial of second part of the leading edge

$at[1]$ $at[2]$ coefficients of polynomial of trailing edge.

s = semi span

xp, yp = co-ordinates of the junction of the first and the second part of the leading edge.

$ygs[i]$ } η -coordinate of a given spanwise station.

$acgs[0, i]$ } $i = 0 \rightarrow ns$ coefficients of the Chebychew polynomials, describing the slope of the camber along the given station $ygs[i]$

$acgs[np, i]$ }

$mon = M_0$ = Mach number of undisturbed flow.

y coordinates of the point where c_p has to be calculated; any desired sequence of x, y values may be given.
 x
 - 1 = number which ends the calculation (see flow diagram)

4 Numerical results

As a check on the correctness of the computer program the described calculation method has been applied to two different wings:

- The F 104 G wing for $M_0 = 2$ (see fig. 6). The bodyside has been treated as a plane of reflection.

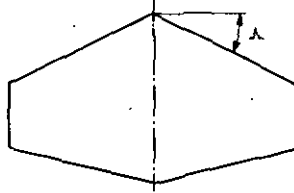


Fig. 6. The F 104 wing $s = 3.3435$ $c(0) = 3.946$ $c(s) = 1.492$ $\Lambda = 26.8^\circ$. $zs(\xi, \eta) = 0$.

- A rectangular wing with camber $\sigma(\xi, \eta) = a\xi^2 + b\xi + c$ semi span $s = 1$, $c(y) = 1$, for $M_0 = \sqrt{2}$. Two different sets of the coefficients a, b and c have been considered.

As these two wings have a simple planform and a simple camber distribution it is also possible to achieve the calculation of c_p analytically. In Appendix D the formulae involved are presented.

TABLE 1
 Comparison of numerical and analytical results for the F 104 wing.

$M_0 = 2$	$\sigma(\xi, \eta) = .0349$		
x	y	$c_{p\text{numerical}}$	$c_{p\text{analytical}}$
.4	.16718	-.036555	-.036554
.8	.16718	-.034674	-.034674
1.2	.16718	-.034384	-.034384
1.6	.16718	-.034285	-.034285
2.0	.16718	-.034240	-.034240
2.4	.16718	-.034216	-.034216
2.8	.16718	-.034201	-.034201
3.2	.16718	-.034192	-.034192
2.2	1.83898	-.042156	-.042156
3.4	1.83898	-.039253	-.039284
2.2	3.17642	-.024891	-.024890
2.6	3.17642	-.017832	-.017832
3.0	3.17642	-.014677	-.014677
3.2	3.17642	-.031623	-.013623

TABLE 2
 Comparison of the numerical and analytical results for the rectangular wing.

$M_0 = \sqrt{2}$	$\sigma(\xi, \eta) = -.4\xi + 0.2$		
x	y	$c_{p\text{numerical}}$	$c_{p\text{analytical}}$
.2	.05	.2399	.2400
.4	.05	.0798	.0800
.6	.05	-.0803	-.0800
.8	.05	-.2404	-.2400
.2	.55	.2399	.2400
.4	.55	.0798	.0800
.6	.55	-.1861	-.1856
.8	.55	-.3320	-.3316
.2	.95	.0359	.0359
.4	.95	-.0490	-.0490
.6	.95	-.0994	-.0993
.8	.95	-.1373	-.1372

$M_0 = \sqrt{2}$	$\sigma(\xi, \eta) = 2.1333\xi^2 - 2.311\xi + 0.3333$		
x	y	$c_{p\text{numerical}}$	$c_{p\text{analytical}}$
.2	.05	-.0876	-.0871
.4	.05	-.5005	-.4995
.6	.05	-.5720	-.5706
.8	.05	-.3024	-.3004
.2	.55	-.0877	-.0871
.4	.55	-.5005	-.4995
.6	.55	-.6520	-.6509
.8	.55	-.2172	-.2160
.2	.95	-.2134	-.2133
.4	.95	-.2766	-.2766
.6	.95	-.1589	-.1589
.8	.95	+.0657	+.0657

In tables 1 and 2 a comparison has been made between the numerical and the analytical results. The agreement is very good. The results are presented in fig. 7 and 8 as well.

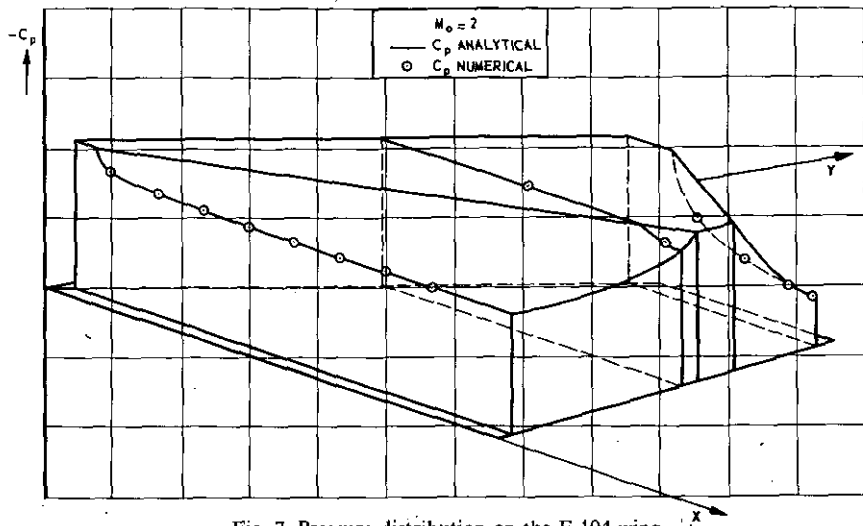
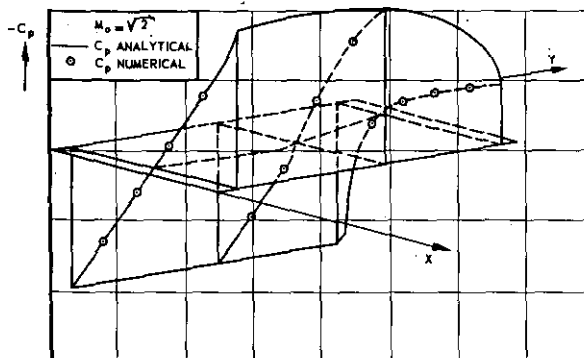
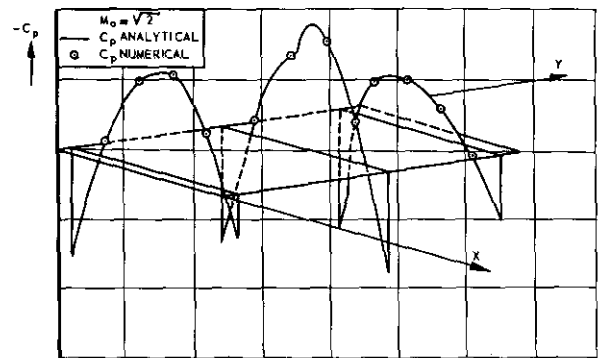


Fig. 7. Pressure distribution on the F 104 wing.

Fig. 8a. Pressure distribution on the rectangular wing $\sigma(\xi, \eta) = -0.4\xi + 0.2$.Fig. 8b. Pressure distribution on the rectangular wing $\sigma(\xi, \eta) = 2.1331\xi^2 - 2.311\xi + 0.3333$.

5 Conclusions

A program has been developed which can be used to determine the lift on a wing in steady supersonic flow. On the condition that the subsonic regions do not interfere, the program in its present form can be applied to wings with leading edges which may be both supersonic and subsonic and trailing edges which are completely supersonic.

In principle the program can be extended to cases with interfering subsonic regions and to cases with subsonic trailing edges but this will require some additional analytical and numerical work.

6 References

- 1 Evvard, J. C., Use of source distributions for evaluating theoretical aerodynamics of thin finite wings at supersonic speeds. NACA rep. no. 951 (1950).
- 2 Krylov V. I., Approximate calculation of integrals. Translated from the Russian book: Priblizhennoe Vychislenie Integralov Moscow 1959 Translation by A. H. Stroud Mac Millan Cy New York.
- 3 Labrujere, Th. E. and Visser, L., The calculation of the pressure distribution due to thickness for thin wings with arbitrary planform at supersonic speeds. NLR-TN G.48 (to be published).

APPENDIX A

Survey of the formulae, used in the Algol program

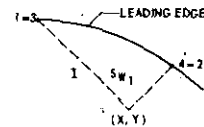
In order to make this appendix more useful for those who wish to study the program itself, all formulae, used in the Algol program, are presented here in the notation of the program.

According to eqs (2.8) to (2.13):

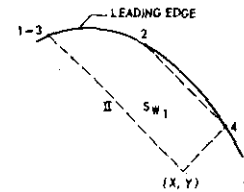
$$c_p = \frac{2}{\pi} \left\{ I_1 - I_2 - I_3 + \frac{2dy_1}{1+dy_1} I_4 + \frac{2dy_4}{1+dy_4} I_5 \right\}, \quad (\text{A1})$$

where I_1 to I_5 are given by the formulae below. The various cases are indicated by the adjoining sketches:

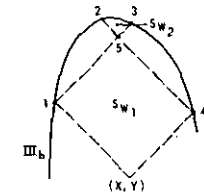
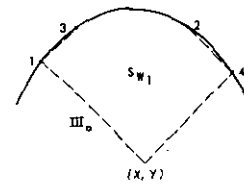
$$\text{I} \left\{ \begin{array}{l} I_1 = \int_{\eta_1}^{\eta_4} \int_{xl(\eta)}^{xb(\eta)} \frac{\frac{d\sigma}{d\xi}}{\sqrt{\{xr(\eta) - \xi\} \{xq(\eta) - \xi\}}} d\xi d\eta \\ I_2 = I_4 = I_5 = 0 \end{array} \right. \quad (\text{A2})$$



$$\text{II} \left\{ \begin{array}{l} I_1 = \int_{\eta_1}^{\eta_4} \int_{x0(\eta)}^{xb(\eta)} \frac{\frac{d\sigma}{d\xi}}{\sqrt{\{xr(\eta) - \xi\} \{xq(\eta) - \xi\}}} d\xi d\eta \\ I_2 = I_4 = 0 \\ I_5 = \int_{\eta_2}^{\eta_4} \frac{\sigma d\eta}{\sqrt{\{xr(\eta) - x_4(\eta)\} \{xq(\eta) - x_4(\eta)\}}} \end{array} \right. \quad (\text{A3})$$



$$\text{III} \left\{ \begin{array}{l} \left. \begin{array}{l} I_1 = \int_{\eta_1}^{\eta_4} \int_{xp(\eta)}^{xb(\eta)} \frac{\frac{d\sigma}{d\xi}}{\sqrt{\{xr(\eta) - \xi\} \{xq(\eta) - \xi\}}} d\xi d\eta \\ I_2 = 0 \end{array} \right\} a \\ \left. \begin{array}{l} I_1 = \int_{\eta_1}^{\eta_2} \int_{xk(\eta)}^{xb(\eta)} \frac{\frac{d\sigma}{d\xi}}{\sqrt{\{xr(\eta) - \xi\} \{xq(\eta) - \xi\}}} d\xi d\eta \\ I_2 = \int_{\eta_2}^{\eta_3} \int_{xl(\eta)}^{xm(\eta)} \frac{\frac{d\sigma}{d\xi}}{\sqrt{\{xr(\eta) - \xi\} \{xq(\eta) - \xi\}}} d\xi d\eta \end{array} \right\} b \end{array} \right. \quad (\text{A4})$$



$$I_3 = \int_{\eta_2}^{\eta_3} \frac{\sigma}{\sqrt{\{xr(\eta) - xl(\eta)\} \{xq(\eta) - xl(\eta)\}}} d\eta \quad \text{in all cases I to III} \quad (\text{A5})$$

$$xb(\eta) = x - \beta|y - \eta| \quad (\text{A6})$$

$$xl(\eta) = \begin{cases} \sum_{i=0}^{n1} a_{1,i} \eta^i & 0 \leq \eta \leq y_p \\ \sum_{i=0}^{n2} a_{2,i} \eta^i & y_p < \eta \leq s \end{cases} \quad (\text{A7})$$

$$xk(\eta) = \begin{cases} x_1(\eta) & \eta_1 \leq \eta \leq \eta_5 \\ x_4(\eta) & \eta_5 \leq \eta \leq \eta_4 \end{cases} \quad (\text{A8})$$

$$xm(\eta) = \begin{cases} x_4(\eta) & \eta_2 \leq \eta \leq \eta_5 \\ x_1(\eta) & \eta_5 \leq \eta \leq \eta_3 \end{cases} \quad (\text{A9})$$

$$xO(\eta) = \begin{cases} xl(\eta) & \eta_1 \leq \eta \leq \eta_2 \\ x_4(\eta) & \eta_2 \leq \eta \leq \eta_4 \end{cases} \quad (\text{A10})$$

$$xp(\eta) = \begin{cases} x_1(\eta) & \eta_1 \leq \eta \leq \eta_3 \\ xl(\eta) & \eta_3 \leq \eta \leq \eta_2 \\ x_4(\eta) & \eta_2 \leq \eta \leq \eta_4 \end{cases} \quad (\text{A11})$$

$$\begin{aligned} xq(\eta) &= x + \beta(y - \eta) & x_1(\eta) &= xl(\eta_1) + \beta(\eta_1 - \eta) \\ xr(\eta) &= x - \beta(y - \eta) & x_4(\eta) &= xl(\eta_4) - \beta(\eta_4 - \eta) \end{aligned} \quad (\text{A12})$$

$$dy_1 = \frac{\beta}{\frac{dxl}{d\eta}(\eta_1)} \quad dy_4 = \frac{\beta}{\frac{dxl}{d\eta}(\eta_4)} \quad (\text{A13})$$

The subscripts of η refer to the intersection points 1 to 5 as indicated in the figures. yp is the η -coordinate of the point where the representation of the leading edge changes its form.

The surface integrals I_1 and I_2 are treated somewhat differently from each other. The area Sw_2 does not contain the singular point (x, y) as Sw_1 does. Hence according to eq. (3.2.10):

$$I_1 = \int_{\eta_1}^{\eta_4} F^*(x, y, \eta) d\eta - \left(\frac{d\sigma}{d\xi} \right)_{x,y} G(x, y) - \left\{ \frac{d^2\sigma}{d\xi d\eta} \right\}_{x,y} H(x, y) \quad (\text{A14})$$

$$I_2 = \int_{\eta_2}^{\eta_3} F(x, y, \eta) d\eta \quad (\text{A15})$$

where:

$$F^*(x, y, \eta) = F(x, y, \eta) + \left\{ \left(\frac{d\sigma}{d\xi} \right)_{x,y} + \left(\frac{d^2\sigma}{d\eta d\xi} \right)_{x,y} (|\eta| - y) \right\} \ln \beta|\eta - y| \quad \text{and} \quad (\text{A16})$$

$$F(x, y, \eta) = \int_{\xi_0}^{\xi_b} \frac{\frac{d\sigma}{d\xi}}{\sqrt{\{xr(\eta) - \xi\} \{xq(\eta) - \xi\}}} d\xi \quad (\text{A17})$$

with $\xi_b = xb(\eta)$ and ξ_0 equal to either xo , xp , xk or $xl(\eta)$.

The integration in chordwise direction is carried out analytically according to eqs (3.2.7) to (3.2.9):

$$F(x, y, \eta) = \frac{2}{c(\eta)} \sum_{i=1}^n iac_i(\eta) \left\{ \sum_{j=1}^N bv_{ij} In_{i+1-2j} \right\} \quad N = (i+1) \div 2 \quad (\text{A18})$$

$$In_p = \int_{u_0}^{u_b} \frac{u^p du}{\sqrt{(u-u_1)^2 - B^2}} \quad (\text{A19})$$

with:

$$\begin{aligned} u_0 &= \frac{2\{\xi_0 - xl(\eta)\}}{c(\eta)} - 1 & u_b &= \frac{2\{\xi_b - xl(\eta)\}}{c(\eta)} - 1 \\ u_1 &= \frac{2\{x - xl(\eta)\}}{c(\eta)} - 1 & B &= \frac{2}{c(\eta)} \beta(y - \eta) \\ c(\eta) &= xt(\eta) - xl(\eta) & xt(\eta) &= at_1 + at_2\eta \end{aligned} \quad (\text{A20})$$

$$(A32) \quad \begin{aligned} gp_5 &= .906179845939 & gp_1 &= -gp_5 & gp_1 &= gw_5 = .2369268885056 \\ gp_4 &= .538469310105 & gp_2 &= -gp_4 & gp_2 &= gw_4 = .478628670499 \\ gp_3 &= 0 & & & gp_3 &= gw_3 = .56888888888889 \end{aligned}$$

gp and gw of eqs (A29) and (A31) are the Gaussian points and weight functions which are given by:

$$(A31) \quad \begin{aligned} &= \int_{-1}^{+1} \frac{2}{x} \int_{n_0-n_1}^{n_0-n_2} f(gp) dgp = \int_{-1}^{+1} \frac{2}{x} \int_{n_0-n_1}^{n_0-n_2} f(gp) dgp \\ &= \int_{n_0-n_1}^{n_0-n_2} \frac{\sqrt{(x_1-x)(x_2-x)}}{\sigma} d\eta = \int_{-\pi}^{\pi} \frac{2}{n_0-n_1} \frac{\sqrt{(x_1-x)(x_2-x)}}{\sigma \sin \theta} d\theta \\ & \quad \eta = \frac{2}{n_1+n_2} + \frac{2}{n_1-n_2} \cos \theta \quad \text{and} \quad \theta = \frac{2}{\pi} (1+gp) \end{aligned}$$

The line integrals I_3 through I_5 are also calculated with the aid of the 5-point Gauss formula, applying the transformation:

$$(A30) \quad \eta = \frac{2}{n_1+n_2} + \frac{2}{n_1-n_2} gp$$

where the following transformation has been applied:

$$(A29) \quad \int_{n_1}^{n_2} F(x, y, \eta) d\eta = \frac{2}{n_2-n_1} \sum_{j=1}^5 F(gp_j) gw_j$$

Gauss formula:

The integration in spanwise direction of the surface integrals I_1 and I_2 is carried out with the aid of the 5-point

$$(A28) \quad H(x, y) = \begin{cases} \frac{(n_1-y)^2}{4} \{ 2 \ln(\beta|n_1-y|) - 1 \} - \frac{4}{(n_1-y)^2} \{ 2 \ln(\beta|n_1-y|) - 1 \} + \frac{4}{(n_1-y)^2} \{ 2 \ln(\beta|n_1-y|) - 1 \} & n_1 \geq 0 \\ \frac{(n_2-y)^2}{4} \{ 2 \ln(\beta|n_1-y|) - 1 \} - \frac{4}{(n_1-y)^2} \{ 2 \ln(\beta|n_1-y|) - 1 \} + \frac{4}{(n_1-y)^2} \{ 2 \ln(\beta|n_1-y|) - 1 \} & n_1 < 0 \end{cases}$$

$$(A27) \quad G(x, y) = (n_1-y) \ln \beta |n_1-y| - (n_1-y) \ln \beta |n_1-y| - (n_1-y) \ln \beta |n_1-y|$$

$$(A26) \quad \frac{dn}{dx} = \sum_{i=2}^f b v_i (i+1-2j) u^{i-2j} \quad n = \frac{c}{2} \{ \xi - x l(n) \} - 1$$

$$(A25) \quad \frac{d}{dx} \left(\frac{d\xi}{dx} \right) = - \frac{1}{4} \left\{ \frac{dc}{dx} \frac{d\xi}{dx} + \frac{c(n)}{4} \left[\xi - x l(n) \right] \frac{dc}{dx} + \frac{d\xi}{dx} \left[\sum_{i=2}^f i a c_i(n) \frac{dn}{dx} \right] + \frac{c(n)}{2} \sum_{i=1}^f i \frac{d a c_i(n)}{dx} \right\} V_i(n)$$

$$(A24) \quad \frac{d\xi}{dx} = \frac{2}{\sum_{i=1}^f i a c_i(n)} V_i(n)$$

Further must be determined:

$$(A23) \quad V_i = 2n V_{i-1} - V_{i-2} \quad V_0 = 0 \quad V_1 = 1$$

$$(A22) \quad V_i(n) = \sum_{j=1}^f b v_j u^{i+1-2j}$$

The coefficients $b v_j$ are determined from the recurrence relations for

$$(A21) \quad \begin{aligned} In_0 &= \ln \frac{n_0-n_1 + \sqrt{(n_0-n_1)^2 - B^2}}{n_0-n_1 + \sqrt{(n_0-n_1)^2 - B^2}} \\ In_1 &= \sqrt{(n_0-n_1)^2 - B^2} - \sqrt{(n_0-n_1)^2 - B^2} - B^2 + n_1 In_0 \end{aligned}$$

$$(p+1) In_{p+1} - (2p+1) n_1 In_p + (n_1^2 - B^2) p In_{p-1} = u b^p \sqrt{(n_0-n_1)^2 - B^2} - u_0^p \sqrt{(n_0-n_1)^2 - B^2}$$

The integrals In_p are determined from the recurrence relation:

At last σ must be determined from:

$$\sigma(\xi \cdot \eta) = \sum_{i=0}^n ac_i(\eta) T_i(u) \quad (\text{A33})$$

$$T_i(u) = \sum_{j=1}^{(i+2) \div 2} bt_{ij} u^{i+2-2j} \quad (\text{A34})$$

The coefficients bt_{ij} are determined from the recurrence relation for T_i :

$$T_i = 2uT_{i-1} - T_{i-2} \quad T_0 = 1 \quad T_1 = u \quad (\text{A35})$$

u is given by eq. (A26) again.

The coefficients $ac_i(\eta)$ of eq. (A33) will be determined by means of quadratic interpolation from:

$$ac_i(\eta) = ap(1, i, k) \{\eta - ygs(k)\}^2 + ap(2, i, k) \{\eta - ygs(k)\} + ap(3, i, k) \quad (\text{A36})$$

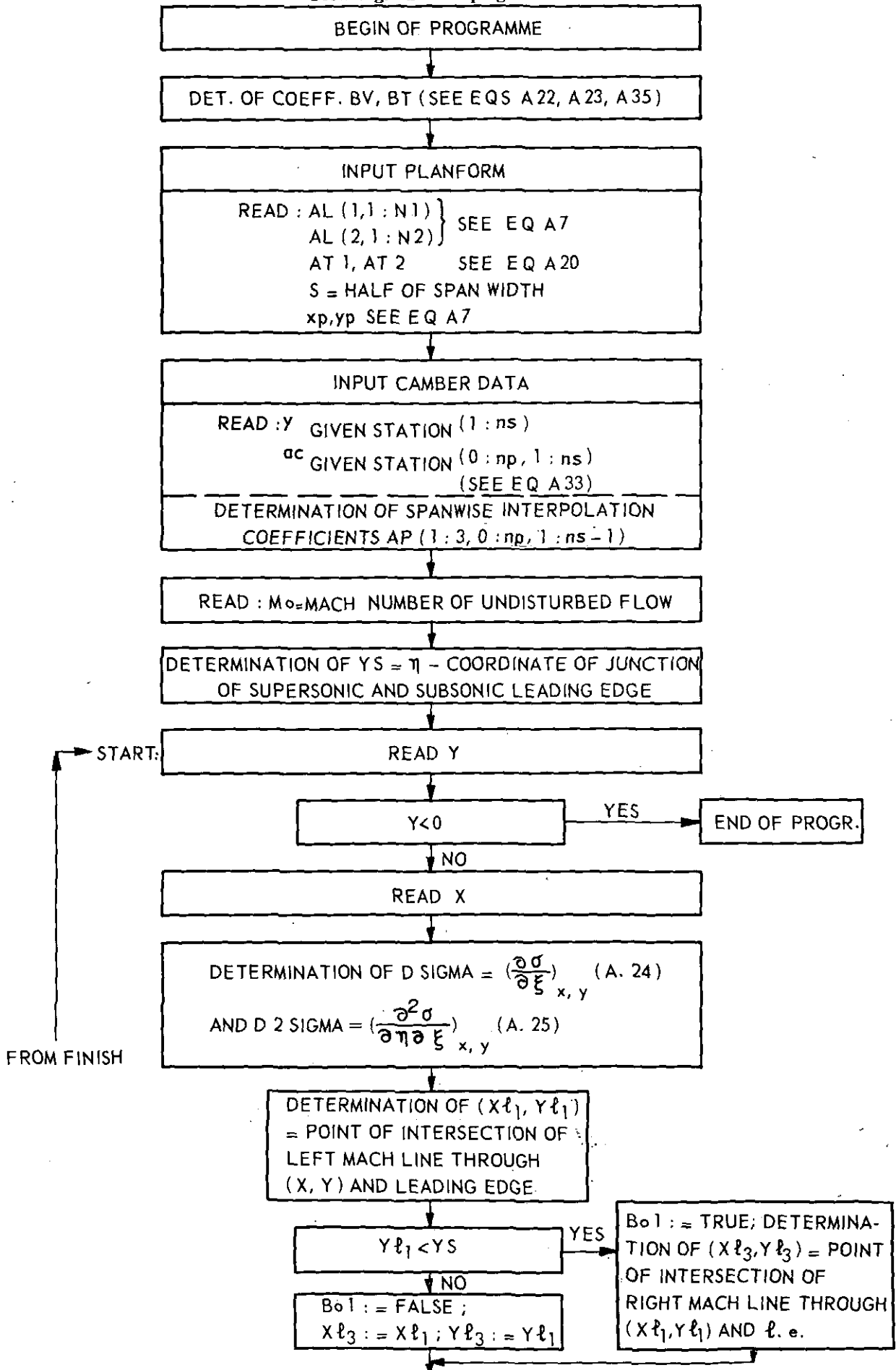
where ap is given by:

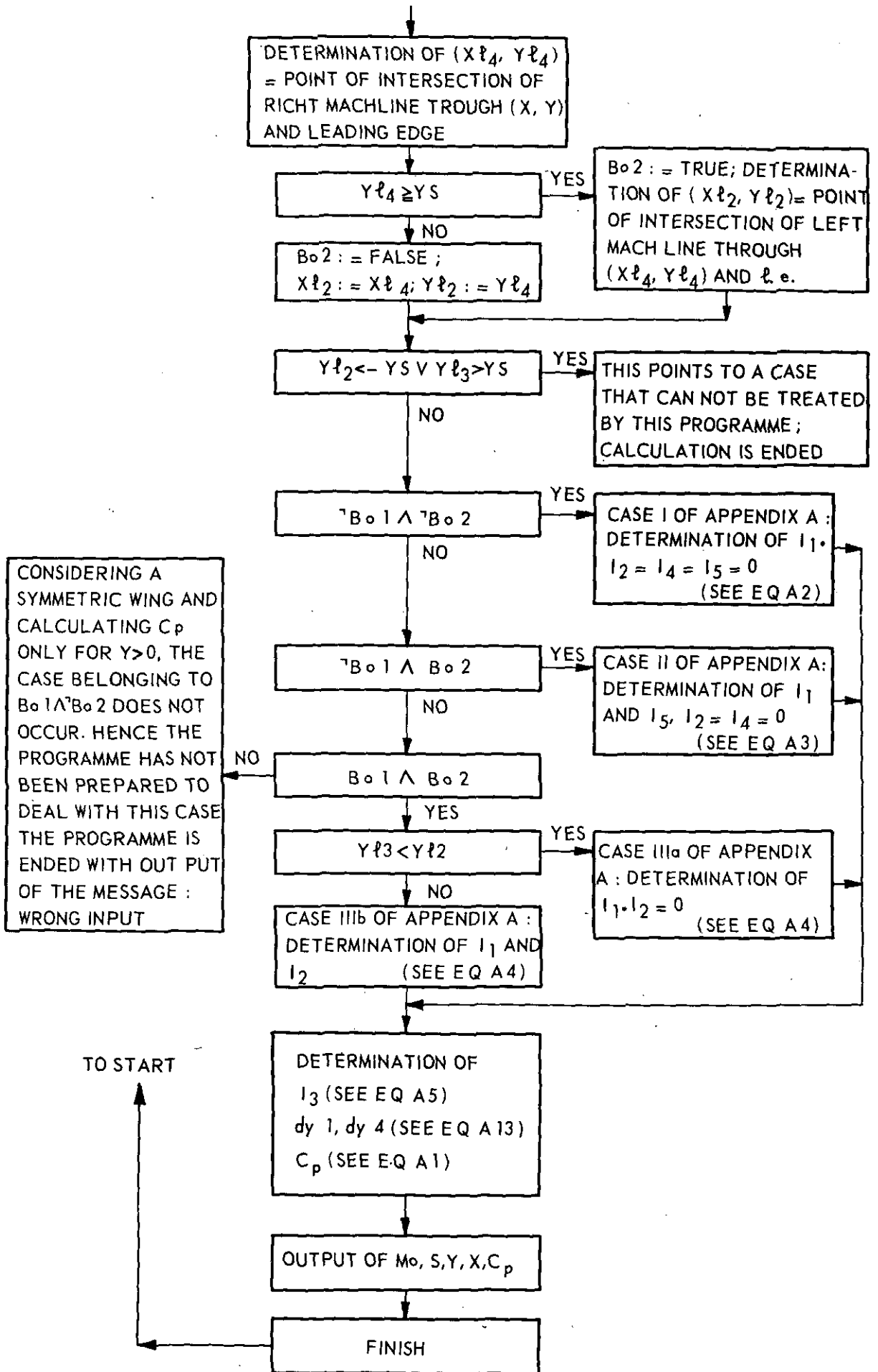
$$\begin{aligned} ap(1, i, k) &= \left\{ \frac{acgs(i, k+1) - acgs(i, k)}{ygs(k+1) - ygs(k)} \quad \frac{acgs(i, k) - acgs(i, k-1)}{ygs(k) - ygs(k-1)} \right\} \frac{1}{ygs(k+1) - ygs(k-1)} \\ ap(2, i, k) &= \frac{acgs(i, k+1) - acgs(i, k)}{ygs(k+1) - ygs(k)} - ap(1, i, k) \{ygs(k+1) - ygs(k)\} \\ ap(3, i, k) &= acgs(i, k) \end{aligned} \quad (\text{A37})$$

$ygs(k)$ denotes the η -coordinate of the given spanwise station nearest to η . $acgs(i, k)$ denotes the coefficients of the Chebyshev polynomials belonging to $ygs(k)$.

In this way a complete survey of all the formulae used in the Algol program has been given.

APPENDIX B
Flowdiagram of the program





APPENDIX C

The Algol program

```

begin comment progr. S.9, Determination of lift field for symmetric wing
with partly subsonic, partly supersonic leading edge
and a supersonic trailing edge: the subsonic regions may
not interact - MC-procedures ZERO(AP230) and XEEN are used
in this program
integer ni,nmax, n1,n2,np,n,i,j,ns,k;
readn(ni,n1,n2,np,ns);
nmax:= if n1>n2 then n1 else n2;
begin real p1,s,xp,yp,x,y,x0,yo,xb,dy1,dy2,dy3,be,mon,dxp,ys,c,dsigma,
d2sigma,dy4, eta, cp;
boolean Bo1,Bo2,Bo3,Bo4,Bo5;
array xl,y1,y1,gp,gw,int[1:5],at,e[1:2],
al[1:2,0:nmax],bv[0:np+2,1:2+(np+1):2],bt[0:np+1,1:1+(np+2):2],
in[0:np],ac,dac[0:np],acgs[0:np,0:ns],ygs[0:ns],
ap[1:3,0:np,0:ns];

real procedure ZERO(x, a, b, fx, e); value a, b; real x, a, b, fx; array e;
begin real c, fa, fb, fc, m, i, tol, re, ae;
re:=e[1]; ae:=e[2];
x:=a; fa:=fx; x:=b; fb:=fx; goto entry;
goon: if abs(1 - b)< tol then i:=b + sign(c - b) × tol;
x:= if sign(i - m)=sign(b - i) then i else m;
a:=b; fa:=fb; b:=x; fb:=fx;
entry: if sign(fc)=sign(fb) then
begin c:=a; fc:=fa end;
if abs(fb)>abs (fc) then
begin a:=b; fa:=fb; b:=c; fb:=fc; c:=a; fc:=fa end;
m:=(b + c)/2;
i:= if fb - fa ≠ 0 then(a × fb - b × fa)/(fb - fa) else m;
tol:=abs(b × re) + ae;
if abs(m - b) > tol then goto goon;
ZERO:=x:=b
end ZERO;

real procedure xle(y); value y; real y;
begin real ya,sum; integer k,n,i;
ya:=abs(y);
if ya<yp ∨ 7 Bo4 then begin k:=1; n:=n1 end
else begin k:=2; n:=n2 end;
sum:=al[k,n];
for i:=n-1 step -1 until 0 do
sum:=sum×ya+al[k,i];
xle:=sum
end;

real procedure dxl(y); value y;real y;
begin real ya, sum; integer k,n,i;
ya:=abs(y);
if ya<yp+9 then begin k:=1; n:=n1 end else
begin k:=2; n:=n2 end;
sum:=n×al[k,n];
for i:=n-1 step -1 until 1 do
sum:=sum×y+ixal[k,i];
dxl:=sign(y)×sum;
end;

```

```

real procedure xte(y); real y;
xte:=at[1]+at[2]*abs(y);
real procedure dxt(y); real y;
dxt:=at[2]*sign(y);
procedure estac(eta,derac); real eta; boolean derac;
begin real y,dy; integer i,k;
y:=abs(eta);
for i:=0 step 1 until ns-1 do
begin if ygs[i]<y/v<ygs[i+1] then
begin k:= if ygs[i+1]-y>y-ygs[i] then i else i+1;
if k=ns then k:=ns-1;
if k=0 then k:=1; goto la
end
end;
la: dy:=y-ygs[k];
for i:=0 step 1 until np do
begin ac[i]:=(ap[1,i,k]*dy+ap[2,i,k])*dy+ap[3,i,k];
if derac then dac[i]:=2*ap[1,i,k]*dy+ap[2,i,k]
end
end;
real procedure intersl(a,b,xi,yb); value a,b,yb; real a,b,xi,yb;
begin real y,y1,xip1,xip2,y1,y2;
integer si;
si:=sign(b); xip1:=a+b*si*xyp; xip2:=a-b*si*xyp;
y1:= if a<0 ^ xip1<xp ^ abs(b)>dxp then
si*xyp else (if a>0 ^ xip1>xp ^ xip2>xp then -si*xyp else 0);
y2:= if a<0 then (if xip1<xp then yb-si*xp-10 else si*xyp)
else (if xip1>xp ^ xip2>xp then -si*xs else -si*xyp);
if a>0 ^ xip1>xp ^ xip2>xp ^ 7Bo4 then
begin xi:=xip2; yi:=s end else
begin yi:=ZERO(y,y1,y2,xle(y)-a-b*x,y,e); xi:=xle(y1)
end;
intersl:=yi
end;
procedure dercamber(ksi,eta); real ksi,eta;
begin real u,xl,c,vi,dvi,dx,dc,sum1,sum2,u2;
integer i,j,n;
xl:=xle(eta); c:=xte(eta)-xl;
u:=2*(ksi-xl)/c-1;
sum1:=sum2:=0; u2:=u^2;
for i:=1 step 1 until np do
begin n:=(i+1):2; vi:=bv[i,1];
for j:=2 step 1 until n do
vi:=bv[i,j]+vi*xu2;
vi:=vi*xu^(i+1-2*xn);
sum1:=sum1+i*ac[i]*vi;
sum2:=sum2+i*dac[i]*vi;
end;
dsigma:=2*sum1/c; sum1:=0;
for i:=2 step 1 until np do
begin n:=i:2; dvi:=(i-1)*bv[i,1];
for j:=2 step 1 until n do
dvi:=dvi*xu2+bv[i,j]*x(i+1-2*xj);
dvi:=dvi*xu^(i-2*xn);
sum1:=sum1+i*ac[i]*dvi;
end;
dx:=dxl(eta); dc:=dxt(eta)-dx;
d2sigma:=(-dc*dsigma-4*x((ksi-xl)/cxdc+dx)/cxsum1+2*sum2)/c;
end;

```

```

procedure chebint(xo,xb,xl,c,eta); real xo,xb,xl,c,eta;
begin integer i,j,n;
real u1,u0,ub,A,B,C,D,sum;
array int[0:np+1];
u1:=2*(x-xl)/c-1; u0:=2*(xo-xl)/c-1;
ub:=2*(xb-xl)/c-1;
B:=abs(2*bx*(y-eta)/c);
A:=sqrt((u0-u1)^2-B^2);
D:= if abs(ub+B-u1)< 10^-7 then 0 else sqrt((ub-u1)^2-B^2);
C:=u1^2-B^2;
int[0]:=ln(abs((ub-u1+D)/(u0-u1+A)));
int[1]:=D-A+u1*int[0];
for i:=1 step 1 until np-1 do
int[i+1]:=(ub^i*D-u0^i*A+(2^i+1)*u1*int[i]-C^i*int[i-1])/(i+1);
for i:=1 step 1 until np do
begin sum:=0;n:=(i+1):2;
for j:=1 step 1 until n do
sum:=sum+bv[i,j]*int[i+1-2*j];
in[i]:=sum
end;
end;
real procedure surfint(iy,xoy,xby,k); real iy,xoy,xby;
integer k;
begin integer q,i,j,p;
real yyo,yyb,sum1,sum2,yo,yb,hs,hd,ciy,xl,sum3,G,H;
sum1:=0;
for i:=1 step 1 until k do
begin yyo:=yi[i]; yyb:=yi[i+1];
for q:=1 step 1 until ni do
begin yo:=yyo+(q-1)*(yyb-yyo)/ni;
yb:=yyo+q*(yyb-yyo)/ni;
hs:=0.5*(yo+yb); hd:=0.5*(yb-yyo);
sum2:=0;
for j:=1 step 1 until 5 do
begin iy:=hs+hd*gp[j]; xl:=xle(iy); ciy:=xte(iy)-xl;
xo:=xoy; xb:=xby; chebint(xo,xb,xl,ciy,iy);
estac(iy,false); sum3:=0;
for p:=1 step 1 until np do
sum3:=sum3+pxac[p]*in[p];
sum2:=sum2+gw[j]*(2*sum3/ciy+( if Bo3 then
(dsigma+d2sigma*(abs(iy)-y))*ln(bxabs(iy-y)) else 0));
end;
sum1:=sum1+sum2*hd;
end;
end;
end;
if Bo3 then
begin real dyb,dy0,lnb,ln0,etab,eta0;
eta0:=yi[1]; etab:=yi[k+1]; dyb:=etab-y;
dy0:=eta0-y;
lnb:=ln(bxabs(dyb)); ln0:=ln(bxabs(dy0));
G:=dyb*lnb-dy0*ln0-(etab-eta0);
H:=0.25*dyb^2*(2*lnb-1)-0.25*dy0^2*(
2*ln0-1)+( if eta0> 0 then 0 else
(eta0+y)*dy0*ln0-dy0*0.5*(eta0-3*y)+
y^2*(ln(bxy)-1.5));
sum1:=sum1-dsigma*G-d2sigma*H;
end;
surfint:=sum1
end;
end;

```

```

real procedure lineint(iy,xli,y0,yb); real iy,xli,y0,yb;
begin real xr,xq,xp,theta,eta,u,xl,hs,hd,sigma,ti,sum,u2,y1,y2;
integer i,p,n,k,m; array yi[1:3];
sum:=0;
if y0 < 0 v yb < 0 then
begin k:=2; yi[2]:=0; yi[3]:=yb end
else begin k:=1; yi[2]:=yb end; yi[1]:=y0;
for m:=1 step 1 until k do
begin y1:=yi[m]; y2:=yi[m+1];
hs:=0.5*(y1+y2); hd:=0.5*(y2-y1);
for i:=1 step 1 until 5 do
begin theta:=0.5*pi*(1+gp[i]); iy:=hs+hd*cos(theta);
xr:=x-bx*(y-iy); xq:=x+bx*(y-iy); xp:=xli;
estac(iy,false); xl:=xle(iy); u:=2*(xp-xl)/(xte(iy)-xl)-1;
sigma:=0; u2:=u^2;
for p:=0 step 1 until np do
begin ti:=bt[p,1]; n:=(p+2):2;
for j:=2 step 1 until n do
ti:=ti*u2+bt[p,j];
sigma:=sigma+ac[p]*ti*u^(p+2-2*n);
end;
sum:=sum+hd*pi*0.5*gw[i]*sigma*sin(theta)/sqrt((xr-xp)*(xq-xp));
end;
end;

end;
lineint:=sum

end;
pi:=3.1415926536;
bv[1,1]:=1; bv[2,1]:=2; bv[2,2]:=0;
for i:=3 step 1 until np do
begin bv[i,1]:=2*bv[i-1,1];
n:=(i+1):2;
for j:=2 step 1 until n do
bv[i,j]:=2*bv[i-1,j]-bv[i-2,j-1];
bv[i,n+1]:=0;
end;
bt[0,1]:=1; bt[1,1]:=1; bt[1,2]:=0;
for i:=2 step 1 until np do
begin bt[i,1]:=2*bt[i-1,1];
n:=(i+2):2;
for j:=2 step 1 until n do
bt[i,j]:=2*bt[i-1,j]-bt[i-2,j-1];
bt[i,n+1]:=0;
end;
begin comment input planform;
for i:=0 step 1 until n1 do al[1,i]:=read;
for i:=0 step 1 until n2 do al[2,i]:=read;
readn(at[1],at[2],s,xp,yp);
Bo4:=abs(s-yp)/s > 1-10;
end;

```

```

begin comment input camber-data and determination
of spanwise interpolation coefficients;
for i:=0 step 1 until ns do
begin ygs[1]:=read;
for j:=0 step 1 until np do acgs[j,1]:=read end;
for i:=1 step 1 until ns-1 do
begin dy1:=ygs[i+1]-ygs[i];
dy2:=ygs[i]-ygs[i-1]; dy3:=dy1+dy2;
for j:=0 step 1 until np do
begin c:=(acgs[j,i+1]-acgs[j,i])/dy1;
ap[1,j,1]:=(c-(acgs[j,i]-acgs[j,i-1])/dy2)/dy3;
ap[2,j,1]:=c-ap[1,j,1]*dy1;
ap[3,j,1]:=acgs[j,i];
end
end
end;
e[1]:=p-8; e[2]:=p-6;
mon:=read; be:=sqrt(mon^2-1);
dpx:=dxl(yp-p-10);
ys:=if dpx>be then ZERO(y,0,yp,dxl(y)-be,e) else
ZERO(y,yp,s,dxl(y)-be,e);
gp[5]:=0.906179845939; gp[1]:=-gp[5];
gw[1]:=gw[5]:=0.236926885056;
gp[4]:=0.538469310105;
gp[2]:=-gp[4];
gw[2]:=gw[4]:=0.478628670499;
gp[3]:=0; gw[3]:=0.568888888889;
if KEEN(-0)=1 then
begin PUTEXT('Intermediate results of S9');
for i:=1 step 1 until np do
begin PUNLCR;
for j:=1 step 1 until (i+1):2 do FIXP(10,0,bv[i,j]);
end; PUNLCR; PUNLCR;
for i:=0 step 1 until np do
begin PUNLCR;
for j:=1 step 1 until (i+2):2 do FIXP(10,0,bt[i,j]);
end; PUNLCR; PUNLCR;
for i:=1 step 1 until ns-1 do
begin PUNLCR;
for j:=0 step 1 until np do
begin PUNLCR; for k:=1,2,3 do
FLOP(9,2,ap[k,j,1]);
end
end; PUNLCR; PUNLCR;
FLOP(9,2,ys);
end;
start:
y:=read; if y<0 then stop;x:=read;
estac(y,true); dercamber(x,y);
if KEEN(-0)=1 then
begin PUNLCR; PUNLCR; FLOP(9,2,dsigma); FLOP(9,2,d2sigma);
for i:=0 step 1 until np do
begin PUNLCR; FLOP(9,2,ac[i]);
FLOP(9,2,dac[i]);
end
end;
yl[1]:=intersl(x-bexy,be,xl[1],y);

```

```

if y1[1] < -ys then
begin Bo1:=true;
y1[3]:=interal(x1[1]+bexy1[1],-be,x1[3],y1[1]);
end else
begin Bo1:=false;
y1[3]:=y1[1]; x1[3]:=x1[1]; end;
y1[4]:=interal(x+bexy,-be,x1[4],y);
if y1[4]>ys∨abs(y1[4]-ys)<ε-10 then
begin Bo2:=true;
y1[2]:=interal(x1[4]-bexy1[4],be,x1[2],y1[4]);
end else
begin Bo2:=false;
x1[2]:=x1[4]; y1[2]:=y1[4] end;
if y1[2] < -ys ∨ y1[3]>ys then
begin PRINTTEXT(⊥Wrong machnumber⊥);
goto finish end;
if XEEN(-0)=1 then begin PUNLCR; PUNLCR;
for i:=1,2,3,4 do FLOP(12,2,y1[1]); end;
if ¬Bo1∧¬Bo2 then
begin y1[1]:=y1[1];
y1[2]:=y; y1[3]:=y1[4]; Bo3:=true;
int[1]:=surfint(eta,xle(eta),x-bexabs(y-eta),2);
int[2]:=int[4]:=int[5]:=0;
end else
if ¬Bo1∧Bo2 then
begin y1[1]:=y1[1]; y1[2]:=
if y<y1[2] then y else y1[2];
y1[3]:= if y<y1[2] then y1[2] else y;
y1[4]:=y1[4]; Bo3:=true;
int[1]:=surfint(eta,( if eta<y1[2] then xle(eta)
else x1[4]-bex(y1[4]-eta)),x-bexabs(y-eta),3);
int[2]:=int[4]:=0;
int[5]:=lineint(eta,x1[4]-bex(y1[4]-eta),y1[2],y1[4]);
end else
if Bo1∧Bo2 then
begin if y1[3]<y1[2] then
begin y1[1]:=y1[1]; y1[2]:=y1[3];
y1[3]:= if y1[2]<y then y1[2] else y;
y1[4]:= if y1[2]<y then y else y1[2];
y1[5]:=y1[4]; Bo3:= true;
int[1]:=surfint(eta, if eta<y1[3] then
x1[1]+bex(y1[1]-eta) else if eta<y1[2]
then xle(eta) else x1[4]-bex(y1[4]-eta),
x-bexabs(y-eta),4);
int[2]:=0;
end else
begin y1[1]:=y1[1];
y1[5]:=(x1[1]-x1[4]+bex(y1[1]+y1[4]))/(2×be);
y1[2]:=if y1[5]<y then y1[5] else y;
y1[3]:=if y1[5]<y then y else y1[5];
y1[4]:=y1[4]; Bo3:=true;
int[1]:=surfint(eta, if eta<y1[5] then
x1[1]+bex(y1[1]-eta) else
x1[4]-bex(y1[4]-eta),x-bexabs(y-eta),3);
y1[1]:=y1[2]; y1[2]:=y;y1[3]:=y1[3]; Bo3:=false;
int[2]:=surfint(eta, xle(eta), if eta<y1[5] then
x1[4]-bex(y1[4]-eta) else
x1[1]+bex(y1[1]-eta),2);

```

```

end;
int[4]:=lineint(eta,xl[1]+be*(yl[1]-eta),yl[1],yl[3]);
int[5]:=lineint(eta,xl[4]-be*(yl[4]-eta),yl[2],yl[4]);
end else begin PRINTTEXT(⟨ wrong input ⟩); goto finish end;
int[3]:=lineint(eta,xle(eta),yl[2],yl[3]);
dy1:= if xl[1]> xp ^ 7 Bo4 then 0 else
      be/dxl(yl[1]);
dy4:= if xl[4]> xp ^ 7 Bo4 then 0 else
      be/dxl(yl[4]);
cp:=2*(int[1]-int[2]-int[3]+2*dy1/(1+dy1)*
int[4]+2*dy4/(1+dy4)*int[5])/pi;
if XEEN(-0)=1 then
begin PUNLCR; PUNLCR;
for i:=1,2,3,4,5 do begin PUNLCR;
FLOP(12,2,int[i]); FLOP(12,2,yl[i]); end;
PUNLCR; FLOP(12,2,dy1); FLOP(12,2,dy4);
end;
PUNLCR; PUNLCR; PUNLCR;
PUTEXT1(⟨ results of S9 ⟩); PUNLCR; PUNLCR;
PUTEXT1(⟨ Mon= ⟩); FIXP(1,4,mon);
PUTEXT1(⟨ s= ⟩); FLOP(9,2,s); PUNLCR;
PUTEXT1(⟨ y= ⟩); FLOP(9,2,y);
PUTEXT1(⟨ x= ⟩); FLOP(9,2,x);
PUTEXT1(⟨ Cp= ⟩); FLOP(12,2,cp);
finish:
goto start
end; S9:
end
end

```

APPENDIX D

Survey of the formulae used to obtain analytical results

The F 104 wing

The camber distribution is given by $\sigma(x, y) = \text{constant}$ and the representation of the leading edge by $x_l(y) = \alpha|y|$ for $0 \leq |y| \leq s$ $s = \text{semi span}$.

At the chosen Mach number $M_0 = 2$ two of the three cases described in app. A arise, namely:

case I to which the following formulae apply:

$$\frac{d\varphi}{dx} = \begin{cases} -\frac{\sigma}{\sqrt{\beta^2 - \alpha^2}} & \text{when } \beta y - x \geq 0 \\ -\frac{\sigma}{\sqrt{\beta^2 - \alpha^2}} + \frac{2\sigma}{\pi\sqrt{\beta^2 - \alpha^2}} \tan^{-1} \left\{ \frac{\alpha}{x} \sqrt{\frac{x^2 - \beta^2 y^2}{\beta^2 - \alpha^2}} \right\} & \text{when } \beta y - x \leq 0 \end{cases} \quad (D1)$$

case II to which the following formulae apply:

$$\frac{d\varphi}{dx} = \begin{cases} -\frac{\sigma}{\pi\sqrt{\beta^2 - \alpha^2}} \cos^{-1} \left\{ \frac{x + \alpha(y - 2s) - 2\beta(y - s)}{x - \alpha y} \right\} & \text{when } \beta y - x \geq 0 \\ -\frac{\sigma}{\pi\sqrt{\beta^2 - \alpha^2}} \cos^{-1} \left\{ \frac{x + \alpha(y - 2s) + 2\beta(y - s)}{x - \alpha y} \right\} + \frac{2\sigma}{\pi\sqrt{\beta^2 - \alpha^2}} \tan^{-1} \left\{ \frac{\alpha}{x} \sqrt{\frac{x^2 - \beta^2 y^2}{\beta^2 - \alpha^2}} \right\} & \text{when } \beta y - x \leq 0 \end{cases} \quad (D2)$$

The rectangular wing

The camber distribution is given by $\sigma(x, y) = ax^2 + bx + c$ $0 \leq x \leq 1$ and the leading edge by $xl(y) = 0$ $0 \leq |y| \leq 1$.

At the chosen Mach number $M_0 = \sqrt{2}$ case I and case II of app. A arise again. For case I the following formula is valid:

$$\frac{d\varphi}{dx} = -\frac{1}{\beta}(ax^2 + bx + c) \quad (\text{D3})$$

and for case II:

$$\frac{d\varphi}{dx} = -\frac{1}{\pi\beta}(ax^2 + bx + c) \cos^{-1}(1-2t) + \frac{1}{\pi\beta} \left\{ \frac{2}{3}(2t-5)ax^2 - 2bx \right\} \sqrt{t(1-t)} \quad t = \frac{\beta(s-y)}{x} \quad (\text{D4})$$

REPORT NLR-TR 68069 U

Binary flutter calculations with theoretical and empirical aerodynamic derivatives for a wing-control surface system in two-dimensional incompressible flow

by

H. Bergh and H. Tijdeman

Summary

A number of comparative flutter calculations for a two-dimensional wing-control surface system has been performed to demonstrate the usefulness of empirical formulae for the control surface derivatives.

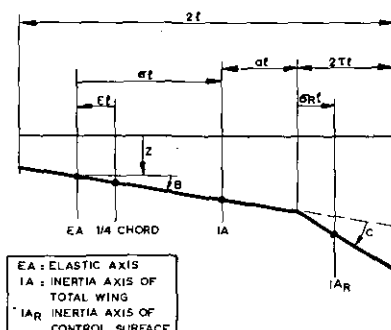
Furthermore attention has been paid to the influence of the chord ratio τ on the flutter behaviour and to the sensitivity of the system to each of the aerodynamic derivatives.

This investigation has been performed under contract for the Netherlands Aircraft Development Board (N.I.V.).

Contents	page	List of symbols
List of symbols	1	A_{ij} empirical coefficients, defined in appendix A
1 Introduction	2	
2 The experimental aerodynamic forces	3	A dimensionless translation amplitude at $\frac{1}{4}$ chord point
2.1 Short description of windtunnel tests	3	
2.2 Results	3	a dimensionless distance between inertia axis and hinge axis
2.3 Empirical formulae for control surface derivatives	3	$B_{1,2}$ empirical coefficients, defined in Appendix A
2.4 Approximations for plain wing derivatives	5	
3 Comparative flutter calculations with measured, approximated and theoretical aerodynamic derivatives	5	C amplitude of control surface rotation $c = 2l$ wing chord
4 Stability diagrams for various chord ratios τ	6	h amount of hysteresis damping
5 Influence of each aerodynamic derivative on the critical speed	7	K normal force, defined in Appendix A k_a } normal force derivatives, defined in Appendix A k_b } k_c }
6 Stability of the wing torsion-control surface rotation system at large values of the reduced frequency	7	l semi wing chord $M_{\frac{1}{4}}$ moment of wing about $\frac{1}{4}$ chord point
7 Conclusions	8	$m = \mu\pi\rho l^2$ mass of total wing
8 References	8	$m_R = \mu_R\pi\rho l^2$ mass of control surface
Appendix A		m_a } moment derivatives for the wing, defined in Appendix A m_b } m_c }
Appendix B		N moment of control surface about hinge axis
6 tables		
37 figures		

n_a	moment derivatives for control surface, defined in Appendix A	v_B	uncoupled wing bending frequency
n_b		v_c	uncoupled wing torsion frequency
n_c		v_T	uncoupled control surface rotation frequency
r_e	normal force derivative for control surface	ρ	air density
$S = \left(\frac{k_{cE}}{k_{cT}} \right)_{\omega=0}$		σ	dimensionless distance between $\frac{1}{4}$ chord axis and inertia axis of wing
V	air speed	σ_R	dimensionless distance between hinge axis and inertia axis of control surface
x	co-ordinate in chordwise direction	τ	ratio of control surface chord to total wing chord
ϵ	dimensionless distance between elastic axis and $\frac{1}{4}$ chord axis	$\omega = \frac{vl}{V}$	reduced frequency
κ	dimensionless radius of inertia of total wing	subscripts:	
κ_R	dimensionless radius of inertia of control surface	E	experimental
$\mu = \frac{m}{\pi \rho l^2}$	wing mass ratio	T	theoretical
$\mu_R = \frac{m_R}{\pi \rho l^2}$	control surface mass ratio	superscripts:	
ν	frequency of oscillation	*	without still air reactions
		'	real part
		"	imaginary part

MODEL GEOMETRY



1 Introduction

In conclusion of an extensive experimental programme conducted to determine aerodynamic derivatives for wings in two-dimensional incompressible flow, a systematic series of unsteady pressure measurements was carried out on various wing-control surface combinations (ref. 1). To reduce scale effects, these tests were performed at highest possible Reynolds numbers, ranging from 2 to 8 million.

An analysis of the test results revealed that for the reduced frequency range considered, the measured aerodynamic derivatives for various control surface chord ratios could be approximated rather well by empirical relations (ref. 2). As certain discrepancies still remain, an assessment of their influence on the flutter behaviour was necessary.

The main purpose of the present report is to demonstrate the usefulness of the empirical expressions for the control surface derivatives. This has been achieved by performing a number of binary flutter calculations for a two-dimensional wing-control surface system, using either measured or empirical aerodynamic derivatives. The flutter calculations have also been performed with purely theoretical derivatives to demonstrate the influence which the differences between experiment and theory have on the critical speed. Attention has been paid to the influence of the relative chord ratio τ and to the sensitivity of the system to each of the aerodynamic derivatives.

For the sake of completeness a short description of the unsteady pressure measurements reported in ref. 1, and the final results of that investigation, have been included in the report.

2 The experimental aerodynamic forces

2.1 Short description of the wind tunnel tests

Since important discrepancies were found to exist between control surface derivatives, measured on similar models at various Reynolds numbers (ref. 3), it was decided to conduct a new series of measurements at sufficiently high values of the Reynolds number. The main aim of these tests was the determination of aerodynamic derivatives for control surfaces of various chord ratios. To make the information as complete as possible detailed instantaneous pressure distributions were required. These have been obtained by employing the NLR pressure measuring technique (ref. 4).

The tests were conducted in the NLR low speed windtunnel LST, having a test section of $2 \times 3 \text{ m}^2$. Three rectangular models were used (fig. 1), which spanned the test section from top to bottom.

Model I representing a wing with a 40 percent control surface, was almost identical to the model described in ref. 3. It only differed from the latter one in that the original convex shape (NACA 0012) of the control surface was modified into a straight contour. The total wingchord was 0.82 m.

Model II consisted of a new wing part, followed by the rearward 80 percent of model I, provided with a semi-circular nose part. The total chord of the new combination was 1.64 m, the profile being almost identical to NACA 16009 with maximum thickness reduced to 6.5 percent. This model may be considered to represent a wing with a 40 percent control surface and a 20 percent tab.

Model III was derived from model II by inserting a rectangular piece of 0.23 m length at the point of maximum thickness, thus obtaining a wing of 1.87 m chord with a 35 percent control surface and a 17.5 percent tab.

The modes of vibration of these models are shown in fig. 2. For various values of reduced frequency ω and for Reynolds numbers between 2 and 8 million (see fig. 3), pressure distributions were measured on the three models oscillating in these modes. The limit values for $\omega \rightarrow 0$ were deduced from stationary tests, while the limit values for $\omega \rightarrow \infty$ were measured directly in still air.

The experimental results were corrected for tunnelwall interference, using an extension of the theory developed in ref. 5. In an attempt to account for the differences between experimental and theoretical pressure distributions, the ratio between local pressure coefficients with and without tunnelwalls was assumed to be equal in theory and experiment.

2.2 Results

From tests at various amplitudes it could be concluded, that the local pressures showed a good linearity with the vibration amplitudes, even near the trailing edge. Measurements on the same configuration at Reynolds numbers between 2 and 8 million did not show a systematic influence of this parameter.

Compared with the limiting case $\omega \rightarrow \infty$ of the incompressible flow theory (ref. 6), the results of still air tests were in close agreement as far as the real part was concerned. In the still air tests always a small imaginary part was measured, which is not predicted by the theory for incompressible flow. This may be due to the fact that the infinitely large propagation speed of small disturbances, assumed in the above mentioned theory, is not an adequate representation of what actually happens at zero airspeed.

On model I pressure distributions were measured corresponding to plain wing rotation about axes at 20 and 40 percent of the chord (see fig. 2). The results have been used to derive the pressure distributions for pure translation and rotation about the quarter chord axis. In order to avoid difficulties from experimental scatter in this separation process, use has been made of a similar correction matrix as described in ref. 7.

The final results for the pressure distributions are given in figs. 4 to 15. The presented values include the still air reactions. Compared with theory, the measured local pressures are generally smaller, except for the real parts in case of pure translation.

The aerodynamic derivatives, obtained by integration of the pressure distributions, are presented in figs. 16 to 21 and in the tables 1 to 3. As could be expected from the pressure distributions, the measured values are generally smaller than the theoretical predictions.

A comparison of results for model I, obtained by direct pressure measurements (ref. 3) and by the special technique used in the present tests, (described in ref. 4) is made in fig. 22. The mutual agreement is very satisfactory.

For tables 1, 2 and 3 see next page.

2.3 Empirical formulae for control surface derivatives

An analysis of the aerodynamic derivatives without still air reactions revealed a surprisingly good phase relation between theoretical and experimental results. Furthermore the ratio between the theoretical and the experimental pressure amplitudes appeared to be rather independent on the type of derivative and on the reduced frequency, although it differed from its static value.

TABLE 1
Measured aerodynamic wing derivatives.

ω	k'_a	k''_a	m'_a	m''_a	k'_b	k''_b	m'_b	m''_b
0	0	0	0	0	1.4500	0	-0.0461	0
0.20	0.0248	0.2082	-0.0249	-0.0058	1.0870	0.0073	-0.0467	0.1442
0.40	-0.0485	0.3577	-0.0879	-0.0100	0.9327	0.3252	-0.0874	0.2610
0.60	-0.2206	0.4975	-0.1896	-0.0141	0.8072	0.6345	-0.1586	0.3790
0.80	-0.4831	0.6360	-0.3306	-0.0183	0.6676	0.9323	-0.2589	0.4976
1.00	-0.8320	0.7749	-0.5109	-0.0225	0.5009	1.2220	-0.3880	0.6167

TABLE 2
Measured aerodynamic control surface derivatives ($\tau = 0.20$)

ω	k'_c	k''_c	m'_c	m''_c	n'_c	n''_c
0	0.79	0	0.039	0	0.017	0
0.40	0.389	-0.005	0.310	0.044	0.011	0.005
0.60	0.370	0.005	0.308	0.063	0.011	0.007
0.80	0.368	0.051	0.308	0.099	0.011	0.010
1.00	0.390	0.077	0.327	0.132	0.011	0.013
1.20	0.327	0.118	0.271	0.151	0.009	0.015
1.50	0.294	0.208	0.235	0.216	0.005	0.018

Measured aerodynamic control surface derivatives ($\tau = 0.175$).

ω	k'_c	k''_c	m'_c	m''_c	n'_c	n''_c
0	0.72	0	0.34	0	0.012	0
0.52	0.322	0.018	0.284	0.050	0.008	0.004
0.78	0.336	0.044	0.297	0.086	0.009	0.007
1.04	0.316	0.065	0.282	0.104	0.008	0.008
1.30	0.309	0.114	0.282	0.145	0.008	0.011
1.56	0.241	0.200	0.202	0.197	0.004	0.013
1.95	0.249	0.254	0.209	0.245	0.004	0.016

TABLE 3
Measured aerodynamic control surface derivatives ($\tau = 0.4$).

ω	n'_a	n''_a	n'_b	n''_b	k'_c	k''_c	m'_c	m''_c	n'_c	n''_c
0	0	0	0.04074	0	1.31	0	0.35	0	0.082	0
0.20	-0.00335	0.00593	0.02715	0.02052	0.826	-0.014	0.316	0.081	0.049	0.019
0.40	-0.01685	0.01019	0.01205	0.04798	0.761	0.073	0.319	0.164	0.050	0.066
0.60	-0.04058	0.01415	-0.00925	0.07530	0.690	0.208	0.291	0.251	0.038	0.039
0.80	-0.07433	0.01807	-0.03795	0.10230	0.676	0.375	0.261	0.336	0.035	0.088
1.00	-0.11800	0.02198	-0.07443	0.12910	0.583	0.449	0.236	0.395	0.027	0.109

Measured aerodynamic control surface derivatives ($\tau = 0.35$).

ω	k'_c	k''_c	m'_c	m''_c	n'_c	n''_c
0	0.99	0	0.33	0	0.051	0
0.52	0.464	0.109	0.248	0.143	0.026	0.028
0.78	0.407	0.205	0.218	0.215	0.017	0.048
1.04	0.397	0.341	0.194	0.301	0.009	0.065
1.30	0.342	0.450	0.135	0.398	-0.008	0.085
1.56	0.289	0.582	0.089	0.445	-0.014	0.097
1.95	0.233	0.772	-0.003	0.638	-0.043	0.139

Finally a correlation was observed between the mentioned amplitude ratio for various models and the static value of the ratio between measured and theoretical mean pressure level. The mentioned observations could be described by the following empirical relations between the flow dependent parts (i.e. without still air reactions) of experimental and theoretical control surface derivatives:

$$\left. \begin{aligned} k_{cE}^* &= 0.84 S \cdot k_{cT}^* \\ m_{cE}^* &= 0.84 S \cdot m_{cT}^* + 0.05 \\ n_{cE}^* &= 0.84 S \cdot n_{cT}^* \\ r_{cE}^* &= 0.84 S \cdot r_{cT}^* \end{aligned} \right\} 0.2 < \omega < 2.0$$

with

$$S = \left(\frac{k_{cE}}{k_{cT}} \right)_{\omega=0}$$

The approximate values of the derivatives with still air reactions included may simply be obtained by adding their corresponding theoretical values, because the measured still air reactions agreed well with the theoretical values.

The empirical expressions approximate the measured aerodynamic derivatives quite well, as is demonstrated for k_c , m_c and n_c in the figs. 18 to 21. Here two remarks have to be made:

- (1) The static values ($\omega=0$) do not fit in the empirical approach, so the empirical relations can only be applied within the ω -range used in the tests, being roughly $0.2 < \omega < 2.0$.
- (2) In case the factor S is derived from three-dimensional tests, it is doubtful whether the constant 0.84 is still applicable.

2.4 Approximations for plain wing derivatives

For the purpose of making systematic flutter-calculations for a wing-control surface system, it was desirable to have also approximate expressions for the aerodynamic derivatives, corresponding to plain wing translation and rotation. These were obtained by using similar formulae as given in eq. 1. As the plain wing derivatives were measured only for one wing profile, it makes little sense to express the constants into a ratio between some measured and theoretical stationary derivatives.

The expressions used to approximate the measured derivatives are given in appendix A. The good agreement is demonstrated in figs. 16 and 17.

3 Comparative flutter calculations based on measured, approximated and theoretical aerodynamic derivatives

In order to investigate whether the remaining discrepancies between measured and approximated aerodynamic derivatives would give unacceptable differences in flutter behaviour, several binary flutter cases were calculated using both types of derivatives. Also calculations with theoretical aerodynamic forces were made for reference. The flutter calculations have been performed for a two-dimensional wing-control surface system of given wing properties (elastic axis at 40% c , inertia axis at 50% c and a density ratio μ of 15).

As only one complete set of aerodynamic derivatives was measured for a wing with a control surface of 40 percent (model I), these comparative flutter calculations were restricted to this chord ratio.

For the binary cases, summarized in table 4, the variation of damping and frequency with airspeed has been calculated.

The results for *wing bending-control surface rotation* are presented in figs. 23 and 24. The points computed by applying approximated derivatives are in good agreement with those obtained with the measured quantities.

Compared with calculations with theoretical aerodynamic derivatives the results based on experimental derivatives

TABLE 4
System parameters for the comparative flutter calculations discussed in section 3.

	ε	σ	μ	κ	τ	σ_a	μ_R	κ_R	ν_c	Fig.
wing bending-control	-0.3	0.2	15	0.55	0.4	0.04	4.5	0.4	0	23
surface rotation	-0.3	0.2	15	0.55	0.4	0.04	4.5	0.4	$0.7\nu_B$	24
wing torsion-control	-0.3	0.2	15	0.55	0.4	0	4.5	0.4	0	25
surface rotation	-0.3	0.2	15	0.55	0.4	0	4.5	0.4	$0.7\nu_T$	26
	-0.3	0.2	15	0.55	0.4	0.04	4.5	0.4	0	27
	-0.3	0.2	15	0.55	0.4	0.04	4.5	0.4	$0.7\nu_T$	28

show a slightly higher critical speed in case of a free floating control surface. For the elastically clamped control surface there is little difference between the variation of damping with airspeed in both cases.

The results for *wing torsion-control surface rotation* are presented in figs. 25 to 28. In all cases considered the mutual agreement between results calculated with approximated and measured aerodynamic derivatives is satisfactory. For the elastically clamped control surface (figs. 26 and 28) the results obtained with theoretical aerodynamic derivatives show already flutter of a very mild type at very low speeds.

Summarizing, it can be stated that the empirical formulae for the control surface derivatives (section 2.3), together with the approximations for the plain wing derivatives (section 2.4) are sufficiently accurate for flutter calculations.

4 Stability diagrams for various chord ratios τ

To study the difference in flutter behaviour predicted with theoretical and experimental derivatives respectively, again binary flutter calculations have been made for a two-dimensional wing-control surface system. In this case the solutions of the characteristic equation for several values of ω have been given as stability diagrams, showing the variation of a non-dimensional flutter speed with the squared ratio of control surface frequency and wing frequency.

As the approximated aerodynamic derivatives were proved to be sufficiently accurate, they have been used to investigate a variation of the chord ratio τ in the flutter calculations. To have a consistent set of experimental aerodynamic derivatives the ratio S in the empirical expressions for the C -modes was taken equal to the value of model I ($S=0.88$). The values of the derivatives for the A - and B modes have been obtained by interpolating the corresponding coefficients A_{ij} to the chord ratio τ . The values of the coefficients A_{ij} used, are given in table 6.

The combinations investigated have been summarized in table 5.

TABLE 5
System parameters for the flutter calculations discussed in section 4.

	ε	σ	μ	κ	σ_R	μ_R	κ_R	Fig.	τ
wing bending-control surface rotation	-0.3	0.2	15	0.55	0.1τ	$0.75 \mu \tau$	τ	29	} $\tau=0.40; 0.30$ $0.20; 0.15$
wing torsion-control surface rotation	-0.3	0.2	15	0.55	0	$0.75 \mu \tau$	τ	31	
wing torsion-control surface rotation	-0.3	0.2	15	0.55	0.1τ	$0.75 \mu \tau$	τ	31	

TABLE 6
Empirical coefficients A_{ij} used for the calculations discussed in section 4.

τ	S	A_{11}	A_{31}	A_{12}	B_1	A_{22}	A_{32}	A_{13}	A_{23}	B_2	A_{33}
0.15	0.88	0.70	0.43	0.64	0.15	0.62	0.43	0.74	0.74	0.05	0.74
0.20	0.88	0.70	0.45	0.64	0.15	0.62	0.45	0.74	0.74	0.05	0.74
0.30	0.88	0.70	0.49	0.64	0.15	0.62	0.49	0.74	0.74	0.05	0.74
0.40	0.88	0.70	0.53	0.64	0.15	0.62	0.53	0.74	0.74	0.05	0.74

The results for *wing bending-control surface rotation* are presented in fig. 29.

In general, the lower flutter boundaries show remarkably small differences for all chord ratios considered, notwithstanding the rather large discrepancies between theoretical and experimental derivatives. The latter apparently have more influence on the upper boundary, which has little importance in practice.

The weakly restrained control surface has the lowest flutter speed in case of theoretical derivatives. This conclusion holds for a fairly large range of $\left(\frac{v_c}{v_B}\right)^2$ -values, depending on τ .

The foregoing is illustrated also in fig. 30, where the influence of the chord ratio τ on the critical speed is shown.

The results for *wing torsion-control surface rotation* are presented in fig. 31 for both $\sigma_R=0$ and $\sigma_R=0.1 \tau$. In these cases, there is a greater difference between the lower flutter boundaries, especially at the higher τ -values. This is clearly demonstrated in figs. 32 and 33 where the variation of the critical speed with the chord ratio τ is shown for several values of the frequency ratio $\frac{v_c}{v_\tau}$.

5 Influence of each aerodynamic derivative on the critical speed

To investigate the sensitivity of the flutter boundary to the various experimental derivatives, a number of calculations with approximated values has been performed, replacing alternatively one of them by its theoretical value. This has been restricted to wing bending-control surface rotation and wing torsion-control surface rotation both with $\tau=0.4$ and $\sigma_R=0.04$.

Wing bending-control surface rotation: The results for this case have been collected in fig. 34. To discuss the results, it should be remembered that for the degrees of freedom considered flutter mainly occurs if the energy input by the lift due to control surface rotation overcomes the damping action of the lift due to wing translation.

Knowing this, it is not surprising that replacement of k_a by its theoretical value, thus enlarging the value of this derivative, gives rise to an increase in critical speed and that enlarging k_c leads to a rather important decrease of the flutter boundary, together with a considerable extension of the unstable region. The influence of the derivative n_a appears to be very small. Taking n_c according to theory gives somewhat lower critical speeds in the range $0 \leq (v_c/v_R)^2 < 0.6$, while at large values of this parameter the flutter boundary is raised.

Wing torsion-control surface rotation: For this system it is more difficult to predict whether it will flutter or not. Unlike the bending motion the damping of the torsion motion of the wing is relatively small and the system is considerably more sensitive to small changes in the derivatives.

The influence of the various derivatives on the critical speed is shown in fig. 35. It appears that taking k_a or n_a according to theory gives rise to an increase in critical speed and a smaller extent of the unstable region. Replacing k_c or n_c by its theoretical value, leads to very small unstable regions. Using the theoretical value of m_b gives no instability at all. On the other hand the derivatives m_c , n_b and k_b have a very large, unfavourable effect on the flutter boundary. In these cases there is no lower flutter boundary at all, in other words flutter occurs directly at zero airspeed.

In the next section attention will be paid to this phenomenon.

6 Stability of the wing torsion-control surface rotation system at large values of the reduced frequency

To get some insight into the mechanism of the observed instabilities at very low speeds, discussed in the foregoing section, the stability of the system at large values of the reduced frequency has been investigated. For simplicity this study has been restricted to a free oscillating control surface.

Before discussing the wing with control surface, the flutter behaviour at vanishing airspeed (i.e. $\omega \rightarrow \infty$) of a plain wing ($\tau=0$), which is free to rotate about a fixed axis, is considered. It is well known from two-dimensional, incompressible flow theory that such a wing reaches a zero flutterspeed if the axis of rotation is located at the three-quarter chord point. For all other axis locations the wing appears to be stable.

It has been shown in appendix B, that flutter may occur at very low speeds for a certain range of axis locations if experimental aerodynamic forces, approximated by the formulae of Appendix A, are used. Then a necessary condition to be fulfilled for flutter is:

$$\frac{A_{11}}{A_{12}} \cdot \frac{A_{22}}{A_{12}} < 1$$

In fig. 36, the axis locations where instability occurs, which depend only on the ratios $\frac{A_{11}}{A_{12}}$ and $\frac{A_{22}}{A_{12}}$, have been plotted against $\frac{A_{11}}{A_{12}} \cdot \frac{A_{22}}{A_{12}}$ for various values of $\frac{A_{22}}{A_{12}}$. Taking all aerodynamic derivatives according to theory, so $A_{ij}=1$, gives the aforementioned axes location at 75 percent chord. Instability is absent for the numerical values of A_{ij} , which have been used in the calculations described in sections 3 and 4 (see table of appendix A).

For the two degree of freedom system, consisting of a rotating wing with a free floating control surface, it is also possible to derive a stability criterium for very high reduced frequencies (see appendix B). The stability is shown to be dependent on the chord ratio τ , the coefficients A_{ij} , the inertia properties and the wing axis location.

Taking theoretical aerodynamic forces this criterion is simplified in Appendix B to:

$$\varepsilon = \frac{-1 + \alpha\phi_2}{1 - \beta\phi_2}$$

The constants α and β , defined in eq. B.8 of Appendix B, are fully determined by the inertia properties and the chord ratio τ (fixing the functions ϕ_i). So with theoretical aerodynamic forces, a given wing-control surface system has again one wing axis location for which the flutter speed is zero. The expression for ε includes the limit case of a plain wing, as $\phi_2=0$ for $\tau=0$, leading to $\varepsilon=-1$.

For the wing-control surface system considered in the present report, fig. 37a shows the variation of the critical axis location with τ . It appears that the critical axis moves forward with increasing τ , but the range of τ -values investigated still gives damped oscillations for a wing axis at 40 percent, as used in this report.

The result of this stability investigation suggests that in practice flutter at low speeds is likely to occur for wing-control surface systems with nodal lines located closely to the critical position.

In contrast with its behaviour based on theoretical aerodynamic forces, the system appears to be completely stable at vanishing airspeed if the approximations for the measured aerodynamic derivatives are used (i.e. A_{ij} values according to table of app. A). However, one has to be careful, as minor changes in one or more of the coefficients A_{ij} may give a completely different result. This is shown in fig. 37b, presenting the unstable region that occurs if only the coefficient A_{12} is raised from 0.64 to 0.70.

To explain the result of fig. 35, where no lower flutter boundary exists in case either m_c , n_b or k_b is taken according to theory, the stability criterion B7 of Appendix B has been used. As this criterion is restricted to a free floated control surface, it only indicates whether the origin of fig. 35 becomes part of a stable or an unstable region. The result has been summarized in the table here under.

Derivative, chosen according to theory	Value of D (eq. B. 7 of App. B)	Conclusion about origin of fig. 35
$k_a^* A_{11} = 1$	+0.0567	stable
$n_a^* A_{31} = 1$	+0.0355	stable
$k_b^* A_{12} = 1$	-0.1863	unstable
$m_b^* A_{22} = 1$	+0.4079	stable
$n_b^* A_{32} = 1$	-0.1088	unstable
$k_c^* A_{13} = 1$	+0.1018	stable
$m_c^* A_{23} = 1$	-0.1459	unstable
$n_c^* A_{33} = 1$	+0.0909	stable
none	+0.0297	stable

note: $ma^* = 0$ in both theory and experiment.

The conclusions about the position of the origin can be easily verified in fig. 35. The magnitude of D appears to give an indication of the size of the unstable region. For instance the unstable region for k_c^* is much smaller than for n_a^* , while for m_b^* the system is even completely stable.

7 Conclusions

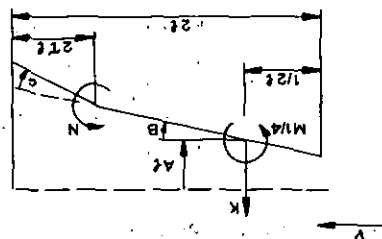
From the investigation of two dimensional wing-control surface systems in incompressible flow, the following conclusions can be drawn:

- 1 The presented empirical formulae for control surface derivatives appear to be sufficiently accurate for flutter calculations.
- 2 Using theoretical aerodynamic forces, any given wing with free control surface is shown to have one wing axis location, for which flutter at zero air speed occurs.
- 3 In case a combination of theoretical and empirical aerodynamic derivatives is used in a flutter calculation, flutter at zero airspeed may occur within a certain range of wing axis locations.

8 References

- ¹ Bergh, H., Results of instationary pressure measurements on three wing-control surface combinations in incompressible flow. (in Dutch), NLR int. report FF 12 (1963).
- ² Bergh, H., Experimentelle und theoretische Bestimmung instationärer Drücke an schwingenden Tragflügeln. DLR Mitt. 65-12. S. 98-134. Bericht über die gemeinsame Sitzung der Ausschüsse Aerodynamik und Festigkeit und Aeroelastizität am 2. April 1965 in Aachen.
- ³ Bergh, H., Unsteady pressure measurements on a wing with oscillating flap in two dimensional flow. Proceedings of the Third European Aeronautical Congress (Brussels 22-27 Sept. 1958). (Also NLR report F. 217).
- ⁴ Bergh, H., A new method for measuring the pressure distribution on harmonically oscillating wings. Proceedings of the 4th ICAS-Congress, Paris 1964 (also NLR report MP. 224).
- ⁵ de Jager, E. M., The aerodynamic forces and moments on an oscillating aerofoil with control surface between two parallel walls. NLR report F. 140 (1954).
- ⁶ Küssner, H. G., Der schwingende Flügel mit aerodynamisch ausgeglichenem Ruder. Luftfahrtforschung 17 (1940), S. 337-354.
- ⁷ Bergh, H., and Zwaan, R. J., A method for estimating unsteady pressure distributions for arbitrary vibration modes from theory and from measured distributions for one single mode. NLR report TR F. 250 (1966).

Aerodynamic derivatives



$$K = \pi \rho V^2 l [k_a A + k_b B + k_c C] e^{i\omega t}$$

$$M = \pi \rho V^2 l^2 [m_a A + m_b B + m_c C] e^{i\omega t}$$

$$N = \pi \rho V^2 l^2 [n_a A + n_b B + n_c C] e^{i\omega t}$$

$$\omega = \frac{V}{l}$$

$$\omega^2 = A_{11} k_a^* - \omega^2$$

$$\frac{1}{2} \omega^2 = -\frac{1}{2} \omega^2$$

$$n_a = A_{31} i \omega \frac{2\pi}{1} (1+T) \phi_8$$

$$-\frac{1}{2} \omega^2 = A_{31} n_a^* - \frac{1}{2} \omega^2$$

$$k_b = A_{12} \{ (1+i\omega)(1+T) + i\omega \} + B_1 - \frac{1}{2} \omega^2$$

$$A_{12} k_b^* + B_1 - \frac{1}{2} \omega^2$$

$$m_b = A_{22} i \omega - \frac{3}{8} \omega^2 = A_{22} m_b^* - \frac{3}{8} \omega^2$$

$$n_b = A_{32} \frac{\pi}{2} (1+i\omega)(1+T) \phi_8 + \frac{2}{1} i \omega \phi_9 \left[-\frac{4\pi}{1} \phi_7 \omega^2 = A_{32} n_b^* - \frac{4\pi}{1} \phi_7 \omega^2 \right]$$

$$k_c = A_{13} \frac{\pi}{2} (1+T) (\phi_1 + \frac{2}{1} i \omega \phi_2) + i \omega \phi_3 \left[-\frac{2\pi}{1} \phi_4 \omega^2 = A_{13} k_c^* - \frac{2\pi}{1} \phi_4 \omega^2 \right]$$

$$m_c = A_{23} \frac{\pi}{2} \left[\phi_5 + \frac{2}{1} i \omega \phi_6 \right] + B_2 - \frac{4\pi}{1} \phi_7 \omega^2 = A_{23} m_c^* + B_2 - \frac{4\pi}{1} \phi_7 \omega^2$$

$$n_c = A_{33} \frac{\pi}{2} (1+T) (\phi_1 + \frac{2}{1} i \omega \phi_2) \frac{2}{1} \phi_8 + \phi_{10} + \frac{2}{1} i \omega \phi_{11} \left[-\frac{4\pi^2}{1} \phi_{12} \omega^2 = A_{33} n_c^* - \frac{4\pi^2}{1} \phi_{12} \omega^2 \right]$$

with $A_{13} = A_{23} = A_{33} = 0.84 S$.

For the functions $T(\omega)$ and $\phi(\tau)$, given in the expressions above, the reader is referred to ref. 6.

The theoretical values of the instantaneous aerodynamic derivatives can be obtained by putting $A_{ij} = 1$ and $B_1 = B_2 = 0$.

To approximate the measured values of the derivatives, the following values of A_{ij} , B_1 and B_2 were taken:

T	S	A_{11}	A_{31}	A_{12}	B_1	A_{22}	A_{32}	A_{13}	A_{23}	B_2	A_{33}
0.175	0.70	0.70	0.44	0.64	0.15	0.62	0.44	0.59	0.59	0.05	0.59
0.20	0.72	0.70	0.45	0.64	0.15	0.62	0.45	0.61	0.61	0.05	0.61
0.35	0.70	0.70	0.51	0.64	0.15	0.62	0.51	0.59	0.59	0.05	0.59
0.40	0.88	0.70	0.53	0.64	0.15	0.62	0.53	0.74	0.74	0.05	0.74

APPENDIX B

Stability criterion for a wing torsion-control surface rotation system at large values of the reduced frequency

The equations of motion for a wing torsion-control surface rotation system in case of a free floating control surface ($v_c=0$) can be written as:

$$\begin{vmatrix} \left[\mu(\sigma^2 + \kappa^2)(1-Z) - \frac{L_{22}}{\omega^2} \right] \left[\mu_R \sigma_R(\sigma + a + \sigma_R) + \mu_R \kappa_R^2 - \frac{L_{23}}{\omega^2} \right] & q_2 \\ \left[\mu_R \sigma_R(\sigma + a + \sigma_R) + \mu_R \kappa_R^2 - \frac{L_{32}}{\omega^2} \right] \left[\mu_R(\sigma_R^2 + \kappa_R^2) - \frac{L_{33}}{\omega^2} \right] & q_3 \end{vmatrix} = 0 \quad (\text{B.1})$$

where $Z = Z' + iZ'' = v_T^2/v^2$ is the unknown quantity to be solved. The aerodynamic quantities L_{ij} of eq. (B.1) can be expressed as:

$$\left. \begin{aligned} L_{22} &= A_{22}m_b^* + A_{11}\varepsilon^2 k_a^* + A_{12}ak_b^* + B_1 - \left(\frac{3}{8} + \varepsilon + \varepsilon^2 \right) \omega^2 \\ L_{23} &= A_{23}m_c^* + B_2 + A_{13}\varepsilon k_c^* - \frac{1}{4\pi}(\phi_7 + 2\varepsilon\phi_4)\omega^2 \\ L_{32} &= A_{32}n_b^* + A_{31}\varepsilon n_a^* - \frac{1}{4\pi}(\phi_7 + 2\varepsilon\phi_4)\omega^2 \\ L_{33} &= A_{33}n_c^* - \frac{1}{4\pi^2}\phi_{12}\omega^2 \\ (\text{Note: } m_a^* &= 0) \end{aligned} \right\} \quad (\text{B.2})$$

Using the expressions for the aerodynamic derivatives given in Appendix A, and assuming $\omega \rightarrow \infty$, the aerodynamic terms in (B.1) are reduced to:

$$\left. \begin{aligned} \frac{L_{22}}{\omega^2} &= i \frac{1}{\omega} [A_{22} + \varepsilon^2 A_{11} + 2\varepsilon A_{12}] - \left(\frac{3}{8} + \varepsilon + \varepsilon^2 \right) \\ \frac{L_{23}}{\omega^2} &= i \frac{1}{2\pi\omega} [A_{23}\phi_6 + \varepsilon A_{13}\phi_2 + 2\varepsilon A_{13}\phi_3] - \frac{1}{4\pi}(\phi_7 + 2\varepsilon\phi_4) \\ \frac{L_{32}}{\omega^2} &= i \frac{1}{2\pi\omega} [A_{32}(\phi_8 + \phi_9) + A_{31}\varepsilon\phi_8] - \frac{1}{4\pi}(\phi_7 + 2\varepsilon\phi_4) \\ \frac{L_{33}}{\omega^2} &= i \frac{1}{\pi^2\omega} \left[\frac{1}{4}\phi_2\phi_8 + \frac{1}{2}\phi_{11} \right] - \frac{1}{4\pi^2}\phi_{12} \end{aligned} \right\} \quad (\text{B.3})$$

The condition for damped oscillations of the system described by eq. (B.1) is

$$Z'' < 0 \quad (\text{B.4})$$

From eq. (B.1) it can be derived:

$$Z'' = -\frac{1}{C_1} \text{Im} \left[\frac{L_{22}}{\omega^2} + \frac{\left(C_2 - \frac{L_{23}}{\omega^2} \right) \left(C_2 - \frac{L_{32}}{\omega^2} \right)}{\left(C_3 - \frac{L_{33}}{\omega^2} \right)} \right] \quad (\text{B.5})$$

where for convenience the following notations have been used:

$$\begin{aligned} C_1 &= \mu(\sigma^2 + \kappa^2) \\ C_2 &= \mu_R \sigma_R(\sigma + a + \sigma_R) + \mu_R \kappa_R^2 \\ C_3 &= \mu_R(\sigma_R^2 + \kappa_R^2) \end{aligned}$$

Thus the condition for damped oscillations (B.4) yields:

$$(B.6) \quad \text{Im} \left[\frac{L_{22} \frac{\omega^2}{2} + \left(C_2 - \frac{L_{23}}{L_{32}} \right) \left(C_2 - \frac{L_{32}}{\omega^2} \right)}{\left(C_3 - \frac{L_{33}}{\omega^2} \right)} \right] > 0$$

The condition for stability in case of $\omega \rightarrow \infty$ can be easily obtained by substituting the expressions of (B.3) into (B.6). The result is:

$$(B.7) \quad D = \epsilon^2 [A_{11} - \beta A_{13}(\phi_2 + 2\phi_3) - \beta A_{31}\phi_8 + \beta^2 A_{33}(\phi_2\phi_8 + 2\phi_{11})] + \\ + \epsilon [2A_{12} - \alpha A_{13}(\phi_2 + 2\phi_3) - \alpha A_{31}\phi_8 - \beta A_{23}\phi_6 - \beta A_{32}(\phi_8 + \phi_9) + 2\alpha\beta A_{33}(\phi_2\phi_8 + 2\phi_{11})] \\ + [A_{22} - \alpha A_{23}\phi_6 - \alpha A_{32}(\phi_8 + \phi_9) + \alpha^2 A_{33}(\phi_2\phi_8 + 2\phi_{11})] > 0,$$

with

$$(B.8) \quad \alpha = \frac{1}{2\pi} \begin{cases} C_2 + \frac{4\pi}{1} \phi_7 \\ C_3 + \frac{4\pi}{1} \phi_{12} \end{cases} \quad \text{and} \quad \beta = \begin{cases} \frac{1}{4\pi} \phi_4 \\ C_3 + \frac{4\pi}{1} \phi_{12} \end{cases}$$

The condition (B.7) shows the stability to depend on the chord ratio r , the value of the coefficients A_{ij} , the inertia properties of the system and the axis location ϵ . Considering the wing without control surface, the system appears to be stable if:

$$(B.9) \quad A_{11}\epsilon^2 + 2A_{12}\epsilon + A_{22} > 0$$

Evidently instability occurs in the range

$$(B.10) \quad -\frac{A_{12}}{A_{11}} \left[1 + \sqrt{1 - \frac{A_{12}}{A_{11}} \cdot \frac{A_{12}}{A_{22}} \cdot \frac{A_{11}}{A_{12}}} \right] \leq \epsilon \leq -\frac{A_{12}}{A_{11}} \left[1 - \sqrt{1 - \frac{A_{12}}{A_{11}} \cdot \frac{A_{12}}{A_{22}} \cdot \frac{A_{11}}{A_{12}}} \right]$$

The inequality (B.10) shows that an unstable region exists for a certain range of axis locations if

$$(B.11) \quad \frac{A_{22}}{A_{12}} \cdot \frac{A_{11}}{A_{12}} \leq 1$$

In case of only theoretical aerodynamic derivatives, i.e. $A_{ij} = 1$, the inequality (B.7) can be rewritten as:

$$(B.12) \quad \text{or:} \quad \epsilon^2 [1 - 2\beta\phi_2 + \beta^2\phi_2^2] + 2\epsilon [1 - \alpha\phi_2 - \beta\phi_2 + \alpha\beta\phi_2^2] + [1 - 2\alpha\phi_2 + \alpha^2\phi_2^2] > 0$$

To derive (B.12) use has been made of the relations

$$(B.13) \quad \begin{cases} 2\phi_3 + \phi_8 = \phi_2 \\ \phi_6 + \phi_8 + \phi_9 = 2\phi_2 \\ \phi_2\phi_8 + 2\phi_{11} = \phi_2^2 \end{cases}$$

These relations can easily be verified from the formula given in ref. 6. From (B.12) it can be seen that the system is not damped aerodynamically for the axis location, determined by:

$$(B.14) \quad \epsilon = \frac{-1 + \alpha\phi_2}{1 - \beta\phi_2}$$

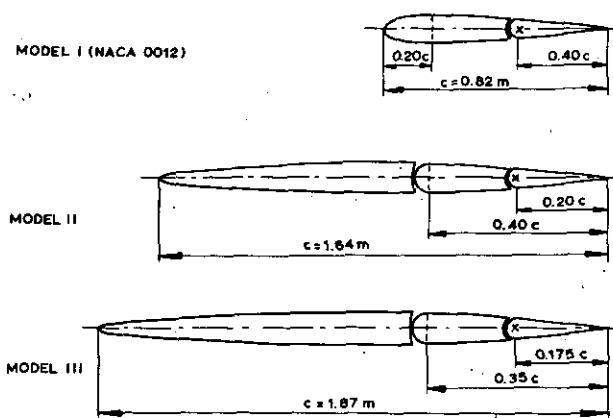


Fig. 1. Tested model configurations.

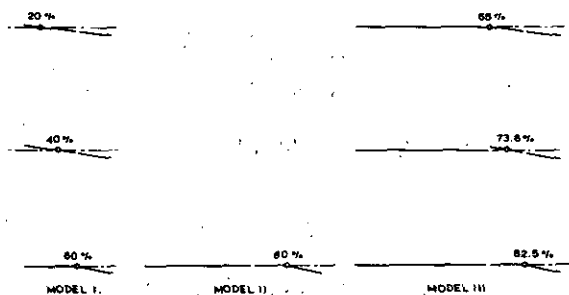


Fig. 2. Tested vibration modes.

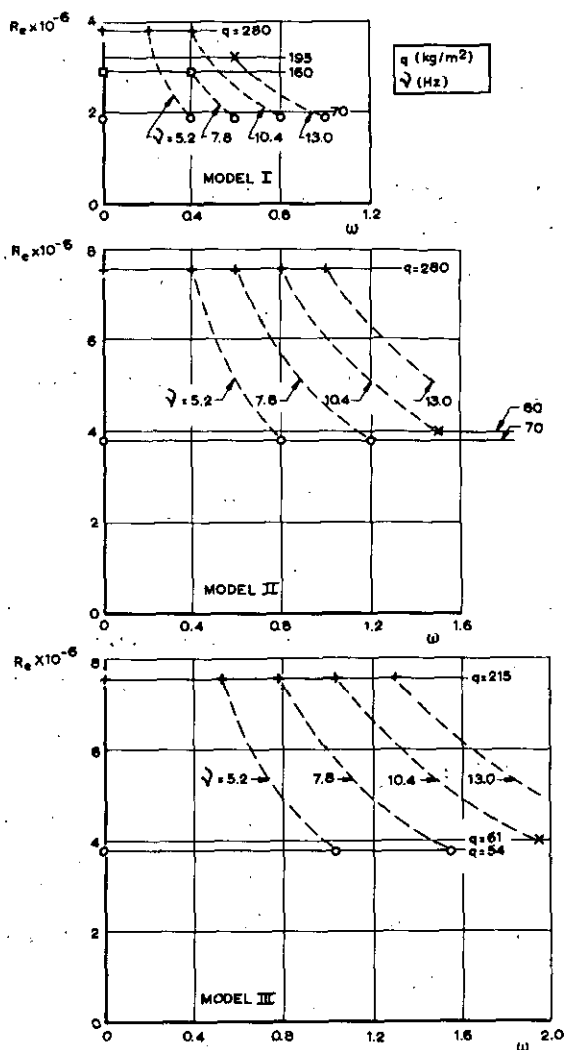


Fig. 3. Investigated combinations of Reynolds number (R_e) and reduced frequency (ω).

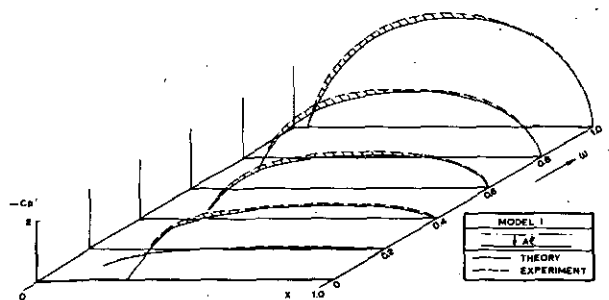


Fig. 4. Real part of pressure distribution for wing translation (note positive direction of C_p being opposite to that in all other figures).

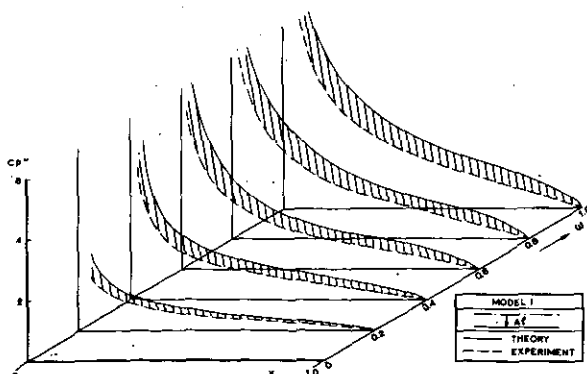


Fig. 5. Imaginary part of pressure distribution for wing translation.

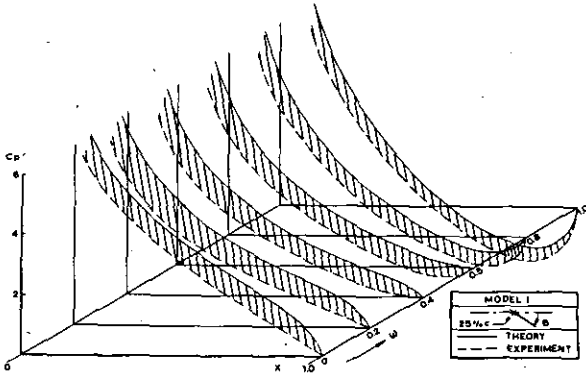


Fig. 6. Real part of pressure distribution for wing rotation.

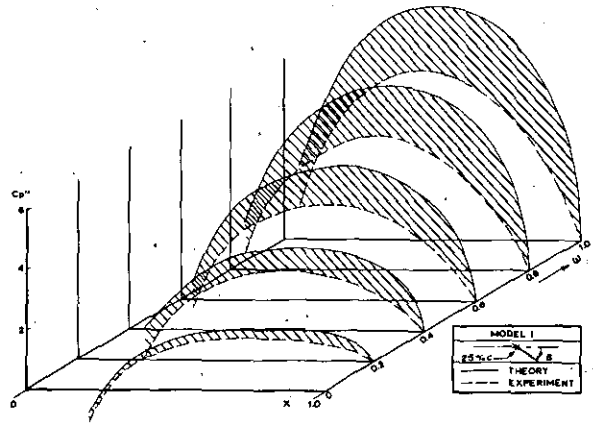


Fig. 7. Imaginary part of pressure distribution for wing rotation.

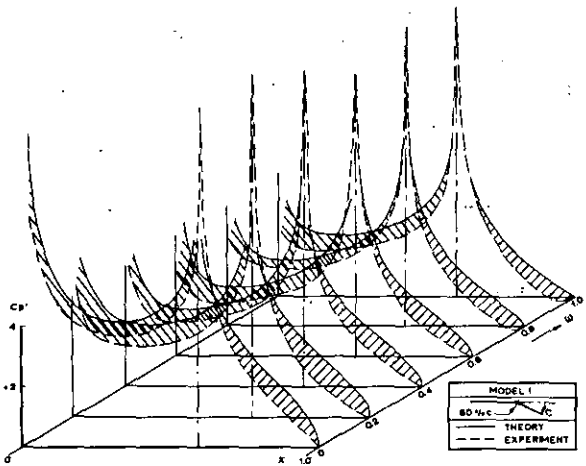


Fig. 8. Real part of the pressure distribution for control surface rotation ($\tau = 0.40$).

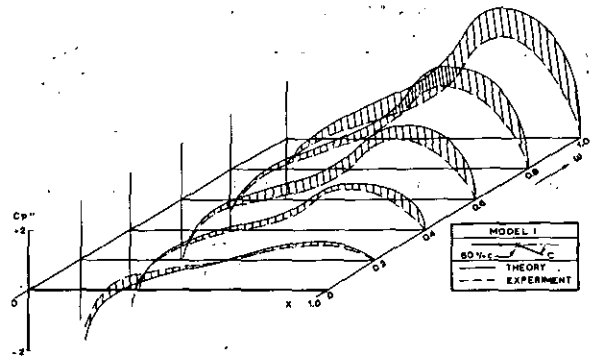


Fig. 9. Imaginary part of pressure distribution for control surface rotation ($\tau = 0.40$).

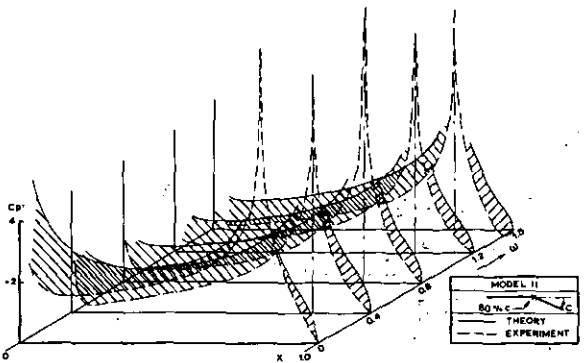


Fig. 10. Real part of pressure distribution for control surface rotation ($\tau = 0.20$).

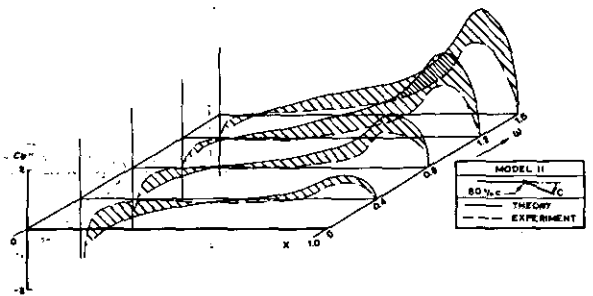


Fig. 11. Imaginary part of pressure distribution for control surface rotation ($\tau = 0.20$).

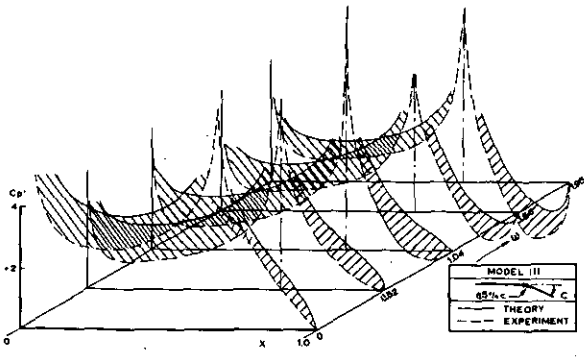


Fig. 12. Real part of pressure distribution for control surface rotation ($\tau = 0.35$).

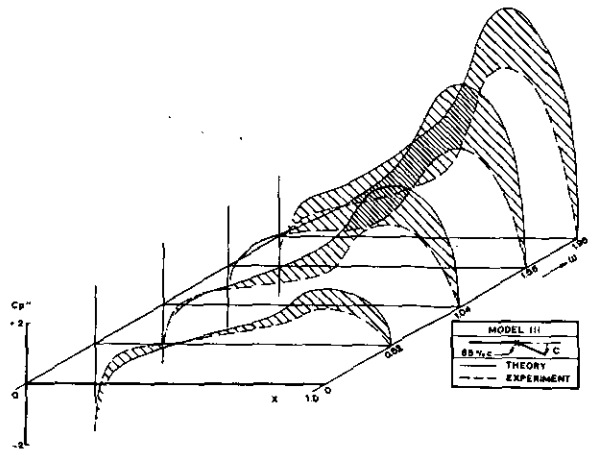


Fig. 13. Imaginary part of pressure distribution for control surface rotation ($\tau = 0.35$).

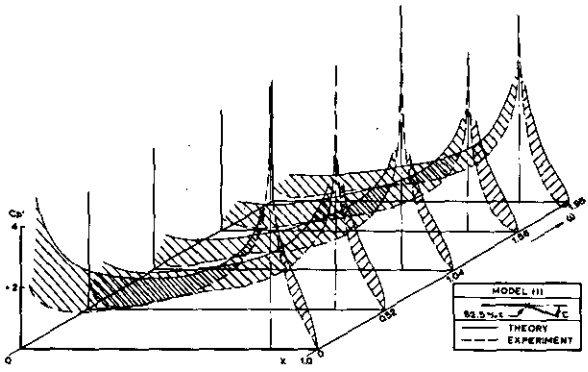


Fig. 14. Real part of pressure distribution for control surface rotation ($\tau = 0.175$).

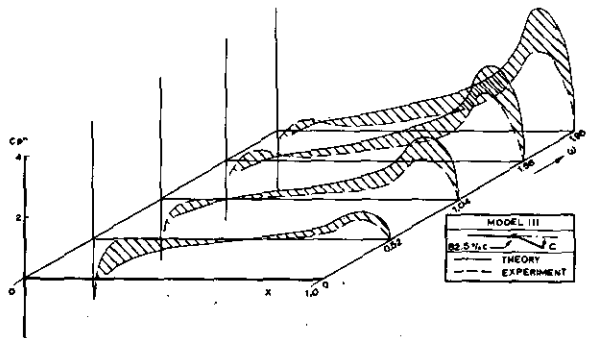


Fig. 15. Imaginary part of pressure distribution for control surface rotation ($\tau = 0.175$).

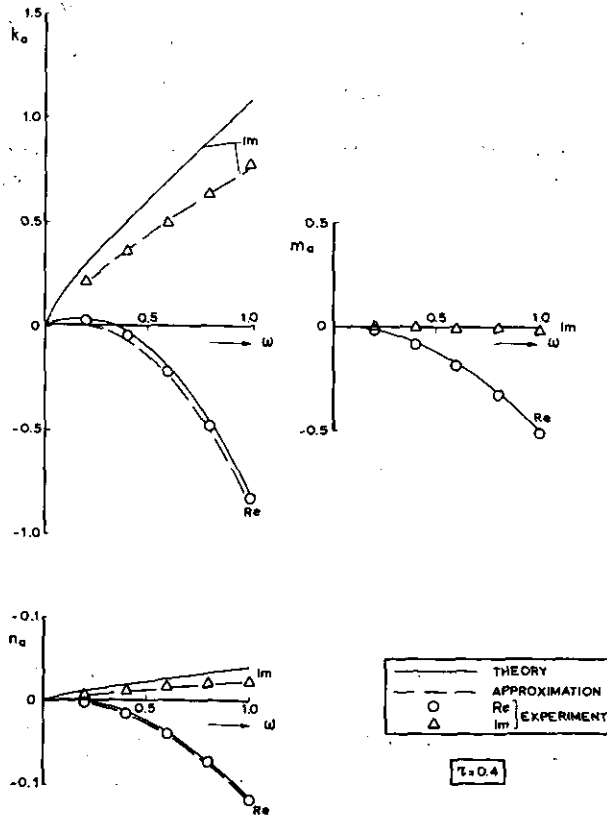


Fig. 16. Aerodynamic derivatives for wing translation (model I; hinge moment derivative n_a for $\tau = 0.40$).

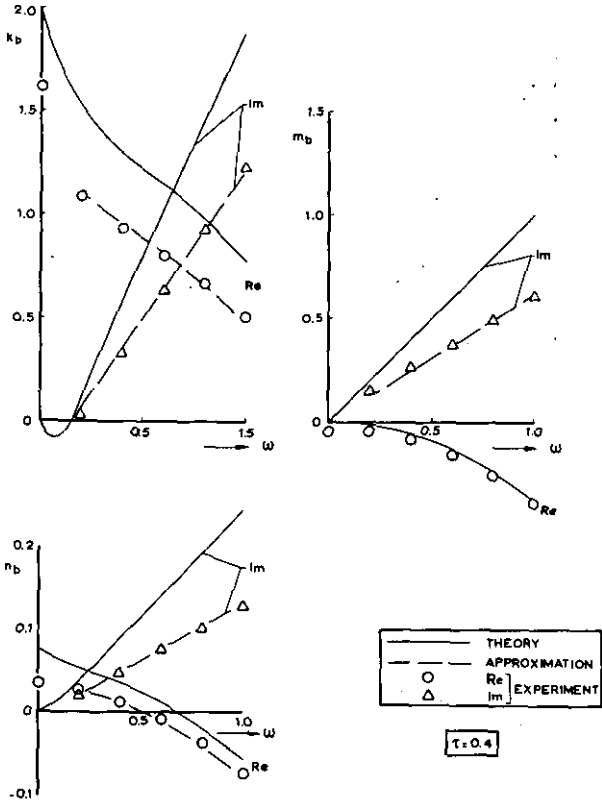


Fig. 17. Aerodynamic derivatives for wing rotation about one quarter chord axis (model I; hinge moment derivative n_b for $\tau = 0.40$).

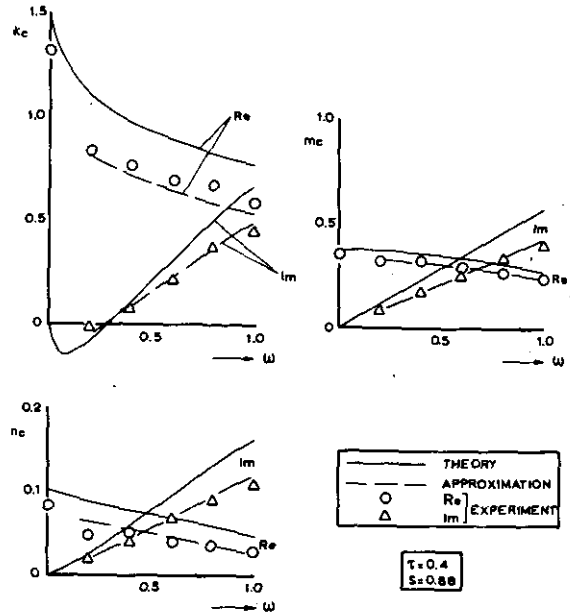


Fig. 18. Aerodynamic derivatives for control surface rotation (model I; $\tau = 0.40$).

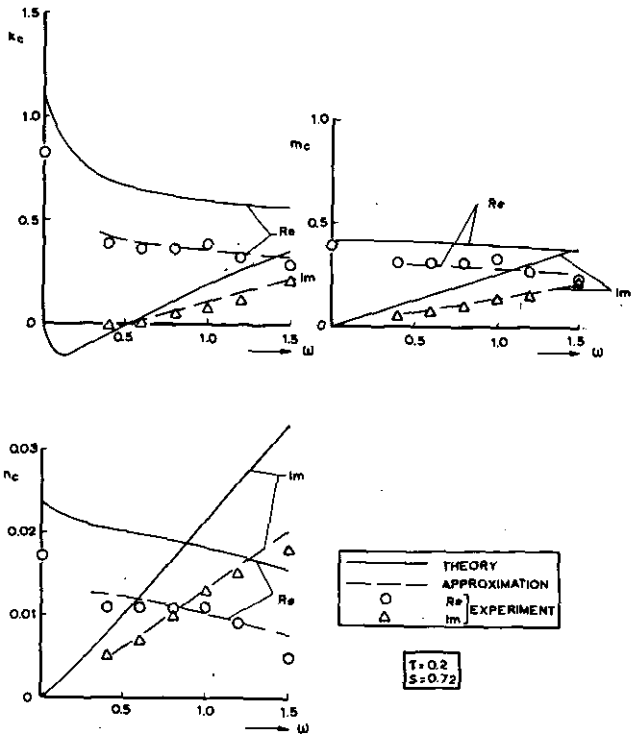


Fig. 19. Aerodynamic derivatives for control surface rotation (model II, $\tau = 0.20$).

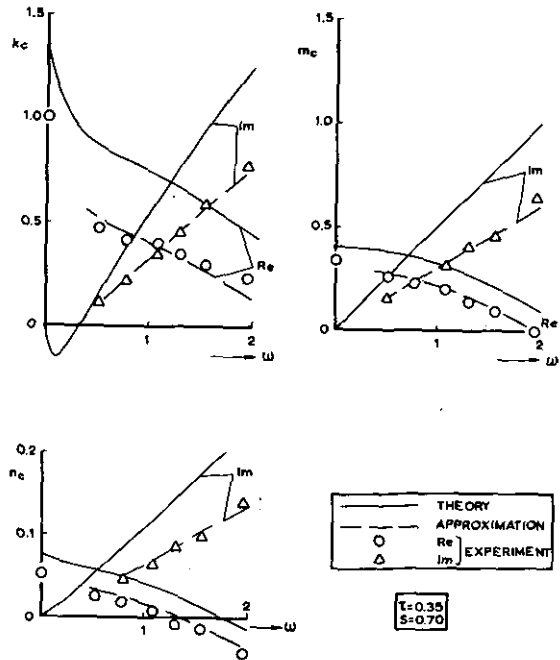


Fig. 20. Aerodynamic derivatives for control surface rotation (model III, $\tau = 0.35$).

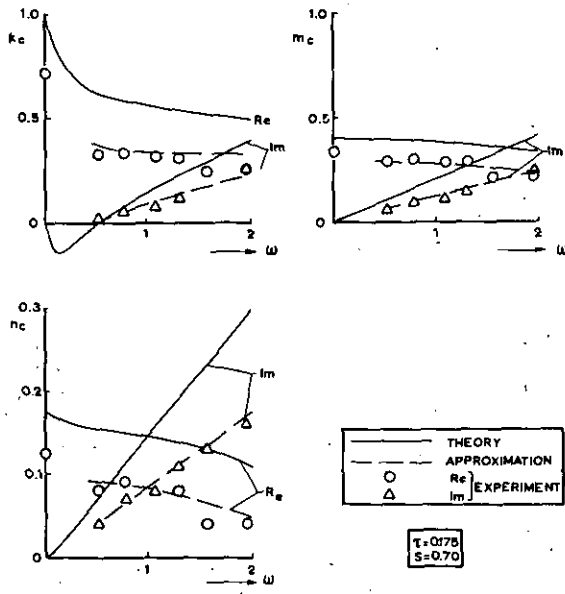


Fig. 21. Aerodynamic derivatives for control surface rotation (model III, $\tau = 0.175$).

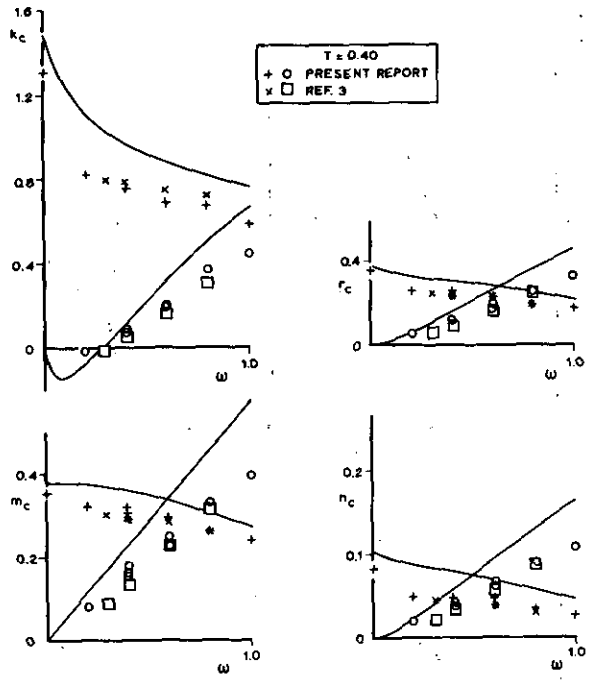


Fig. 22. Comparison between results of the present tests and the results of ref. 3, obtained by direct pressure measurements.

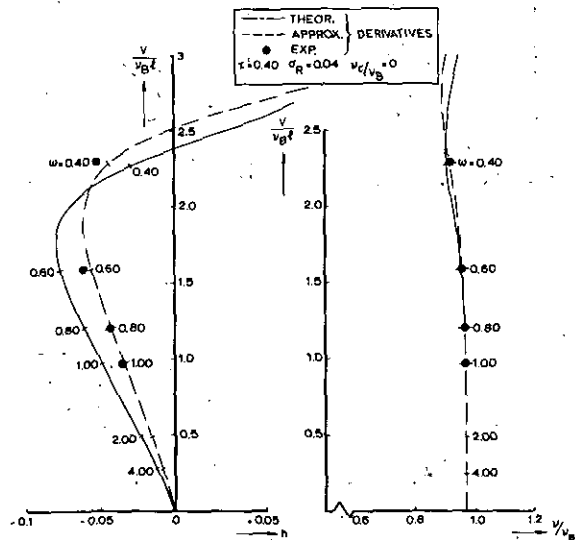


Fig. 23. Wing bending-control surface rotation flutter ($v/v_B = 0$).

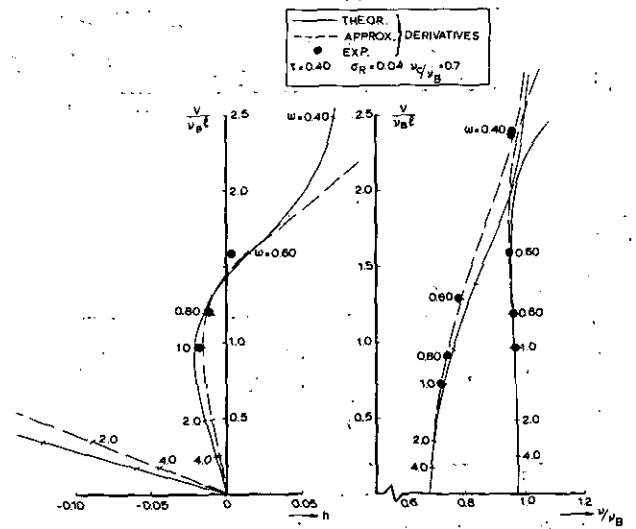


Fig. 24. Wing bending-control surface rotation flutter ($v/v_B = 0.7$).

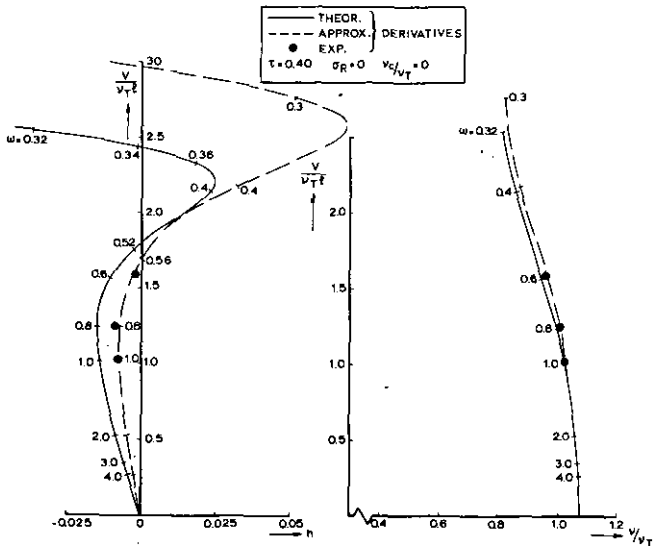


Fig. 25. Wing torsion-control surface rotation flutter ($v_c/v_T = 0$).

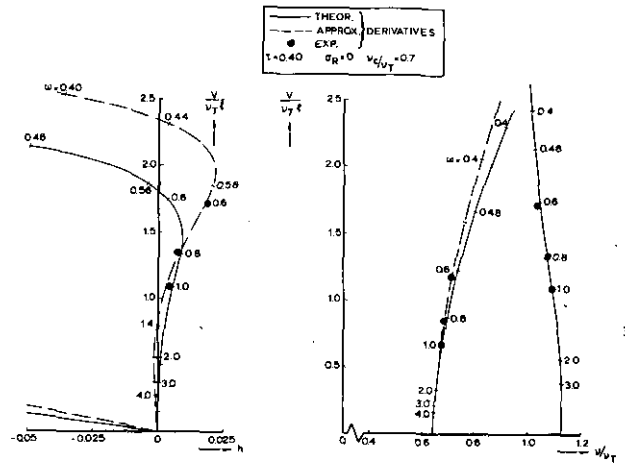


Fig. 26. Wing torsion-control surface rotation flutter ($v_c/v_T = 0.7$).

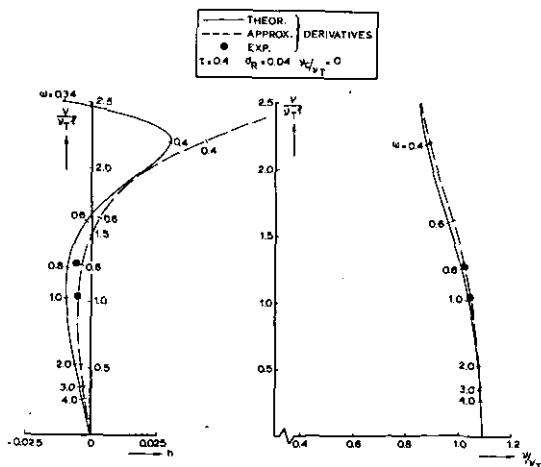


Fig. 27. Wing torsion-control surface rotation flutter ($v_c/v_T = 0$).

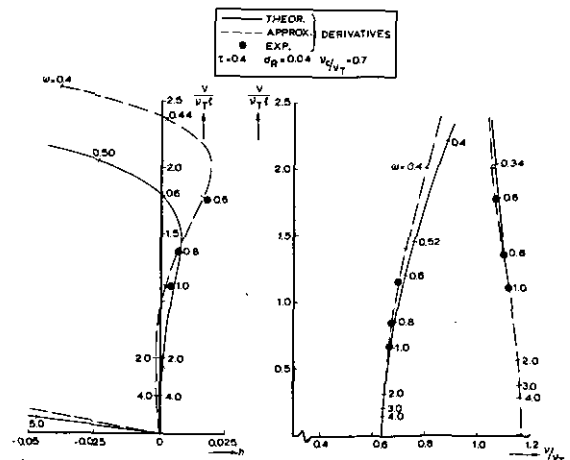


Fig. 28. Wing torsion-control surface rotation flutter ($v_c/v_T = 0.7$).

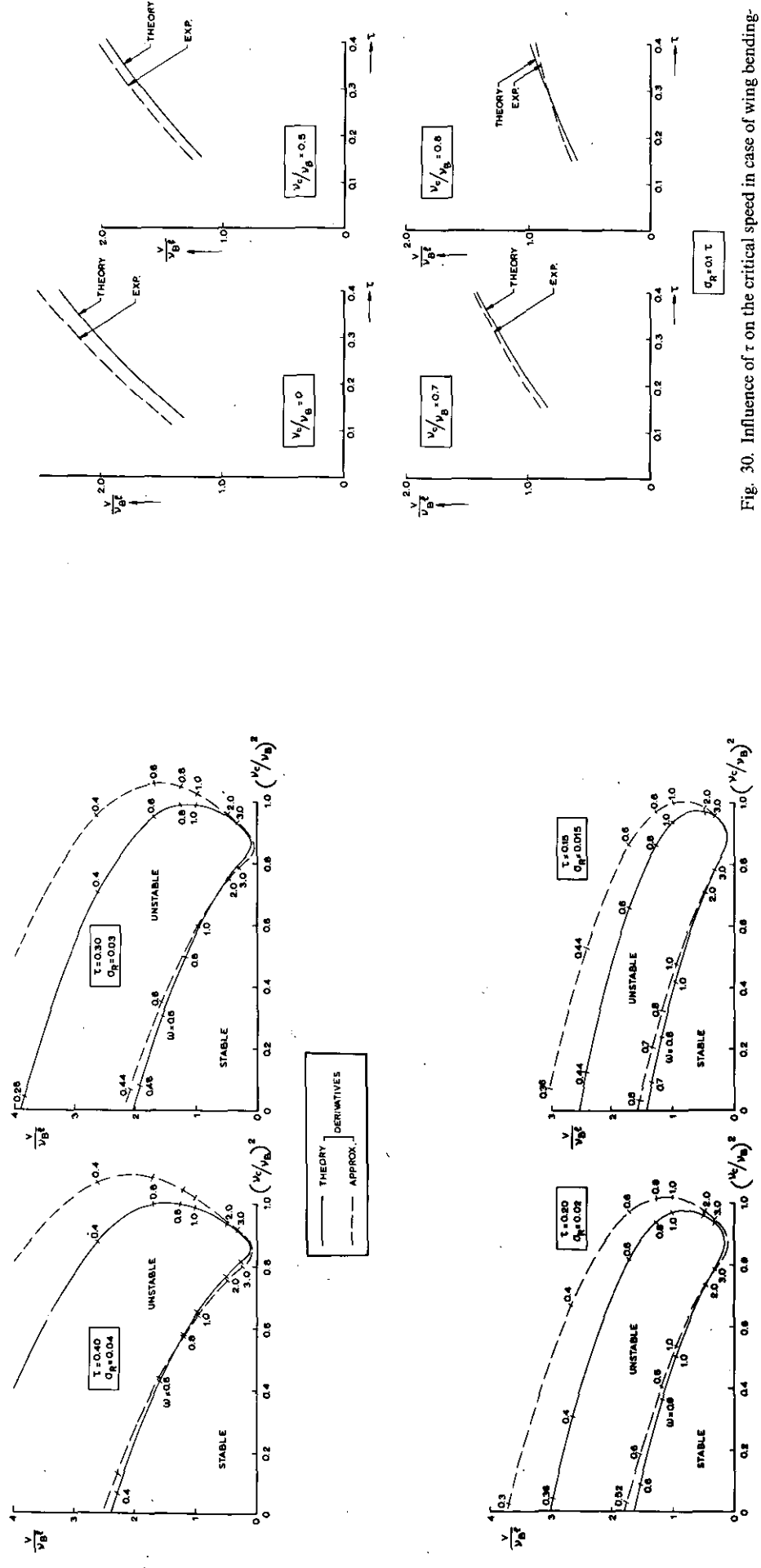


Fig. 29. Stability diagrams for wing bending-control surface rotation.

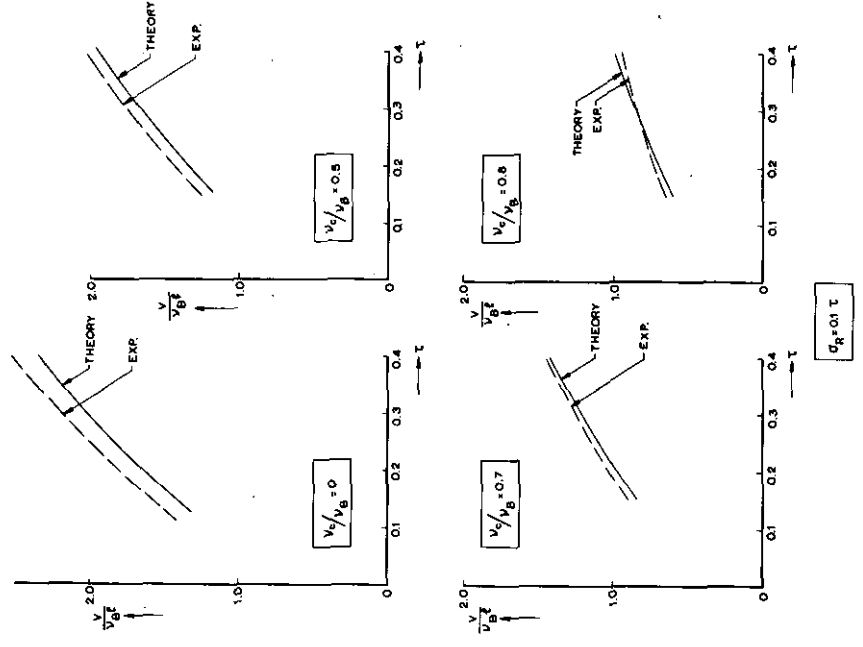


Fig. 30. Influence of τ on the critical speed in case of wing bending-control surface rotation.

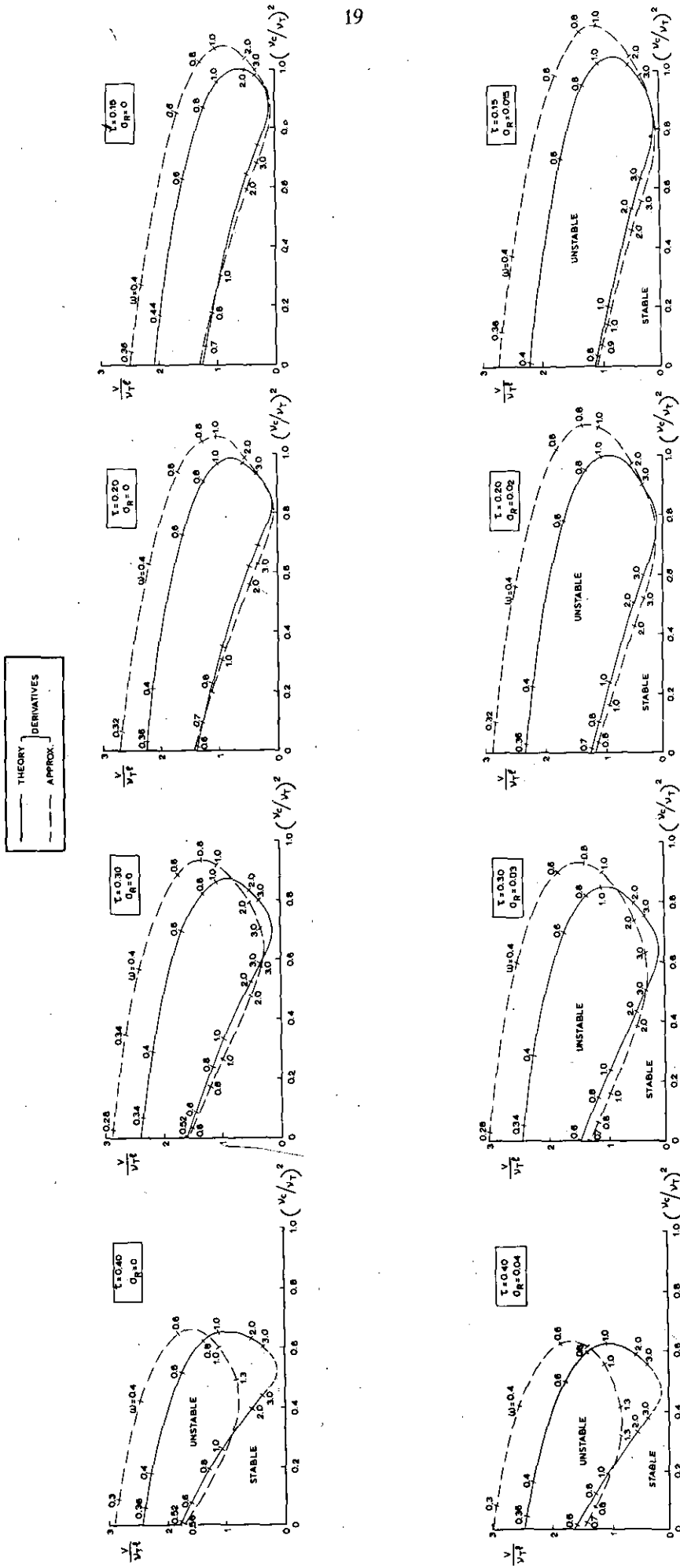


Fig. 31. Stability diagrams for wing torsion-control surface rotation.

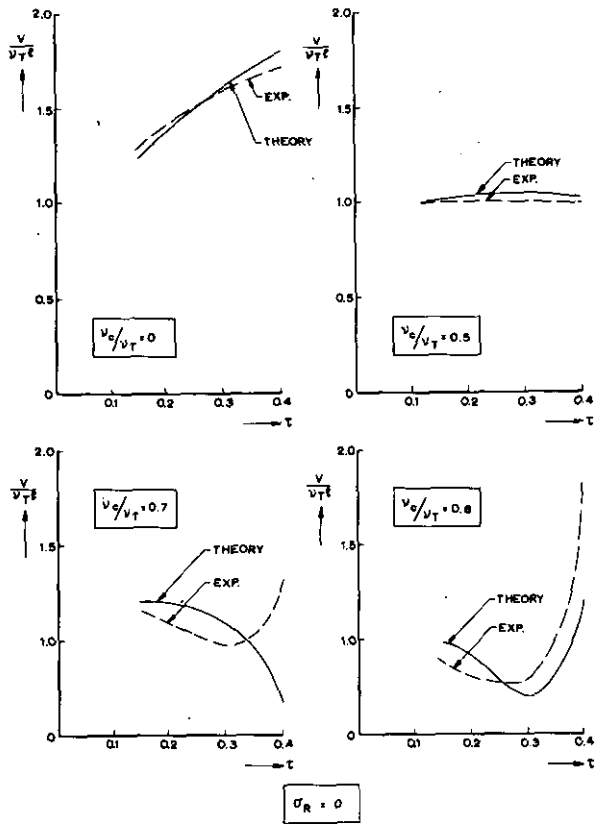


Fig. 32. Influence of τ on the critical speed in case of wing torsion-control surface rotation ($\sigma_R = 0$).

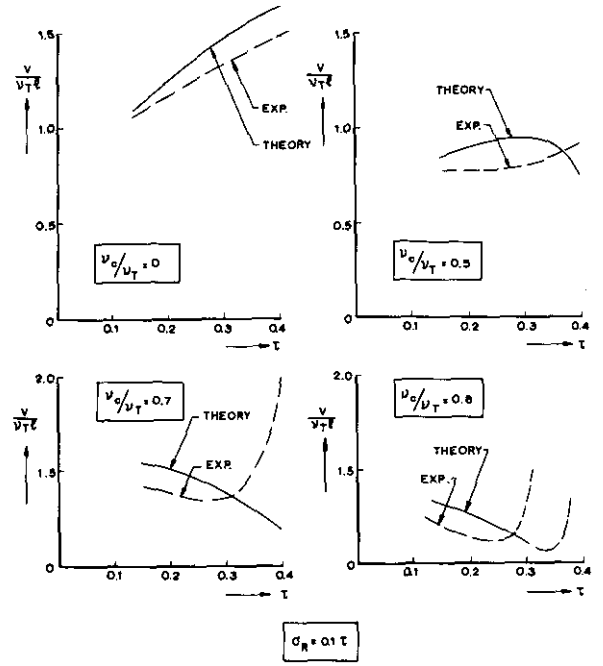


Fig. 33. Influence of τ on the critical speed in case of wing torsion-control surface rotation ($\sigma_R = 0.1 \tau$).

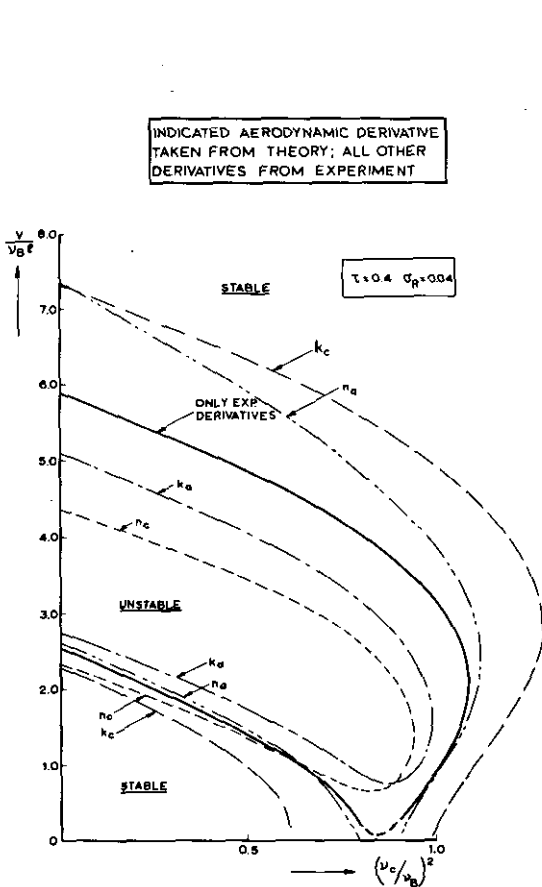


Fig. 34. Influence of the various aerodynamic derivatives on the flutter boundary in case of wing bending-control surface rotation.

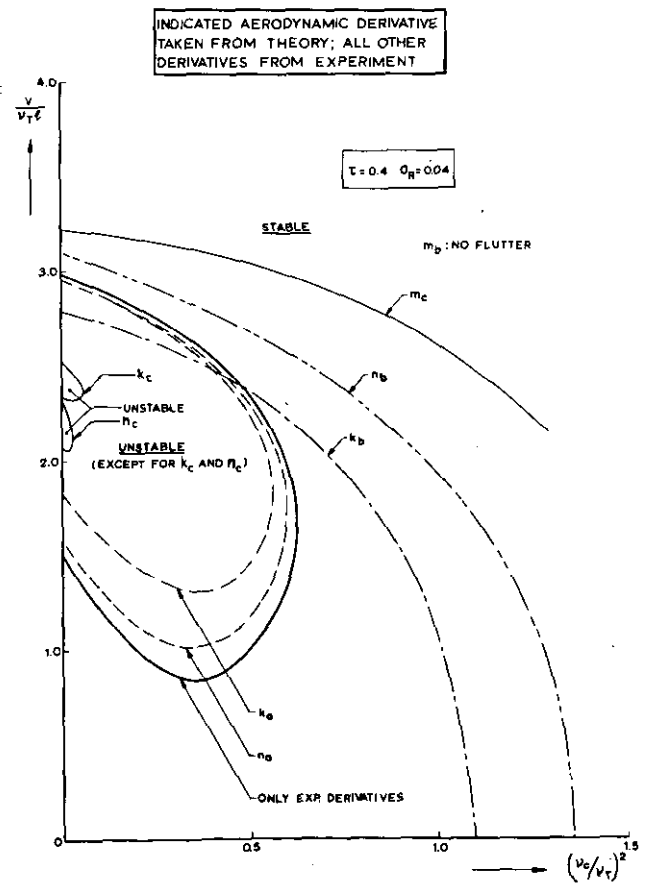


Fig. 35. Influence of the various aerodynamic derivatives on the flutter boundary in case of wing torsion-control surface rotation.

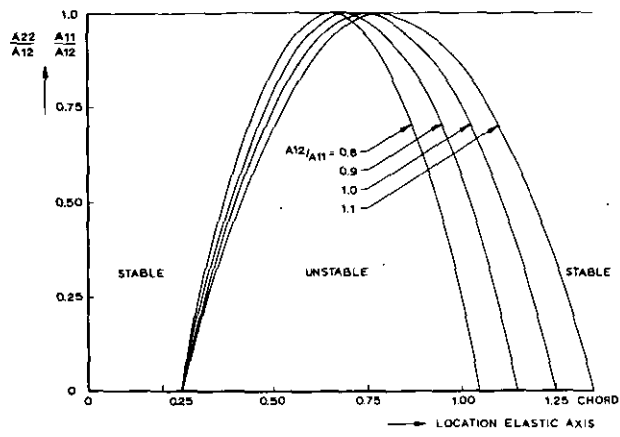


Fig. 36. Axis locations for unstable wing oscillations ($\tau = 0$).

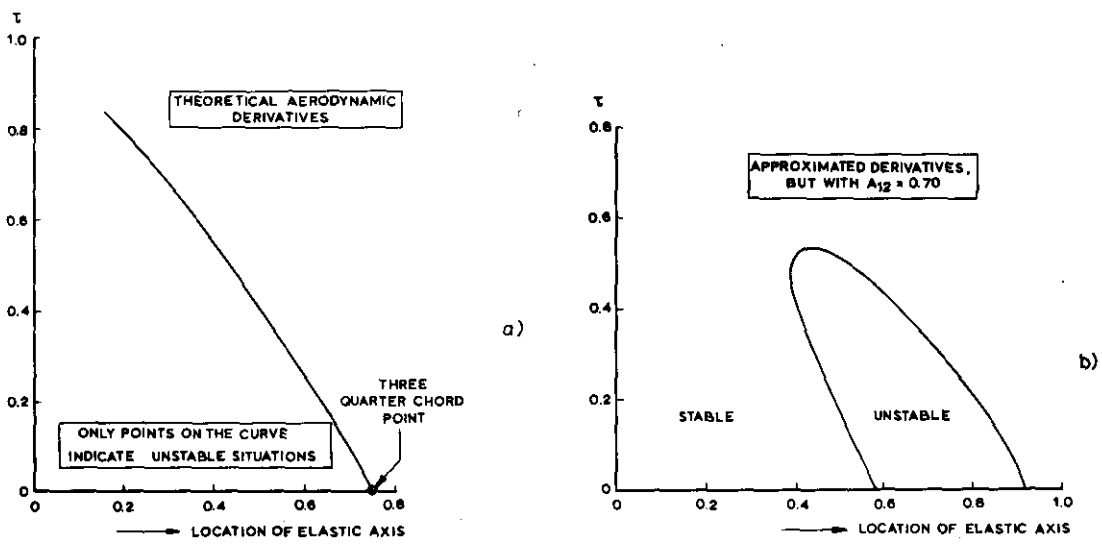
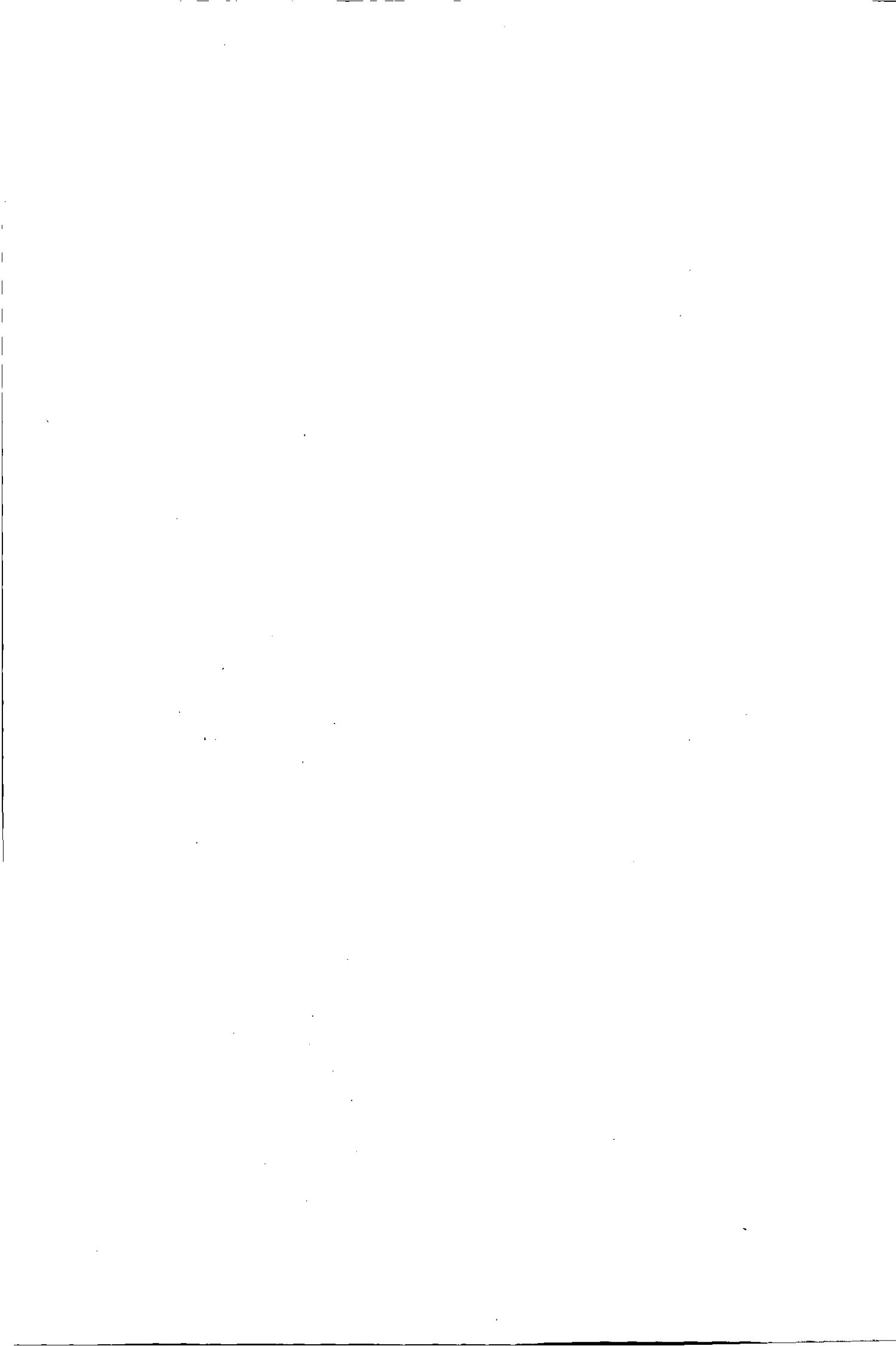


Fig. 37. Wing axis location for which wing with free floating control surface is unstable.



REPORT NLR-TR 68117 U

Crack propagation in aluminum alloy sheet materials under flight-simulation loading

by

J. SCHIJVE, F. A. JACOBS and P. J. TROMP

Summary

A large number of flight-simulation tests were carried out on sheet specimens of 7075-T6 and 2024-T3 clad material. A gust load spectrum was adopted and a flight-by-flight loading was applied. The investigation is essentially concerned with macro-crack propagation though a few exploratory tests were conducted on the crack nucleation period. The major trends emerging from tests with a variety of loading programs are:

1. The omission of taxiing loads from the ground-to-air cycles did not affect the crack propagation.
2. The sequence of the gust cycles in a flight (random, programmed, reversed gust cycles) did not have a significant influence on the crack propagation.
3. Omission of gust cycles with small amplitudes systematically increased the crack propagation life.
4. The most predominant effect on the crack propagation was coming from the maximum gust amplitude included in the test. Increasing this amplitude gave a large increase of the crack propagation life.
5. Application in each flight of a single gust load only, namely the largest upward gust load, increased the crack propagation life three times.
6. Omission of the ground-to-air cycle increased the life 1.5-1.8 times.

The discussion and the analysis of the results include such aspects as fractographic analysis, possible mechanisms for interaction effects between load cycles of different magnitudes and damage calculations. The conclusions at the end of the report have a number of implications for testing procedures to be applied in full-scale testing aiming at crack propagation data for fail-safe considerations. A recommendation is made for selecting the maximum load level in such a test. Recommendations for further study are also made.

Contents

	<i>Page</i>		<i>Page</i>
List of abbreviations and symbols	2	7.1 Interaction between load cycles of different magnitudes	7
1 Introduction	2	7.2 The omission of the taxiing loads (TL) from the ground-to-air cycle (GTAC)	8
2 Survey and scope of the test series	2	7.3 The minimum stress of the GTAC	8
3 Materials and specimens	3	7.4 Omission of the small gust loads	9
4 Experimental procedures	4	7.5 The effect of the gust cycles with a high amplitude	9
4.1 The anti-buckling guides	4	7.6 Random or programmed gust sequences in each flight and reversion of the gust cycle	10
4.2 The fatigue apparatus	4	7.7 Application of a single gust load per flight	11
4.3 The crack propagation tests	4	7.8 Omission of the GTAC	11
5 The fatigue loads	4	7.9 Comparison between the two alloys, 7075 and 2024	11
5.1 The gust loads	4	7.10 Damage calculations	11
5.2 The ground-to-air cycles and the taxiing loads	5	8 Discussion	12
6 Test results	5	8.1 Recommendation for the maximum load in a flight-simulation test	12
6.1 Results of the flight-simulation tests	5	8.2 Alternatives to flight-simulation	12
6.2 Results of the constant-amplitude tests and damage calculations	6	8.3 Suggestions for further work	13
6.3 Results of the tests on specimens with a central hole	6	9 Conclusions	13
6.4 Some fractographic observations	6	10 List of references	14
7 Analysis of the present results and comparison with data from the literature	7	19 tables	
		19 figures	

This research has been sponsored in part by the Air Force Flight Dynamics Laboratory through the European Office of Aerospace Research, OAR, United States Air Force under Contract F 61052 67 C 0076.

List of Abbreviations and Symbols

GTAC	ground to air cycle (in the literature sometimes: GAG = ground-air-ground transition)
TL	taxiing loads
Crack propagation life:	number of flights for crack growth from $l = 10$ mm to complete failure of the specimen.
l	semi crack length, see fig. 4
n	number of flights (or cycles)
dl/dn	crack propagation rate
Δn	number of flights (or cycles) to cover the crack growth interval from l_i to l_{i+1}
N	crack propagation life, or fatigue life
S_a	stress amplitude
S_m	mean stress
S_{min}	minimum stress
S_{max}	maximum stress
$S_{a,min}$	minimum S_a of the gust cycles
$S_{a,max}$	maximum S_a of the gust cycles
	gross stress (in kg/mm^2 if not specified otherwise)
1 mm	$= 10^{-3}$ meter $= 0.04$ inch; 1 inch $= 25.4$ mm
1 kg/mm^2	$= 1,422$ psi; 1000 psi $= 0.703$ kg/mm^2
1 kc	$= 1$ kilocycle $= 1000$ cycles
1 $\mu/\text{fl.}$	$=$ crack rate of 1 micron (10^{-6} meter) per flight

1 Introduction

Full-scale fatigue testing at the present time is generally accepted as a useful procedure, if not the only one, for evaluating the fatigue qualities of an aircraft structure. Major goals to be achieved are:

- Indication of structural deficiencies, fatigue critical elements.
- Determination of fatigue lives until visible cracking occurs.
- Determination of crack propagation rates in view of inspections.
- Evaluation of inspection procedures.
- Measurements on residual strength.

In order to obtain realistic data on (b) and (c) it will be clear that the fatigue loads to be applied in a full-scale test should be a realistic representation of the load-time history in service. This problem was extensively discussed in ref. 1, which was the Final Report of a preceding investigation. It was concluded in this report that the load sequence should have the character of a flight by flight simulation. This conclusion still leaves various questions to be answered, such as:

- The sequence of loads within each flight, should it be a random sequence or could a programmed sequence be allowed? A fully randomized sequence and a

programmed sequence are thought to be the most extreme possibilities.

- What is the maximum load to be applied in the test (truncation of load spectrum)?
- Could small load fluctuations be omitted from the test in view of time saving?

These three questions were also extensively discussed in ref. 1 and certain recommendations were made. Nevertheless it had to be admitted that more empirical data was urgently desirable.

The present investigation deals with fatigue crack propagation tests on sheet specimens of two aluminum alloys (2024 and 7075). Load sequences were selected in such a way as to shed some further light on the three questions mentioned above. In addition test series were carried out to study the damaging effect of ground-to-air cycles, the effect of reversing the order of positive and negative gusts and the effect of applying only the most severe gust load in each flight. Some constant-amplitude tests were made for damage calculations. A survey of all test series is given in the following chapter.

It should be pointed out that the present test series involves the propagation of visible cracks only. It is thought that the results will be helpful in planning fatigue tests with flight simulation loading on full-scale structures or components, especially if crack propagation has to be studied (fail-safe structures). This report gives a full description of the experiments and the results obtained. The analysis of the data (chapter 7) includes a discussion of related test programs reported in the literature. The report is completed by a general discussion and a number of conclusions.

2 Survey and scope of the test series

A gust load spectrum was approximated by a stepped function as indicated in fig. 1. This spectrum was subsequently broken down into 10 different types of flight (A-K), each characterized by its own load spectrum, varying from "good weather" conditions to "storm" conditions (see chapter 5). The sequence of the various types of flights in the tests was random, while the gusts in each flight were also applied in a random order. A schematic picture of a flight is shown in fig. 1 and a load record of the severest flight is presented in fig. 2. Each gust cycle consisted of an upward gust load immediately followed by a downward gust load of the same magnitude, the mean stress being 7.0 kg/mm^2 (10.0 ksi). Taxiing loads applied in the ground-to-air cycle (GTAC) or air-ground-air transition had a constant amplitude ($S_a = 1.4$ kg/mm^2) and the number of these cycles per GTAC was 20.

As outlined in the introduction, the main purpose of the present investigation was a comparative study of several load sequences to be adopted for flight-simula-

tion testing. A summary of the variables studied in the present test program is given in the table in fig. 1 and a survey of the test parameters is presented in table 1.

a *Truncation of the gust load spectrum.* Extremely high gust loads are very rare. Unfortunately they may have a large effect on crack propagation and since one can not be sure that all aircraft of a fleet will meet the same high gust loads it is a delicate issue to assess the maximum load to be applied in a flight simulation test (ref. 1). In view of this problem comparative tests were carried out with the maximum gust load level (truncation of load spectrum, see fig. 1) as a variable.

b *Omission of small gust loads.* The omission of small gust load cycles in a flight simulation test would save a considerable amount of time since these cycles are relatively numerous, see fig. 3. Since these cycles may still contribute to crack growth comparative tests were made with and without the smallest gust cycles.

c *S_{\min} in the GTAC (ground-to-air cycle).* In some exploratory tests S_{\min} in the GTAC was -1.4 kg/mm^2 whereas in the major part of the investigation a value of -3.4 kg/mm^2 was adopted. This allows a limited comparison to be made.

d *Taxiing loads.* Taxiing loads (TL) are superimposed on the GTAC. For a wing structure they are thought to be relatively unimportant for the fatigue life, except for decreasing the minimum stress level in the GTAC (ref. 1). Comparative tests were made to explore this question, since the omission of the taxiing loads implies again an appreciable time saving. Since the present test program confirmed the negligible damage contribution of the taxiing loads these loads were omitted in various test series of the program when studying other variables (see fig. 3).

e *Omission of the GTAC.* Two test series were carried out without ground-to-air cycles in order to estimate the damaging effect of the GTAC.

f *One gust cycle per flight.* Flight-simulation tests were carried out with only the largest positive gust load of each flight being applied. It implies that in each flight all smaller gust cycles are omitted except for the positive half of the largest one, see fig. 3. This simplification, implying a further time saving, was based on the idea (ref. 2) that the highest (and the lowest) stress level in a flight will have a predominant effect on the fatigue damage contribution of the flight.

g *Reversed random sequence.* In the present tests a positive gust load was always followed by a negative gust load of equal magnitude since this was thought to

be just slightly conservative (ref. 3). The other extreme is that each positive gust load is preceded by a negative one of equal magnitude. In view of a possible influence two test series were carried out with the sequence of each gust cycle in this reversed sequence, see fig. 3.

h *Programmed sequences.* Several test series were carried out with programmed gust load sequences, that means that within each flight the gust load cycles were applied in an increasing-decreasing order of amplitudes, see fig. 3. The sequence of the flights, however, remained unchanged. Such a programmed flight simulation may give indications on the importance of load sequences within a flight.

j *Materials.* Apart from the exploratory tests almost all load sequences were applied to both 7075-T6 and 2024-T3 specimens. This allows a comparison of the two alloys and in addition it may show whether certain influences are more important for one material than for the other.

A small number of tests were carried out on sheet specimens with a central hole instead of a sharp notch. The aim of these tests was to see whether the significant effect of truncation as found for crack propagation also applies to crack nucleation. These tests on specimens of 2024-T3 material, see table 2, were of an exploratory nature only.

After the completion of the flight-simulation tests, a small number of specimens was still left. These specimens have been used for constant-amplitude tests. The results allow some damage calculations to be made. A survey of these tests is given in table 3.

3 Materials and specimens

Specimens were cut from 2024-T3 Alclad and 7075-T6 Clad sheet materials. The nominal thickness of the sheets was 2 mm (0.08 inch). The material properties as determined on tensile specimens cut in the longitudinal and transverse direction from the sheets are given in table 4. The results are considered as being typical for these alloys.

The specimens were cut to a width of 160 mm and a length of 235 mm. The free length between the clampings was 160 mm, that is equal to the specimen width, see figure 4. A sharp central notch was made by drilling a small hole and making two short saw cuts at both sides of the hole. The specimens were subsequently precracked to a crack length $l = 10 \text{ mm}$ (0.4 in) by cycling between $S_{\max} = 10 \text{ kg/mm}^2$ and $S_{\min} = 0 \text{ kg/mm}^2$. Since the stresses in the flight-simulation tests are beyond these values it was thought that an effect of precracking on subsequent crack growth should be negligible.

4 Experimental procedures

4.1 The anti-buckling guides

In order to prevent buckling of the specimens two aluminum alloy plates were used as anti-buckling guides, see fig. 4 and the picture in fig. 5. At the inner side felt was bonded to the plates to minimize the friction between the specimens and the guide plates. Each plate was provided with a window for observation of the crack growth.

The bolts connecting the two plates were hand tightened. The NLR had previously used such a device for riveted joints. Nevertheless it was checked by strain gages whether no load was transmitted through the plates. At the same time these measurements were used to check the stress distribution in the sheet specimen. A dummy specimen without central notch and cracks was provided with three strain gages at each side of the specimen, located at the two ends and the centre of the windows. It turned out that no load transmission through the guide plates could be indicated, provided the bolts were loosely tightened. Moreover sheet bending was practically absent and the stress distribution was satisfactory. Differences between dynamic and static strain readings were in the order of 1% or less. The measurements covered the stress ranges to be applied in the fatigue tests.

After the first preliminary tests were carried out it became desirable to speed up the test program by testing two specimens in series. The specimens are interconnected by two relatively heavy strap plates of steel and a single row of bolts in each specimen. A rigid clamping had to be made since the clamping in the machine itself is also a rigid one. Fig. 6 shows the various parts involved. The anti-buckling guides had to be made larger in order to cover both specimens. Tests were continued until one of the two specimens fractured completely. Since the scatter of the crack rate was low crack growth in the second specimen covered a large part of the cross section.

4.2 The fatigue apparatus

The specimens are loaded in an MTS fatigue machine, type 901.55, maximum dynamic capacity 25 tons. In this hydraulic machine the load control occurs by an electro-hydraulic servo valve in a closed circuit feed back system. The valve is fed by an electric signal representing the required fatigue load. This signal is generated by a piece of apparatus, called PAGE (Programmed Amplitude GEnerator) developed at the NLR. It employs the function generator of the MTS-machine for producing half sine wave functions. PAGE allows any sequence of half sine waves with different amplitudes to be selected as well as a shift between two selected mean values of the cyclic load. The latter is required in view of the GTAC (ground-to-air cycle).

The sequence of amplitudes and the selection of the corresponding mean load is punched into a binary digit tape. A Creed model 92 tape reader is part of the PAGE apparatus. It further includes a patch board on which the cycling frequency can be set separately for each amplitude. In general a lower frequency will be selected for a large amplitude and vice versa.

A sample of a load sequence (recorded at a low loading rate in view of the recorder) is shown in fig. 2. Load frequencies adopted in the tests are 10 cps for the taxiing loads and the lower gust loads ($S_a = 1.1-4.4 \text{ kg/mm}^2$) while for the higher gust loads the frequency was inversely proportional to the stress amplitude, varying from 8 to 3.6 cps for S_a from 5.5 to 12.1 kg/mm^2 .

4.3 The crack propagation tests

Pre-cracking of the specimens occurred in an Amsler High Frequency Pulsator (frequency 100 cycles per second). After pre-cracking the specimens were mounted into the MTS machine and flight simulation loading was started. The propagation of the cracks was observed continuously with a magnifying glass or a stereomicroscope ($30\times$).

The specimens were provided with fine scribe-line markings, see fig. 4. If the tip of a crack just reached such a line the number of flights covered was recorded and these data were used for the evaluation of the crack propagation.

If one specimen of a pair tested in series failed the fatigue life until failure for the other one was obtained by extrapolation of the crack propagation curve employing the data of the fractured specimen, see fig. 7. It will be clear that this will not introduce inaccuracies of any importance. Results obtained did not indicate systematic differences between the results of specimens tested in series and specimens tested separately.

5 The fatigue loads

5.1 The gust loads

A gust spectrum was recently derived in the Netherlands from flight data obtained in England, Australia and the USA. The shape of the spectrum is shown in fig. 1. The gust spectrum was converted into a stress spectrum, by using a conversion factor $1 \text{ ft/sec} \cong 0.3 \text{ kg/mm}^2$ (430 psi), a value frequently adopted by the NLR for program tests. As a mean stress a value $S_m = 7.0 \text{ kg/mm}^2$ (10 ksi) was selected.

For the flight simulation tests the load spectrum as given in fig. 1 had to be distributed over a number of different flights. It will be clear that the load spectrum cannot be the same for all flights since the more severe gusts have an average frequency of occurrence of less than once in a flight. Ten different types of flights were designed, each characterized by its own load spectrum varying from "good weather" conditions to "storm"

conditions. This was done in such a way that the shape of the load spectrum (statistically speaking: the distribution function) is approximately the same for all flights except for the severity which is different. Justification for this procedure is found in gust load measurements evaluated by Bullen (ref. 4), and in the modern power spectral density conception indicating that the shape of the spectral density function of the gust is invariable but the intensity is depending on weather conditions and flying height (ref. 5). Starting from the stepped function in fig. 1 numbers of gust cycles for the flights A–K were obtained as shown in table 5.

The sequence of the gust cycles in the flights is one of the variables to be studied in the present program, that means a random sequence has to be compared with a programmed sequence. It should be noted that each positive gust amplitude is immediately followed by a negative one of equal magnitude. In other words gust cycles are applied as complete cycles around a mean load. This applies to both the random and the programmed sequence, see figure 3. For the random gust loads this is a restriction on the randomness, which is thought to be slightly conservative (ref. 3), see also the discussion in section 7.5.

The sequence of gust cycles of different magnitudes in each flight is a random sequence produced by a computer. An example is shown in fig. 2, see also fig. 3. The sequence of the flights is also random, with the exception of the very severe flights. Since it had to be expected that the severe flights may have a predominant effect on crack growth it was thought undesirable that these flights have a chance to cluster together, which is the risk of a random selection. The most severe flights were therefore uniformly distributed over the total sequence. This is diagrammatically indicated in table 6.

In the tests such a block of 5000 flights was repeated periodically. Since a block of 5000 flights contains approximately 200.000 gust cycles in a random sequence the repetition of the block is thought to be irrelevant with respect to the randomness of the load-time history. It was recommended in ref. 1 that the maximum load in a full-scale flight simulation test should not exceed the load level anticipated 10 times in the desired life time in view of the predominant and favorable effect of larger loads on the fatigue life. If the desired fatigue life is taken as 50.000 flights this leads to a truncation at the load level that will be reached or exceeded once in 5000 flights, that means the maximum level shown in fig. 1.

A similar recommendation was made in ref. 1 for crack propagation. Assuming an inspection period of 500 flights the stress amplitude that is equalled or exceeded 10 times in 500 flights (or 100 times in 5000 flights) according to fig. 1 is about 6.6 kg/mm². This truncation level was used in several test series, but in

addition two higher truncation levels ($S_a=7.7$ and 8.8 kg/mm²) and two lower ones ($S_a=5.5$ and 4.4 kg/mm²) were employed. The test results clearly confirmed the slower crack propagation at higher truncation levels. A few preliminary tests were carried out with the load spectrum shown in fig. 1 fully untruncated.

5.2 The ground-to-air cycles and the taxiing loads

In the preliminary tests the mean stress of the ground-to-air cycles (GTAC) was more or less arbitrarily assessed at $S_m=0$. On this mean stress 20 taxiing loads cycles were superimposed with an amplitude of $S_a=1.4$ kg/mm², the stress range 2.8 kg/mm² thus being 40% of the S_m -value of the gust cycles. A similar pattern for the taxiing loads was adopted previously by Gassner and Jacoby (ref. 6). It was considered to be a relatively severe air-ground-air transition, which was made somewhat more severe for the major part of the tests by adopting $S_m=-2.0$ kg/mm² for the taxiing loads. Since it was expected that the damaging effect of the taxiing loads would be negligible (the tests have confirmed this view) it was thought unnecessary to refine the GTAC by varying both the number and the amplitude of these load cycles, although that would have been possible.

6 Test results

6.1 Results of the flight-simulation tests

In each specimen two cracks were started by the central notch. In general crack propagation was symmetric, that means $l_1 \approx l_2$, and hence all data presented will refer to the average crack length l as defined in fig. 4. The complete crack propagation records for all specimens are presented in tables 7 and 8 by giving the incremental numbers of flights, Δn_i , corresponding to successive crack growth intervals, $l_i \rightarrow l_{i+1}$. The l_i -values were associated to the scribe-line markings on the specimens. The plotting positions for crack propagation curves have not been presented, but they can easily be calculated from the tables. An example with two crack propagation curves is given in fig. 7.

The crack growth data were converted into crack propagation rates by taking at $l=(l_i+l_{i+1})/2$:

$$\frac{\Delta l}{\Delta n} = \frac{l_{i+1} - l_i}{\Delta n_i}$$

This formula in fact gives the average crack rate of the crack growth interval, which is assumed to apply to midpoint of the interval, a sufficient approximation for small intervals. Calculations of the crack rate were made only for the mean result of each test series. The results have been plotted in figs 8–11.

The crack propagation life is defined as the number of flights for crack growth from $l=10$ mm until complete failure. The crack propagation life turned out

to be useful for a first appreciation of the trends emerging from the tests. Results are given in tables 11–17 and figs 13 and 14, which will be used as a starting point for the discussion. For a more refined approach the crack propagation data will be used.

6.2 Results of the constant-amplitude tests and damage calculations

The evaluation of the data was performed in a similar way as for the flight-simulation tests, see table 9. In fig. 15 the results have been plotted as S – N data. Damage calculations could not be made for all tests since insufficient S – N data were obtained. However, it was possible to calculate the $\Sigma n/N$ value for the random tests (2024 specimens) with the GTAC being omitted (series No. 45). This has been done in table 18 and the result was $\Sigma n/N = 3.4$. A still higher value has to be expected for the 7075 specimens since the n -values are approximately half as large as for the 2024 specimens, see table 16, while the N -values are only one fourth approximately (see fig. 15).

Secondly the constant-amplitude data for both materials obtained at $S_a = 1.1$ and 2.2 kg/mm² allowed a prediction on the difference between the crack propagation lives with and without small gust cycles. Adopting the symbols: M = crack propagation life with small gust cycles included, and M' = crack propagation life without small gust cycles being applied, then the Palmgren–Miner rule for a test with the small gust cycles included can be written as:

$$\frac{M}{M'} + M \left(\sum \frac{n}{N} \text{ for the small gust cycles per flight} \right) = 1.$$

With this equation M' may be derived from M or vice versa. In the former case M' becomes infinite for many test series since the damage of the small gust cycles (second term in the equation) is already equalling or exceeding 1. This clearly illustrates that the Palmgren–Miner rule is highly overestimating the damage contribution of the small gust cycles. The same trend is observed when deriving M from M' , that means calculating the reduced fatigue life when small gust cycles are included. The results are shown in table 19 and a comparison is made with the test results. The table shows that the prediction of the reduced fatigue life is much smaller than the reduced test life, again implying an overestimation of the damage contribution of the small gust cycles. This feature is also thought responsible for the high $\Sigma n/N$ obtained in the random tests without GTAC (table 18).

It is noteworthy that the overestimation of the damage contribution of the small gust cycles appears to be larger for the 7075 specimens than for the 2024 specimens, compare the ratios in the last column of table 19.

6.3 Results of the tests on the specimens with a central hole

These tests were carried out on 2024 specimens only. The crack propagation records are given in table 10, while the average crack propagation curves are shown in figure 16. Crack nucleation occurs at the edge of the hole and the nucleation period was arbitrarily defined as the number of flights to create a crack with a length of 2 mm ($l' = 2$ mm or $l = 12$ mm, see fig. 16). The crack propagation life then started and lasted until failure. The variable studied was the truncation level and fig. 16 shows that this level had a large effect on the crack propagation life, similar to the results as found in the normal crack propagation tests, see table 14. However, for the crack-nucleation period the truncation effect is much smaller as clearly illustrated by the life ratios in fig. 16.

In fig. 17 the crack rates in the specimens with a central hole are compared with those of specimens with a small central notch. Comparative results were available only for $S_{a,\max} = 6.6$ kg/mm² (and $S_{a,\min} = 2.2$ kg/mm²). The figure shows that after some crack growth the two curves practically coincide, as might be expected.

6.4 Some fractographic observations

Although the 200 specimens tested would have allowed an extensive fractographic examination this was beyond the scope of the investigation. Some macroscopic observations will be recapitulated below, since they may have some meaning for explaining the trends of the crack propagation results. A few fractographs obtained with the electron microscope will be presented also.

A large number of specimens showed growing bands on the fracture surfaces, that could easily be detected by the unaided eye, see fig. 18. The bands were better visible if the difference between the maximum and the minimum gust amplitude ($S_{a,\max} - S_{a,\min}$) was large, while the bands were virtually absent when this difference was small. A similar correlation was found for the macroscopic roughness of the fracture surface, that means that the surface was relatively smooth for a high value of $S_{a,\max} - S_{a,\min}$ and relatively rough if this difference was small. Both observations indicate that the interaction between high and low amplitude cycles had some effect on the cracking mechanism. Since fatigue striations could not be detected in the dark bands whereas they could be found between the dark bands the dash bands have to be associated with the load cycles with a high amplitude. The dark bands have been associated previously (ref. 7) with some kind of a "brittle" crack extension. Since the bands were more clearly present for a high value of $S_{a,\max} - S_{a,\min}$ the numerous low amplitude cycles apparently are conditioning the material in order to promote the brittle

crack extension in the high amplitude cycles.

Macroscopically the fracture plane of a slowly propagating fatigue crack is perpendicular to the loading direction. When the crack propagation is accelerating the growing direction remains the same but the fracture plane will make an angle of 45 degrees with the loading direction. This transition from the "tensile" mode to the "shear" mode has frequently been observed and has been correlated with the transition from plane strain to plane stress conditions.

In the present investigation the transition was observed in all specimens, but this phenomenon in general did not develop as clearly as under constant-amplitude loading. This is probably a consequence of the variety of amplitudes applied. Low amplitudes will promote the tensile mode, whereas high amplitudes will promote the shear mode. These then are two competing influences and the result is a slow transition from one mode into the other one when the crack is growing.

Unfortunately the transition also occurred during the precracking of the 2024 specimens, while it has occurred to a minor degree in the 7075 specimens, see fig. 18. Consequently the very first part of crack growth in the 2024 specimens may have been influenced by the retransition to the tensile mode. In order to check this point some test series were carried out on specimens precracked to a crack length $l=6$ mm and $l=5$ mm for the 2024 and the 7075 specimens respectively. As shown by plotting the crack rate as a function of the crack length in figs 8b and 8d a noticeable effect of the precracking was found only for the 2024 specimens truncated at a low $S_{a,max}$ value ($S_{a,max}=8.8$ kg/mm²) and this effect was restricted to the very first part of the crack growth. Therefore it will not be considered any further.

It is noteworthy that the macrobands were still visible after the transition from the tensile mode to the shear mode was completed, although it should be said that the bands were less distinct then.

Two-stage carbon replicas for observation in the electron microscope were obtained from the fracture surfaces of several specimens, but as said before, a systematic study was not made. Striations could be observed in all specimens examined and two pictures are shown in fig. 19. In general the striations were more clearly observed in the 7075 specimens than in the 2024 specimens, while several features were found that have been described elsewhere (recently in ref. 8). If it had been possible to indicate the GTAC in the electron graphs this would have been a promising result. However, no confirmation of this possibility was obtained for the random flight simulation tests. In the programmed flight simulation tests certain batches of gust cycles of equal magnitude could easily be indicated, see for instance the lower picture in fig. 19. From this information the striations corresponding to the GTAC

could be indicated in some cases, although in general this still remained difficult.

7 Analysis of the present results and comparison with data from the literature

In the literature comparative investigations concerning macro-crack growth under flight simulation loading could hardly be found. This is somewhat surprising since the problem is an essential part of the fail-safe conception. However, the fatigue life of notched elements under flight simulation was studied in the literature and reference will be made to this work. Secondly some crack propagation studies under random loading without GTAC were also reported in the literature.

In this chapter the various aspects of the present investigation are discussed separately while a general discussion is given in the following chapter. Before the present results will be analysed the possibilities for interaction effects between load cycles of different magnitudes will be discussed first, since that may be helpful for explaining the empirical trends.

7.1 Interaction between load cycles of different magnitudes

If the fatigue load is changed from one level to a second level (by either changing S_a or S_m or both) the fatigue crack propagation at the second level will initially be different from the propagation occurring when the second level had been applied from the beginning of the test. This interaction effect according to macroscopic observations was practically negligible if the change was an increase of the stress amplitude, whereas important crack growth delays were observed if the stress amplitude was reduced (refs 9 and 10). Positive peak loads could most drastically reduce the crack growth. The explanation was based on residual stresses set up in the crack tip region.

In recent publications of the group of McMillan, Pelloux and Herzberg (refs 11, 12 and 13) it has been suggested that crack tip blunting and sharpening as well as cyclic strain hardening may be of more than just secondary importance. This view was based on excellent electron fractography. In addition it appears that changes of the state of stress may also be significant. Low stress amplitudes are associated with slow crack propagation and plane strain at the tip of the crack (tensile mode fracture, macroscopically), while high stress amplitudes will induce fast crack propagation with predominantly plane stress at the tip of the crack (shear mode fracture). Changing from a low amplitude to a high amplitude may then imply that the crack front has not the spatial configuration associated with the high amplitude. The same applies to the reversed amplitude change and this phenomenon will also lead

to interaction effects. It is partly confirmed by the fractographic observations presented in section 6.4.

Listing the various arguments for interaction effects during crack propagation gives:

1. Residual stresses.
2. Crack blunting or sharpening.
3. Cyclic strain hardening (or softening) and associated influences on the material structure.
4. Mismatch between the macroscopic fracture planes as a consequence of different states of stress at the tip of the crack.

It has been known for a long time that crack growth at a certain stress amplitude is depending of the mean stress (or the maximum stress). This result is substantiated by physical conceptions about crack extension (refs 14 and 15). It is then a natural consequence that residual compressive stresses will reduce the crack propagation rate. It is much more difficult to make qualitative predictions on the effect of the other aspects listed above. Crack blunting is a matter of plastic deformations and it therefore will introduce residual stresses. Hence the effect of crack blunting cannot be separated from an additional effect of residual stresses. It is noteworthy, however, that the interaction effects are more significant for the 7075 alloy as compared to the 2024 alloy, see section 7.9. In the former alloy higher residual stresses can be introduced due to the higher yield stress, and secondly crack blunting will be less than in the more ductile 2024 alloy. The larger interactions in the 7075 alloy are then in favor of the residual stress argument rather than crack blunting.

The third and the fourth argument do not readily allow simple speculations. In section 6.4 it was said that low amplitude cycles may condition the material and thus stimulate brittle crack extension at a higher amplitude, which would be an unfavorable interaction.

It is noteworthy that McMillan and Pelloux (refs 11 and 12) on the basis of electron fractography came to the conclusion that interaction effects when changing the fatigue load are hardly observed on the fracture surface. An exception, however, was made for the first cycle applied after changing the fatigue load. There were some indications that interactions might be active then. It was further observed by McMillan and Herzberg (ref. 13) that a drop of S_{max} first induced an increased striation spacing followed by a decreased spacing afterwards. The latter as well as the macroscopically delayed crack growth are compatible with the residual stress argument, whereas the former is not.

An important conclusion from the above discussion is that changing the fatigue load may introduce an interaction that is only significant for the first cycle following that change. The implication is that interaction effects could be very important for random load sequences, since the amplitude is changing from cycle to cycle. However, for tests with a programmed load

sequence such interaction effects may remain almost unnoticed since changing the stress amplitude is a relatively infrequent occurrence.

In conclusion it has to be admitted that with the exception of the influence of residual stresses the qualitative understanding of the other interaction effects is still partly speculative and requires a further systematic study.

7.2 The omission of the taxiing loads (TL) from the ground-to-air cycle (GTAC)

As shown by table 11 the omission of the TL had a practically negligible effect on the crack propagation life. Important arguments are:

- a. The minimum stress in the GTAC (S_{min}) was the same for tests with and without TL.
- b. S_{min} in the GTAC was the lowest stress of a flight.
- c. The TL had a compressive mean stress (-2.0 kg/mm^2).

In view of the last argument it is difficult to see how the TL should contribute to crack growth. In view of arguments (a) and (b) the omission of the TL does not affect the overall loading cycle of a flight. Hence one should expect a negligible effect on the crack propagation life as shown by the tests. This justifies the omission of TL in a flight simulation test, provided that the minimum stress of the GTAC has been adjusted in order to account for the largest taxiing load cycle¹. The omission may save a considerable amount of testing time.

The same reasoning was already presented in ref. 1 for full-scale testing in general. Reference was made there to results of Gassner and Jacoby (ref. 6) who found that the omission of 20 TL cycles per GTAC did not affect the fatigue life in flight simulation tests on notched bars ($K_t=3.1$) of 2024-T3 material.

7.3 The minimum stress of the GTAC

The minimum stress (S_{min}) of the GTAC was in fact not a parameter to be studied in the present test series. However, since some exploratory tests were carried out at $S_{min} = -1.4 \text{ kg/mm}^2$ while for other tests a value of -3.4 kg/mm^2 was adopted a limited comparison could be made. Table 12 shows that the effect of S_{min} for the 7075 specimens was negligible whereas for the 2024 specimens there might be a small systematic effect, that means a shorter crack propagation life if the GTAC is going further downwards. The latter trend has not been well substantiated in view of the small number of tests.

In the GTAC the specimens were loaded in compression and one may expect the crack to be closed and to be no longer a severe stress raiser, since it then can transmit compressive loads. As a consequence the

¹ If a part of a structure is carrying a significant tensile stress during the GTAC it will be clear that TL may give the major fatigue damage contribution and TL should obviously be considered.

effect of S_{\min} should be unimportant. This argument was suggested by Illg and McEvily (ref. 16) who found it to be more applicable to 7075 sheet material as compared to 2024 sheet material. The latter was explained by the higher ductility of the 2024 alloy, implying more crack opening due to plastic deformation in the crack tip area, and hence a larger compressive stress before crack closure occurs. This reasoning is in agreement with the effect of S_{\min} in the GTAC as indicated above.

The meaning of S_{\min} of the GTAC for notched elements will be more important than for macro-cracks, since the crack-closing argument does no longer apply. Hence the assessment of S_{\min} in a full-scale test on a structure should be made most carefully, the more since there is ample evidence of the large damaging influence of the GTAC (refs 1 and 17).

7.4 Omission of the small gust loads

Omission of the smaller gust load cycles implies that a relatively large part of the gust cycles is omitted (see table 5) and hence much shorter durations of the flights will be the result, see fig. 3. Testing times for 5000 flights were:

All gust cycles included: 346 minutes

Gusts with $S_a = 1.1$ kg/mm² omitted: 96 minutes

Gusts with $S_a = 1.1$ and 2.2 kg/mm² omitted: 30 minutes.

The attractive feature of omitting the smaller gust cycles is thus clearly illustrated. However, the omission in general increased the crack propagation life, see table 13 and fig. 13. If the cycles with both $S_a = 1.1$ and $S_a = 2.2$ kg/mm² were omitted the increase of life was about twofold, for both random and programmed flight simulation tests and for two truncation levels ($S_{a,\max} = 6.6$ and 7.7 kg/mm²). When omitting only the smallest cycles ($S_a = 1.1$ kg/mm²) the increase was about 20% for the 2024 specimens and 40% for the 7075 specimens (table 13). The former result is a moderate increase and it might be acceptable under certain circumstances.

The effect of omitting small gust loads is shown in more detail in fig. 9 by plotting the crack rate as a function of the crack length. It turns out that the larger differences are found if the crack rate is low while for relatively large cracks and high crack rates the effect has vanished. The trend is more clear for the 7075 alloy.

For an explanation two lines of thoughts may be considered:

- During the small gust cycles there will be some crack extension. In other words these cycles give some direct contribution to the crack propagation.
- Secondly the small gust cycles may induce an unfavorable interaction effect on the crack extension during larger amplitude cycles, see the discussion in section 7.1.

The fractographic observations (section 6.4) seem to favor the latter view, since the macro growth bands were more readily visible if the small gust cycles were included. However, as pointed out in section 7.1 it remains difficult to separate the contributions of the possibilities (a) and (b).

Comparable evidence was not found in the literature. Tests of McMillan and Pelloux (ref. 11) with programmed sequences (without GTAC and not conforming to a gust spectrum) indicate little if any damage of the low amplitude cycles, but these cycles were so less numerous that a comparison with the present data is hardly justified.

Flight simulation tests on notched elements, involving the effect of omitting small gust cycles were reported by Naumann (ref. 3) and by Gassner and Jacoby (ref. 6). Naumann employing random flight-simulation loading found a small life increase when omitting gust cycles with $S_a = 1.05$ kg/mm², namely 16 and 7 per cent depending of S_{\min} in the GTAC (7075 edge notched specimens, $K_t = 4.0$, $S_m = 14$ kg/mm²). Gassner and Jacoby reported a 2.5 times longer fatigue life in programmed flight simulation tests if the cycles with the smallest amplitude ($S_a = 1.3$ kg/mm²) were omitted (2024 central-notch specimens, $K_t = 3.1$, $S_m = 9.5$ kg/mm²).

7.5 The effect of the gust cycles with a high amplitude

The truncation of the gust spectrum (see fig. 1), implies that the amplitude of the more severe gust cycles are reduced to a common $S_{a,\max}$ -value. The present results have shown that this value has a predominant effect on the crack propagation life, see table 14 and fig. 14. The latter figure clearly illustrates that the effect is large, irrespective of random or programmed gust sequences being adopted and taxiing loads being applied or not. Table 14 further shows that the effect is of a similar magnitude if the two smallest gust cycles are omitted ($S_{a,\min} = 3.3$ kg/mm²). Figure 14 also shows that the effect is slightly larger for the 7075 alloy than for the 2024 material.

The effect of the truncation level is shown in more detail in fig. 8. The figures 8a and 8b indicate that the effect for the 7075 material has a maximum at $l \approx 20$ mm, whereas such a maximum is less clear for the 2024 specimens. Figure 8c including some data for $S_{a,\max} = 12.1$ kg/mm² most dramatically demonstrates the significance of truncating the gust spectrum. A test with $S_{a,\max} = 12.1$ kg/mm² on a 2024 specimen had to be stopped in view of the extremely slow crack growth.

For an explanation the interaction effects mentioned in section 7.1 have to be considered. Since the trends were the same for programmed and random gust sequences and also for random sequences with and without small gust cycles it is thought that residual stresses were indeed the main agent responsible for the

effect of the truncation level.

In view of the predominant and almost frightening effect of $S_{a,max}$ on the crack propagation a few tests were carried out to explore this effect with regard to the life time for crack nucleation from a central hole. These tests were restricted to 2024 specimens and as fig. 16 shows the effect fortunately is much smaller for the nucleation period. It has to be admitted, however, that for the nucleation period the truncation levels were relatively low when considering for instance a target life of 50000 flights. More tests on this topic with respect to the pre-crack life appear to be desirable.

In the literature similar tests concerning crack propagation were not found and there was only one reference for the fatigue life under flight simulation loading for notched elements. Gassner and Jacoby (ref. 6) for a notched bar (2024-T3, $K_t=3.1$, $S_m=9.5$ and 11.0 kg/mm^2) with programmed flight simulation loading reported a 30 and 10 percent life reduction when $S_{a,max}$ was reduced from $2.1 S_m$ to $1.55 S_m$. Qualitatively it is the same trend as in the present investigation.

7.6 Random or programmed sequences in each flight and reversion of the gust cycle

Within a flight the gusts were applied in either a random or a programmed sequence, see fig. 3. As table 15 shows the differences between the crack propagation lives for the two sequences were very small. This is further substantiated by fig. 11. Table 15 gives the impression that the truncation level might have a small systematic effect on the comparison that means that for $S_{a,max}=8.8 \text{ kg/mm}^2$ the crack propagation life with a programmed gust sequence is some 10 percent longer than for the random sequence, while for $S_{a,max}=4.4 \text{ kg/mm}^2$ it is about 7 percent shorter. However, these differences are so small that it cannot be said with any certainty that a systematic trend was found.

In two test series the reversion of the gust cycles

is of secondary importance. Apparently the $S_{a,max}$ -value, within the limits of flight-simulation loading, was the predominant parameter for crack propagation rather than the load sequence in each flight.

Crack propagation under random loading, however, without GTAC but axial loading and positive mean stresses was studied by Smith (refs 18 and 19) for 2024 and 7075 sheet material and for different shapes of the spectral density function of the loading. The results indicated a small influence of the spectral shape. A similar trend was observed for the fatigue life of notched aluminum alloys by Kowalewski (ref. 20, $K_t=1.8$, plane bending, $S_m=0$), Naumann (ref. 21, $K_t=4$, axial loading, $S_m=12.2 \text{ kg/mm}^2$) and Clevenson and Steiner (ref. 22, $K_t=2.2$, axial loading, $S_m=0$). Since the "degree" of randomness is a function of the spectral shape those test programs suggest the sequence of loads to be of minor importance as long as it is random (see also the discussion of Swanson in ref. 23). If periodic loads such as the GTAC are then added to a random load history it may be expected that the sequence effect will be limited even further.

Interesting information is coming from random tests published by Naumann (ref. 3) and Gassner and Jacoby (ref. 24). Naumann performed tests on an edge notched specimen ($K_t=4$) of 7075 material with a random gust loading with and without GTAC. Three types of randomness were adopted, indicated by Naumann as:

1. Random cycle: Each positive half cycle was followed by a negative half cycle of the same magnitude.
2. Random half cycle, restrained: Each positive half cycle was followed by a negative half cycle, the magnitude of which was selected at random from the load spectrum and which therefore was generally not equal to that of the preceding positive half cycle.
3. Random half cycle, unrestrained: Positive and negative half cycles were randomly selected with no restrictions on the sequence of positive and negative.

The results are summarized in the table below.

Randomness	Fatigue life in flights		Fatigue life ratio ^(a)	
	No GTAC	GTAC	No GTAC	GTAC
1. Random cycle	5815	1334	0.66	0.84
2. Random half cycle, restrained	7358	1515	0.84	0.95
3. Random half cycle, unrestrained	8798	1588	1	1

^(a) Ratio = 1 for case (3)

(random sequence) implied that each gust cycle now started with the negative half cycle followed by the positive one of the same amplitude. It turned out that the effect on the crack propagation was practically negligible, see table 16 and fig. 10. This is a second indication that the sequence of the gust loads in a flight

Gassner and Jacoby (ref. 24) performed flight simulation tests with a random gust sequence and with two different programmed sequences. The tests on 2024-T3 specimens ($K_t=3.1$) yielded fatigue lives of 2500, 2800 and 5800 flights respectively. There were approximately 400 gust cycles per flight programmed

in a high-low-high amplitude sequence (life=2800 flights) or in a low-high-low sequence (5800 flights). With such a large number of gust cycles per flight different programming techniques apparently may cause significantly different fatigue lives. Hence a realistic sequence should be preferred. In an additional study (ref. 25) Jacoby performed flight simulation tests on the same specimen loaded with a random sequence of complete gust cycles, or with a random sequence of maxima and minima. The fatigue lives were practically the same. Jacoby also performed tests without GTAC and then found large differences between the fatigue lives under random and programmed load sequences, that means much larger as found in other investigations. The latter result requires further clarification and a discussion is beyond the scope of the present report.

7.7 Application of a single gust load per flight

In the load sequence as shown in fig. 3f, only the largest upward gust of each flight was applied. As a result the crack propagation life was more than 3 times longer as compared to the standard random sequence, see table 16. In fact such a highly simplified load sequence can be envisaged as a simulation of flights from which all gust cycles were omitted except for the positive half cycle with the largest amplitude. The fatigue life is longer than for omitting gust cycles with $S_a = 1.1$ and 2.2 kg/mm^2 as shown by table 16. The effect on the crack rate is illustrated by figs 9c and 9g. Apparently the simplification of applying a simple gust load per flight is unacceptable for crack propagation studies.

7.8 Omission of the GTAC

Omission of the GTAC increased the fatigue life with some 50 and 80 percent for the 7075 and 2024 specimens respectively, see the bottom line of table 16. That means adding the GTAC reduced the fatigue life with 33 and 44 percent respectively. Hence the omission seems to be unjustified. The larger figure for the 2024 alloy may be explained in a similar way as the influence of S_{min} of the GTAC, see section 7.2.

In a previous investigation of this laboratory (ref. 26) crack propagation in 2024 and 7075 sheet material under random and programmed load sequences was studied in an indoor and an outdoor environment. Data on the effect of the GTAC were available for the 2024 material only. The GTAC induced life reductions of 27 and 2 percent for the indoor and the outdoor environment respectively. The small reductions are not surprising when taking notice of the stress levels (kg/mm^2): gusts: $S_m = 12.1$, $S_{a,max} = 11.6$, $S_{a,min} = 1.15$, GTAC: $S_{min} = +2.6$.

In another test series on 2024-T3 Alclad specimens (ref. 27) a constant-amplitude loading ($S_m = 9$ and $S_a = 3 \text{ kg/mm}^2$) was interspersed with GTAC ($S_{min} =$

$+0.7 \text{ kg/mm}^2$) every 50 or every 10 cycles. Reductions of the crack propagation life were 12 and 28 percent respectively.

Much larger reductions have been found in several flight-simulation test series for notched specimens and structures (see for a survey Appendix G of ref. 1) and hence realistic fatigue information requires a flight by flight testing. Although the present data have shown a smaller effect during macro-crack propagation it has to be said that a flight-simulation loading should be preferred also, then, rather than testing without GTAC or testing with ground-to-air cycles applied in groups.

7.9 Comparison between the two alloys, 7075 and 2024

In general all tests were carried out on specimens of both alloys using the same stress-time histories. Without any exception the crack propagation life was larger for the 2024 alloys, and as shown by table 17 approximately twice as large. It was already illustrated by fig. 14 that this ratio was dependent of the $S_{a,max}$ -value, the ratio becoming smaller at higher truncation levels. In this respect it is interesting to compare the crack rates as a function of the crack length, see figures 10 to 12. This shows that the differences between the two alloys become smaller at higher values of the crack length (higher stress intensities), larger values of $S_{a,max}$ and smaller values of $S_{a,min}$. Apparently these trends indicate that favorable interaction effects become more significant in the 7075 material as compared to the more ductile 2024 alloy if the stress intensity at the tip of the crack is increased (higher l and $S_{a,max}$). This argument was referred to in section 7.1.

It is noteworthy that the differences between the two alloys were considerably larger in the constant-amplitude tests, see fig. 15, than in the flight-simulation tests. This is another indication for the more favorable interaction effects in the 7075 alloy.

7.10 Damage calculations

It was shown in section 6.2 that $\sum n/N = 1$ highly underestimates the crack propagation life for the tests without GTAC. Calculations for tests with GTAC could not be made since constant-amplitude data for the GTAC were lacking.

A comparison between predicted crack rates and actual crack rates under random loading conditions (without GTAC) was made by several authors. For a positive mean stress Smith (ref. 18) found the linear damage rule to be conservative (2024 and 7075 material) while Swanson *et al.* (ref. 28) arrived at good estimates (7079 alloy). Both investigations apply to axial load tests. For program loading $\sum n/N$ far in excess of one had previously been found (ref. 29).

As shown by table 18 the damage contribution in the flight-simulation tests should be very small for the higher S_a -values. However, according to the test results,

load cycles with the high S_a -values had a large positive effect on the crack propagation life, rather than a small negative one.

It was already mentioned in section 6.2 that the Palmgren–Miner rule also gave a very bad prediction of the damage of the small gust cycles (table 19). The invalidity of the Palmgren–Miner rule is not a surprising conclusion since interaction effects as discussed in section 7.1 are essentially ignored by this rule. However, from the present data the conclusion can also be given as follows: The effect of changing the load spectrum on the fatigue life cannot be predicted from the Palmgren–Miner rule.

8 Discussion

8.1 Recommendation for the maximum load in a flight-simulation test

The main theme of the present investigation is the question: Which load sequences can be adopted in a flight-simulation test in order to obtain crack propagation data with practical significance? This is an urgent question if fail-safe tests are carried out on a full-scale structure. It appears that the present investigation has shown some variables to be of minor importance and some others to be of major importance.

1. The omission of taxiing loads did not affect the crack propagation.
2. The minimum stress in the GTAC, being compressive, had only a small influence if any.
3. The sequence of the gust cycles in a flight turned out to be of secondary importance.

Influences of major importance were concerned with the following topics:

4. Omission of the gust cycles with small amplitudes did systematically increase the fatigue life, see fig. 13, and should therefore be limited to very small amplitudes (say $S_a \leq 1 \text{ kg/mm}^2$).
5. The predominant effect on the crack propagation was exerted by the maximum gust amplitude ($S_{a,\max}$) included in the test, see fig. 14. Increasing this amplitude gave a considerable decrease of the crack propagation rate.

In fact the selection of $S_{a,\max}$ now appears to be the most delicate issue when planning a flight-simulation program for crack propagation studies. Although it may appear realistic to apply all gust loads that are anticipated to occur, it has to be recognized that one then applies an averaged expected load spectrum. The load spectrum is statistically variable in such a way that the spectrum for a certain aircraft will be more severe, while it will be less severe for another nominally identical aircraft. If the target for the crack propagation life is 2000 flying hours (as an example) the gust load that on the average is reached or exceeded once in that period will be met more than once by some aircraft

while others will not see it. If we then know that this high gust load is highly beneficial for a slow crack propagation it would be both unrealistic and unconservative to include it in a test. A truncation of the load spectrum to a lower level has therefore to be proposed.

In ref. 1 a similar argumentation was already used for full-scale testing in general and it was proposed that a load level exceeded 10 times in the target life should be the maximum level applied in the test. The number of 10 admittedly has been chosen somewhat arbitrary, but the number is thought to be large enough for being sure that each aircraft will meet the load at least a few times. The recommendation presupposes that the load spectrum was estimated as accurately as possible without any unduly over-conservatism.

It now appears that the same recommendation is equally applicable to crack propagation studies. The question then arises as what shall be the target life for crack propagation. For a fail-safe structure the target may obviously be much lower than the anticipated useful life of the aircraft. It has to be associated with the inspection period in service. The proposal is to truncate the load spectrum at the level that will be equalled or exceeded 10 times in the service inspection period. The question of safety factors is again difficult and will not be discussed here. It should be pointed out, however, that the truncation as suggested is in some way accounting for the scatter of the load spectrum.

8.2 Alternatives to flight-simulation

For full-scale fatigue testing only one structure will in general be available and there appears to be no reasonable alternative to a realistic flight-simulation test. This view has been expressed several times, notably by Branger (ref. 30). It appears to be true also for crack propagation. Fortunately the problems of load control in such a test are no longer an objection.

If smaller structural elements have to be tested during the design stage it may be worthwhile to adopt simpler testing methods such as program tests or even constant-amplitude tests. For crack propagation there appears to be as yet no empirical justification for such a procedure. On the contrary the present investigation suggests that interaction effects between load cycles of different amplitudes are important enough to retrieve the main line of service loading. This is the flight-by-flight character, at least for a wing structure mainly loaded by gusts. In other words also then a flight-simulation test has to be advocated. As discussed by Jacoby (ref. 25) this is no longer a problem for modern fatigue machines. A major difficulty, however, is to arrive at a useful flight-simulation load-time history.

If one still uses simpler loading programs in view of available fatigue apparatus one has to consider the uncertainties regarding the relevance of the test results.

Finally an alternative solution might be "calcula-

tions", or borrowing and extrapolating from data in the literature. It is almost euphemistic to state that this problem has not yet been solved. Nevertheless there are certain prospects for the future. A discussion would be beyond the scope of this report.

8.3 Suggestions for further work

1. An obvious recommendation is to perform a similar test program as the present one, but now with typical notched elements as a specimen in order to cover the fatigue life part of the problem. Although some studies were reported in the literature as referred to in the previous chapter (see also the exploratory tests of the present investigation, fig. 16) several aspects have to be studied in more detail.
2. Regarding crack propagation in aluminum alloys systematic studies of interaction effects are certainly worthwhile. In other words the accumulation of fatigue damage is still a topic of present interest, both for practical and fundamental reasons.
3. Fatigue under random loads generally appears to be a useful field for investigations. This topic was extensively reviewed by Swanson (ref. 23) and the recommendations at the end of his recent paper are well taken.
4. A study of the characteristics of flight-simulation loading should be recommended. The application of such load histories in fatigue tests for various purposes has to be considered. One aspect of this problem is the mixture of random and non-random loads.

9 Conclusions

Flight-simulation tests with various load sequences were carried out to study the macro-crack propagation in sheet specimens of 7075-T6 and 2024-T3 clad material. A gust load spectrum was adopted, the mean stress being 7.0 kg/mm^2 (10 ksi). In each test 10 different types of flight were simulated varying from good to bad weather conditions. A variety of load sequences has been adopted related to the truncation of high-amplitude gust cycles, to the omission of low-amplitude gust cycles, taxiing loads and ground to air cycles, and to random and programmed gust sequences in a flight (see figs 1 and 3 and table 1). About 200 specimens were tested. The main results of the investigation are summarized in the conclusions below.

1. Omission of the taxiing loads from the ground-to-air cycles did not affect the crack propagation.
2. In the majority of tests S_{min} of the ground to air cycle was -3.4 kg/mm^2 (4.8 ksi) but in a few exploratory tests a value of -1.4 kg/mm^2 (2.0 ksi) was used. The limit data indicated a practically negligible effect on the crack propagation.
3. Omission of the gust cycles with $S_a = 1.1 \text{ kg/mm}^2$

(75 percent of the cycles) increased the crack propagation life with 20 and 40 percent for the 7075 and 2024 material respectively. Omitting the gust cycles with $S_a = 1.1$ and 2.2 kg/mm^2 (95 percent of the cycles) increased the life with some 100 percent (fig. 13).

4. The predominant effect on the crack propagation life was exerted by the maximum amplitude of the gust cycles (truncation level). Increasing this amplitude from 4.4 to 8.8 kg/mm^2 (6.3 ksi to 12.6 ksi) linearly increased the crack propagation life from 2500 to 15000 flights and from 6000 to 25000 flights for the 7075 and 2024 specimens respectively (fig. 14). The effect was somewhat larger for the 7075 alloy.
5. A programming of the gust cycles in each flight in a low-high-low sequence has given the same crack propagation as for the random sequence.
6. In the majority of tests complete gust cycles were applied, starting with the positive gust followed by the negative one of equal amplitude. Reversion of this sequence in negative-positive did not noticeably affect the crack propagation.
7. Application in each flight of the largest upward gust load only increased the crack propagation life approximately three times.
8. Omission of the ground-to-air cycle increased the crack propagation life approximately 1.5 and 1.8 times for the 7075 and the 2024 specimens respectively. This effect is smaller than usual for the fatigue life of notched elements.
9. The crack propagation life in the flight-simulation tests for the 2024 specimens were on the average twice as long as for the 7075 specimens. The ratio in some additional constant-amplitude tests was larger, namely approximately four.
10. Damage calculations have shown that the Palmgren-Miner rule highly misjudges the effect of changing the load spectrum both in the high-amplitude and in the low-amplitude region.
11. In some exploratory tests on specimens notched by a central hole the effect of truncating the high-amplitude gust cycles was smaller for the crack-nucleation period (up to crack length 2 mm) as compared to the large effect on the subsequent macro-crack propagation (fig. 16).
12. A discussion on interaction effects between load cycles of different magnitudes indicates residual stresses, crack blunting, (cyclic) strain-hardening effects and mismatch between macro-fracture planes as the possible mechanisms for an explanation. It is thought that for the present test series residual stresses had a predominant effect with respect to the trends observed.
13. Conclusions 1-8 have some bearing upon procedures for full-scale tests conducted for obtaining

crack propagation data in view of fail-safe considerations. With respect to the maximum load in such a test it has to be recommended that this load should not exceed the level which is anticipated to be equalled or exceeded ten times in the related inspection period.

List of references

- ¹ Schijve, J., Broek, D., de Rijk, P., Nederveen, A. and Sevenhuysen, P. J., Fatigue tests with random and programmed load sequences with and without ground-to-air cycles. A comparative study on full-scale wing center sections. NLR Report S. 613, Amsterdam, Dec. 1965. Also AFFDL-TR-66-143, Oct. 1966.
- ² Buxbaum, O., and Gassner, E., Häufigkeitsverteilungen als Bestandteil der Lastannahmen für Verkehrsflugzeuge. Luftfahrttechnik-Raumfahrttechnik, Vol. 13, p. 78, 1967.
- ³ Naumann, E. C., Evaluation of the influence of load randomization and of ground-to-air cycles on fatigue life. NASA TN D-1584, Oct. 1964.
- ⁴ Bullen, N. I., The chance of a rough flight. Royal Aircraft Establishment, TR No. 65039, February 1965.
- ⁵ Hoblit, F. H., Paul, N., Shelton, J. D., and Asford, F. E., Development of a power-spectral gust design procedure for civil aircraft. FAA Techn. Report ADS-53, Jan. 1966.
- ⁶ Gassner, E., and Jacoby, G., Betriebsfestigkeitsversuche zur Ermittlung zulässiger Entwurfsspannungen für die Flügelunterseite eines Transportflugzeuges. Luftfahrttechnik-Raumfahrttechnik, Vol. 10, p. 6, 1964.
- ⁷ Proceedings of the Crack Propagation Symposium, Vols 1 and 2, Cranfield 1961.
- ⁸ Broek, D., and Van der Vet, W. J., Systematic electron fractography of fatigue in aluminium alloys. NLR TR 68002, Nov. 1967.
- ⁹ Schijve, J., Fatigue crack propagation in light alloy sheet material and structures. Advances in Aeronautical Sciences, Vol. 3, p. 387. Pergamon Press, 1961.
- ¹⁰ Hudson, C. M., and Hardrath, H. F., Investigation of the effects of variable-amplitude loadings on fatigue crack propagation patterns. NASA TN D-1803, Aug. 1963.
- ¹¹ McMillan, J. C., and Pelloux, R. M. N., Fatigue crack propagation under program and random loads. Fatigue Crack Propagation, ASTM STP 415, p. 505. Am. Soc. Testing Mats., 1967.
- ¹² McMillan, J. C., and Pelloux, R. M. N., Fatigue crack propagation under programmed and random loads. Boeing Scientific Research Laboratories, Doc. D1-82-0558, July 1966.
- ¹³ McMillan, J. C., and Hertzberg, R. W., The application of electron fractography to fatigue studies. ASTM Paper No. 42, 70th Annual Meeting ASTM, Boston, June 1967.
- ¹⁴ Schijve, J., Analysis of the fatigue phenomenon in aluminium alloys. NLR TR M. 2122, July 1964.
- ¹⁵ Schijve, J., Significance of fatigue cracks in micro-range and macro-range. Fatigue Crack Propagation, ASTM STP 415, p. 415. Am. Soc. Testing Mats., 1967.
- ¹⁶ Illg, W., and McEvily, A. J., The rate of fatigue crack propagation for two aluminum alloys under completely reversed loading. NASA TN. D-52, 1959.
- ¹⁷ Jacoby, G., Comparison for fatigue life estimation processes for irregularly varying loads. Proc. 3rd Conference on Dimensioning and Strength Calculations, Hungarian Academy of Sciences, p. 81, Budapest 1968.
- ¹⁸ Smith, S. H., Fatigue crack growth under axial narrow and broad band random loading. Paper in: Acoustical Fatigue in Aerospace Structures, (ed. by W. J. Trapp and D. M. Forney Jr.), p. 331. Syracuse Un. Press, 1965.
- ¹⁹ Smith, S. H., Random-loading fatigue crack growth behavior of some aluminium and titanium alloys. Structural Fatigue in Aircraft, ASTM STP 404. P. 76 Am. Soc. Testing Mats., 1966.
- ²⁰ Kowalewski, J., On the relation between fatigue lives under random loading and under corresponding program loading. Full-Scale Fatigue Testing of Aircraft Structures (ed. by F. J. Plantema and J. Schijve), p. 60, Pergamon Press, 1961.
- ²¹ Naumann, E. C., Fatigue under random and programmed loads. NASA TN D-2629, Febr. 1965.
- ²² Clevenston, S. A., and Steiner, R., Fatigue life under random loading for several power spectral shapes. NASA TR R-266, Sept. 1967.
- ²³ Swanson, S. R., Random load fatigue testing: A state of the art survey. Materials Research and Standards, Vol. 8, No. 4, p. 11, April 1968.
- ²⁴ Gassner, E., and Jacoby, G., Experimentelle und Rechnerische Lebensdauerbeurteilung von Bauteilen mit Start-Lande-Lastwechsel. Luftfahrttechnik-Raumfahrttechnik, Vol. 11, p. 138, 1965.
- ²⁵ Jacoby, G., Comparison of fatigue lives under conventional program loading and digital random loading. Paper presented at the ASTM Fall Meeting, Atlanta, 29 Sept.-4 Oct. 1968.
- ²⁶ Schijve, J., and de Rijk, P., The crack propagation in two aluminium alloys in an indoors and an outdoors environment under random and programmed load sequences. NLR-TR M. 2156, Nov. 1965.
- ²⁷ Schijve, J., and de Rijk, P., The effect of ground-to-air cycles on the fatigue crack propagation in 2024-T3 Alclad sheet material. NLR Report M. 2148, July 1965.
- ²⁸ Swanson, S. R., Cicci, F., and Hoppe, W., Crack propagation in clad 7079-T6 aluminum alloy sheet under constant and random amplitude fatigue loading. Fatigue Crack Propagation, ASTM STP 415, p. 312. Am. Soc. Testing Mats., 1967.
- ²⁹ Schijve, J., and Broek, D., Crack propagation. The results of a test programme based on a gust spectrum with variable amplitude loading. Aircraft Engineering, Vol. 34, p. 314, 1962. Also NLR MP. 208, Dec. 1961.
- ³⁰ Branger, J., The full-scale fatigue test on the DH-112 Venom AC carried out on the fatigue history simulator by F and W, Emmen. Eidg. Flugzeugwerk Emmen, Bericht S-163, 1964.

TABLE 1: Survey of the test parameters in the various test series

Stresses in kg/mm^2 , $1 \text{ kg}/\text{mm}^2 = 1.422 \text{ ksi}$; Gust cycles: $S_m = 7.0 \text{ kg}/\text{mm}^2$; Taxiing loads: $S_{\max} - S_{\min} = 2.8 \text{ kg}/\text{mm}^2$, 20 cycles per GTAC

Load sequence	GTAC		Gust loads		Test series No. ^(a)		
	S_{\min}	Taxiing loads	$S_{a,\max}$	$S_{a,\min}$	7075-T6	2024-T3	
Random (exploratory tests)	-1.4	yes	12.1	1.1	1 (1)	2 (1)	
			7.7		3 (1)		
			6.6		4 (1)	7 (1)	
			5.5		5 (1)		
			4.4		6 (1)	8 (2)	
Random	-3.4	yes	8.8	1.1	9 (1)		
			7.7		10 (5)	21 (1)	
			6.6		11 (5)	22 (5)	
			7.7	3.3		23 (1)	
					6.6	12 (4)	24 (4)
		no	8.8	1.1		13 (4)	25 (4)
						13a (2)	25a (2)
						14 (4)	26 (5)
						15 (6)	27 (4)
						15a (2)	27a (2)
						16 (4)	28 (4)
						17 (4)	29 (4)
			17a (4)	29a (2)			
			6.6	2.2	18 (4)	30 (4)	
			7.7	3.3	19 (2)	31 (3)	
	6.6		20 (4)	32 (4)			
	1 gust load per flight ^(b)			46 (4)	47 (4)		
	GTAC omitted		6.6	1.1	44 (4)	45 (4)	
Random, reversed gusts	-3.4	no	6.6	1.1	42 (4)	43 (4)	
Programmed	-3.4	yes	7.7	1.1	41 (1)		
		no	8.8	1.1	33 (4)	37 (4)	
			6.6		34 (4)	38 (4)	
			4.4		35 (4)	39 (4)	
	6.6	3.3	36 (4)	40 (4)			

^(a) The numbers between brackets indicate the number of tests carried out.

^(b) $S_{a,\max} = 6.6$.

TABLE 2: Survey of the flight-simulation tests on sheet specimens with a central hole.

Specimen size: Length and width similar to crack propagation specimen, see fig. 4. Central hole with diameter 20 mm.

Material: 2024-T3 Alclad; Gust cycles: $S_m = 7.0 \text{ kg}/\text{mm}^2$; Stresses in kg/mm^2 , $1 \text{ kg}/\text{mm}^2 = 1.422 \text{ ksi}$.

Load sequence	GTAC		Gust loads		Test series No. ^(a)
	S_{\min}	Taxiing loads	$S_{a,\max}$	$S_{a,\min}$	
Random	-3.4	no	8.8	2.2	48 (4)
			6.6		49 (4)
			4.4		50 (4)

^(a) The numbers between brackets indicate the number of tests carried out.

TABLE 3

Survey of the constant-amplitude tests.

 $S_m = 7.0 \text{ kg/mm}^2$, load frequency 10 cycles per second.

Material	S_a (kg/mm^2)	Specimen No.	Crack propagation life (kilocycles)
7075-T6	2.2	B19/B7	31.3/32.0
	1.1	B80/B93 B6/B13	192/181 (^a)
2024	8.8	A61	2.65
	6.6	A55	8.63
	4.4	A54	21.2
	2.2	A50/A105	124/125
	1.1	A44 A7/A57	1031 (^b)

^(a) Crack propagation started at $l \geq 18 \text{ mm}$ } Specimens previously used for^(b) Crack propagation started at $l \geq 14 \text{ mm}$ } flight-simulation tests.

TABLE 4

Static properties of the materials.

Material	Direction of loading	S_u		$S_{0.2}$		Elongation (2 in. gage length)
		(kg/mm^2)	(ksi)	(kg/mm^2)	(ksi)	
2024-T3 Alclad	Longitudinal	47.4	67.4	36.0	51.2	18%
	Transverse	45.6	64.8	31.0	44.1	21%
7075-T6 Clad	Longitudinal	53.9	76.6	48.5	69.0	13%
	Transverse	54.1	76.9	47.2	67.1	13%

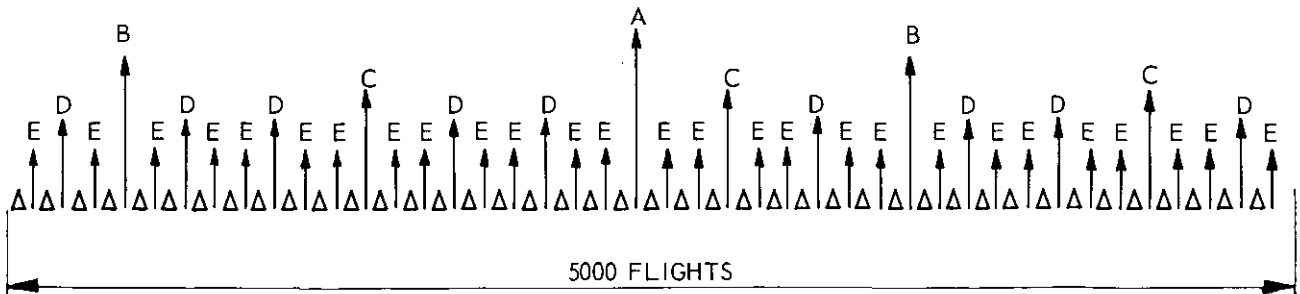
All data in this table are mean values of six tests.

TABLE 5

Gust load occurrences in the 10 different types of flights

Flight type	Number of flights in 5000 flights	Number of gust cycles with amplitude S_a (kg/mm^2)											Total number of cycles per flight
		$S_a=12.1$	$S_a=11.0$	$S_a=9.9$	$S_a=8.8$	$S_a=7.7$	$S_a=6.6$	$S_a=5.5$	$S_a=4.4$	$S_a=3.3$	$S_a=2.2$	$S_a=1.1$	
A	1	1	0	1	1	2	3	5	9	15	27	43	107
B	2		1	1	1	1	2	4	8	14	26	43	101
C	2			1	1	1	2	3	7	12	25	43	95
D	10				1	1	1	3	5	11	24	43	89
E	27					1	1	2	3	9	22	43	81
F	91						1	1	3	7	18	43	73
G	301							1	2	4	15	42	64
H	858								1	3	11	38	53
J	3165									1	7	28	36
K	543										1	19	20
Total number of cycles in all flights		1	2	5	15	43	139	495	1903	8000	39252	149902	
Number of exceedings, see fig. 1		1	3	8	23	66	205	700	2603	10603	49855	199757	

TABLE 6
Diagrammatic picture of the sequence of the various flights in 5000 flights



The most severe flights A, B, C, D, E, are shown separately. These flights are homogeneously distributed over a sequence of 5000 flights. Δ indicates a group of 118 flights.

The 42 groups Δ consist of a random sequence of: 91 flights type F; 301 flights type G; 858 flights type H; 3165 flights type J; 543 flights type K.

TABLE 7

Crack propagation records of the flight-simulation tests. Values of Δ*n* in numbers of flights.

First column: crack length interval. First and second line: Test series No. and Specimen No. A dash indicates that the two specimens were tested in series. Arithmetical mean values of Δ*n* are given in the last columns of the test series. The two bottom values in these columns are the arithmetical and the geometrical mean values of the crack propagation lives (*l*=10-80 mm).

<i>l_i-l_{i+1}</i> (mm)	3		4		5		6		7		8		9		10		
	B21	B90	B50	B41	A2	A47	A1	Mean	B2	B20/B89	B22/B71	Mean					
10-12	584	668	407	366	1631	951	—	951	589	452	661	591	602	577			
12-14	748	390	304	229	1999	848	—	848	764	642	652	566	725	646			
14-16	668	392	301	208	1862	705	—	705	1027	735	688	657	717	699			
16-18	708	359	223	176	1723	585	—	585	909	716	657	594	701	667			
18-20	706	316	212	162	1496	517	783	650	973	818	781	658	785	761			
20-25	1800	328	596	306	3270	989	1141	1065	3151	1805	1826	1718	1795	1795			
25-30	1762	428	408	225	1892	883	786	835	2569	1568	1561	1572	1624	1581			
30-35	1368	936	350	200	1390	455	524	480	1789	1106	1089	1177	1076	1112			
35-40	947	302	223	184	675	271	319	295	1073	535	—	736	484	585			
40-45	342	129	78	85	342	141	165	153	338	127	—	339	—	233			
45-50	111	45	52	44		69	64	67	148	—	—	74	—	74			
50-55	—	—	—	16	28	15	24	20	49	—	—	17	—	17			
10-80	9617	4800	3075	2205	16308	6240	6793	6516 6511	13406	8568	8641	8716	8956	8720 8719			

<i>l_i-l_{i+1}</i> (mm)	11					12					13					
	B67/B24	B42	B4/B53	Mean	B27/B76	B47/B96	Mean	B25/B60	B45/B94	Mean						
10-12	1227	556	632	612	575	594	1444	1236	1787	1845	1578	819	548	912	588	717
12-14		571	606	587	700	616	1594	1580	1621	2982	1598	912	863	891	777	861
14-16	448	545	474	585	625	535	1332	1390	1448		1390	1064	1081	918	887	988
16-18	452	416	362	502	546	456	1005	1198	1269	1262	1184	1253	1282	1179	1051	1191
18-20	397	359	424	474	486	428	875	958	1052	1100	996	1167	1187	1275	1270	1225
20-25	1020	1113	911	1088	1253	1077	1440	1629	1358	1795	1556	3274	3345	3442	3028	3272
25-30	902	933	911	895	994	927	523	—	736	891	717	2570	2427	2959	2592	2637
30-35	834	750	785	701	631	600	370	—	400	404	391	—	1217	—	1655	1436
35-40	181	—	424	345	—	317	245	—	230	—	238	—	585	—	664	625
40-45	86	—	136	109	—	110	103	—	108	—	106	—	254	—	295	275
45-50	64	—	44	51	—	53	58	—	—	—	58	—	120	—	39	80
50-55	24	—	2	45	—	24	—	—	—	—	—	—	27	—	—	14
10-80	5637	5600	5809	6001	6437	5897 5889	9010	9311	10089	11182	9898 9863	13269	12943	14298	12915	13356 13329

(continued)

TABLE 7 (continued)

$l_i - l_{i+1}$ (mm)	14					15							16				
	B40/B69		B8/B77		Mean	B88/B39		B68/B15		B5/B54		Mean	B57/B28		B48/B91		Mean
10-12	611	733	657	552	640	514	625	650	470	1164	752	602	435	472	436	503	462
12-14	591	778	712	710	698	475	429	500	486		581	494	379	443	452	405	420
14-16	659	721	750	733	716	387	440	479	432	558	573	477	328	317	342	364	338
16-18	651	687	713	673	681	395	397	429	503	448	405	430	282	343	319	337	320
18-20	786	762	811	723	773	346	364	395	334	414	449	384	309	299	289	278	294
20-25	1994	2230	1985	1812	2005	863	950	900	874	1123	1115	971	587	627	624	621	615
25-30	1943	1825	1765	1634	1792	763	848	841	797	1027	877	859	466	751	825	887	509
30-35	1374	1351	1239	1210	1294	475	—	521	545	—	487	507	267				887
35-40	749	565	—	654	656	183	—	203	227	—	206	205	197	156	134	141	157
40-45	168	—	—	227	198	104	—	82	—	—	81	89	71	94	63	—	76
45-50	—	—	—	80	80	37	—	47	—	—	38	41	35	—	40	—	38
50-55	—	—	—	—	—	14	—	—	—	—	13	14	—	—	—	—	—
10-80	9583	10061	9624	9019	9572 9565	4555	4865	5047	4738	5685	5583	5079 5062	3390	3571	3541	3656	3540 3538

$l_i - l_{i+1}$ (mm)	17					18					19			20				
	B30/B73		B10/B59		Mean	B43/B92		B29/B78		Mean	B51/B85		Mean	B72/B23		B3/B52		Mean
10-12	417	322	359	345	361	810	810	927	979	882	2406	2776	2591	1660	1628	2016	1945	1812
12-14	316	274	342	222	289	773	770	846	808	799	2048	2534	2309	1770	1802	1681	1608	1715
14-16	234	248	168	219	217	771	810	849	811	810	2418	2400	2409	1576	1121	1219	1418	1334
16-18	237	231	417	174	214	893	845	759	758	814	2247	2820	2534	1162	1055	1141	1239	1149
18-20	202	161		194	186	591	566	1880	2054	579	1765	1746	1756	902	925	991	936	939
20-25	402	392	413	299	377	1571	1278			1425	5200	4919	5060	1125	1455	1335	1605	1380
25-30	359	317	337	288	325	1020	917	675	1078	923	2774	2937	2856	807	773	675	749	751
30-35	151	184	—	193	176	371	554	405	—	443	940	—	940	254	381	310	218	291
35-40	128	121	—	133	127	203	323	159	—	228	370	—	370	185	211	219	—	205
40-45	—	66	—	65	66	—	112	89	—	101	—	—	—	85	92	131	—	103
45-50	—	40	—	21	31	—	34	34	—	34	—	—	—	—	—	43	—	13
50-55	—	8	—	9	9	—	—	14	—	14	—	—	—	—	—	9	—	9
10-80	2565	2369	2461	2165	2390 2385	7159	7029	6649	7200	7009 7006	20552	21826	21189 21179	9515	9532	9872	10214	9783 9779

$l_i - l_{i+1}$ (mm)	21	22					23	24				25						
	A81	A24	A84/A43		A99/A4	Mean	A48	A63/A6		A22/A79	Mean	A12/A69		A35/A85		Mean		
10-12	1790	1655	1466	1198	1267	1237	1365	3093	3117	3528	2916	3436	3249	1706	1663	2194	1881	1861
12-14	2150	1269	1450	1461	1357	1473	1402	4893	2801	3038	3132	3297	3063	3365	2993	3336	3727	3355
14-16	2004	1127	1234	1369	1402	1482	1323	3839	2300	2760	2817	2667	2638	3420	3444	2946	3804	3404
16-18	1848	1019	1211	1256	1108	1280	1175	3608	2117	2114	2255	2426	2228	3205	2858	2899	3383	3086
18-20	1548	950	906	1070	1023	1084	1007	3122	1792	2261	1871	1842	1942	2615	2541	2127	2430	2428
20-25	2829	1748	1940	2119	2073	2376	2051	—	3427	3805	3672	3797	3675	4573	4362	3980	4635	4388
25-30	1848	1233	1259	1406	1407	1453	1352	—	2070	—	2156	2233	2153	2838	2418	2407	—	2554
30-35	1067	816	784	852	802	—	814	—	1094	—	1005	—	1050	—	1474	1194	—	1334
35-40	502	367	361	—	404	—	377	—	319	—	383	—	351	—	657	613	—	635
40-45	216	193	141	—	181	—	172	—	145	—	158	—	152	—	170	—	—	170
45-50	110	37	33	—	—	—	35	—	43	—	35	—	39	—	84	311	—	84
50-55		—	—	—	—	—	—	—	—	—	—	—	—	—	—	14	—	—
10-80	15921	10427	10808	11189	11112	10860	10879 10876	31000	19236	21196	20405	21284	20530 20513	24126	22683	22034	24410	23313 23292

(continued)

TABLE 7 (continued)

$l_i - l_{i+1}$ (mm)	26					27					28				
	A11/A68		A34/A91		Mean	A78/A28		A5/A100		Mean	A31/A88		A8/A65		Mean
10-12	1896	1440	1599	1816	1688	1542	1404	1381	1665	1498	1177	1202	1201	1210	1198
12-14	2231	2306	1915	2267	2180	1352	1398	1549	1542	1460	973	1008	1053	977	1003
14-16	2170	2197	2010	2205	2146	1260	1391	1466	1403	1380	832	898	967	839	884
16-18	1785	1996	1873	1875	1882	1148	1227	1146	1216	1184	812	750	713	742	754
18-20	1601	1647	1487	1493	1557	955	1117	1197	1046	1079	687	684	670	639	670
20-25	3063	3311	2502	2725	2900	1968	2130	2151	2218	2116	1226	1271	1235	1236	1242
25-30	1874	1957	1670	1788	1822	1370	1482	1447	1445	1436	953	982	915	921	943
30-35	1137	1115	1081	—	1111	817	855	913	870	864	594	622	570	565	588
35-40	633	519	428	—	527	441	—	469	423	444	301	334	282	306	306
40-45	194	—	187	—	191	193	—	216	203	204	46	—	120	147	138
45-50	60	—	50	—	55	63	—	81	—	72	70	—	40	61	57
50-55	36	—	—	—	36	29	—	26	—	28	12	—	—	—	12
10-80	16685	16783	14798	15915	16045 16025	11144	11736	12056	12217	11788 11781	7768	7984	7809	7676	7814 7813

$l_i - l_{i+1}$ (mm)	29					30					31				
	A33/A90		A10/A67		Mean	A9/A66		A32/A89		Mean	A82	A3/A104		Mean	
10-12	904	997	949	889	935	1982	2288	1733	1595	1900	2690	3105	3848	3214	
12-14	736	789	763	769	764	1899	1939	1791	1859	1872	4657	4387	5367	4804	
14-16	628	658	649	656	648	1741	1902	1581	1506	1683	4073	4078	4217	4123	
16-18	567	592	593	664	604	1547	1424	1574	1370	1479	3460	3660	4124	3748	
18-20	490	450	527	506	493	1281	1312	1224	1215	1258	2852	3513	3549	3305	
20-25	891	880	900	916	897	2508	2583	2453	2260	2451	5739	6133	6275	6050	
25-30	580	620	557	654	603	1732	1742	1639	1512	1656	3425	4213	3926	3855	
30-35	380	—	384	393	386	981	977	—	912	957	1854	2090	—	1972	
35-40	266	—	254	—	260	527	485	—	364	459	642	—	—	642	
40-45	131	—	124	—	128	—	188	—	170	179	206	976	—	206	
45-50	57	—	53	—	55	—	61	—	73	67	49	97	—	73	
50-55	—	—	15	—	15	—	21	—	—	21	26	—	—	26	
10-80	5661	5849	5767	5898	5794 5793	14470	14924	13536	12858	13947 13924	29482	32249	34466	32066 32000	

$l_i - l_{i+1}$ (mm)	32					33					34				
	A42/A83		A60/A26		Mean	B14/B84		B35/B61		Mean	B12/B55		B46/B75		Mean
10-12	2823	2554	2141	2740	2565	593	781	719	745	710	505	568	500	488	515
12-14	3153	3141	2907	3265	3117	821	1056	904	1051	958	575	527	413	479	499
14-16	2511	2725	2680	2737	2663	939	1043	1070	1029	1020	404	490	430	436	440
16-18	2166	2314	2400	2503	2346	1048	1386	1035	1196	1166	456	414	402	397	417
18-20	1950	2035	2105	2005	2024	1299	1514	1254	1377	1361	351	436	389	375	388
20-25	3685	3765	3675	4177	3826	3188	2958	3696	3815	3414	966	1035	945	955	975
25-30	2405	2460	2518	2693	2519	2493	3800	2823	2520	2909	826	837	815	809	822
30-35	760	120	1202	—	994	2036	—	1989	1741	1922	593	—	747	536	626
35-40	550	—	444	—	497	828	—	833	910	857	212	—	—	225	219
40-45	180	—	149	—	165	—	—	228	—	228	74	—	—	111	93
45-50	50	—	72	—	61	—	—	110	—	110	—	—	—	45	45
50-55	—	—	31	—	31	—	—	40	—	40	—	—	—	—	—
10-80	20170	20571	20327	22021	20772 20759	13534	15614	14710	14833	14673 14670	5045	5269	5052	4886	5063 5061

(continued)

TABLE 7 (continued)

$l_i - l_{i+1}$ (mm)	35					36					37				
	B18/B66		B33/B82		Mean	B16/B63		B31/B83		Mean	A16/A94		A40/A71		Mean
10-12	352	331	351	302	334	1135	1306	1079	1090	1153	2848	2458	2990	2115	2603
12-14	257	236	229	253	244	1105	1261	1079	1094	1135	4394	5024	4463	3230	4278
14-16	218	210	226	219	218	1359	1177	1016	1037	1147	3874	4434	4675	3502	4121
16-18	207	212	187	205	203	1103	1188	1072	1140	1126	3148	3787	3756	2850	3385
18-20	160	166	174	162	166	943	1142	773	945	951	2542	2960	2710	2682	2724
20-25	349	326	380	360	354	1855	1596	1473	1674	1650	4373	4695	—	4109	4392
25-30	312	303	235	263	278	890	1126	915	830	940	2558	2615	—	2257	2477
30-35	215	197	196	201	202	461	—	750	—	606	1200	—	—	1505	1353
35-40	—	137	120	122	126	—	—	232	—	232	633	—	—	612	623
40-45	—	49	51	—	50	—	—	97	—	97	189	—	—	149	169
45-50	—	21	22	—	22	—	—	53	—	53	—	—	—	—	—
50-55	—	11	9	—	10	—	—	—	—	—	—	—	—	—	—
10-80	2289	2170	2186	2179	2206 2205	9271	9667	8161	8660	8940 8921	25856	28092	27418	23203	26142 26072

$l_i - l_{i+1}$ (mm)	38					39					40				
	A13/A70		A29/A86		Mean	A14/A64		A53/A87		Mean	A17/A95		A41/A72		Mean
10-12	1370	1364	1558	1492	1446	790	851	940	799	845	2627	2869	3292	3684	3118
12-14	1438	1496	1468	1370	1443	766	737	813	694	753	2961	2858	3102	2751	2918
14-16	1920	1654	1332	1237	1536	619	613	560	664	614	2667	2742	3128	2843	2845
16-18	698	883	1112	1253	987	560	525	497	527	527	1958	2226	2115	2524	2206
18-20	1033	1057	957	1066	1028	476	468	436	445	456	1897	1916	2037	1843	1923
20-25	2070	2043	2015	2063	2048	802	856	879	890	857	3557	3640	3752	3744	3673
25-30	1496	1434	1266	1400	1399	474	597	611	547	557	2025	2224	2344	2158	2188
30-35	888	835	781	878	846	416	412	406	337	393	984	—	1110	1033	1042
35-40	—	455	355	—	405	253	219	—	234	235	408	—	439	443	430
40-45	—	158	176	—	167	93	—	—	107	100	159	—	—	161	160
45-50	—	46	56	—	51	57	—	—	42	50	40	—	—	55	48
50-55	—	—	21	—	21	25	—	—	17	21	—	—	—	24	24
10-80	11572	11423	11101	11371	11367 11365	5384	5445	5546	5307	5421 5420	19290	20071	21356	21278	20499 20480

$l_i - l_{i+1}$ (mm)	41	42					43					44				
	A59	B17/B79		B32/B64		Mean	A18/A96		A36/A73		Mean	B9/B58		B26/B86		Mean
10-12	1509	522	577	460	591	538	1594	1630	1431	1507	1541	797	594	786	771	737
12-14	2237	463	492	409	488	463	1214	1626	1330	1321	1373	720	682	703	670	694
14-16	2376	463	430	393	415	425	1292	1453	1341	1363	1362	655	630	548	651	621
16-18	2145	406	439	380	433	415	924	1285	1204	1009	1106	663	560	557	566	587
18-20	1826	379	368	367	327	360	942	1164	946	994	1012	637	599	535	546	579
20-25	3565	842	944	701	846	833	1986	2173	1894	1950	2001	1349	1382	1184	1304	1305
25-30	2362	743	847	680	782	763	1349	—	1472	1336	1386	1074	1015	1014	1082	1046
30-35	1316	643	643	555	—	614	821	—	867	882	857	923	956	856	962	924
35-40	655	372	—	261	—	316	368	—	382	422	391	713	706	649	682	688
40-45	237	102	—	93	—	98	159	—	150	—	155	—	—	175	—	175
45-50	136	27	—	28	—	28	64	—	58	—	61	—	—	91	—	91
50-55	36	—	—	28	—	28	21	—	—	—	21	—	—	—	—	—
10-80	18413	4975	5254	4359	4861	4862 4851	10737	12116	10941	11002	11199 11184	7921	7514	7127	7529	7523 7518

(continued)

TABLE 7 (continued)

$l_i - l_{i+1}$ (mm)	45					46					47				
	A45/A101		A30/A93		Mean	B37/B56		B11/B74		Mean	A19/A74		A37/A97		Mean
10-12	2451	2576	2881	3083	2748	2394	2550	2384	2135	2366	6337	8573	5516	5980	6602
12-14	2092	2354	2392	2498	2334	1980	2320	2027	2125	2113	6089	4672	5924	5668	5588
14-16	2128	2219	2251	2242	2210	2225	2150	2180	2210	2191	4780	4741	4701	4317	4635
16-18	1861	1914	1930	2093	1950	1827	2162	1765	1726	1870	4179	4353	4138	3869	4135
18-20	1740	1745	1802	1812	1775	1508	1508	1802	1296	1529	3700	3839	3498	3110	3537
20-25	3610	3670	3721	3830	3708	—	2340	—	1860	2100	6771	6948	6284	6050	6513
25-30	2664	2689	2640	2778	2693	—	1465	—	945	1205	2963	3523	3801	3025	3328
30-35	1716	1899	1810	1829	1814	—	493	—	619	556	1542	—	—	1369	1456
35-40	1010	—	994	—	1002	—	337	—	339	338	596	—	—	447	522
40-45	456	—	490	—	473	—	139	—	204	172	203	—	—	233	218
45-50	115	—	139	—	127	—	81	—	87	84	81	—	—	71	76
50-55	—	—	54	—	54	—	23	—	24	24	—	—	—	—	—
10-80	19870	20674	21121	21859	20881 20869	14916	15572	14239	13573	14575 14556	37266	39096	35995	34152	36627 36583

TABLE 8

Crack propagation records of the additional flight-simulation tests. Values of Δn in numbers of flights.

First column: crack length interval. First and second line: test series No. and specimen No. Mean values are arithmetical averages.

Material 7075-T6 Clad

$l_i - l_{i+1}$ (mm)	13a			15a			17a				
	B44/B62		Mean	B36/B49		Mean	B87/B95		B6/B13		Mean
5-6	381	495	438	434	404	419	260	317	333	318	307
6-7	590	509	550	432	408	420	250	285	274	236	261
7-8	439	402	421	334	286	310	222	186	231	226	216
8-9	425	430	428	264	270	267	162	183	194	191	183
9-10	386	353	370	263	317	290	185	182	185	214	192
10-12	761	737	749	417	409	413	224	240	266	224	239
12-14	819	744	782	398	480	439	204	202	232	211	212
14-16	1021	903	962	394	367	381	189	185	199	218	197
16-18	1009	1237	1123	331	375	353	137	140	161	145	146

Material 2024-T3 Alclad

$l_i - l_{i+1}$ (mm)	25a			27a			29a		
	A46/A102		Mean	A23/A75		Mean	A7/A57		Mean
6-7	2354	1663	2008	1446	1531	1489	932	1072	1002
7-8	2888	2926	2907	1168	938	1053	712	781	746
8-9	2697	2658	2677	1059	993	1026	649	706	677
9-10	2637	2878	2757	954	885	920	568	586	577
10-12	5175	5047	5111	1817	1681	1749	948	1016	982
12-14	3947	4358	4152	1448	1493	1470	738	829	783

TABLE 9: Crack propagation records of the constant-amplitude tests. Values of Δn in cycles.First column: Crack length interval. Second line: stress amplitude in kg/mm^2 . Third line: specimen No. Mean values are arithmetical averages.

7075-T6							2024-T3							
$l_i - l_{i+1}$ (mm)	$S_a = 2.2$		$S_a = 1.1$				$S_a = 8.8$	$S_a = 6.6$	$S_a = 4.4$	$S_a = 2.2$		$S_a = 1.1$		
	B19/B7	Mean	B6/B13	B80/B93	Mean	A61	A55	A54	A50/A105	Gem.	A44	A7/A57	Mean	
10-12	4941 5277	5109	— —	56410 34168	45289	855	1795	4220	23700 21785	22743	247080 — —	— —	247080	
12-14	3361 3320	3341	— —	21545 26035	23790	558	1470	3195	15700 18470	17085	155240 — —	— —	155240	
14-16	2942 2708	2825	— —	17200 19735	18468	338	1145	2790	14320 13590	13955	101735 — —	— —	101735	
16-18	2396 2465	2431	— —	12005 14495	13250	210	945	1930	11315 11880	11598	89740 73219 91344	— —	84768	
18-20	2230 2250	2240	— —	12035 12405	12220	185	620	1790	8920 10185	9553	70615 67695 59066	— —	65792	
20-25	4315 4475	4395	23600 19900	20205 23790	21874	240	1200	3040	17455 17215	17335	124945 112803 121636	— —	119795	
25-30	3165 3248	3207	16795 16000	14985 15443	15806	140	715	1855	12363 11765	12064	86805 76322 77489	— —	80205	
30-35	2645 2726	2686	11850 11250	11330 10838	11317	73	—	1140	8152 —	8152	52340 52143 51020	— —	51834	
35-40	2213 2121	2167	9085 8480	8555 7960	8520	22	—	645	5320 —	5320	39815 36475 —	— —	38145	
40-45	1506 1805	1656	— 6160	6330 9555	6148	—	100	310	3333 —	3333	27255 24760 —	— —	26008	
45-50	924 —	924	— 4370	4855 4105	4443	—	—	—	2127 —	2127	19190 17565 —	— —	18378	
50-55	— —	—	— 3170	3200 2955	3108	—	—	—	1100 —	1100	10430 11185 —	— —	10808	
10-80	31274 31955	31615	— —	191951 180948	186450	2653	8626	21165	124306 125423	124865	1031470 — —	— —	1031470	

TABLE 10: Crack propagation records for the 2024-T3 specimens with a central hole

l (mm)	48								49			
	A27		A62		A56		A110		A20		A75	
12	21055	23542	19906	14580	19291	18604	19400	25858	18304	12285	19603	15698
14	23542	24980	21143	16869	20845	20279	22208	28078	19195	13903	20239	16914
16	26237	27347	23387	20000	22731	22280	25081	30073	20032	15432	21065	18522
18	28882	30078	25745	22543	—	24693	28052	32426	21025	—	22078	19868
20	31572	32219	27347	24835	27185	26722	30428	34271	22188	18904	22943	21025
25	—	—	31000	29805	31365	31086	34983	—	23856	21611	24863	23599
30	—	—	33666	32616	34247	33881	—	—	25188	23838	26057	25220
35	—	—	34950	34380	35571	35407	—	—	25882	25078	—	26311
40	—	—	35455	35276	36130	36087	—	—	26204	25851	—	—
45	—	—	35534	35427	36328	36283	—	—	26307	26220	—	—
50	—	—	35594	35566	36385	36371	—	—	26339	26300	—	—
55	—	—	35615	35608	36394	36388	—	—	—	26335	—	—
80	41422	41422	35617	35617	36396	36396	41792	41792	—	26354	27480	27480

l (mm)	49				50							
	A38		A98		A21		A77		A15		A92	
12	14328	17458	13576	15842	15491	13976	12360	14980	14278	12700	11202	12654
14	15295	18548	15105	16644	16096	14614	13047	15421	14910	13520	11888	13160
16	16644	19488	16374	17627	16560	15311	13856	15834	15402	14252	12674	13653
18	18216	20326	17404	18600	16988	15918	14448	16194	15828	14880	13180	14044
20	19382	21223	18548	19495	17382	16447	—	—	16243	15402	13738	14436
25	21793	23033	20802	21352	—	17492	16270	17145	—	—	14783	15153
30	—	—	22308	22740	—	—	17014	17492	—	—	15453	15657
35	—	—	23365	23574	—	—	17477	17736	—	—	15840	15954
40	—	—	23843	—	—	—	17718	17866	—	—	16057	16136
45	—	—	23960	24033	—	—	17858	17943	—	—	16186	16227
50	—	—	24043	24051	—	—	17936	17970	—	—	16243	16230
55	—	—	—	—	—	—	17965	—	—	—	—	—
80	25392	25392	24056	24056	19112	19112	17981	17981	18004	18004	16268	16268

Values in the table are numbers of flights as counted from the beginning of the test. For each specimen two values are given, corresponding to the cracks at both sides of the hole. The first column gives the crack length as measured from the center of the hole. First and second line: Test series No. and specimen No.

(a) See table 11; (b) The life for $S_{a, min} = 1.1 \text{ kg/mm}^2$ was taken as being 1.

Material	Test conditions		Crack propagation life (flights) ^(a)	Life ratios ^(b)
	Sequence	$S_{a, max}$		
2024	yes	7.7	15921 (1)	3.3
	no	6.6	11365 (4)	1.1
7075	yes	6.6	5889 (5)	1.1
	no	7.7	5062 (6)	2.2
2024	yes	7.7	31000 (1)	1.1
	no	6.6	20480 (4)	1.1
7075	yes	6.6	9863 (4)	1.1
	no	7.7	20759 (4)	1.18
2024	yes	7.7	16025 (4)	1.01
	no	6.6	11781 (4)	1.03
7075	yes	7.7	13329 (4)	1.01
	no	6.6	11781 (4)	1.08
2024	yes	7.7	16025 (4)	1.01
	no	6.6	11781 (4)	1.03
7075	yes	7.7	13329 (4)	1.01
	no	6.6	11781 (4)	1.08

TABLE 13: Effect of omitting small gust loads

Values of stresses in kg/mm^2

(a) See table 11.

Material	Test conditions		Crack propagation life (flights) ^(a)	Life ratio
	$S_{a, max}$	$S_{a, min}$		
2024	6.6	1.1	16308 (1)	1.4
	4.4	1.1	6516 (2)	1.1
7075	7.7	1.1	9617 (1)	1.1
	6.6	1.1	4800 (1)	0.9
2024	6.6	1.1	16025 (4)	1.01
	4.4	1.1	11781 (4)	1.03
7075	7.7	1.1	13329 (4)	1.01
	6.6	1.1	11781 (4)	1.08

TABLE 12: Effect of the minimum stress in the GTAC

Values of stresses in kg/mm^2

(a) Mean values drawn from table 7. The numbers between brackets indicate the number of tests carried out. (b) In both cases $S_{a, min}$ in the GTAC is equal to -3.4 kg/mm^2 . For the taxiing loads $S_{a, min} \pm S_a = -2 \pm 1.4 \text{ kg/mm}^2$.

Material	Test conditions		Crack propagation life (flights) ^(a)	Life ratio
	$S_{a, max}$	$S_{a, min}$		
2024	6.6	1.1	16025 (4)	1.01
	7.7	1.1	11781 (4)	1.03
7075	8.8	1.1	13329 (4)	1.01
	7.7	1.1	11781 (4)	1.08
2024	6.6	1.1	16025 (4)	1.01
	7.7	1.1	11781 (4)	1.03
7075	8.8	1.1	13329 (4)	1.01
	7.7	1.1	11781 (4)	1.08

TABLE 11: Effect of taxiing loads

Values of stresses in kg/mm^2

TABLE 14: Effect of truncating the gust spectrum
Values of stresses in kg/mm²

Test conditions					Crack propagation life (flights) ^(a)					Life ratios ^(b)				
Material	Load sequence	Taxiing loads	GTAC S_{min}	Gusts $S_{a,min}$	$S_{a,max}$ of gust cycles					$S_{a,max}$ of gust cycles				
					8.8	7.7	6.6	5.5	4.4	8.8	7.7	6.6	5.5	4.4
7075	Random	yes	-1.4 -3.4	1.1	13406 (1)	9617 (1)	4800 (1)	3075 (1)	2714 (1)	2.28	2.00	1	0.64	0.57
		no	-3.4	1.1		13329 (4)	8719 (4)	5889 (5)	3538 (4)		2385 (4)	1.48	1	0.70
	Program	no	-3.4	1.1	14670 (4)	21179 (2)	5062 (6)	9779 (4)	2205 (4)	2.63	1.89	1	0.70	0.47
2024	Random	yes	-1.4 -3.4	1.1	23292 (4)	15921 (1)	16308 (1)	7813 (4)	6516 (2)	1.98	1.46	1	0.66	0.49
		no	-3.4	1.1		16025 (4)	10876 (5)		20513 (4)		5793 (4)	1.51		1
	Program	no	-3.4	1.1	26072 (4)	32000 (3)	11781 (4)	20759 (4)	5420 (4)	1.54	1	0.66	0.49	
		no	-3.4	1.1	26072 (4)	11365 (4)	20759 (4)	5420 (4)	2.29	1.54	1	0.66	0.48	

^(a) Mean values drawn from table 7. The numbers between brackets indicate the numbers of tests carried out.

^(b) The life for $S_{a,max} = 6.6$ kg/mm² was taken as being 1.

TABLE 15: Comparison between the random and the programmed flight simulation tests.
Values of stresses in kg/mm², GTAC without GL.

Test conditions			Crack propagation life ^(a) (flights)		Life ratio
Material	Gust cycles		Random gust sequence	Programmed gust sequence	Programmed/Random
	$S_{a,min}$	$S_{a,max}$			
7075	1.1	8.8	13329 (4)	14670 (4)	1.10
		6.6	5062 (6)	5061 (4)	1.00
	3.3	4.4	2385 (4)	2205 (4)	0.92
		6.6	9779 (4)	8921 (4)	0.91
2024	1.1	8.8	23292 (4)	26072 (4)	1.12
		6.6	11781 (4)	11365 (4)	0.96
	3.3	4.4	5793 (4)	5420 (4)	0.94
		6.6	20759 (4)	20480 (4)	0.99
Average					0.99

^(a) See table 16.

TABLE 16: Effects of reversing the gust cycles, of applying one gust per flight and of omitting the GTAC.
Gust cycles in random sequence ($S_{a,max} = 6.6$ kg/mm²). GTAC without TL.

Characteristic test conditions (see also fig. 3)	$S_{a,min}$ of gusts (kg/mm ²)	Crack propagation life ^(a) (flights)		Relative crack propagation life ^(b)	
		7075	2024	7075	2024
Standard random sequence	1.1	5062 (6)	11781 (4)	1	1
Reversed gust cycles	1.1	4851 (4)	11184 (4)	0.96	0.95
Small gusts omitted	2.2	7006 (4)	13924 (4)	1.38	1.18
	3.3	9779 (4)	20759 (4)	1.93	1.76
Only one gust per flight ^(c)	—	14556 (4)	36583 (4)	2.88	3.10
GTAC omitted	1.1	7518 (4)	20869 (4)	1.49	1.77

^(a) Mean values drawn from table 7. The numbers between brackets indicate the number of tests carried out. ^(b) The life for the standard random sequence was taken as being 1. ^(c) The largest positive gust load of each flight was applied.

TABLE 17: Comparison between the two alloys; Values of stresses in kg/mm²

Test conditions				Crack propagation life (flights) ^(a)		Life ratio (2024)/(7075)
Gust sequence	Taxiing loads	Gust cycles		7075	2024	
		S _{a,min}	S _{a,max}			
Random	yes	1.1	7.7	8719 (4)	15921 (1)	1.8
			6.6	5889 (5)	10876 (5)	1.8
		3.3	6.6	9863 (4)	20513 (4)	2.1
	no	1.1	8.8	13329 (4)	23292 (4)	1.7
				7.7	9565 (4)	16025 (4)
		6.6	5062 (6)	11781 (4)	2.3	
			5.5	3538 (4)	7813 (4)	2.2
			4.4	2385 (4)	5793 (4)	2.4
		2.2	6.6	7006 (4)	13924 (4)	2.0
		3.3	7.7	21179 (2)	32000 (3)	1.5
		6.6	6.6	9779 (4)	20759 (4)	2.1
(b)	6.6	14556 (4)	36583 (4)	2.5		
1.1 ^(c)	6.6 ^(c)	4851 (4)	11184 (4)	2.3		
Random, no GTAC	—	1.1	6.6	7518 (4)	20869 (4)	2.8
Programmed		1.1	8.8	14670 (4)	26072 (4)	1.8
			6.6	5061 (4)	11365 (4)	2.2
		4.4	2205 (4)	5420 (4)	2.5	
			3.3	6.6	8921 (4)	20480 (4)
Average					2.1	

^(a) Mean values drawn from table 7. The numbers between brackets indicate the numbers of tests carried out; ^(b) Only one gust load (the largest one) per flight; ^(c) Gust cycles in reversed sequence.

TABLE 18: Damage calculations for test series No. 45. Material: 2024-T3 Alclad; S_{a,max}=6.6 kg/mm²; S_{a,min}=1.1 kg/mm²; GTAC omitted.

S _a (kg/mm ²)	1.1	2.2	3.3	4.4	5.5	6.6	7.7 ^(a)	8.8 ^(a)
n/N in 5000 flights ^(b)	0.145	0.312	0.115	0.077	0.016	0.006	0.003	0.002

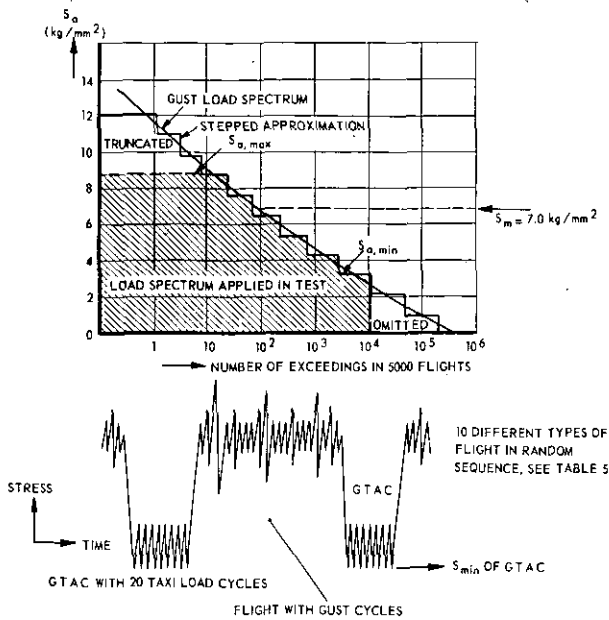
^(a) Not applied in test series No. 45; ^(b) n from table 5, N from fig. 15.

Sum of damage increments for S_a=1.1 – 6.6 is 0.808.

Predicted life: 1/0.808 · 5000 = 6188 flights } Test result corresponds to
 Crack propagation life in tests = 20869 flights. } ∑(n/N) = 3.4.

TABLE 19: Fatigue life reduction if small gust cycles are included. Comparison between tests and predictions. M = crack propagation life with small gust cycles included; M' = crack propagation life without small gust cycles. The predicted M values have been calculated from M' and the constant-amplitude test data, see section

Material	Test conditions			Small gust cycles S _a -values	M/M' (percentage)		Ratio test/predicted	
	Taxiing loads	S _{a,max}	Load sequence		test	predicted		
7075	yes	6.6	Random	1.1 and 2.2	60	20	3.0	
					44	10	4.4	
	no	6.6	Programmed	1.1	52	20	2.6	
					47	22	2.1	
					72	47	1.5	
2024	yes	7.7	Random	1.1 and 2.2	51	26	2.0	
					53	35	1.5	
	no	7.7	Programmed	1.1	50	25	2.0	
					57	35	1.6	
					55	35	1.6	
			6.6	Random		85	71	1.2



NOTE: EACH GUST CYCLE CONSISTED OF A POSITIVE GUST FOLLOWED BY A NEGATIVE GUST OF EQUAL AMPLITUDE (EXCEPT FOR TESTS WITH REVERSED GUST CYCLES)

Variables of test program (see also fig. 3)	
Gust load spectrum	$S_{a,max}$ (truncation) $S_{a,min}$ (omission of many small cycles)
GTAC	S_{min} (2 values)
Taxiing loads	Omission of taxiing loads (same S_{min})
Flight profile	Omission of GTAC Only one gust cycle per flight
Sequence	Random Gust cycles in reversed sequence Programmed per flight
Material	2 Al-alloys, 2024-T3 and 7075-T6

Fig. 1. Survey of variables studied in the present test series.

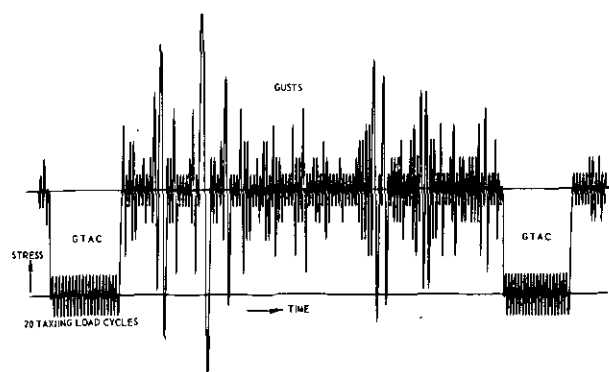


Fig. 2. The load sequence in the most severe flight (type A).

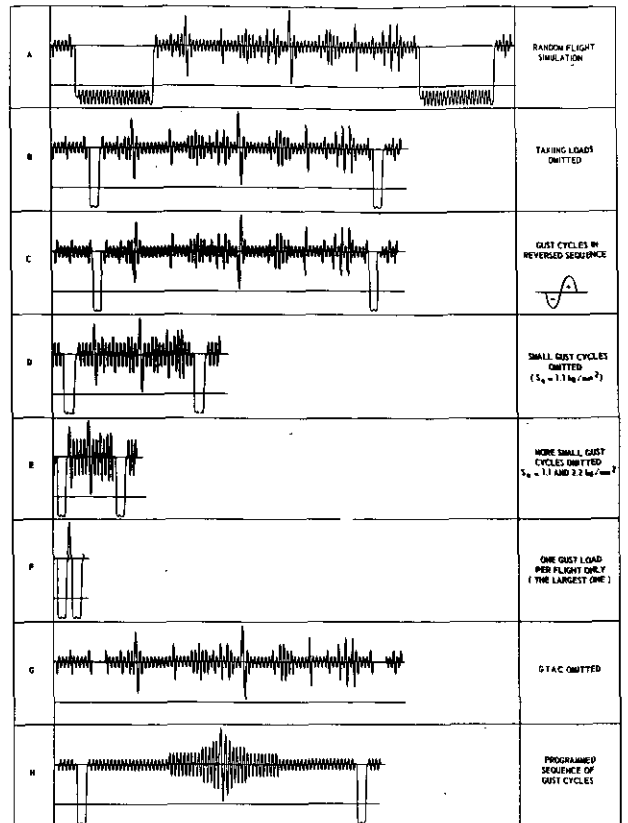


Fig. 3. Load records of flight no. 19 (type F) for different types of flight simulation.

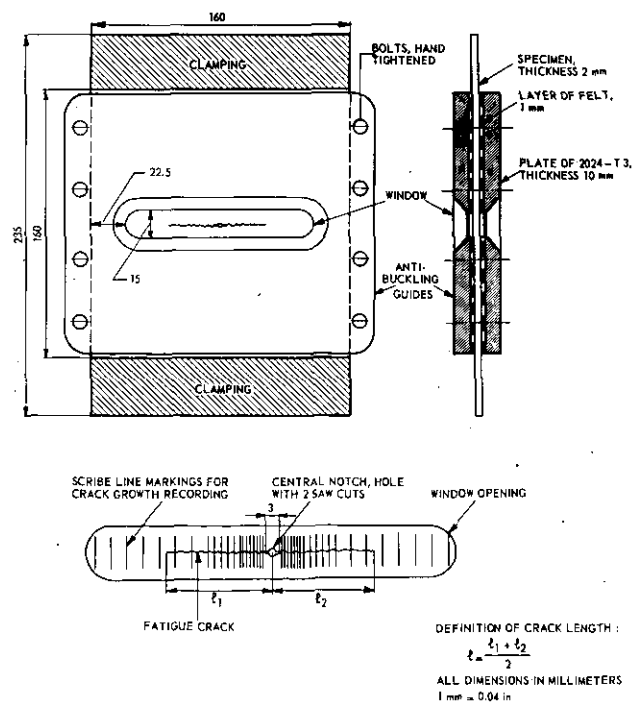


Fig. 4. Dimensions of the specimen and anti-buckling guides.

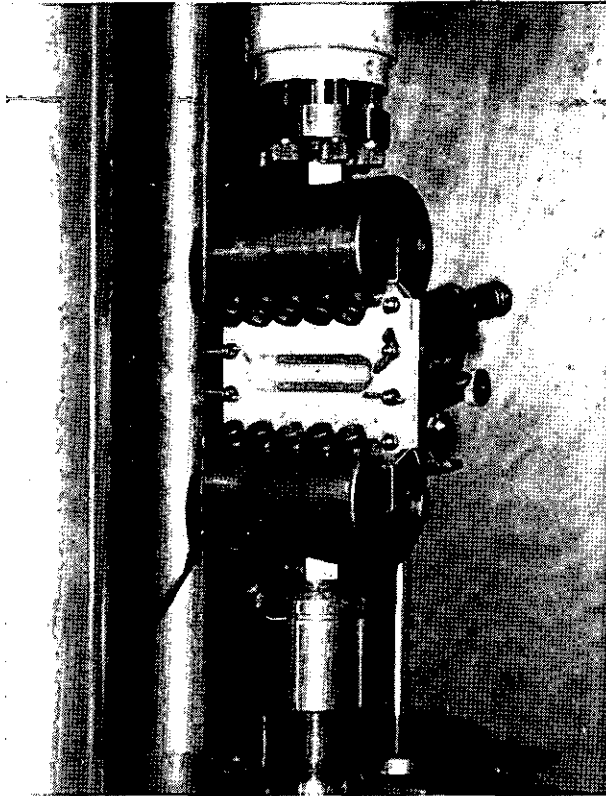


Fig. 5. Picture of the specimen, anti-buckling guides with window and clampings. Stereo-microscope ($30\times$) for crack observation in the background.

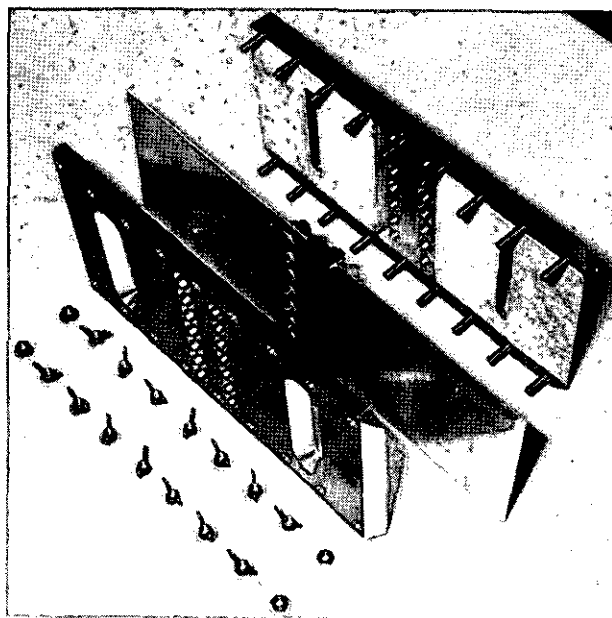


Fig. 6. Two specimens connected by a double strap joint, anti-buckling guides covered by felt at the inner side and provided with two windows each.

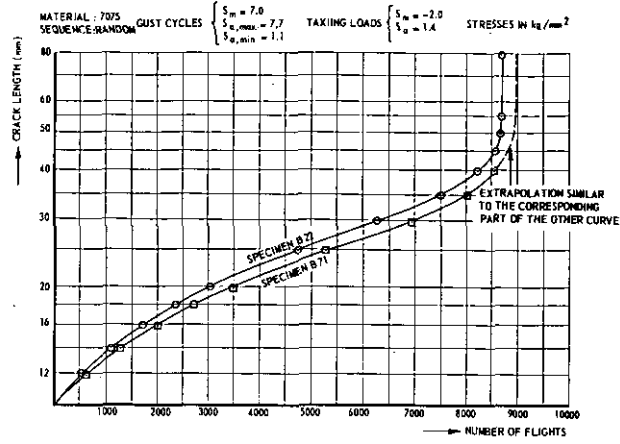


Fig. 7. Example of two crack propagation curves for two specimens simultaneously tested in series.

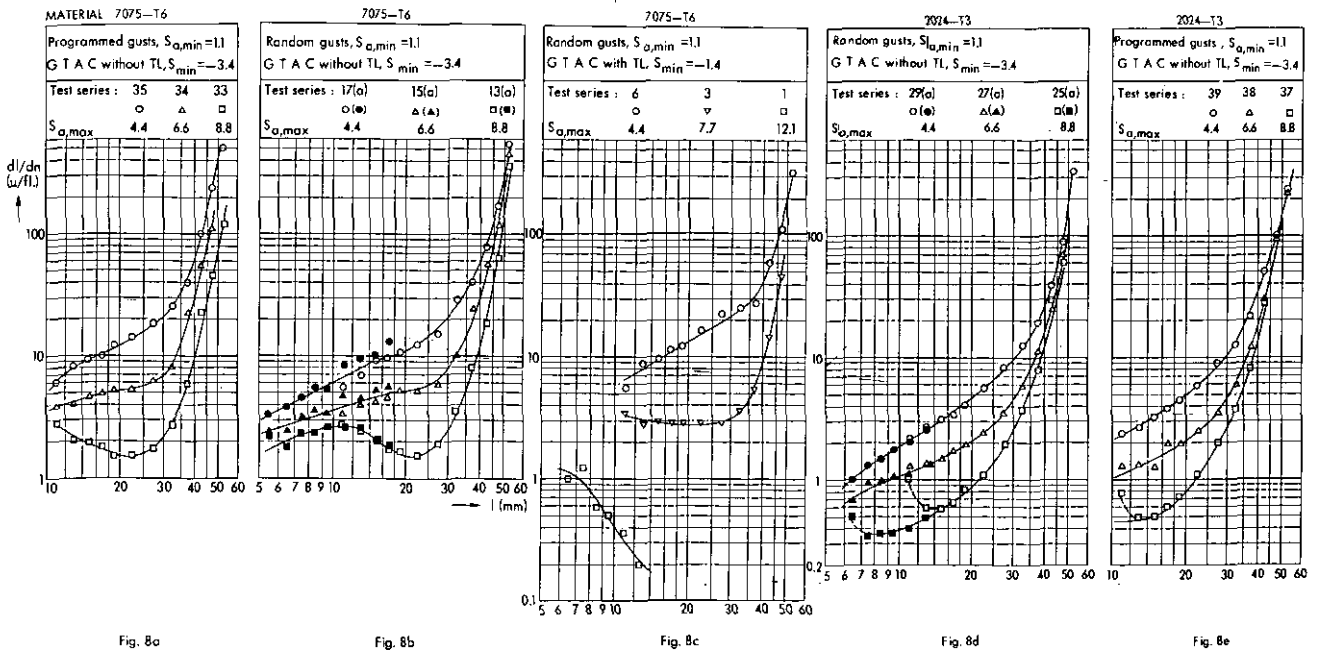


Fig. 8a-c. Effect of truncation ($S_{a,max}$) on the crack propagation rate for material 7075-T6.
 Fig. 8d-e. The same as in figure 8a-c, but for material 2024-T3.

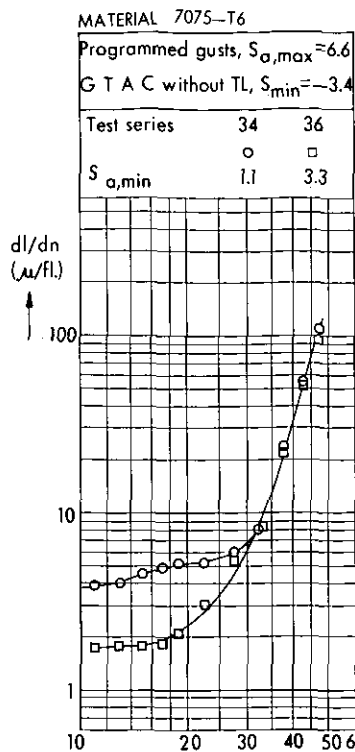


Fig. 9a

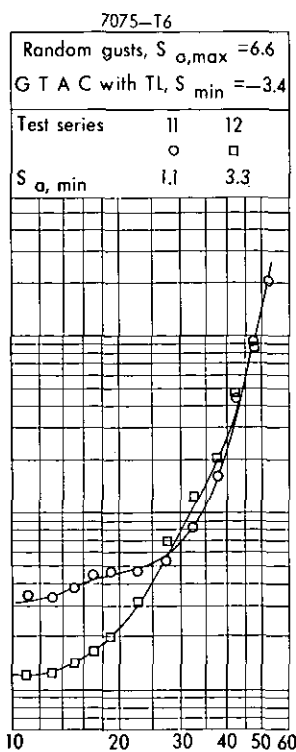


Fig. 9b

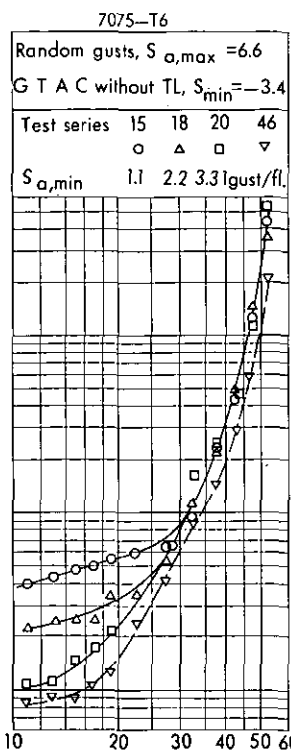


Fig. 9c

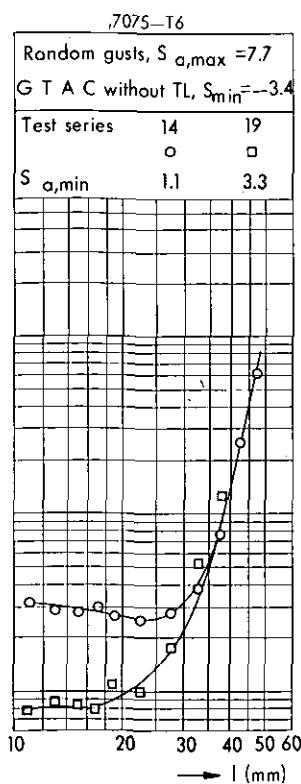


Fig. 9d

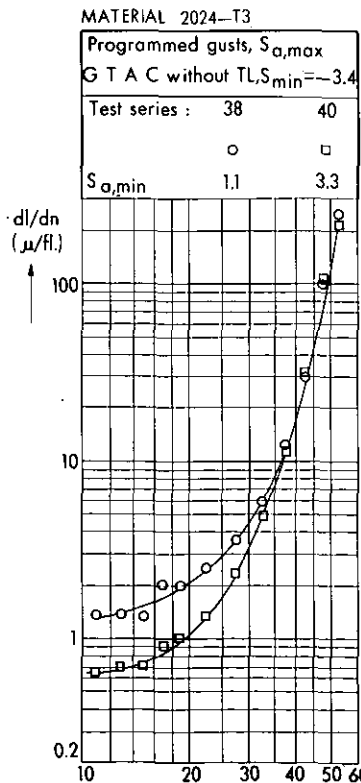


Fig. 9e

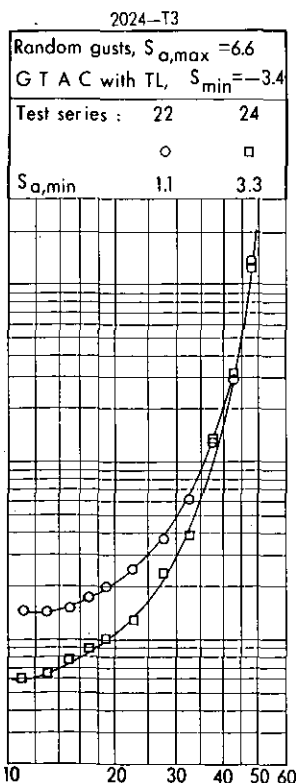


Fig. 9f

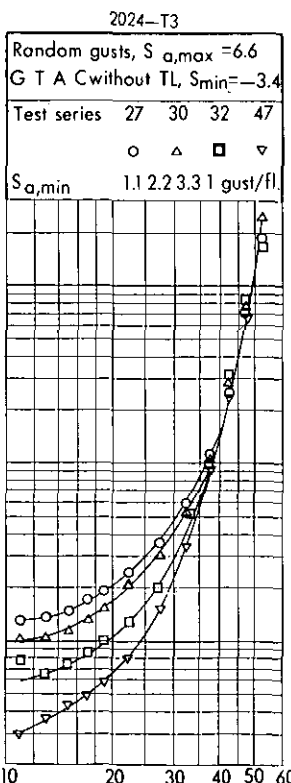


Fig. 9g

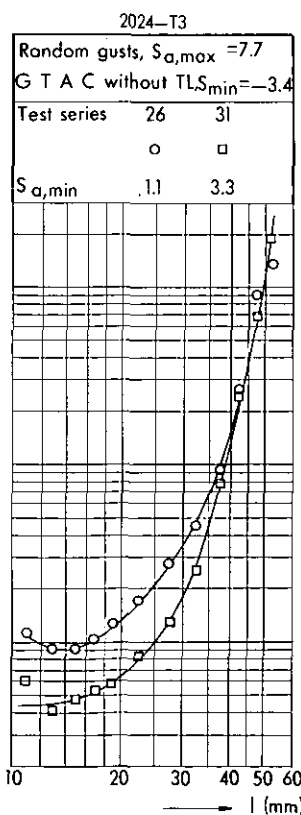


Fig. 9h

Fig. 9a-d. Effect of omitting small gust loads on the crack propagation rate for material 7075-T6.

Fig. 9e-h. The same as in figure 9a-d, but for material 2024-T3.

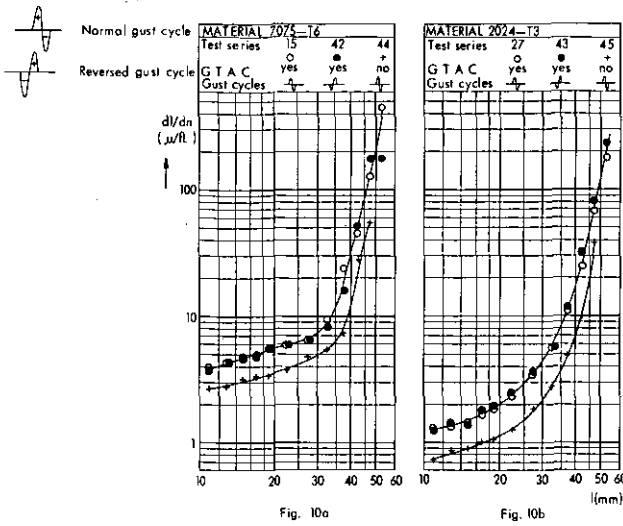


Fig. 10. The effects of omitting the GTAC and of reversing the gust cycles on the crack propagation rate.

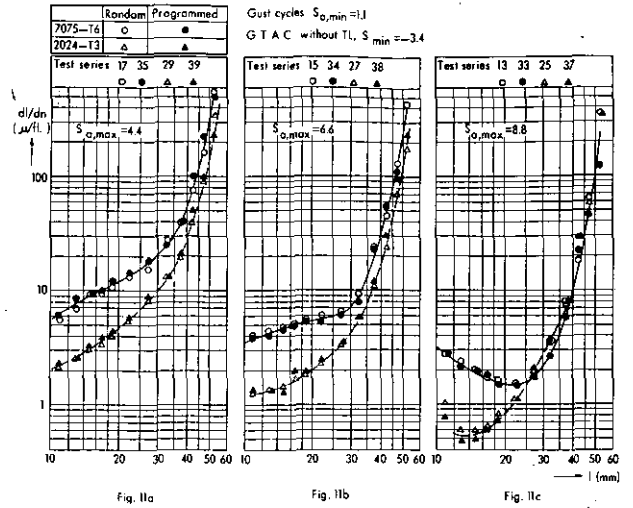


Fig. 11. Comparison between the crack rates for random and programmed flight simulation.

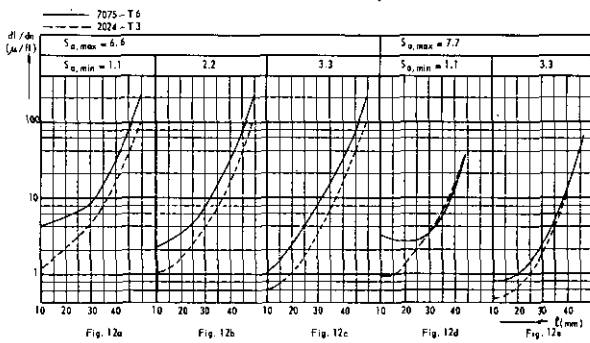


Fig. 12. Comparison between the crack rates in the two alloys. Effect of $S_{a,max}$ and $S_{a,min}$, see also fig. 11: Random gusts, GTAC without TL, $S_{min} = -3.4$.

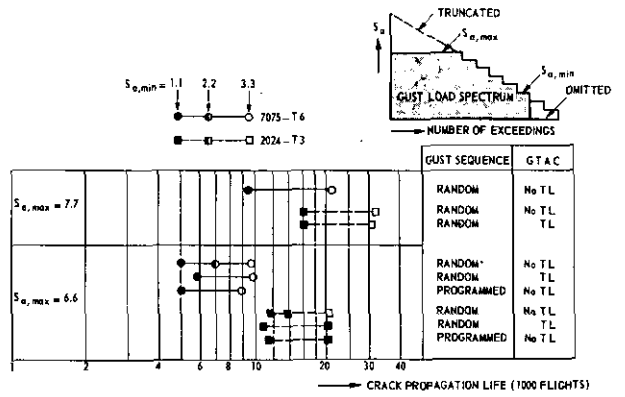


Fig. 13. The effect of omitting small gust loads on the crack propagation life.

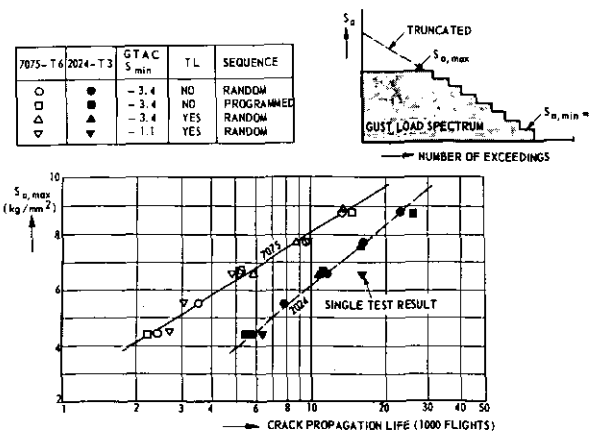


Fig. 14. The effect of truncating the gust load spectrum on the crack propagation life.

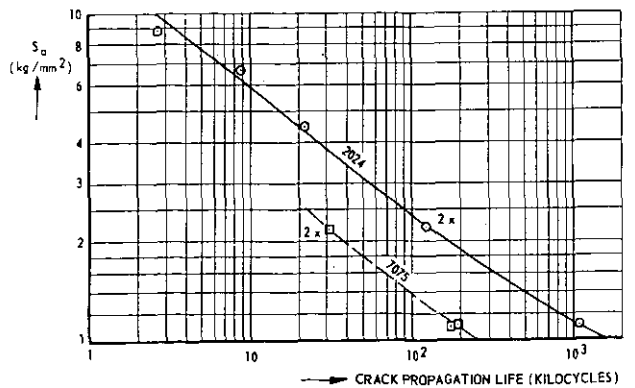


Fig. 15. The constant-amplitude test data plotted as S-N curves.

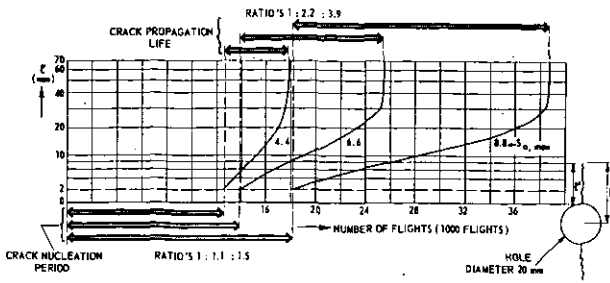
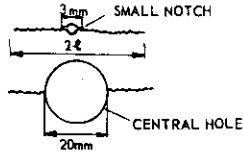


Fig. 16. Crack propagation curves for the 2024-T3 specimens with a central hole. Effect of truncation level ($S_{a,max}$) on the crack-nucleation period (to $l' = 2$ mm) and the crack propagation life.

MATERIAL 2024 - T3
 RANDOM GUSTS, $S_{a,max} = 6.6$, $S_{a,min} = 2.2$
 GTAC WITHOUT TL, $S_{min} = -3.4$



TEST SERIES	SPECIMEN
30 ●	SMALL NOTCH
49 ○	CENTRAL HOLE

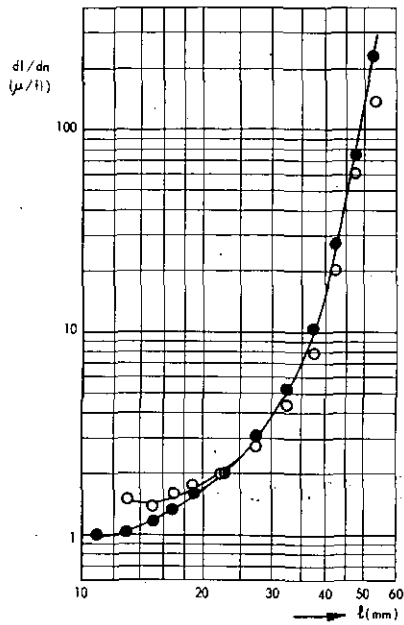
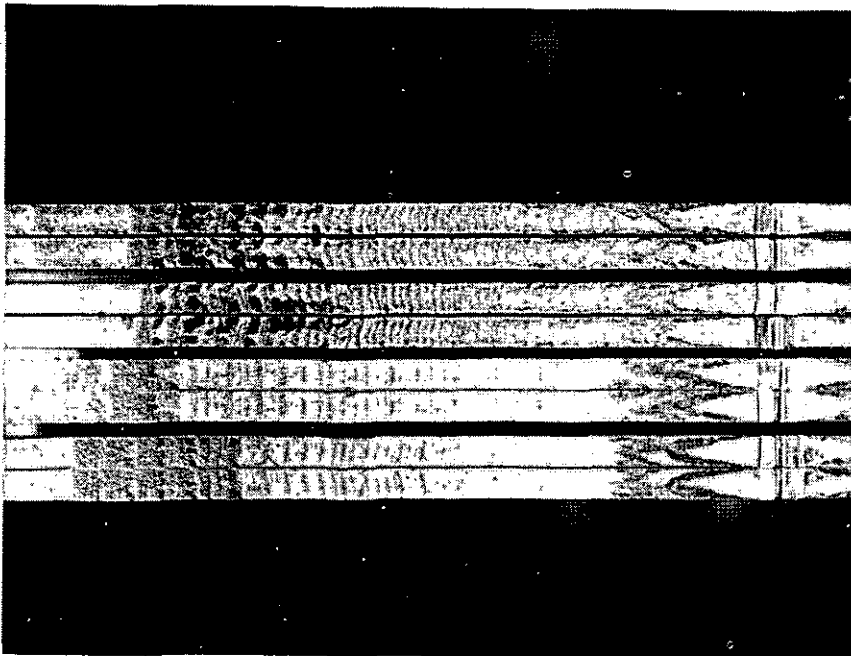


Fig. 17. Comparison between the crack propagation rates in specimens with a small notch or a central hole.



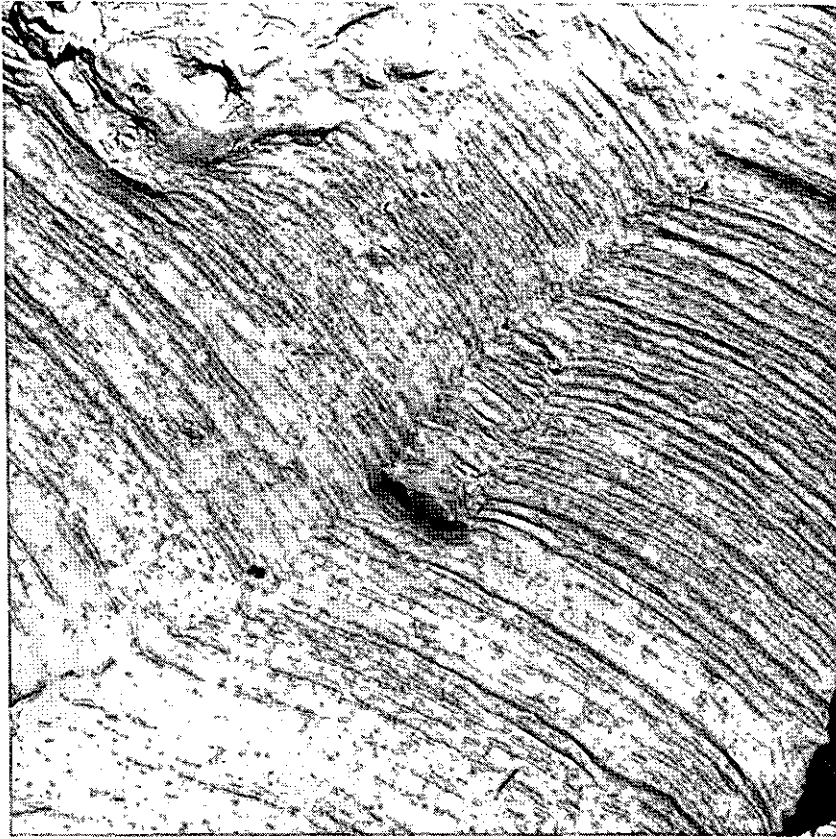
Magnification 2x
 Central notch at right side of picture

← Random }
 ← Programmed } 7075-T6

← Random }
 ← Programmed } 2024-T3

$S_{a,max} = 8.8 \text{ kg/mm}^2$
 $S_{a,min} = 1.1 \text{ kg/mm}^2$
 GTAC without TL,
 $S_{min} = -3.4 \text{ kg/mm}^2$

Fig. 18. Fracture surfaces of 4 specimens showing macro fatigue bands.



Specimen B47, 7075-T6
 Random flight simulation.
 $S_{a,max} = 6.6 \text{ kg/mm}^2$
 $S_{a,min} = 3.3 \text{ kg/mm}^2$
 GTAC with TL
 $l = 14 \text{ mm}$ $dl/dn = 1.3 \text{ } \mu\text{/flight}$
 Magnification $5000\times$



Specimen B18, 7075-T6
 Programmed flight simulation.
 $S_{a,max} = 4.4 \text{ kg/mm}^2$
 $S_{a,min} = 1.1 \text{ kg/mm}^2$
 GTAC without TL
 $l = 20 \text{ mm}$ $dl/dn = 13 \text{ } \mu\text{/flight}$
 Magnification $5000\times$

Fig. 19. Two examples of fatigue striations as observed with the electron microscope

Report NLR-TR69007U

Symmetrical transonic potential flows around quasi-elliptical aerofoil sections

by

H. I. BAURDOUX and J. W. BOERSTOEL

Summary

The results of the computation of 10 symmetrical non-lifting quasi-elliptical aerofoil sections in transonic potential flows are presented. No approximations have been made in the potential theory. Results are summarized in figures and tables. The figures permit a rapid appraisal of the overall properties. More detailed information is given in the tables.

The precision of the given data in the tables is a few units of the last decimal place specified. The data can serve as a reference for the testing of (approximate) computational methods for transonic flows.

Contents

List of Symbols	page	1
1 Introduction	1	1
2 The computations	2	2
3 Results	2	2
4 References	2	2
Appendix A: Formulae for the interpolation with a fifth degree polynomial		
11 tables		
12 figures		

List of symbols

c	— chord length
c_p	— pressure coefficient
c_p	— pressure coefficient for $M=1$

M	— Mach number
M_1	— free stream Mach number
M_m	— maximum value of M on aerofoil section contour
M_s	— rate of change of M along aerofoil section contour
R	— radius of curvature of aerofoil section contour
R_0	— radius of curvature at leading edge
$1/R$	— curvature of aerofoil section contour
t	— maximum thickness of aerofoil section
x	— chordwise co-ordinate
x_{le}	— chordwise position of leading edge
y	— co-ordinate normal to chord
γ	— ratio of specific heats ($\gamma=1.4$)
ε	— thickness parameter
τ	— velocity parameter
τ_1	— free stream value of τ
θ	— flow angle

1 Introduction

The pressure distribution on aerofoil sections, calculated by an exact potential theory, is of great interest for many aerodynamicists for different reasons. Such an exact potential theory is described by Nieuwland in ref. 1. This theory has been used to calculate 10 transonic symmetrical non-lifting aerofoil sections. A variety of section shapes and related pressure distribution curves have been computed at different free stream Mach numbers.

The results can be used in evaluating the validity of computational methods for transonic flows, for example finite difference methods.

Section 2 gives some information on the computations. In section 3 the results are presented.

2 The computations

For the computations use has been made of three ALGOL programmes. The sections with a blunt leading edge have been calculated by the programme of ref. 5, while for the lenticular aerofoil sections and the flow field of one of the sections the programme of ref. 3 has been used. The results have been checked and, where necessary, corrected by a smoothing method discussed in ref. 4 and 5.

3 Results

3.1 The steady potential flow around a quasi-elliptical aerofoil section is characterized by three parameters *viz.* τ_1 , ε and λ . The free stream Mach number M_1 is determined by τ_1 according to

$$M_1^2 = \frac{2\tau_1}{(\gamma-1)(1-\tau_1)}$$

The thickness ratio, t/c , is mainly determined by ε ; the parameter λ mainly determines the leading edge radius R_0 and governs the flow expansion on the front part of the sections. The values of τ_1 , ε and λ are used to identify the sections. For example, section 0.1025-0.675-1.3 has $\tau_1=0.1025$, $\varepsilon=0.675$ and $\lambda=1.3$. In choosing these parameters use has been made of results of ref. 2.

3.2 The results are presented in tables and figures. In table 1 all profiles are listed together with their identification as a quasi-elliptical aerofoil section, M_1 , M_m , t/c , c , R_0/c , x_{le} and an index referring to the figures and the other tables. In the figures 1 through 10, c_p - x curves and the contour have been plotted; the value of c_p^* has also been indicated. The figures and table 1 allow a rapid appraisal of the most important section properties. More detailed information is contained in the tables 2 through 11, where values of τ , x , y , c_p , M , M_s , θ and $1/R$ are given. The given quantities have a precision up to some units of the last decimal place specified (see ref. 3 and 4). The figures 11 and 12 contain detailed information about the flow field around quasi-ellipse 0.1025-0.675-1.375 and can be used for example to check results of other computation methods in points in the flow field.

If more values of the ordinates are needed than are given in the tables, it is advised to interpolate between two successive points by means of a fifth-degree polynomial making use of the given values of x , y , θ and $1/R$ in the two points. The formulae, needed for the interpolation, are given in the appendix. In this way values of the ordinates are obtained which are in the experience of the authors sufficiently accurate for most purposes.

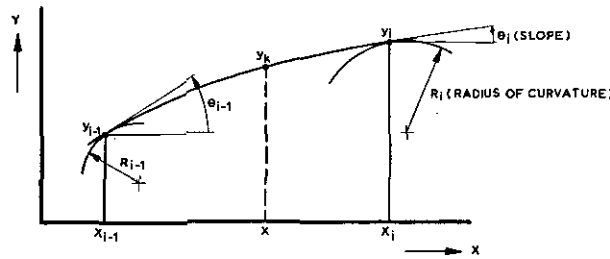
4 References

- ¹ NIEUWLAND, G. Y., Transonic potential flow around a family of quasi-elliptical aerofoil sections, NLR TR T.172, 1967.
- ² BOERSTOEL, J. W., A survey of symmetrical transonic potential flows around quasi-elliptical aerofoil sections, NLR TR T.136, 1967.
- ³ GENNIP, M. J. M. G. VAN BOERSTOEL, J. W., Numerical analysis and ALGOL program for the computation of subsonic and transonic potential flows around quasi-elliptical aerofoil sections, NLR-TN W.27 (Restricted).
- ⁴ BOERSTOEL, J. W., The smoothing and interpolation of discrete sets of data using weighted splines (report to be pub.).
- ⁵ BAURDOUX, H. I., An ALGOL programme for the determination of nonlifting symmetrical quasi-elliptical aerofoils, NLR TR 68111 C (Restricted).

APPENDIX A

Formulae for the interpolation with a fifth-degree polynomial

For the interpolation of the ordinates use is made of the given values of y , θ and $1/R$ in two successive points. The ordinates of these points are indicated by x_{i-1} and x_i . The values of y , θ and $1/R$ are indicated accordingly, cf. the figure below.



To interpolate the ordinate y_k in the point x the following formula is recommended:

$$y_k = a_0 + a_1 x_k + a_2 x_k^2 + x_k^3 [a_3 + a_4(x_k - \Delta_i) + a_5(x_k - \Delta_i)^2] \quad (\text{A.1})$$

where $x_k = x - x_{i-1}$, $\Delta_i = x_i - x_{i-1}$, and the coefficients a_0 - a_5 can be calculated as given below. First θ and $1/R$ have to be transformed to first and second derivatives:

$$y'_i = \tan \theta_i \quad y'_{i-1} = \tan \theta_{i-1} \quad (\text{A.2})$$

$$y''_i = -(1 + y_i'^2)^{3/2} \cdot (1/R)_i \quad y''_{i-1} = -(1 + y_{i-1}'^2)^{3/2} \cdot (1/R)_{i-1} \quad (\text{A.3})$$

Then a_0 , a_1 and a_2 are given by:

$$a_0 = y_{i-1} \quad (\text{A.4})$$

$$a_1 = y'_{i-1} \quad (\text{A.5})$$

$$a_2 = \frac{1}{2} \cdot y''_{i-1} \quad (\text{A.6})$$

The coefficients a_3 , a_4 and a_5 can be computed from the expressions:

$$a_3 = \frac{1}{\Delta_i^3} [y_i - y_{i-1} - \Delta_i y'_{i-1} - \frac{1}{2} \Delta_i^2 y''_{i-1}] \quad (\text{A.7})$$

$$a_4 = \frac{1}{\Delta_i^4} [-3y_i + 3y_{i-1} + \Delta_i(y'_i + 2y'_{i-1}) + \frac{1}{2} \Delta_i^2 y''_{i-1}] \quad (\text{A.8})$$

$$a_5 = \frac{1}{\Delta_i^5} [6y_i - 6y_{i-1} - 3\Delta_i(y'_i + y'_{i-1}) + \frac{1}{2} \Delta_i^2 (y''_i - y''_{i-1})] \quad (\text{A.9})$$

Using the equations (A.2)-(A.9) and substituting in eq. (A.1), the ordinate for any given value of x_k ($x_{i-1} \leq x_k \leq x_i$) can be calculated.

TABLE I
Main aerofoil characteristics

Profile number	quasi-elliptical aerofoil section	M_1	M_m	t/c	c	R_0/c	x_{te}	figure number	table number
5	0.1025 -0.6750 -1.300	0.7557	1.222	0.1572	3.20343	0.046109	-1.69058	1	2
6	0.1100 -0.7500 -1.250	0.7861	1.136	0.1162	3.30546	0.032469	-1.79504	2	3
7	0.1075 -0.6750 -1.050	0.7760	1.257	0.1466	3.22519	0.026685	-1.69718	3	4
8	0.1100 -0.7500 -0.900	0.7861	1.060	0.1137	3.37728	0.006030	-1.79504	4	5
10	0.1125 -0.7500 -1.325	0.7961	1.280	0.1138	3.27161	0.040094	-1.79929	5	6
11	0.1150 -0.7500 -1.200	0.8061	1.257	0.1092	3.28558	0.029408	-1.80375	6	7
12	0.1175 -0.8000 -1.260	0.8159	1.291	0.0894	3.32802	0.029981	-1.87247	7	8
14	0.1200 -0.7000 -0.000	0.8257	1.083	0.1077	3.38080	—	-1.69040	8	9
15	0.1200 -0.7500 -0.000	0.8257	1.121	0.0953	3.45960	—	-1.72980	9	10
13	0.1025 -0.6750 -1.375	0.7557	1.291	0.1578	3.19192	0.052543	-1.69058	10, 11, 12	11

Tab. 2

QUASI-ELLIPTICAL AEROFOIL SECTION 0.1025 — 0.6750 — 1.3000
 PROFILE NUMBER 5
 FREE STREAM MACH NUMBER 0.7557

τ	x	y	c_p	M	M_s	θ	$1/R$
0.00000	-1.69058	0.00000	1.1510	0.0000	0.000000	1.57080	6.770223
0.01000	-1.68621	0.03569	1.0248	0.2247	6.22	1.328	6.70
0.02000	-1.68179	0.05028	0.9017	0.3194	6.19	1.226	6.64
0.03000	-1.67731	0.06135	0.7817	0.3932	6.16	1.147	6.56
0.04000	-1.67277	0.07059	0.6647	0.4564	6.110	1.0797	6.49
0.05000	-1.66813	0.07865	0.5508	0.5130	6.046	1.0198	6.40
0.06000	-1.66341	0.08589	0.4398	0.5649	5.961	0.9648	6.306
0.07000	-1.65855	0.09252	0.3317	0.6135	5.851	0.9134	6.194
0.08000	-1.65355	0.09868	0.2265	0.6594	5.710	0.8648	6.062
0.09000	-1.64836	0.10449	0.1241	0.7032	5.531	0.8181	5.903
0.10000	-1.64292	0.11005	0.0245	0.7454	5.307	0.7730	5.713
0.11000	-1.63717	0.11541	-0.0724	0.7861	5.032	0.7290	5.480
0.12000	-1.63098	0.12070	-0.1666	0.8257	4.703	0.6857	5.203
0.13000	-1.62424	0.12598	-0.2582	0.8644	4.321	0.6424	4.880
0.14000	-1.61674	0.13133	-0.3471	0.9022	3.894	0.5991	4.506
0.15000	-1.60824	0.13686	-0.4336	0.9393	3.437	0.5554	4.088
0.16000	-1.59840	0.14267	-0.5175	0.9759	2.977	0.5112	3.6390
0.16667	-1.59091	0.14672	-0.5721	1.0000	2.686	0.4814	3.3341
0.17000	-1.58684	0.14881	-0.5989	1.0120	2.550	0.4668	3.1813
0.18000	-1.57321	0.15529	-0.6780	1.0476	2.1986	0.4220	2.7510
0.19000	-1.55746	0.16194	-0.7546	1.0830	1.9626	0.3782	2.3851
0.20000	-1.54022	0.16838	-0.8290	1.1180	1.8748	0.3370	2.1195
0.21000	-1.52276	0.17412	-0.9010	1.1529	1.9363	0.2995	1.9714
0.22000	-1.50592	0.17901	-0.9708	1.1875	1.9726	0.2658	1.8657
0.23000	-1.48560	0.18415	-1.0384	1.2221	1.1429	0.2314	1.3890
0.23000	-1.36595	0.20607	-1.0384	1.2221	-0.27150	0.14972	0.40402
0.22000	-1.24047	0.22218	-0.9708	1.1875	-0.26246	0.10853	0.268234
0.21000	-1.10064	0.23500	-0.9010	1.1529	-0.232942	0.07582	0.205308
0.20000	-0.94358	0.24456	-0.8290	1.1180	-0.210504	0.04666	0.168193
0.19667	-0.88716	0.24693	-0.8044	1.1064	-0.203479	0.03746	0.158587
0.19333	-0.82862	0.24886	-0.7797	1.0947	-0.195858	0.02844	0.149674
0.19000	-0.76752	0.25032	-0.7546	1.0830	-0.187417	0.01956	0.141263
0.18750	-0.71967	0.25110	-0.7357	1.0742	-0.180545	0.01294	0.135256
0.18500	-0.66984	0.25158	-0.7166	1.0653	-0.173373	0.00634	0.129552
0.18250	-0.61772	0.25173	-0.6974	1.0565	-0.166155	-0.00026	0.124235
0.18000	-0.56321	0.25154	-0.6780	1.0476	-0.159202	-0.00690	0.119399
0.17750	-0.50625	0.25095	-0.6584	1.0388	-0.152823	-0.01357	0.115132
0.17500	-0.44687	0.24995	-0.6388	1.0299	-0.147280	-0.02027	0.111497

Tab. 3

QUASI-ELLIPTICAL AEROFOIL SECTION 0.1100 — 0.7500 — 1.2500
 PROFILE NUMBER 6
 FREE STREAM MACH NUMBER 0.7861

τ	x	y	c_p	M	M_s	θ	$1/R$
0.00000	-1.79504	0.00000	1.1642	0.0000	0.000000	1.57080	9.317575
0.01000	-1.79217	0.02463	1.0440	0.2247	9.13	1.339	9.35
0.02000	-1.78932	0.03453	0.9269	0.3194	9.26	1.242	9.40
0.03000	-1.78650	0.04192	0.8127	0.3932	9.40	1.168	9.46
0.04000	-1.78369	0.04797	0.7014	0.4564	9.55	1.105	9.53
0.05000	-1.78090	0.05314	0.5930	0.5130	9.70	1.048	9.60
0.06000	-1.77813	0.05767	0.4874	0.5649	9.84	0.997	9.69
0.07000	-1.77538	0.06172	0.3845	0.6135	9.97	0.9494	9.79
0.08000	-1.77263	0.06539	0.2844	0.6594	10.07	0.9044	9.88
0.09000	-1.76987	0.06874	0.1870	0.7032	10.12	0.8613	9.96
0.10000	-1.76709	0.07184	0.0922	0.7454	10.09	0.8197	10.01
0.11000	-1.76426	0.07475	0.0000	0.7861	9.95	0.7790	10.01
0.12000	-1.76133	0.07754	-0.0896	0.8257	9.63	0.7387	9.928
0.13000	-1.75823	0.08025	-0.1768	0.8644	9.07	0.6981	9.717
0.14000	-1.75483	0.08298	-0.2614	0.9022	8.22	0.6565	9.310
0.15000	-1.75091	0.08586	-0.3437	0.9393	7.015	0.6127	8.647
0.16000	-1.74603	0.08912	-0.4235	0.9759	5.460	0.5647	7.655
0.16667	-1.74181	0.09169	-0.4754	1.0000	4.273	0.5297	6.772
0.17000	-1.73918	0.09319	-0.5010	1.0120	3.659	0.5109	6.259
0.18000	-1.72718	0.09933	-0.5762	1.0476	1.833	0.4385	4.491
0.19000	-1.69756	0.11116	-0.6492	1.0830	0.6891	0.3328	2.4312
0.19333	-1.67876	0.11721	-0.6730	1.0947	0.5223	0.2916	1.8405
0.19667	-1.65489	0.12383	-0.6966	1.1064	0.4312	0.2516	1.3921
0.20000	-1.62597	0.13068	-0.7199	1.1180	0.3528	0.2154	1.05898
0.20167	-1.60850	0.13434	-0.7315	1.1239	0.29757	0.1978	0.91374
0.20333	-1.58624	0.13858	-0.7430	1.1297	0.21417	0.1789	0.76322
0.20500	-1.53958	0.14625	-0.7545	1.1355	0.04288	0.1489	0.53715
0.20500	-1.50975	0.15050	-0.7545	1.1355	-0.04834	0.1344	0.43619
0.20333	-1.44272	0.15869	-0.7430	1.1297	-0.11921	0.10979	0.304970
0.20167	-1.39820	0.16331	-0.7315	1.1239	-0.137868	0.09732	0.255216
0.20000	-1.35734	0.16710	-0.7199	1.1180	-0.144678	0.08754	0.223082
0.19750	-1.29775	0.17195	-0.7024	1.1093	-0.146745	0.07526	0.189977
0.19500	-1.23794	0.17613	-0.6848	1.1005	-0.144955	0.06459	0.166710
0.19250	-1.17688	0.17978	-0.6671	1.0918	-0.141727	0.05496	0.149229
0.19000	-1.11402	0.18295	-0.6492	1.0830	-0.137925	0.04603	0.135506
0.18750	-1.04951	0.18566	-0.6312	1.0742	-0.133864	0.03763	0.124383
0.18500	-0.98246	0.18792	-0.6130	1.0653	-0.129568	0.02962	0.115105
0.18250	-0.91303	0.18971	-0.5947	1.0565	-0.125065	0.02191	0.107210

0.17250	-0.38528	0.24849	-0.6189	1.0209	-0.142758	-0.02707	0.108525
0.17000	-0.32179	0.24655	-0.5989	1.0120	-0.139361	-0.03391	0.106218
0.16667	-0.23495	0.24321	-0.5721	1.0000	-0.136619	-0.04303	0.104128
0.16333	-0.14669	0.23900	-0.5449	0.9880	-0.135833	-0.05217	0.103065
0.16000	-0.05818	0.23397	-0.5175	0.9759	-0.136832	-0.06130	0.102898
0.15750	0.00771	0.22970	-0.4967	0.9668	-0.138624	-0.06810	0.103278
0.15500	0.07279	0.22504	-0.4758	0.9577	-0.141223	-0.07486	0.104034
0.15250	0.13672	0.22003	-0.4548	0.9485	-0.144557	-0.08156	0.105117
0.15000	0.19924	0.21472	-0.4336	0.9393	-0.148566	-0.08820	0.106485
0.14750	0.26016	0.20913	-0.4122	0.9301	-0.153200	-0.09476	0.108097
0.14500	0.31936	0.20331	-0.3907	0.9208	-0.158431	-0.10125	0.109917
0.14250	0.37675	0.19729	-0.3690	0.9115	-0.164210	-0.10765	0.111921
0.14000	0.43227	0.19112	-0.3471	0.9022	-0.170538	-0.11396	0.114069
0.13750	0.48588	0.18481	-0.3251	0.8928	-0.177399	-0.12017	0.116336
0.13500	0.53759	0.17841	-0.3030	0.8834	-0.184784	-0.12630	0.118690
0.13250	0.58740	0.17193	-0.2807	0.8739	-0.192699	-0.13232	0.121105
0.13000	0.63535	0.16540	-0.2582	0.8644	-0.2011	-0.1383	0.1236
0.12667	0.69650	0.15666	-0.2279	0.8516	-0.2132	-0.1460	0.1268
0.12333	0.75448	0.14791	-0.1974	0.8387	-0.2263	-0.1535	0.1300
0.12000	0.80917	0.13924	-0.1666	0.8257	-0.240	-0.161	0.132
0.11667	0.86149	0.13056	-0.1355	0.8126	-0.256	-0.168	0.136
0.11333	0.91080	0.12202	-0.1041	0.7994	-0.272	-0.175	0.138
0.11000	0.95748	0.11362	-0.0724	0.7861	-0.290	-0.181	0.139
0.10500	1.02282	0.10131	-0.0243	0.7659	-0.319	-0.191	0.140
0.10000	1.08317	0.08938	0.0245	0.7454	-0.350	-0.200	0.139
0.09500	1.13860	0.07794	0.0739	0.7245	-0.387	-0.207	0.133
0.09000	1.18969	0.06702	0.1241	0.7032	-0.4282	-0.2139	0.1207
0.08000	1.28002	0.04694	0.2265	0.6594	-0.52608	-0.22275	0.068266
0.07750	1.30036	0.04232	0.2525	0.6481	-0.55473	-0.22396	0.045542
0.07500	1.31988	0.03786	0.2787	0.6367	-0.58538	-0.22463	0.017130
0.07250	1.33861	0.03358	0.3051	0.6252	-0.61820	-0.22462	-0.018353
0.07000	1.35653	0.02949	0.3317	0.6135	-0.65345	-0.22388	-0.06274
0.06000	1.42125	0.01508	0.4398	0.5649	-0.8245	-0.21080	-0.39397
0.05500	1.44972	0.00920	0.4949	0.5394	-0.9337	-0.19462	-0.7486
0.05000	1.47583	0.00439	0.5508	0.5130	-1.0649	-0.1663	-1.4436
0.04147	1.51285	0.00000	0.6478	0.4651		0.00000	

0.18000	-0.84082	0.19102	-0.5762	1.0476	-0.120437	0.01442	0.100421
0.17833	-0.79105	0.19161	-0.5639	1.0417	-0.117368	0.00952	0.096435
0.17667	-0.73988	0.19197	-0.5514	1.0358	-0.114406	0.00468	0.092856
0.17500	-0.68732	0.19209	-0.5389	1.0299	-0.111640	-0.00012	0.089674
0.17333	-0.63341	0.19196	-0.5263	1.0239	-0.109156	-0.00487	0.086883
0.17167	-0.57824	0.19156	-0.5137	1.0179	-0.107042	-0.00960	0.084479
0.17000	-0.52200	0.19089	-0.5010	1.0120	-0.105343	-0.01429	0.082450
0.16667	-0.40708	0.18871	-0.4754	1.0000	-0.103381	-0.02358	0.079461
0.16417	-0.31976	0.18635	-0.4561	0.9910	-0.103196	-0.03046	0.078069
0.16167	-0.23250	0.18339	-0.4366	0.9819	-0.104079	-0.03724	0.077310
0.16000	-0.17477	0.18111	-0.4235	0.9759	-0.105222	-0.04170	0.077112
0.15833	-0.11767	0.17861	-0.4104	0.9698	-0.106776	-0.04610	0.077129
0.15667	-0.06138	0.17589	-0.3972	0.9638	-0.108702	-0.05046	0.077338
0.15500	-0.00605	0.17297	-0.3839	0.9577	-0.111015	-0.05475	0.077711
0.15333	0.04823	0.16988	-0.3705	0.9516	-0.113648	-0.05899	0.078233
0.15167	0.10127	0.16664	-0.3571	0.9455	-0.116600	-0.06316	0.078882
0.15000	0.15304	0.16326	-0.3437	0.9393	-0.119846	-0.06727	0.079639
0.14750	0.22818	0.15797	-0.3233	0.9301	-0.125243	-0.07332	0.080943
0.14500	0.30026	0.15246	-0.3028	0.9208	-0.131244	-0.07922	0.082405
0.14250	0.36924	0.14679	-0.2822	0.9115	-0.137802	-0.08498	0.083970
0.14000	0.43512	0.14099	-0.2614	0.9022	-0.144919	-0.09058	0.085598
0.13750	0.49800	0.13511	-0.2405	0.8928	-0.1526	-0.0960	0.0873
0.13500	0.55793	0.12917	-0.2194	0.8834	-0.1608	-0.1013	0.0889
0.13250	0.61502	0.12322	-0.1982	0.8739	-0.1696	-0.1065	0.0904
0.13000	0.66941	0.11727	-0.1768	0.8644	-0.177	-0.111	0.091
0.12667	0.73787	0.10938	-0.1480	0.8516	-0.192	-0.118	0.093
0.12333	0.80231	0.10155	-0.1190	0.8387	-0.206	-0.124	0.095
0.12000	0.86255	0.09387	-0.0896	0.8257	-0.221	-0.130	0.095
0.11667	0.91903	0.08635	-0.0600	0.8126	-0.238	-0.135	0.095
0.11333	0.97203	0.07901	-0.0302	0.7994	-0.255	-0.140	0.093
0.11000	1.02106	0.07197	0.0000	0.7861	-0.275	-0.145	0.091
0.10500	1.09187	0.06139	0.0458	0.7659	-0.307	-0.151	0.084
0.10000	1.15349	0.05181	0.0922	0.7454	-0.342	-0.157	0.071
0.09000	1.26405	0.03402	0.1870	0.7032	-0.4216	-0.1612	0.0123
0.08000	1.35614	0.01916	0.2844	0.6594	-0.52499	-0.15672	-0.12424
0.07000	1.43353	0.00757	0.3845	0.6135	-0.6592	-0.13575	-0.48710
0.06500	1.46744	0.00330	0.4356	0.5896	-0.7422	-0.11225	-0.9446
0.06000	1.49854	0.00043	0.4874	0.5649	-0.8392	-0.0637	-2.4983
0.05791	1.51042	0.00000	0.5092	0.5544		0.00000	

Tab. 4

QUASI-ELLIPTICAL AEROFOIL SECTION 0.1075—0.6750—1.0500
 PROFILE NUMBER 7
 FREE STREAM MACH NUMBER 0.7760

τ	x	y	c_p	M	M_ϵ	θ	$1/R$
0.00000	-1.69718	0.00000	1.1598	0.0000	0.000000	1.57080	11.619188
0.01000	-1.69357	0.02482	1.0377	0.2247	8.48	1.286	10.72
0.02000	-1.68964	0.03575	0.9187	0.3194	7.80	1.167	9.82
0.03000	-1.68534	0.04463	0.8026	0.3932	7.14	1.074	8.97
0.04000	-1.68060	0.05259	0.6895	0.4564	6.51	0.995	8.14
0.05000	-1.67536	0.06006	0.5794	0.5130	5.894	0.9242	7.35
0.06000	-1.66953	0.06728	0.4720	0.5649	5.307	0.8595	6.592
0.07000	-1.66300	0.07439	0.3675	0.6135	4.752	0.7994	5.877
0.08000	-1.65566	0.08152	0.2658	0.6594	4.229	0.7427	5.205
0.09000	-1.64735	0.08874	0.1668	0.7032	3.744	0.6889	4.578
0.10000	-1.63790	0.09612	0.0705	0.7454	3.300	0.6376	4.001
0.11000	-1.62711	0.10369	-0.0232	0.7861	2.899	0.5885	3.474
0.12000	-1.61479	0.11149	-0.1143	0.8257	2.546	0.5414	3.0024
0.13000	-1.60073	0.11951	-0.2028	0.8644	2.2431	0.4962	2.5879
0.14000	-1.58487	0.12765	-0.2888	0.9022	1.9955	0.4533	2.2311
0.15000	-1.56704	0.13589	-0.3724	0.9393	1.8083	0.4126	1.9360
0.16000	-1.54763	0.14394	-0.4535	0.9759	1.6911	0.3745	1.7054
0.16667	-1.53416	0.14905	-0.5063	1.0000	1.6601	0.35079	1.5901
0.17000	-1.52737	0.15149	-0.5323	1.0120	1.6619	0.33959	1.5450
0.18000	-1.50744	0.15817	-0.6087	1.0476	1.7591	0.30793	1.4695
0.19000	-1.48953	0.16360	-0.6828	1.0830	2.0777	0.28039	1.5148
0.20000	-1.47545	0.16748	-0.7547	1.1180	2.9022	0.25658	1.7984
0.21000	-1.46652	0.16973	-0.8244	1.1529	5.454	0.23687	2.8355
0.22000	-1.46280	0.17061	-0.8918	1.1875	21.24	0.22011	9.58
0.23000	-1.46192	0.17080	-0.9572	1.2221	19.94	0.20463	9.45
0.24000	-1.44519	0.17386	-1.0205	1.2566	0.36860	0.1795	0.73395
0.24000	-1.40359	0.18088	-1.0205	1.2566	-0.15930	0.15687	0.41750
0.23500	-1.32573	0.19206	-0.9891	1.2393	-0.24217	0.13003	0.29022
0.23000	-1.25484	0.20063	-0.9572	1.2221	-0.23740	0.11131	0.238669
0.22667	-1.20570	0.20584	-0.9357	1.2106	-0.228017	0.10013	0.214822
0.22333	-1.15426	0.21073	-0.9139	1.1991	-0.217678	0.08954	0.195721
0.22000	-1.10024	0.21530	-0.8918	1.1875	-0.207518	0.07937	0.180001
0.21667	-1.04344	0.21954	-0.8696	1.1760	-0.198078	0.06950	0.166881
0.21333	-0.98389	0.22339	-0.8471	1.1644	-0.189572	0.05989	0.155839
0.21000	-0.92167	0.22682	-0.8244	1.1529	-0.182099	0.05048	0.146516
0.20667	-0.85689	0.22980	-0.8014	1.1413	-0.175651	0.04124	0.138626
0.20333	-0.78979	0.23226	-0.7782	1.1297	-0.170112	0.03216	0.131925
0.20000	-0.72039	0.23418	-0.7547	1.1180	-0.165370	0.02321	0.126220

Tab. 5

QUASI-ELLIPTICAL AEROFOIL SECTION 0.1100—0.7500—0.9000
 PROFILE NUMBER 8
 FREE STREAM MACH NUMBER 0.7861

τ	x	y	c_p	M	M_ϵ	θ	$1/R$
0.00000	-1.79504	0.00000	1.1642	0.0000	0.000000	1.57080	49.100807
0.01000	-1.79307	0.00918	1.0440	0.2247	18.9	1.18	30.8
0.02000	-1.79046	0.01432	0.9269	0.3194	14.2	1.031	21.5
0.03000	-1.78714	0.01920	0.8127	0.3932	11.04	0.923	15.79
0.04000	-1.78303	0.02414	0.7014	0.4564	8.77	0.834	12.01
0.05000	-1.77798	0.02928	0.5930	0.5130	7.05	0.758	9.33
0.06000	-1.77184	0.03470	0.4874	0.5649	5.710	0.6904	7.34
0.07000	-1.76437	0.04048	0.3845	0.6135	4.635	0.6287	5.822
0.08000	-1.75528	0.04668	0.2844	0.6594	3.760	0.5716	4.630
0.09000	-1.74418	0.05340	0.1870	0.7032	3.038	0.5181	3.681
0.10000	-1.73052	0.06073	0.0922	0.7454	2.440	0.4674	2.916
0.11000	-1.71360	0.06873	0.0000	0.7861	1.9438	0.4190	2.295
0.12000	-1.69241	0.07756	-0.0896	0.8257	1.5328	0.3724	1.7910
0.13000	-1.66555	0.08733	-0.1768	0.8644	1.1955	0.32736	1.3831
0.14000	-1.63114	0.09815	-0.2614	0.9022	0.9227	0.28406	1.05582
0.15000	-1.58661	0.11009	-0.3437	0.9393	0.70583	0.24180	0.79811
0.16000	-1.52848	0.12310	-0.4235	0.9759	0.53469	0.20059	0.59896
0.16667	-1.47946	0.13236	-0.4754	1.0000	0.43638	0.17360	0.49208
0.17000	-1.45077	0.13718	-0.5010	1.0120	0.38760	0.16001	0.44399
0.17500	-1.39976	0.14485	-0.5389	1.0299	0.30655	0.13901	0.37417
0.18000	-1.32987	0.15376	-0.5762	1.0476	0.19932	0.11539	0.297747
0.18167	-1.29638	0.15748	-0.5886	1.0536	0.152049	0.10591	0.267000
0.18333	-1.24843	0.16228	-0.6008	1.0595	0.093757	0.09399	0.229433
0.18333	-0.94118	0.18268	-0.6008	1.0595	-0.048027	0.04422	0.120369
0.18167	-0.83289	0.18680	-0.5886	1.0536	-0.059795	0.03194	0.106563
0.18000	-0.73948	0.18933	-0.5762	1.0476	-0.066266	0.02239	0.098506
0.17833	-0.65319	0.19090	-0.5639	1.0417	-0.070852	0.01414	0.093190
0.17667	-0.57171	0.19175	-0.5514	1.0358	-0.074641	0.00670	0.089533
0.17500	-0.49395	0.19200	-0.5389	1.0299	-0.078088	-0.00016	0.086994
0.17333	-0.41934	0.19175	-0.5263	1.0239	-0.081398	-0.00658	0.085257
0.17167	-0.34754	0.19106	-0.5137	1.0179	-0.084670	-0.01266	0.084117
0.17000	-0.27837	0.18998	-0.5010	1.0120	-0.087952	-0.01845	0.083436
0.16667	-0.14708	0.18684	-0.4754	1.0000	-0.094633	-0.02938	0.083092
0.16417	-0.05444	0.18376	-0.4561	0.9910	-0.099816	-0.03709	0.083498
0.16167	0.03372	0.18016	-0.4366	0.9819	-0.105203	-0.04449	0.084339
0.16000	0.09011	0.17752	-0.4235	0.9759	-0.108941	-0.04928	0.085101
0.15833	0.14468	0.17470	-0.4104	0.9698	-0.112795	-0.05395	0.086004
0.15667	0.19748	0.17173	-0.3972	0.9638	-0.116816	-0.05853	0.087030

0.19750	-0.66701	0.23524	-0.7369	1.1093	-0.162233	0.01657	0.122487
0.19500	-0.61256	0.23597	-0.7190	1.1005	-0.159378	0.01000	0.119157
0.19250	-0.55706	0.23634	-0.7010	1.0918	-0.156768	0.00347	0.116187
0.19000	-0.50057	0.23635	-0.6828	1.0830	-0.154390	-0.00302	0.113555
0.18750	-0.44313	0.23599	-0.6645	1.0742	-0.152260	-0.00948	0.111253
0.18500	-0.38483	0.23525	-0.6460	1.0653	-0.150456	-0.01590	0.109292
0.18250	-0.32578	0.23412	-0.6274	1.0565	-0.149055	-0.02231	0.107685
0.18000	-0.26615	0.23260	-0.6087	1.0476	-0.148138	-0.02869	0.106445
0.17750	-0.20612	0.23069	-0.5898	1.0388	-0.147770	-0.03506	0.105575
0.17500	-0.14594	0.22839	-0.5708	1.0299	-0.147991	-0.04140	0.105068
0.17250	-0.08582	0.22570	-0.5516	1.0209	-0.148830	-0.04772	0.104910
0.17000	-0.02599	0.22266	-0.5323	1.0120	-0.150234	-0.05401	0.105076
0.16667	0.05290	0.21807	-0.5063	1.0000	-0.153024	-0.06233	0.105766
0.16333	0.13038	0.21291	-0.4800	0.9880	-0.156789	-0.07059	0.106931
0.16000	0.20608	0.20725	-0.4535	0.9759	-0.161475	-0.07877	0.108517
0.15750	0.26154	0.20270	-0.4335	0.9668	-0.165569	-0.08484	0.109950
0.15500	0.31570	0.19793	-0.4132	0.9577	-0.170143	-0.09086	0.111569
0.15250	0.36852	0.19296	-0.3929	0.9485	-0.175192	-0.09683	0.113354
0.15000	0.42001	0.18781	-0.3724	0.9393	-0.180702	-0.10273	0.115285
0.14667	0.48622	0.18072	-0.3448	0.9270	-0.188777	-0.11051	0.118057
0.14333	0.54990	0.17341	-0.3169	0.9146	-0.197687	-0.11817	0.121012
0.14000	0.61092	0.16593	-0.2888	0.9022	-0.207445	-0.12571	0.124102
0.13667	0.66933	0.15833	-0.2604	0.8897	-0.2181	-0.1331	0.1273
0.13333	0.72514	0.15066	-0.2317	0.8771	-0.2296	-0.1404	0.1305
0.13000	0.77851	0.14292	-0.2028	0.8644	-0.2421	-0.1474	0.1337
0.12500	0.85381	0.13135	-0.1588	0.8452	-0.263	-0.158	0.135
0.12000	0.92383	0.11987	-0.1143	0.8257	-0.286	-0.167	0.142
0.11500	0.98885	0.10859	-0.0690	0.8061	-0.311	-0.176	0.145
0.11000	1.04913	0.09751	-0.0232	0.7861	-0.340	-0.187	0.144
0.10500	1.10500	0.08667	0.0233	0.7659	-0.372	-0.196	0.140
0.10000	1.15669	0.07624	0.0705	0.7454	-0.406	-0.203	0.135
0.09000	1.24894	0.05669	0.1668	0.7032	-0.4923	-0.2145	0.1142
0.08000	1.32780	0.03919	0.2658	0.6594	-0.60032	-0.22116	0.044607
0.07000	1.39510	0.02405	0.3675	0.6135	-0.7410	-0.21945	-0.12184
0.06000	1.45240	0.01166	0.4720	0.5649	-0.9301	-0.20236	-0.5417
0.05500	1.47771	0.00670	0.5253	0.5394	-1.0510	-0.1831	-1.0030
0.05000	1.50099	0.00275	0.5794	0.5130	-1.1963	-0.1494	-1.9694
0.04321	1.52801	0.00000	0.6539	0.4752		0.00000	

0.15500	0.24861	0.16861	-0.3839	0.9577	-0.120983	-0.06301	0.088171
0.15333	0.29799	0.16539	-0.3705	0.9516	-0.125319	-0.06741	0.089412
0.15167	0.34589	0.16205	-0.3571	0.9455	-0.129835	-0.07173	0.090744
0.15000	0.39217	0.15863	-0.3437	0.9393	-0.134536	-0.07597	0.092156
0.14750	0.45876	0.15335	-0.3233	0.9301	-0.141961	-0.08220	0.094401
0.14500	0.52204	0.14795	-0.3028	0.9208	-0.149836	-0.08827	0.096768
0.14250	0.58223	0.14244	-0.2822	0.9115	-0.158200	-0.09419	0.099225
0.14000	0.63943	0.13687	-0.2614	0.9022	-0.167067	-0.09997	0.101737
0.13750	0.69383	0.13126	-0.2405	0.8928	-0.1765	-0.1056	0.1043
0.13500	0.74555	0.12563	-0.2194	0.8834	-0.1864	-0.1111	0.1068
0.13250	0.79471	0.12002	-0.1982	0.8739	-0.1969	-0.1164	0.1092
0.13000	0.84152	0.11442	-0.1768	0.8644	-0.208	-0.122	0.112
0.12667	0.90033	0.10703	-0.1480	0.8516	-0.224	-0.128	0.116
0.12333	0.95545	0.09974	-0.1190	0.8387	-0.240	-0.135	0.115
0.12000	1.00698	0.09258	-0.0896	0.8257	-0.258	-0.141	0.117
0.11500	1.07833	0.08214	-0.0451	0.8061	-0.288	-0.150	0.120
0.11000	1.14317	0.07210	0.0000	0.7861	-0.321	-0.158	0.118
0.10500	1.20234	0.06249	0.0458	0.7659	-0.357	-0.165	0.113
0.10000	1.25596	0.05332	0.0922	0.7454	-0.395	-0.172	0.111
0.09000	1.35001	0.03656	0.1870	0.7032	-0.4925	-0.1786	0.0520
0.08000	1.42858	0.02234	0.2844	0.6594	-0.61322	-0.17808	-0.070293
0.07000	1.49459	0.01079	0.3845	0.6135	-0.7697	-0.16506	-0.37512
0.06500	1.52352	0.00617	0.4356	0.5896	-0.8665	-0.14975	-0.7015
0.06000	1.55001	0.00250	0.4874	0.5649	-0.9796	-0.1229	-1.3626
0.05285	1.58224	0.00000	0.5626	0.5282		0.00000	

Tab. 6

QUASI-ELLIPTICAL AEROFOIL SECTION 0.1125—0.7500—1.3250
 PROFILE NUMBER 10
 FREE STREAM MACH NUMBER 0.7961

τ	x	y	c_p	M	M_e	θ	$1/R$
0.00000	-1.79929	0.00000	1.1687	0.0000	0.000000	1.57080	7.623522
0.01000	-1.79617	0.02844	1.0503	0.2247	7.98	1.352	7.69
0.02000	-1.79311	0.03974	0.9350	0.3194	8.21	1.261	7.78
0.03000	-1.79012	0.04807	0.8226	0.3932	8.47	1.192	7.89
0.04000	-1.78721	0.05481	0.7130	0.4564	8.77	1.133	8.01
0.05000	-1.78438	0.06048	0.6062	0.5130	9.10	1.082	8.16
0.06000	-1.78164	0.06536	0.5022	0.5649	9.47	1.0361	8.34
0.07000	-1.77899	0.06962	0.4009	0.6135	9.90	0.9937	8.55
0.08000	-1.77645	0.07337	0.3024	0.6594	10.38	0.9545	8.79
0.09000	-1.77400	0.07669	0.2064	0.7032	10.92	0.9177	9.07
0.10000	-1.77167	0.07963	0.1131	0.7454	11.52	0.8830	9.40
0.11000	-1.76944	0.08225	0.0223	0.7861	12.20	0.8500	9.78
0.12000	-1.76732	0.08459	-0.0660	0.8257	12.95	0.8185	10.21
0.13000	-1.76532	0.08667	-0.1518	0.8644	13.76	0.7882	10.70
0.14000	-1.76341	0.08854	-0.2351	0.9022	14.60	0.7590	11.24
0.15000	-1.76159	0.09022	-0.3161	0.9393	15.43	0.7305	11.80
0.16000	-1.75984	0.09174	-0.3947	0.9759	16.13	0.7025	12.36
0.16667	-1.75871	0.09268	-0.4459	1.0000	16.46	0.6841	12.68
0.17000	-1.75814	0.09314	-0.4710	1.0120	16.55	0.6748	12.82
0.18000	-1.75644	0.09446	-0.5451	1.0476	16.43	0.6469	13.06
0.19000	-1.75466	0.09576	-0.6169	1.0830	15.48	0.6183	12.91
0.20000	-1.75268	0.09713	-0.6866	1.1180	13.48	0.5880	12.21
0.21000	-1.75023	0.09870	-0.7541	1.1529	10.42	0.5544	10.86
0.22000	-1.74672	0.10078	-0.8195	1.1875	6.66	0.5163	8.884
0.23000	-1.73983	0.10441	-0.8828	1.2221	2.844	0.457	6.452
0.24000	-1.71256	0.11536	-0.9442	1.2566	0.809	0.322	3.373
0.24333	-1.70112	0.11893	-0.9642	1.2680	1.127	0.2845	2.956
0.24667	-1.69193	0.12149	-0.9839	1.2795	1.182	0.2579	2.6352
0.24667	-1.65132	0.13050	-0.9839	1.2795	-0.5969	0.1905	0.9622
0.24333	-1.63314	0.13385	-0.9642	1.2680	-0.6237	0.17518	0.75546
0.24000	-1.61458	0.13701	-0.9442	1.2566	-0.59274	0.16229	0.62537
0.23667	-1.59468	0.14015	-0.9239	1.2451	-0.54590	0.15075	0.52968
0.23333	-1.57281	0.14334	-0.9035	1.2336	-0.49637	0.13988	0.45458
0.23000	-1.54863	0.14662	-0.8828	1.2221	-0.44782	0.12960	0.39320
0.22000	-1.45871	0.15692	-0.8195	1.1875	-0.32862	0.10059	0.265015
0.21500	-1.40258	0.16219	-0.7871	1.1702	-0.284593	0.08688	0.222154
0.21000	-1.33737	0.16742	-0.7541	1.1529	-0.250195	0.07354	0.189181
0.20667	-1.28925	0.17075	-0.7318	1.1413	-0.231962	0.06486	0.171573
0.20333	-1.23751	0.17389	-0.7093	1.1297	-0.216932	0.05637	0.156792
0.20000	-1.18237	0.17677	-0.6866	1.1180	-0.204565	0.04807	0.144321

Tab. 7

QUASI-ELLIPTICAL AEROFOIL SECTION 0.1150—0.7500—1.2000
 PROFILE NUMBER 11
 FREE STREAM MACH NUMBER 0.8061

τ	x	y	c_p	M	M_e	θ	$1/R$
0.00000	-1.80375	0.00000	1.1732	0.0000	0.000000	1.57080	10.349575
0.01000	-1.80103	0.02276	1.0566	0.2247	9.81	1.333	10.31
0.02000	-1.79830	0.03200	0.9430	0.3194	9.85	1.234	10.28
0.03000	-1.79556	0.03896	0.8322	0.3932	9.88	1.157	10.25
0.04000	-1.79280	0.04472	0.7242	0.4564	9.89	1.092	10.22
0.05000	-1.79002	0.04972	0.6190	0.5130	9.89	1.034	10.18
0.06000	-1.78721	0.05416	0.5166	0.5649	9.86	0.980	10.13
0.07000	-1.78436	0.05819	0.4168	0.6135	9.80	0.9303	10.07
0.08000	-1.78146	0.06190	0.3197	0.6594	9.68	0.8830	9.98
0.09000	-1.77848	0.06536	0.2252	0.7032	9.48	0.8377	9.86
0.10000	-1.77549	0.06865	0.1332	0.7454	9.20	0.7936	9.67
0.11000	-1.77214	0.07180	0.0438	0.7861	8.80	0.7504	9.41
0.12000	-1.76868	0.07489	-0.0432	0.8257	8.25	0.7075	9.05
0.13000	-1.76490	0.07799	-0.1277	0.8644	7.540	0.6644	8.569
0.14000	-1.76064	0.08117	-0.2098	0.9022	6.662	0.6204	7.934
0.15000	-1.75564	0.08457	-0.2896	0.9393	5.636	0.5748	7.138
0.16000	-1.74949	0.08835	-0.3671	0.9759	4.523	0.5265	6.187
0.16667	-1.74444	0.09116	-0.4174	1.0000	3.783	0.4932	5.479
0.17000	-1.74149	0.09272	-0.4423	1.0120	3.429	0.4761	5.111
0.18000	-1.73045	0.09801	-0.5152	1.0476	2.506	0.4201	4.030
0.19000	-1.71535	0.10422	-0.5860	1.0830	1.909	0.3629	3.0776
0.20000	-1.69684	0.11068	-0.6546	1.1180	1.7508	0.3100	2.4404
0.21000	-1.67917	0.11592	-0.7211	1.1529	2.1709	0.2670	2.2592
0.22000	-1.66710	0.11902	-0.7855	1.1875	3.944	0.2358	2.850
0.23000	-1.66180	0.12026	-0.8480	1.2221	12.96	0.21503	6.828
0.24000	-1.65932	0.12079	-0.9084	1.2566	5.726	0.1969	3.665
0.24000	-1.60196	0.13020	-0.9084	1.2566	-0.41992	0.14875	0.48781
0.23000	-1.51504	0.14164	-0.8480	1.2221	-0.35181	0.11571	0.29898
0.22500	-1.46284	0.14732	-0.8170	1.2048	-0.30677	0.10148	0.246192
0.22000	-1.40279	0.15301	-0.7855	1.1875	-0.268263	0.08791	0.206596
0.21500	-1.33406	0.15864	-0.7536	1.1702	-0.236113	0.07479	0.175969
0.21000	-1.25633	0.16398	-0.7211	1.1529	-0.210966	0.06205	0.152497
0.20667	-1.19960	0.16726	-0.6992	1.1413	-0.197519	0.05376	0.139923
0.20333	-1.13913	0.17026	-0.6770	1.1297	-0.186621	0.04562	0.129443
0.20000	-1.07525	0.17292	-0.6546	1.1180	-0.177716	0.03763	0.120612
0.19750	-1.02527	0.17466	-0.6376	1.1093	-0.171996	0.03175	0.114832
0.19500	-0.97373	0.17615	-0.6206	1.1005	-0.166792	0.02595	0.109598
0.19250	-0.92024	0.17738	-0.6033	1.0918	-0.161741	0.02023	0.104740
0.19000	-0.86498	0.17834	-0.5860	1.0830	-0.156552	0.01457	0.100133
0.18750	-0.80795	0.17901	-0.5685	1.0742	-0.151015	0.00897	0.095701

∞

0.19667	-1.12382	0.17934	-0.6636	1.1064	-0.194071	0.03994	0.133612	0.18500	-0.74816	0.17938	-0.5509	1.0653	-0.145095	0.00340	0.091440
0.19333	-1.06211	0.18156	-0.6404	1.0947	-0.184528	0.03199	0.124141	0.18250	-0.68591	0.17942	-0.5331	1.0565	-0.138984	-0.00217	0.087424
0.19000	-0.99702	0.18339	-0.6169	1.0830	-0.175055	0.02419	0.115458	0.18000	-0.62068	0.17909	-0.5152	1.0476	-0.133028	-0.00775	0.083769
0.18750	-0.94559	0.18448	-0.5992	1.0742	-0.167471	0.01842	0.109254	0.17750	-0.55252	0.17838	-0.4972	1.0388	-0.127635	-0.01335	0.080594
0.18500	-0.89142	0.18532	-0.5813	1.0653	-0.159361	0.01268	0.103269	0.17500	-0.48145	0.17723	-0.4790	1.0299	-0.123164	-0.01898	0.077984
0.18250	-0.83460	0.18588	-0.5633	1.0565	-0.150845	0.00696	0.097553	0.17250	-0.40793	0.17563	-0.4607	1.0209	-0.119848	-0.02463	0.075975
0.18000	-0.77411	0.18612	-0.5451	1.0476	-0.142266	0.00123	0.092223	0.17000	-0.33255	0.17356	-0.4423	1.0120	-0.117775	-0.03031	0.074552
0.17750	-0.70978	0.18601	-0.5268	1.0388	-0.134089	-0.00455	0.087420	0.16667	-0.23040	0.17007	-0.4174	1.0000	-0.116915	-0.03787	0.073479
0.17500	-0.64144	0.18550	-0.5084	1.0299	-0.126780	-0.01038	0.083267	0.16417	-0.15354	0.16695	-0.3987	0.9910	-0.117554	-0.04351	0.073208
0.17250	-0.56921	0.18454	-0.4898	1.0209	-0.120706	-0.01626	0.079841	0.16167	-0.07719	0.16341	-0.3798	0.9819	-0.119223	-0.04910	0.073312
0.17000	-0.49352	0.18308	-0.4710	1.0120	-0.116076	-0.02220	0.077161	0.16000	-0.02687	0.16084	-0.3671	0.9759	-0.120808	-0.05280	0.073557
0.16667	-0.38843	0.18033	-0.4459	1.0000	-0.112246	-0.03017	0.074688	0.15750	0.04723	0.15672	-0.3479	0.9668	-0.123858	-0.05829	0.074147
0.16417	-0.30766	0.17765	-0.4268	0.9910	-0.111045	-0.03616	0.073573	0.15500	0.11984	0.15229	-0.3286	0.9577	-0.127631	-0.06370	0.074954
0.16167	-0.22627	0.17446	-0.4076	0.9819	-0.111135	-0.04212	0.072997	0.15250	0.19026	0.14761	-0.3092	0.9485	-0.132057	-0.06902	0.075928
0.16000	-0.17209	0.17207	-0.3947	0.9759	-0.111841	-0.04608	0.072872	0.15000	0.25839	0.14272	-0.2896	0.9393	-0.137088	-0.07425	0.077025
0.15833	-0.11826	0.16948	-0.3818	0.9698	-0.113004	-0.05001	0.072924	0.14750	0.32419	0.13766	-0.2699	0.9301	-0.142688	-0.07937	0.078203
0.15667	-0.06494	0.16671	-0.3688	0.9638	-0.114593	-0.05390	0.073133	0.14500	0.38756	0.13246	-0.2500	0.9208	-0.148824	-0.08438	0.079429
0.15500	-0.01235	0.16377	-0.3557	0.9577	-0.116573	-0.05776	0.073475	0.14250	0.44850	0.12715	-0.2300	0.9115	-0.1555	-0.0893	0.0807
0.15333	0.03939	0.16068	-0.3426	0.9516	-0.118911	-0.06158	0.073935	0.14000	0.50703	0.12177	-0.2098	0.9022	-0.1627	-0.0941	0.0819
0.15167	0.09017	0.15745	-0.3294	0.9455	-0.121577	-0.06536	0.074491	0.13750	0.56312	0.11635	-0.1895	0.8928	-0.1704	-0.0987	0.0830
0.15000	0.13990	0.15410	-0.3161	0.9393	-0.124553	-0.06909	0.075129	0.13500	0.61690	0.11090	-0.1691	0.8834	-0.1786	-0.1032	0.0840
0.14750	0.21237	0.14888	-0.2961	0.9301	-0.129552	-0.07458	0.076206	0.13250	0.66858	0.10544	-0.1484	0.8739	-0.187	-0.108	0.085
0.14500	0.28219	0.14348	-0.2759	0.9208	-0.135155	-0.07996	0.077388	0.13000	0.71785	0.10001	-0.1277	0.8644	-0.197	-0.112	0.085
0.14250	0.34930	0.13792	-0.2556	0.9115	-0.141347	-0.08521	0.078617	0.12667	0.78055	0.09279	-0.0998	0.8516	-0.210	-0.117	0.086
0.14000	0.41365	0.13226	-0.2351	0.9022	-0.1481	-0.0904	0.0803	0.12333	0.83947	0.08570	-0.0716	0.8387	-0.224	-0.122	0.085
0.13750	0.47531	0.12652	-0.2145	0.8928	-0.1553	-0.0953	0.0807	0.12000	0.89516	0.07872	-0.0432	0.8257	-0.239	-0.127	0.084
0.13500	0.53427	0.12074	-0.1937	0.8834	-0.1631	-0.1002	0.0822	0.11667	0.94741	0.07193	-0.0145	0.8126	-0.256	-0.131	0.082
0.13250	0.59069	0.11493	-0.1728	0.8739	-0.1714	-0.1049	0.0833	0.11333	0.99738	0.06521	0.0145	0.7994	-0.275	-0.136	0.079
0.13000	0.64446	0.10915	-0.1518	0.8644	-0.180	-0.109	0.084	0.11000	1.04352	0.05881	0.0438	0.7861	-0.293	-0.139	0.073
0.12667	0.71280	0.10144	-0.1234	0.8516	-0.193	-0.115	0.085	0.10500	1.10885	0.04950	0.0882	0.7659	-0.323	-0.144	0.054
0.12333	0.77687	0.09384	-0.0948	0.8387	-0.206	-0.121	0.085	0.10000	1.16866	0.04076	0.1332	0.7454	-0.3580	-0.1465	0.0394
0.12000	0.83710	0.08636	-0.0660	0.8257	-0.221	-0.126	0.084	0.09917	1.17814	0.03936	0.1408	0.7419	-0.3643	-0.1468	0.0350
0.11667	0.89390	0.07901	-0.0368	0.8126	-0.236	-0.131	0.083	0.09833	1.18746	0.03798	0.1484	0.7384	-0.3704	-0.1471	0.0303
0.11333	0.94707	0.07185	-0.0074	0.7994	-0.253	-0.136	0.080	0.09750	1.19665	0.03662	0.1560	0.7350	-0.3768	-0.1474	0.0252
0.11000	0.99694	0.06485	0.0223	0.7861	-0.270	-0.140	0.076	0.09667	1.20576	0.03527	0.1636	0.7315	-0.3833	-0.1476	0.0198
0.10500	1.07061	0.05421	0.0674	0.7659	-0.302	-0.145	0.067	0.09583	1.21467	0.03394	0.1712	0.7280	-0.3899	-0.1477	0.0141
0.10000	1.13137	0.04524	0.1131	0.7454	-0.3348	-0.1476	0.0474	0.09500	1.22347	0.03263	0.1789	0.7245	-0.3967	-0.1478	0.0078
0.09667	1.17099	0.03931	0.1439	0.7315	-0.3590	-0.1492	0.0307	0.09417	1.23218	0.03133	0.1866	0.7210	-0.40355	-0.14788	0.001205
0.09333	1.20835	0.03368	0.1750	0.7174	-0.3851	-0.1500	0.0083	0.09333	1.24074	0.03006	0.1942	0.7174	-0.41057	-0.14786	-0.005936
0.09000	1.24360	0.02835	0.2064	0.7032	-0.41331	-0.14978	-0.021396	0.09250	1.24922	0.02880	0.2019	0.7139	-0.41773	-0.14778	-0.013593
0.08000	1.33792	0.01440	0.3024	0.6594	-0.51296	-0.14123	-0.18762	0.09167	1.25739	0.02758	0.2097	0.7103	-0.42502	-0.14763	-0.021828
0.07500	1.37936	0.00872	0.3513	0.6367	-0.57324	-0.13015	-0.35776	0.09083	1.26574	0.02634	0.2174	0.7068	-0.43247	-0.14741	-0.030661
0.07000	1.41741	0.00407	0.4009	0.6135	-0.6425	-0.11090	-0.67871	0.09000	1.27385	0.02514	0.2252	0.7032	-0.44007	-0.14713	-0.040152
0.06152	1.47232	0.00000	0.4866	0.5725			0.00000	0.08000	1.36263	0.01233	0.3197	0.6594	-0.54432	-0.13647	-0.23229
								0.07500	1.40174	0.00719	0.3679	0.6367	-0.60744	-0.12381	-0.43356
								0.07000	1.43769	0.00307	0.4168	0.6135	-0.6799	-0.10174	-0.8346
								0.06292	1.48183	0.00000	0.4872	0.5794		0.00000	

Tab. 8

QUASI-ELLIPTICAL AEROFOIL SECTION 0.1175 — 0.8000 — 1.2600
 PROFILE NUMBER 12
 FREE STREAM MACH NUMBER 0.8159

τ	x	y	c_p	M	M_s	θ	$1/R$
0.0000	-1.87247	0.00000	1.1777	0.0000	0.000000	1.57080	10.022243
0.01000	-1.87026	0.02085	1.0628	0.2247	11.0	1.359	10.2
0.02000	-1.86812	0.02907	0.9508	0.3194	11.38	1.272	10.32
0.03000	-1.86605	0.03508	0.8416	0.3932	11.87	1.206	10.51
0.04000	-1.86407	0.03989	0.7352	0.4564	12.44	1.151	10.74
0.05000	-1.86216	0.04389	0.6315	0.5130	13.10	1.103	11.02
0.06000	-1.86035	0.04730	0.5305	0.5649	13.86	1.060	11.34
0.07000	-1.85863	0.05023	0.4322	0.6135	14.75	1.020	11.73
0.08000	-1.85701	0.05277	0.3365	0.6594	15.80	0.984	12.19
0.09000	-1.85549	0.05497	0.2433	0.7032	17.04	0.951	12.74
0.10000	-1.85408	0.05689	0.1527	0.7454	18.52	0.920	13.40
0.11000	-1.85279	0.05854	0.0645	0.7861	20.31	0.8912	14.20
0.12000	-1.85160	0.05997	-0.0212	0.8257	22.50	0.8639	15.20
0.13000	-1.85053	0.06119	-0.1045	0.8644	25.20	0.8383	16.41
0.14000	-1.84957	0.06223	-0.1855	0.9022	28.56	0.8142	17.94
0.15000	-1.84872	0.06311	-0.2641	0.9393	32.81	0.7912	19.89
0.16000	-1.84799	0.06384	-0.3404	0.9759	38.23	0.7694	22.41
0.16667	-1.84756	0.06425	-0.3901	1.0000	42.67	0.7554	24.49
0.17000	-1.84736	0.06444	-0.4146	1.0120	45.2	0.7486	25.70
0.18000	-1.84682	0.06492	-0.4865	1.0476	54.1	0.7286	29.90
0.19000	-1.84637	0.06532	-0.5562	1.0830	64.8	0.7091	35.3
0.20000	-1.84599	0.06564	-0.6239	1.1180	76.5	0.6901	41.5
0.21000	-1.84566	0.06591	-0.6894	1.1529	84.4	0.6711	46.6
0.22000	-1.84534	0.06616	-0.7529	1.1875	81.2	0.652	46.9
0.23000	-1.84496	0.06644	-0.8144	1.2221	63.0	0.631	40.1
0.24000	-1.84439	0.06685	-0.8740	1.2566	37.9	0.610	29.1
0.25000	-1.84324	0.06762	-0.9316	1.2910	15.88	0.581	18.63
0.25000	-1.83108	0.07414	-0.9316	1.2910	-4.145	0.433	7.249
0.24000	-1.82355	0.07738	-0.8740	1.2566	-4.018	0.3806	5.587
0.23000	-1.81436	0.08079	-0.8144	1.2221	-2.976	0.3329	4.127
0.22000	-1.79972	0.08540	-0.7529	1.1875	-1.647	0.2809	2.7325
0.21000	-1.75929	0.09518	-0.6894	1.1529	-0.3607	0.2037	1.3026
0.20833	-1.73705	0.09946	-0.6786	1.1471	-0.1784	0.1779	0.98529
0.20667	-1.69234	0.10661	-0.6678	1.1413	-0.11462	0.1422	0.62459
0.20500	-1.64793	0.11241	-0.6569	1.1355	-0.14578	0.11881	0.43082
0.20333	-1.61066	0.11658	-0.6460	1.1297	-0.16206	0.10461	0.33516
0.20167	-1.57548	0.12008	-0.6349	1.1239	-0.166081	0.09387	0.275680
0.20000	-1.54046	0.12321	-0.6239	1.1180	-0.164606	0.08494	0.234554
0.19750	-1.48649	0.12748	-0.6072	1.1093	-0.157894	0.07345	0.191551

Tab. 9

QUASI-ELLIPTICAL AEROFOIL SECTION 0.1200 — 0.7000 — 0.0000
 PROFILE NUMBER 14
 FREE STREAM MACH NUMBER 0.8257

τ	x	y	c_p	M	M_s	θ	$1/R$
0.0339	-1.69040	0	0.8097	0.4188		0	
0.0400	-1.67783	0.00208	0.7459	0.4564	3.0632	0.21257	-4.9004
0.0500	-1.65718	0.00729	0.6437	0.5130	2.3252	0.26946	-1.35505
0.0508	-1.65530	0.00781	0.6353	0.5175	2.27669	0.27191	-1.21974
0.0517	-1.65340	0.00835	0.6269	0.5219	2.22981	0.27419	-1.09629
0.0533	-1.64952	0.00945	0.6102	0.5307	2.14044	0.27815	-0.88019
0.0550	-1.64553	0.01059	0.5935	0.5394	2.05649	0.28140	-0.69846
0.0567	-1.64144	0.01178	0.5770	0.5480	1.97751	0.28405	-0.54478
0.0583	-1.63723	0.01301	0.5605	0.5565	1.90307	0.28613	-0.41416
0.0600	-1.63292	0.01429	0.5441	0.5649	1.83280	0.28770	-0.30271
0.0617	-1.62850	0.01560	0.5277	0.5732	1.76642	0.28887	-0.20730
0.0633	-1.62396	0.01695	0.5115	0.5814	1.70356	0.28966	-0.12539
0.0650	-1.61930	0.01834	0.4953	0.5896	1.64400	0.29008	-0.05494
0.0675	-1.61210	0.02049	0.4711	0.6016	1.56028	0.29011	0.03282
0.0700	-1.60463	0.02272	0.4471	0.6135	1.48273	0.28957	0.10314
0.0725	-1.59688	0.02505	0.4233	0.6252	1.41071	0.28851	0.15940
0.0750	-1.58884	0.02740	0.3996	0.6367	1.34371	0.28693	0.20438
0.0800	-1.57186	0.03238	0.3527	0.6594	1.22293	0.28262	0.26851
0.0850	-1.55364	0.03761	0.3065	0.6815	1.11734	0.27714	0.30774
0.0900	-1.53413	0.04309	0.2608	0.7032	1.02459	0.27066	0.33005
0.1000	-1.49100	0.05471	0.1715	0.7454	0.87056	0.25556	0.34375
0.1100	-1.44196	0.06708	0.0845	0.7861	0.75021	0.23835	0.33552
0.1200	-1.38694	0.07991	0.0000	0.8257	0.65695	0.21991	0.31799
0.1300	-1.32593	0.09292	-0.0822	0.8644	0.58688	0.20070	0.29844
0.1400	-1.25968	0.10572	-0.1620	0.9022	0.53867	0.18116	0.28116
0.1500	-1.18985	0.11780	-0.2395	0.9393	0.51321	0.16165	0.26949
0.1600	-1.11918	0.12863	-0.3148	0.9759	0.51508	0.14255	0.26719
0.1667	-1.07356	0.13489	-0.3638	1.0000	0.53516	0.13015	0.27326
0.1700	-1.05168	0.13769	-0.3879	1.0120	0.55158	0.12406	0.27913
0.1800	-0.99074	0.14474	-0.4588	1.0476	0.61281	0.10614	0.30642
0.1875	-0.94765	0.14904	-0.5106	1.0742	0.58291	0.09265	0.30876
0.1900	-0.93185	0.15047	-0.5276	1.0830	0.52338	0.08785	0.29286
0.1925	-0.91344	0.15204	-0.5444	1.0918	0.42836	0.08271	0.26347
0.1950	-0.88961	0.15395	-0.5612	1.1005	0.38855	0.07692	0.22277
0.1975	-0.85282	0.15664	-0.5778	1.1093	0.17945	0.06965	0.17457
0.1983	-0.83436	0.15795	-0.5833	1.1122	0.13757	0.06658	0.15763
0.1992	-0.80939	0.15963	-0.5888	1.1151	0.09785	0.06286	0.14099
0.1995	-0.78840	0.16093	-0.5913	1.1164		0.06000	0.13003
0.2000	-0.77096	0.16199	-0.5943	1.1180	0.05758	0.05786	0.12210

0.19500	-1.42971	0.13137	-0.5903	1.1005	-0.149590	0.06348	0.161657
0.19250	-1.36945	0.13492	-0.5733	1.0918	-0.141451	0.05443	0.139758
0.19000	-1.30525	0.13814	-0.5562	1.0830	-0.134022	0.04607	0.123111
0.18750	-1.23812	0.14096	-0.5390	1.0742	-0.127388	0.03822	0.110087
0.18500	-1.16758	0.14339	-0.5216	1.0653	-0.121324	0.03080	0.099601
0.18250	-1.09282	0.14542	-0.5041	1.0565	-0.115622	0.02370	0.090965
0.18000	-1.01425	0.14700	-0.4865	1.0476	-0.109997	0.01685	0.083671
0.17833	-0.95951	0.14780	-0.4746	1.0417	-0.106305	0.01239	0.079425
0.17667	-0.90274	0.14838	-0.4627	1.0358	-0.102712	0.00799	0.075622
0.17500	-0.84395	0.14872	-0.4508	1.0299	-0.099309	0.00364	0.072243
0.17333	-0.78307	0.14881	-0.4388	1.0239	-0.096208	-0.00066	0.069284
0.17167	-0.72035	0.14863	-0.4267	1.0179	-0.093520	-0.00493	0.066739
0.17000	-0.65557	0.14818	-0.4146	1.0120	-0.091339	-0.00918	0.064602
0.16667	-0.52224	0.14639	-0.3901	1.0000	-0.088723	-0.01756	0.061486
0.16417	-0.42034	0.14428	-0.3716	0.9910	-0.088340	-0.02375	0.060056
0.16167	-0.31842	0.14155	-0.3530	0.9819	-0.089236	-0.02983	0.059278
0.16000	-0.25114	0.13941	-0.3404	0.9759	-0.090479	-0.03381	0.059062
0.15833	-0.18486	0.13704	-0.3279	0.9698	-0.092189	-0.03773	0.059049
0.15667	-0.11981	0.13445	-0.3152	0.9638	-0.094322	-0.04158	0.059208
0.15500	-0.05613	0.13169	-0.3026	0.9577	-0.096847	-0.04536	0.059509
0.15333	0.00589	0.12875	-0.2898	0.9516	-0.099732	-0.04907	0.059926
0.15167	0.06619	0.12568	-0.2770	0.9455	-0.102844	-0.05270	0.060474
0.15000	0.12469	0.12249	-0.2641	0.9393	-0.106453	-0.05626	0.061016
0.14833	0.18143	0.11920	-0.2512	0.9332	-0.110280	-0.05974	0.061654
0.14667	0.23611	0.11584	-0.2381	0.9270	-0.1144	-0.0631	0.0623
0.14500	0.28906	0.11240	-0.2251	0.9208	-0.1187	-0.0665	0.0630
0.14333	0.34017	0.10892	-0.2119	0.9146	-0.1233	-0.0697	0.0637
0.14167	0.39007	0.10535	-0.1987	0.9084	-0.1281	-0.0729	0.0643
0.14000	0.43707	0.10185	-0.1855	0.9022	-0.1333	-0.0760	0.0649
0.13750	0.50524	0.09651	-0.1654	0.8928	-0.1414	-0.0804	0.0658
0.13500	0.57011	0.09114	-0.1453	0.8834	-0.150	-0.085	0.066
0.13250	0.63088	0.08585	-0.1250	0.8739	-0.159	-0.089	0.067
0.13000	0.68878	0.08058	-0.1045	0.8644	-0.168	-0.093	0.067
0.12750	0.74415	0.07533	-0.0839	0.8548	-0.179	-0.097	0.067
0.12500	0.79591	0.07023	-0.0632	0.8452	-0.189	-0.100	0.065
0.12250	0.84374	0.06536	-0.0423	0.8355	-0.201	-0.103	0.065
0.12000	0.89219	0.06028	-0.0212	0.8257	-0.213	-0.106	0.063
0.11667	0.95223	0.05378	0.0071	0.8126	-0.231	-0.110	0.057
0.11333	1.00525	0.04786	0.0357	0.7994	-0.249	-0.113	0.051
0.11000	1.05235	0.04236	0.0645	0.7861	-0.268	-0.116	0.043
0.10500	1.12803	0.03320	0.1083	0.7659	-0.2992	-0.1178	0.0222
0.10000	1.19259	0.02553	0.1527	0.7454	-0.3343	-0.1183	-0.0088
0.09000	1.30480	0.01247	0.2433	0.7032	-0.41716	-0.11109	-0.135133
0.08000	1.39844	0.00299	0.3365	0.6594	-0.52188	-0.08458	-0.52282
0.07260	1.45555	0.00000	0.4070	0.6256		0.00000	

0.2008	--0.67726	0.16692	-0.5998	1.1209	0.01256	0.04773	0.09643
0.2009	-0.60230	0.17024	-0.6006	1.1214		0.04101	0.08433
0.2008	-0.53150	0.17294	-0.5998	1.1209	-0.00760	0.03518	0.07823
0.201	-0.46940	0.17500	-0.600	1.1222		0.03120	0.07085
0.201	-0.40780	0.17678	-0.598	1.1201		0.02642	0.07103
0.200	-0.31940	0.17884	-0.596	1.1189		0.02003	0.06795
0.2000	-0.22714	0.18041	-0.5943	1.1180	-0.00760	0.01405	0.06348
0.1999	--0.16310	0.18118	-0.5936	1.1176		0.01006	0.06130

Tab. 10

QUASI-ELLIPTICAL AEROFOIL SECTION 0.1200—0.7500—0.000
 PROFILE NUMBER 15
 FREE STREAM MACH NUMBER 0.8257

τ	x	y	c_p	M	M_x	θ	$1/R$
0.0428	-1.7298	0	0.7175	0.4725		0	
0.0500	-1.71287	0.00223	0.6437	0.5130	2.3038	0.17261	-3.2286
0.0508	-1.71093	0.00257	0.6353	0.5175	2.2534	0.17862	-2.8875
0.0517	-1.70896	0.00293	0.6269	0.5219	2.2045	0.18407	-2.5917
0.0533	-1.70495	0.00370	0.6102	0.5307	2.1115	0.19365	-2.1032
0.0550	-1.70092	0.00451	0.5935	0.5394	2.0242	0.20165	-1.71774
0.0567	-1.69657	0.00541	0.5770	0.5480	1.9420	0.20839	-1.40714
0.0583	-1.69221	0.00635	0.5605	0.5565	1.86457	0.21408	-1.15284
0.0600	-1.68773	0.00734	0.5441	0.5649	1.79147	0.21888	-0.94206
0.0617	-1.68311	0.00837	0.5277	0.5732	1.72238	0.22290	-0.76564
0.0633	-1.67837	0.00945	0.5115	0.5814	1.65702	0.22626	0.61676
0.0650	-1.67350	0.01058	0.4953	0.5896	1.59500	0.22901	-0.49047
0.0667	-1.66850	0.01176	0.4791	0.5976	1.53617	0.23125	-0.38268
0.0683	-1.66336	0.01297	0.4631	0.6056	1.48026	0.23302	-0.29030
0.0700	-1.65807	0.01423	0.4471	0.6135	1.42712	0.23435	-0.21092
0.0725	-1.64988	0.01619	0.4233	0.6252	1.35208	0.23570	-0.11182
0.0750	-1.64135	0.01824	0.3996	0.6367	1.28212	0.23632	-0.03216
0.0775	-1.63249	0.02038	0.3761	0.6481	1.21702	0.23632	0.03193
0.0800	-1.62325	0.02260	0.3527	0.6594	1.15609	0.23563	0.08368
0.0850	-1.60365	0.02728	0.3065	0.6815	1.04555	0.23318	0.15853
0.0900	-1.58245	0.03228	0.2608	0.7032	0.94811	0.22911	0.20617
0.1000	-1.53475	0.04313	0.1715	0.7454	0.78512	0.21788	0.25087
0.1100	-1.47910	0.05503	0.0845	0.7861	0.65468	0.20340	0.25737
0.1200	-1.41447	0.06777	0.0000	0.8257	0.55277	0.18639	0.24875
0.1300	-1.33982	0.08113	-0.0822	0.8644	0.47162	0.16815	0.23194
0.1400	-1.25460	0.09474	-0.1620	0.9022	0.40908	0.14897	0.21344
0.1500	-1.15886	0.10813	-0.2395	0.9393	0.36343	0.12914	0.19705
0.1600	-1.05412	0.12065	-0.3148	0.9759	0.33166	0.10904	0.18479
0.1667	-0.97977	0.12828	-0.3638	1.0000	0.31295	0.09547	0.17855
0.1700	-0.94094	0.13186	-0.3879	1.0120	0.30062	0.08862	0.17508
0.1800	-0.80573	0.14231	-0.4588	1.0476	0.21171	0.06629	0.14941
0.1833	-0.74041	0.14635	-0.4820	1.0595	0.15069	0.05719	0.12902
0.1850	-0.69597	0.14879	-0.4935	1.0653	0.11497	0.05174	0.11595
0.1867	-0.63413	0.15185	-0.5049	1.0712	0.07736	0.04505	0.10096
0.1883	-0.52990	0.15601	-0.5163	1.0771	0.03960	0.03549	0.08378
0.1892	-0.43000	0.15915	-0.5220	1.8000	0.02108	0.02765	0.07378
0.1896	-0.32040	0.16175	-0.5252	1.0817		0.01977	0.07024
0.1899	-0.16470	0.16403	-0.5271	1.0827		0.00981	0.06181

Tab. 11

QUASI-ELLIPTICAL AEROFOIL SECTION 0.1025—0.6750—1.3750
 PROFILE NUMBER 13
 FREE STREAM MACH NUMBER 0.7557

τ	x	y	c_p	M	M_x	θ	$1/R$
0.00000	-1.69058	0.00000	1.1510	0.0000	0.000000	1.57080	5.962550
0.01000	-1.68599	0.03897	1.0248	0.2247	5.75	1.336	5.95
0.02000	-1.68141	0.05473	0.9017	0.3194	5.79	1.239	5.94
0.03000	-1.67683	0.06656	0.7817	0.3932	5.85	1.163	5.94
0.04000	-1.67225	0.07630	0.6647	0.4564	5.897	1.0995	5.94
0.05000	-1.66767	0.08469	0.5508	0.5130	5.946	1.0428	5.941
0.06000	-1.66310	0.09208	0.4398	0.5649	5.991	0.9911	5.943
0.07000	-1.65851	0.09873	0.3317	0.6135	6.028	0.9431	5.944
0.08000	-1.65391	0.10477	0.2265	0.6594	6.052	0.8979	5.940
0.09000	-1.64928	0.11033	0.1241	0.7032	6.057	0.8550	5.929
0.10000	-1.64460	0.11550	0.0245	0.7454	6.034	0.8137	5.904
0.11000	-1.63984	0.12034	-0.0724	0.7861	5.973	0.7737	5.858
0.12000	-1.63497	0.12492	-0.1666	0.8257	5.862	0.7347	5.787
0.13000	-1.62993	0.12929	-0.2582	0.8644	5.689	0.6965	5.671
0.14000	-1.62464	0.13355	-0.3471	0.9022	5.442	0.6585	5.509
0.15000	-1.61905	0.13771	-0.4336	0.9393	5.114	0.6206	5.282
0.16000	-1.61286	0.14195	-0.5175	0.9759	4.706	0.5823	4.991
0.16667	-1.60840	0.14481	-0.5721	1.0000	4.398	0.5565	4.760
0.17000	-1.60605	0.14625	-0.5989	1.0120	4.237	0.5436	4.633
0.18000	-1.59830	0.15072	-0.6780	1.0476	3.742	0.5039	4.225
0.19000	-1.58935	0.15542	-0.7546	1.0830	3.284	0.4635	3.797
0.20000	-1.57912	0.16027	-0.8290	1.1180	2.942	0.4226	3.402
0.21000	-1.56790	0.16505	-0.9010	1.1529	2.814	0.3832	3.1064
0.22000	-1.55664	0.16935	-0.9708	1.1875	3.006	0.3468	2.992
0.23000	-1.54660	0.17279	-1.0384	1.2221	3.580	0.3145	3.111
0.24000	-1.53798	0.17546	-1.1039	1.2566	3.814	0.2863	3.130
0.25000	-1.52414	0.17926	-1.1672	1.2910	1.0314	0.2521	1.6930
0.25000	-1.48295	0.18874	-1.1672	1.2910	-0.36631	0.2070	0.75233
0.24000	-1.40363	0.20334	-1.1039	1.2566	-0.42304	0.16107	0.44926
0.23000	-1.31607	0.21597	-1.0384	1.2221	-0.35718	0.12744	0.32544
0.22500	-1.26589	0.22200	-1.0049	1.2048	-0.32686	0.11211	0.284110
0.22000	-1.21107	0.22773	-0.9708	1.1875	-0.30110	0.09740	0.251461
0.21500	-1.15159	0.23310	-0.9362	1.1702	-0.280100	0.08318	0.225478
0.21000	-1.08781	0.23797	-0.9010	1.1529	-0.263337	0.06946	0.204587
0.20500	-1.02005	0.24223	-0.8653	1.1355	-0.249612	0.05618	0.187383
0.20000	-0.94843	0.24579	-0.8290	1.1180	-0.237050	0.04329	0.172493
0.19667	-0.89843	0.24774	-0.8044	1.1064	-0.228189	0.03489	0.163222
0.19333	-0.84606	0.24935	-0.7797	1.0947	-0.218278	0.02658	0.154169

0.1900 -0.03231 0.16481 -0.5276 1.0830 0.00058 0.00195 0.06021

0.19000	-0.79100	0.25059	-0.7546	1.0830	-0.207051	0.01835	0.145239
0.18667	-0.73255	0.25141	-0.7293	1.0712	-0.194709	0.01011	0.136536
0.18333	-0.66998	0.25179	-0.7038	1.0595	-0.181884	0.00183	0.128305
0.18000	-0.60268	0.25162	-0.6780	1.0476	-0.169471	-0.00654	0.120864
0.17750	-0.54889	0.25110	-0.6584	1.0388	-0.160973	-0.01291	0.115972
0.17500	-0.49222	0.25018	-0.6388	1.0299	-0.153512	-0.01936	0.111760
0.17250	-0.43282	0.24884	-0.6189	1.0209	-0.147289	-0.02589	0.108267
0.17000	-0.37098	0.24703	-0.5989	1.0120	-0.142407	-0.03250	0.105494
0.16667	-0.28542	0.24387	-0.5721	1.0000	-0.138001	-0.04140	0.102864
0.16333	-0.19766	0.23984	-0.5449	0.9880	-0.135869	-0.05037	0.101343
0.16000	-0.10880	0.23496	-0.5175	0.9759	-0.135782	-0.05936	0.100786
0.15750	-0.04222	0.23077	-0.4967	0.9668	-0.136902	-0.06609	0.100911
0.15500	0.02383	0.22618	-0.4758	0.9577	-0.138923	-0.07278	0.101436
0.15250	0.08893	0.22122	-0.4548	0.9485	-0.141754	-0.07943	0.102308
0.15000	0.15259	0.21594	-0.4336	0.9393	-0.145320	-0.08602	0.103478
0.14750	0.21513	0.21034	-0.4122	0.9301	-0.149557	-0.09254	0.104903
0.14500	0.27584	0.20451	-0.3907	0.9208	-0.154419	-0.09899	0.106546
0.14250	0.33476	0.19847	-0.3690	0.9115	-0.159866	-0.10535	0.108370
0.14000	0.39183	0.19225	-0.3471	0.9022	-0.165876	-0.11163	0.110343
0.13750	0.44699	0.18590	-0.3251	0.8928	-0.172426	-0.11781	0.112434
0.13500	0.50021	0.17944	-0.3030	0.8834	-0.179509	-0.12390	0.114613
0.13250	0.55152	0.17289	-0.2807	0.8739	-0.187111	-0.12989	0.116848
0.13000	0.60092	0.16629	-0.2582	0.8644	-0.1953	-0.1358	0.1192
0.12667	0.66387	0.15744	-0.2279	0.8516	-0.2070	-0.1435	0.1226
0.12333	0.72358	0.14859	-0.1974	0.8387	-0.2196	-0.1509	0.1245
0.12000	0.78037	0.13974	-0.1666	0.8257	-0.233	-0.158	0.130
0.11667	0.83405	0.13097	-0.1355	0.8126	-0.248	-0.165	0.129
0.11333	0.88490	0.12230	-0.1041	0.7994	-0.264	-0.172	0.132
0.11000	0.93307	0.11377	-0.0724	0.7861	-0.281	-0.179	0.133
0.10500	1.00051	0.10125	-0.0243	0.7659	-0.309	-0.188	0.134
0.10000	1.06262	0.08914	0.0245	0.7454	-0.340	-0.197	0.131
0.09500	1.11930	0.07762	0.0739	0.7245	-0.376	-0.204	0.125
0.09000	1.17250	0.06644	0.1241	0.7032	-0.4156	-0.2100	0.1121
0.08500	1.22095	0.05598	0.1749	0.6815	-0.4602	-0.2150	0.0910
0.08000	1.26560	0.04614	0.2265	0.6594	-0.51079	-0.21843	0.057322
0.07000	1.34448	0.02855	0.3317	0.6135	-0.63463	-0.21848	-0.07781
0.06000	1.41119	0.01412	0.4398	0.5649	-0.8010	-0.20369	-0.42141
0.05500	1.44054	0.00830	0.4949	0.5394	-0.9072	-0.18610	-0.7959
0.05000	1.46746	0.00362	0.5508	0.5130	-1.0348	-0.1549	-1.5593
0.04255	1.50134	0.00000	0.6353	0.4714		0.00000	

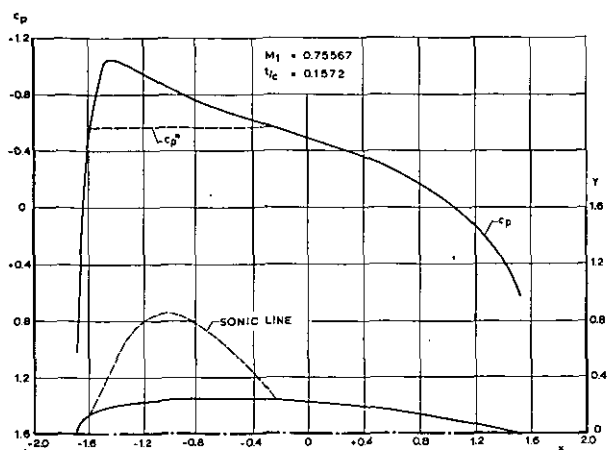


Fig. 1 Section 0.1025-0.675-1.3.

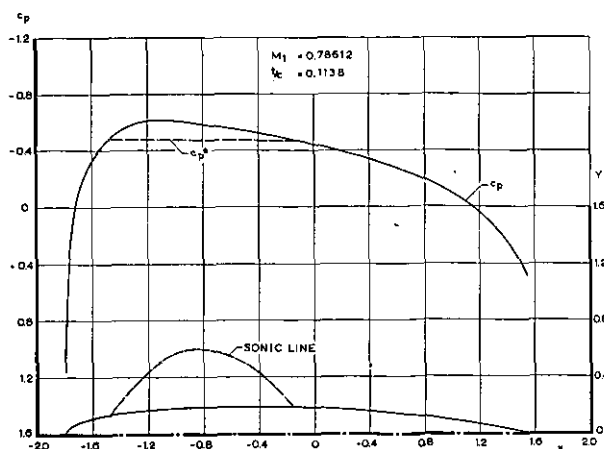


Fig. 4 Section 0.1100-0.75-0.9.

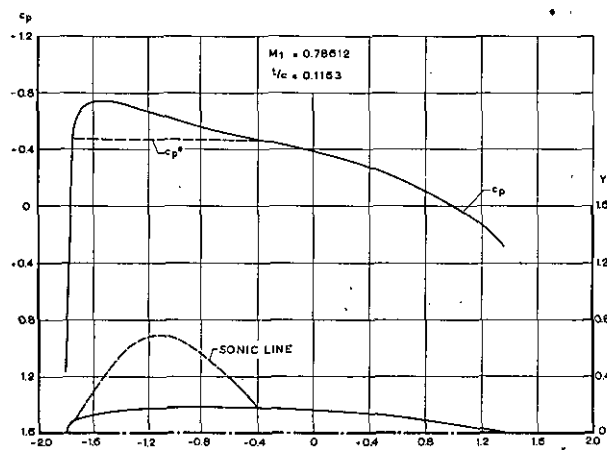


Fig. 2 Section 0.11-0.75-1.25.

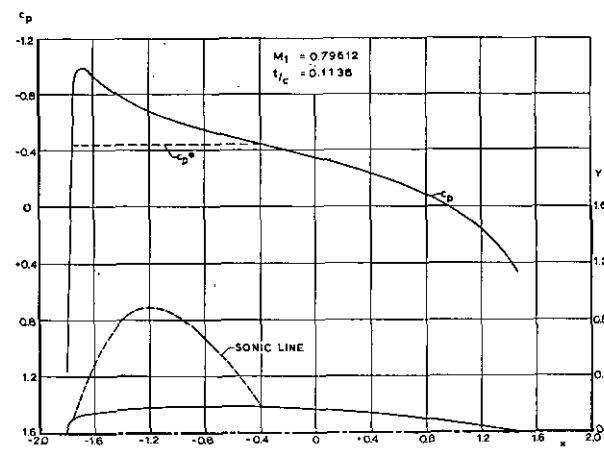


Fig. 5 Section 0.1125-0.75-1.325.

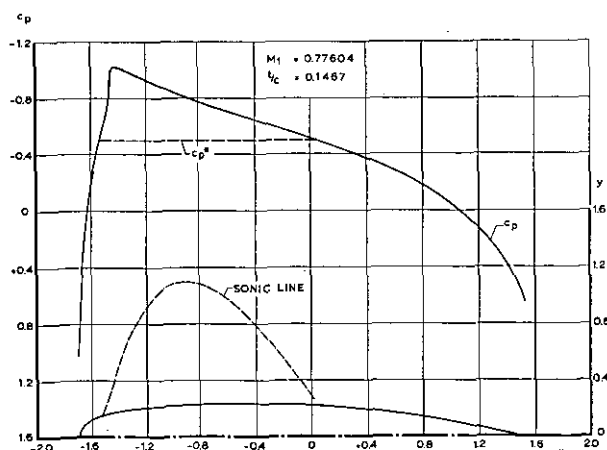


Fig. 3 Section 0.1075-0.675-1.05.

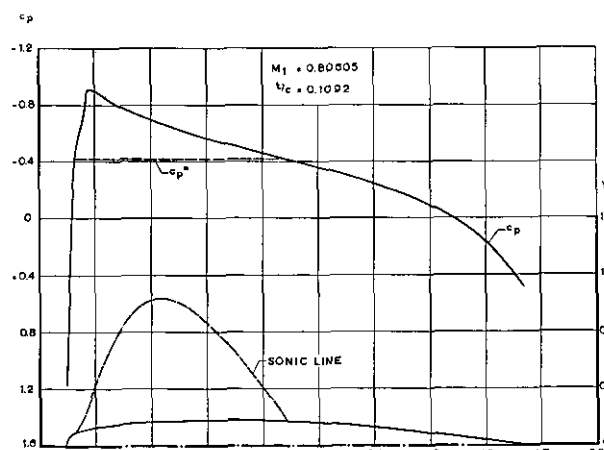


Fig. 6 Section 0.1150-0.85-1.20.

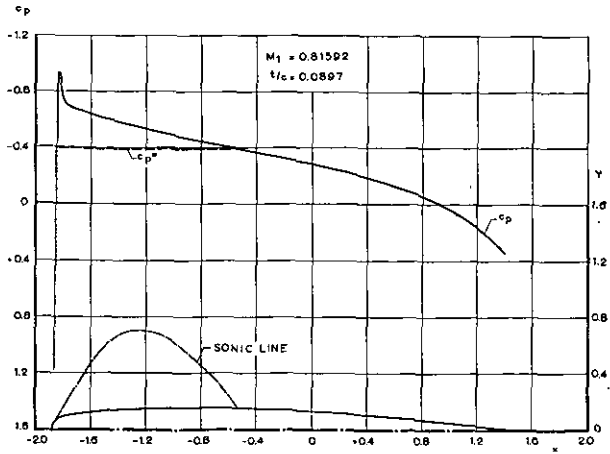


Fig. 7 Section 0.1175-0.8-1.26.

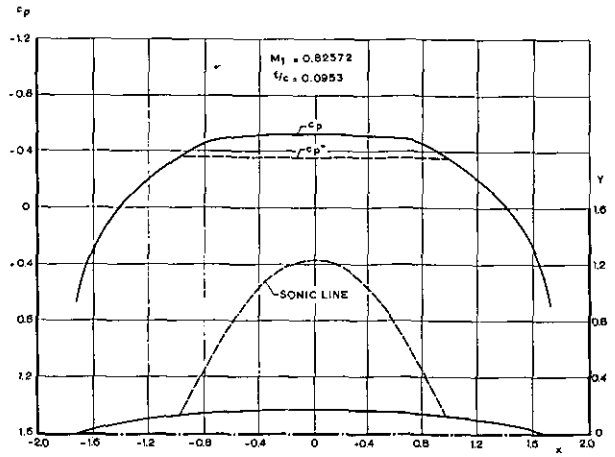


Fig. 9 Section 0.12-0.75-0.0.

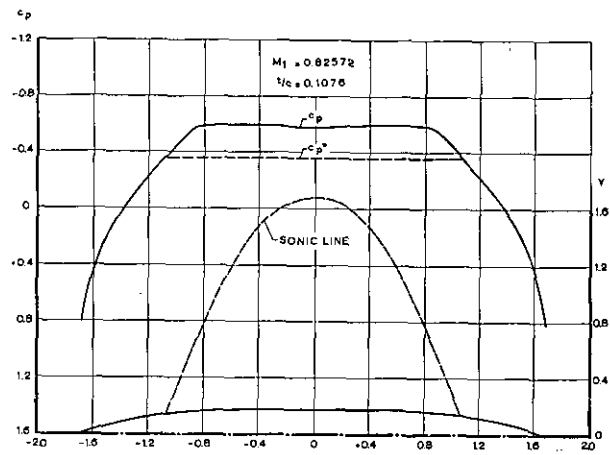


Fig. 8 Section 0.12-0.7-0.0.

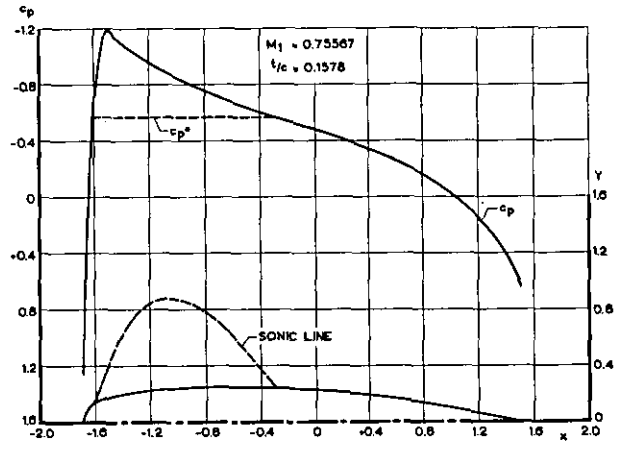
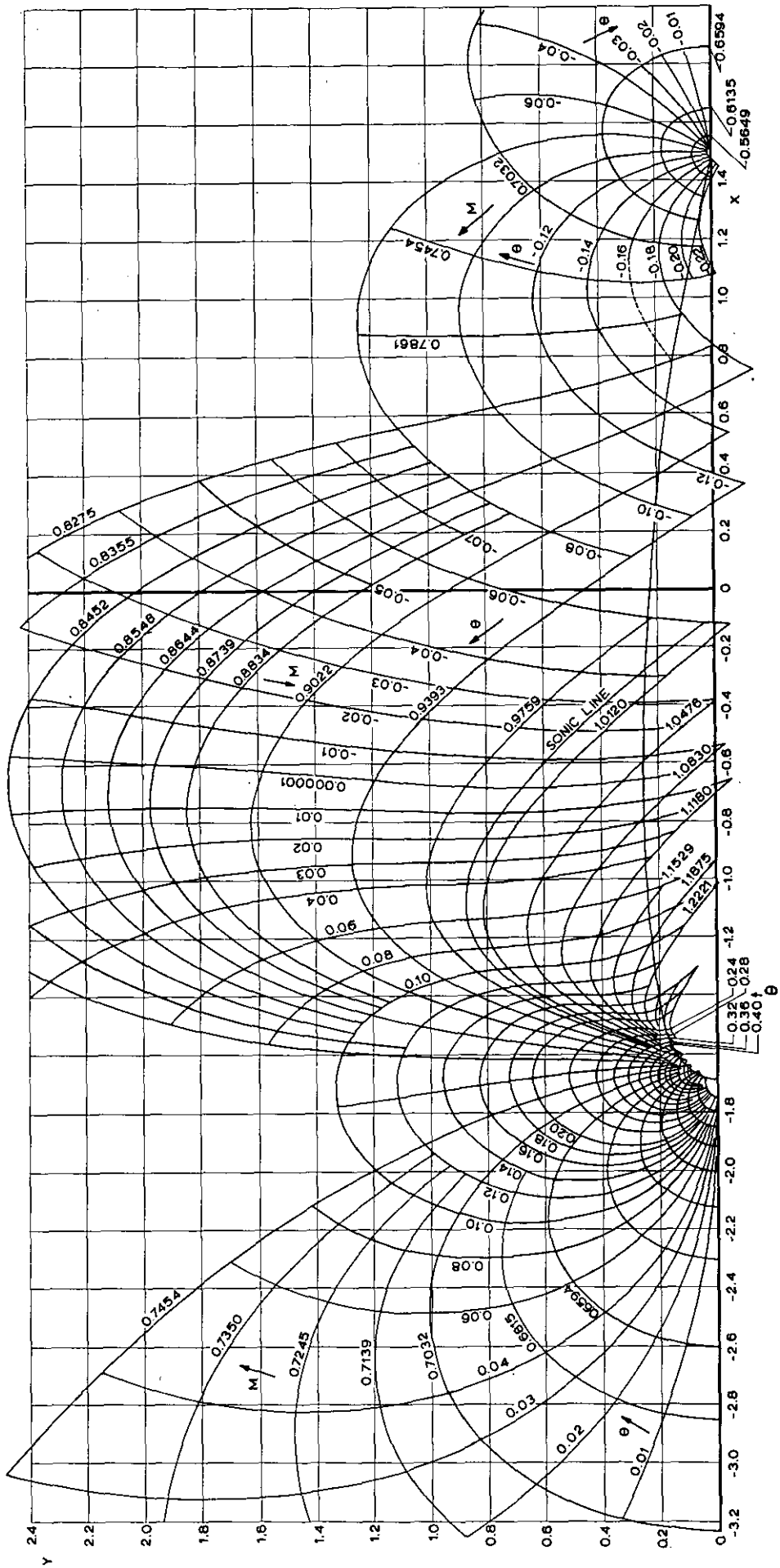


Fig. 10 Section 0.1025-0.675-1.375.



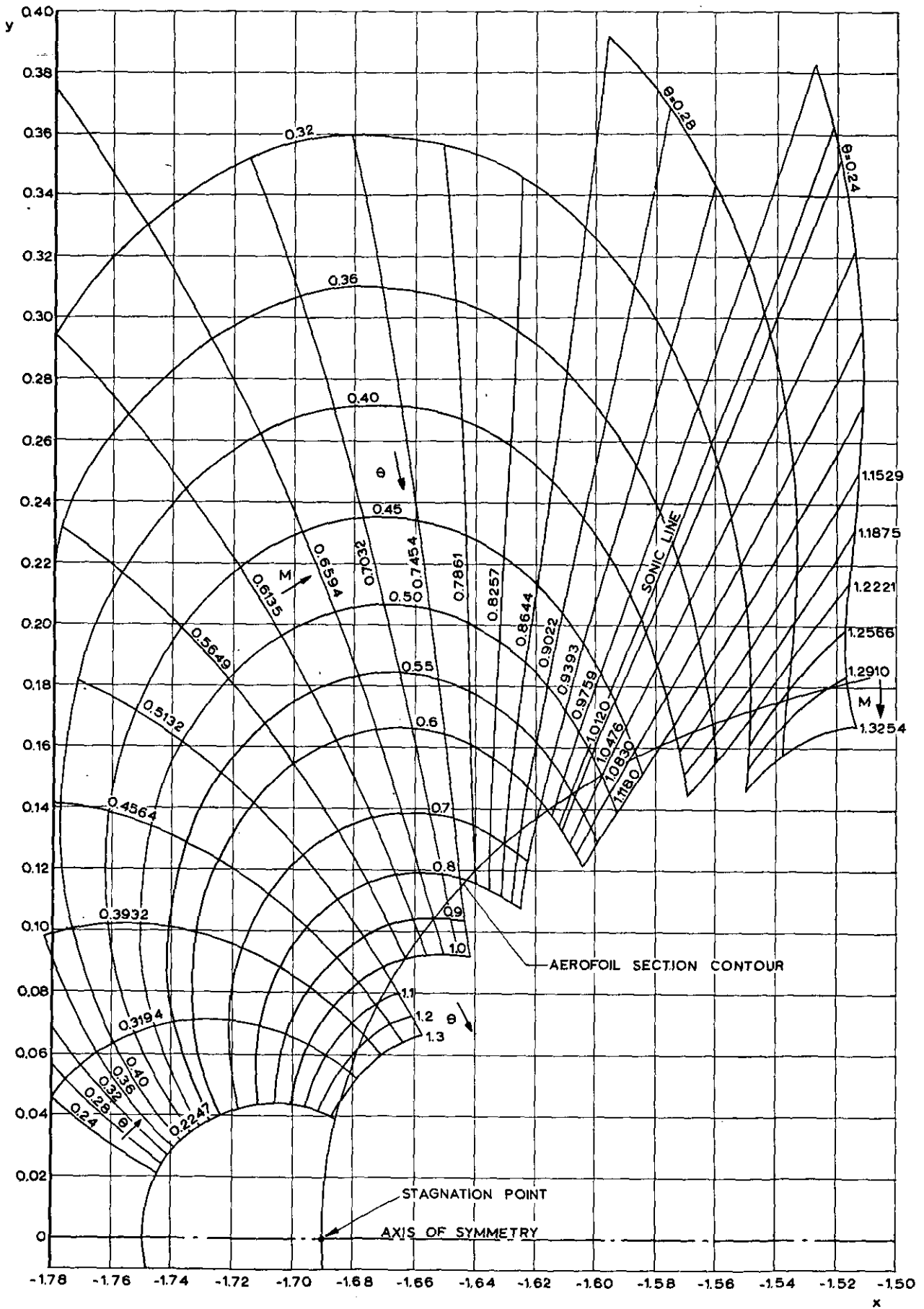


Fig. 12 Flow field around leading edge of section 0.1025-0.675-1.375.

